Cathodoluminescence Microscopy of Inorganic Solids

B. G. Yacobi and D. B. Holt

Cathodoluminescence Microscopy of Inorganic Solids

Cathodoluminescence Microscopy of Inorganic Solids

B. G. Yacobi
Gatan Research and Development
Pleasanton, California

and

D. B. Holt
Imperial College of Science and Technology
University of London
London, England

Springer Science+Business Media, LLC

Library of Congress Cataloging-in-Publication Data

Yacobi, B. G.
Cathodoluminescence microscopy of inorganic solids / B.G. Yacobi and D.B. Holt.
p. cm.
Includes bibliographical references.
ISBN 978-1-4757-9597-4 ISBN 978-1-4757-9595-0 (eBook)
DOI 10.1007/978-1-4757-9595-0
1. Cathodoluminescence. 2. Solids--Optical properties.
3. Materials--Optical properties. 4. Chemistry, Inorganic.
I. Holt, D. B. II. Title.
QC479.5.Y33 1990
620.1'1295--dc20 89-26631
CIP

Originally published by Plenum Press, New York in 1990
Softcover reprint of the hardcover 1st edition 1990

Preface

Microcharacterization of materials is a rapidly advancing field. Among the many electron and ion probe techniques, the cathodoluminescence mode of an electron probe instrument has reached a certain maturity, which is reflected by an increasing number of publications in this field. The rapid rate of progress in applications of cathodoluminescence techniques in characterizing inorganic solids has been especially noticeable in recent years.

The main purpose of the book is to outline the applications of cathodoluminescence techniques in the assessment of optical and electronic properties of inorganic solids, such as semiconductors, phosphors, ceramics, and minerals. The assessment provides, for example, information on impurity levels derived from cathodoluminescence spectroscopy, analysis of dopant concentrations at a level that, in some cases, is several orders of magnitude lower than that attainable by x-ray microanalysis, the mapping of defects, and the determination of carrier lifetimes and the charge carrier capture cross sections of impurities. In order to make the book self-contained, some basic concepts of solid-state physics, as well as various cathodoluminescence techniques and the processes leading to luminescence phenomena in inorganic solids, are also described.

We hope that this book will be useful to both scientists and graduate students interested in microcharacterization of inorganic solids. This book, however, was not intended as a definitive account of cathodoluminescence analysis of inorganic solids. In considering the results presented here, readers should remember that many materials have properties that vary widely as a function of preparation conditions.

We are grateful to many authors for supplying illustrations and reprints of their work, and for their permission, together with the permission of the publishers, to reproduce their diagrams and micrographs.

B. G. Yacobi
D. B. Holt

Newton and London

Contents

1

Introduction

Cathodoluminescence is the emission of light as the result of electron ("cathode-ray") bombardment. This phenomenon, first reported in the middle of the last century, was observed during the experiments on electrical discharges in evacuated glass tubes, which exhibited luminescence when cathode rays struck the glass. In fact, the observation of luminescence due to cathode ray bombardment led Thomson at the end of the nineteenth century to the discovery of the electron and the determination of its charge-to-mass ratio e/m (Thomson, 1897). Other luminescence phenomena, such as, for example, photoluminescence, have been known and studied for much longer periods of time, since they do not require vacuum and concentrated sources of electrons, which are not readily available in the terrestrial environment.

Cathodoluminescence is an important technological phenomenon that is most widely used in modern cathode-ray tube (CRT)-based instruments, such as oscilloscopes and television and computer terminals, and in electron microscope fluorescent screens. With the developments of electron microscopy techniques in recent decades, cathodoluminescence has emerged as an important microcharacterization tool for the analysis of luminescent materials.

Advances in understanding and applications of materials require parallel developments in characterization techniques. In order to elucidate macroscopic phenomena in solids, one must understand and characterize their properties on a microscopic level. This task is accomplished by using, for example, a battery of techniques that utilize effects of irradiating materials with photons, electrons, or ions. The signals from a solid under bombardment in terms of, for example, backscattered and transmitted particles and photons, diffracted waves, or processes that occur in the bulk of a solid provide the information utilized in characterization techniques.

The continuing progress in solid-state electronics directed toward further miniaturization of electronic devices presents a great challenge from the characterization point of view. It is now feasible to generate patterns on the submicron scale, and there is even an ongoing discussion on feasibility of ultra-submicron-level electronic devices. Naturally, we need microcharacterization techniques to investigate these devices.

In an electron probe instrument, electron irradiation of a solid results in a variety of useful signals (Figure 1.1). Primary (i.e., incident or beam) electrons may be backscattered from the specimen with little or no energy loss, or they will lose energy to produce secondary electrons. Some primary electrons, absorbed in the bulk of the material, will dissipate their energy in various electronic excitations, leading to the emission of characteristic x-rays; the generation of electron-hole pairs, which themselves may lead to the emission of photons in the ultraviolet, visible, and infrared spectral ranges (i.e., cathodoluminescence) or to various charge collection signals in devices; the generation of Auger electrons; and thermal effects, including electroacoustic (thermal wave) signals. In thin specimens, transmitted electrons may be scattered elastically (with no energy loss) or inelastically (with energy loss). All these processes lead to the formation of signals that can be used in the characterization of structural, chemical, and electronic properties of the material.

Scanning electron microscopy (SEM) and scanning transmission electron microscopy (STEM) techniques are well suited for the microcharacterization of

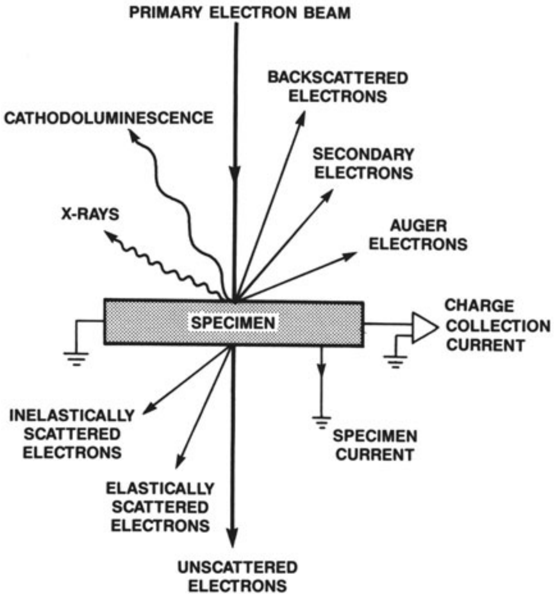

Figure 1.1. Schematic diagram of types of interaction (or signal) available due to electron beam interaction with a solid.

materials, since they provide high spatial resolution and the simultaneous availability of a variety of modes, such as x-ray microanalysis; secondary (voltage contrast), backscattered, and transmitted electron images; scanning electroacoustic microscopy (SEAM); cathodoluminescence (CL); and charge collection signals. The last three modes constitute the electronic microcharacterization capability of the SEM (or STEM). Note that CL is unique among all the SEM modes in that it is the only contactless method that provides microcharacterization of the optical and electronic properties of luminescent materials. Recent applications in a variety of studies have demonstrated the great value of the CL mode in characterizing the optical and electronic properties of materials with a spatial resolution of the order of 1 μm and less. An important consideration in STEM applications is that transmitted signals will depend on the thickness of the material, in addition to its properties.

In general, CL analysis performed in an electron microscope can be divided into *microscopy* and *spectroscopy*. In the former, luminescence images or maps of regions of interest can be displayed; in the latter, a spectrum corresponding to a selected area of the sample (a *point analysis* in the terminology of x-ray microanalysis) can be obtained.

Many SEM modes have been described in books listed in the bibliography. Several of these modes were also described in *Journal of Applied Physics* reviews by Niedrig (1982) on electron backscattering, Leamy (1982) on charge collection, Joy, Newbury, and Davidson (1982) on electron channeling, Seiler (1983) on secondary electron emission, and Yacobi and Holt (1986) on cathodoluminescence.

Cathodoluminescence analysis can also be performed in a relatively simple high-vacuum chamber equipped with an electron gun and optical windows. Although the absence of scanning capability limits its applications, it is still very useful in, for example, depth-resolved studies of ion-implanted samples and characterization of semiconductor interfaces. Nondestructive depth-resolved CL studies are performed by varying the range of the electron penetration, which depends on the electron beam energy (see Chapters 4 and 6), in order to excite CL from different depths in the material. Moreover, simple "flood illumination" electron bombardment can produce large total CL intensities, enabling higher spectral resolution to be attained. For this reason, a SEM intended for CL use should provide the largest possible maximum electron beam current (1 μA at least) with a widely defocused electron probe size.

Cathodoluminescence offers a contactless and relatively "nondestructive" method for microcharacterization of luminescent materials. Some clarification of the term "nondestructive" is required. Often an analysis is considered to be nondestructive if the physical integrity of the material remains intact. However, in certain cases electron irradiation may ionize or create defects and so alter electronic properties of the material temporarily or permanently.

The mechanisms leading to the emission of light in a solid are similar for different forms of the excitation energy. Cathodoluminescence and other luminescence phenomena, such as photoluminescence (PL), yield similar results with some possible differences associated with the details of the excitation of electron-hole pairs, for example in the generation rate and excitation volume. Electron beam excitation in general leads to emission by all the luminescence mechanisms present in the semiconductor. On the other hand, PL emission may strongly depend on the excitation (photon) energy, which can provide additional important information. An advantage of CL, in addition to the high spatial resolution, is its ability to obtain more detailed depth-resolved information by varying the electron beam energy. An additional advantage of CL-SEM analysis is the availability of complementary information obtained from such SEM modes as electron beam–induced current (EBIC) and x-ray microanalysis (or, as often referred to, electron probe microanalysis, EPMA).

The need for microcharacterization of the electronic properties of inorganic solids, and especially of semiconductors, led to the development of the quantitative capabilities of EM techniques. In this context, it is useful to compare the CL technique with the x-ray microanalysis technique. Both utilize the detection of electromagnetic radiation from the electron-bombarded material. Quantitative interpretation of cathodoluminescence, however, is difficult because, unlike x-ray microanalysis, it cannot be unified under a simple law. Characteristic x-rays are emitted due to electronic transitions between sharp, inner-core levels (Figure 1.2). The lines, therefore, are narrow, characteristic of the particular chemical element, and are unaffected by the environment of the atom in the lattice. In addition, there is a general rule for identifying the element using Moseley's law, which relates the frequency ν of an x-ray line to the atomic number Z ($\nu \propto Z^2$). The CL signal is formed by detecting photons of the ultraviolet, visible, and near-infrared regions of the spectrum. These photons are emitted as the result of electronic transitions between the conduction and valence bands and levels lying in the band gap of the material (Figure 1.2). Many useful signals in these cases are due to transitions that involve impurities and a variety of defects. Therefore, there is no general rule, analogous to Moseley's law, that would serve to identify

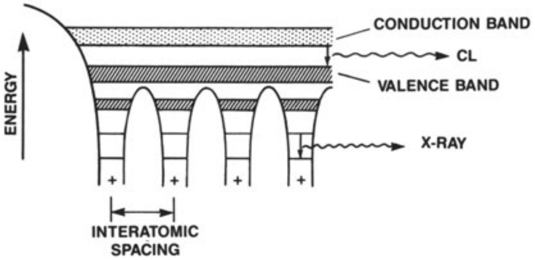

Figure 1.2. Energy band diagram of a one-dimensional lattice.

bands or lines in the CL spectrum. The influence of defects, of the surface and of various external perturbations, such as temperature, electric field, and stress, have to be considered in the analysis of the CL signal. (For a summary of effects of various external perturbations on the properties of semiconductors, see Pankove, 1971.) Correction of CL signals for all the factors that may affect the emission of photons from a material is a formidable task compared with the analogous *ZAF* correction procedure for x-ray photons (the correction for the atomic number Z, which affects the efficiency of characteristic x-ray emission; the absorption A of x-ray photons of one element by another, which may reduce the count rate; and fluorescence F, i.e., the increase in the count rate of one element that absorbs x-ray photons from another element and reemits photons at its characteristic energy). The *ZAF* correction can be easily performed for most cases by using microcomputers. In comparison, quantitative CL analysis is still in its infancy because of the lack of any generally applicable theory for the wide variety of possible types of luminescence centers and radiative recombination mechanisms. In addition to these problems, luminescence can describe *only* radiative emission processes. Nonradiative recombination events can be deduced only from CL images, provided the contrast between radiative and nonradiative sites is sufficiently strong. However, quantitative information on defect-induced nonradiative processes is unavailable in spectroscopic CL analysis. And even though in some cases the demonstrated sensitivity of CL point analysis is several orders of magnitute better than EPMA, some elements do not emit CL, or they emit with subsequent strong absorption, or they emit in an energy range where no efficient detectors are available. The nature of an impurity can best be determined by comparison with luminescence data in the literature, and its concentration can best be found by comparison with intentionally doped standards (provided no additional factors, such as the presence of nonradiative defects, affect the luminescence signal). If no published data are available about the observed emission band, an *ab initio* study must be carried out. The absence of any general method of identification and the lack of any universally applicable quantitative theory impose general limitations on developments of CL as an analytical technique.

There are three main advantages which motivate further developments of the CL technique: (1) CL is the only contactless method (in an electron probe instrument) that provides microcharacterization of the optical and electronic properties (related to the fundamental band structure) of luminescent materials; (2) in favorable cases (i.e., when an impurity is an efficient recombination center and competing centers and self-absorption are absent), the detection limit can be as low as 10^{14} atoms cm^{-3}, which is several orders of magnitude lower than that of the x-ray mode; (3) in light-emitting optoelectronic materials and devices, the emission properties are of practical importance.

To summarize, no universal theoretical approach is available to describe the luminescence centers and processes, and thus no unified theory of quantitative CL analysis can be presented and correlated with experimental data at this juncture. Compared to x-ray microanalysis, quantitative CL is in its infancy. The major purpose of this book is to provide a basis for further developments of quantitative CL and to outline its applications in the analysis of inorganic solids.

Solids are investigated by scientists from many fields, such as physics, materials science, chemistry, and engineering. Naturally, some ambiguity about materials classification is to be expected. From the view of a materials scientist, for example, most inorganic solids can be classified as ceramics, whereas a physicist would rather distinguish between metals, semiconductors, and insulators. Materials such as SiC, ZnO, and SiO_2, for example, could have been treated in several chapters of the book. The subject index, however, should help in locating specific material of interest.

To develop a systematic description of cathodoluminescence of inorganic solids, we need some basic principles of solid-state physics. Chapter 2 highlights some of these concepts.

There are two basic needs for development of CL analysis. First, theoretical analysis of luminescence spectra in general and semiempirical expressions relating CL signal characteristics to materials properties are required for the quantitative interpretation of results. Second, the CL detection system should be available to provide a high sensitivity and spectral resolution with carefully calibrated characteristics. The basic principles of luminescence and cathodoluminescence phenomena are discussed in Chapters 3 and 4; various CL techniques are described in Chapter 5.

Applications of CL analysis to various materials are discussed in Chapter 6, with emphasis placed on studies of semiconductors, which are described in more detail in Chapter 7. Chapter 8 is devoted to CL processes in phosphors, with emphasis on CL microcharacterization of these materials. In Chapters 9 and 10, applications of CL analysis to ceramics and minerals are discussed. Some ideas on future developments are presented in Chapter 11.

2

Introduction to Basic Concepts of Solid State Physics

The purpose of this chapter is to highlight some basic concepts of the solid state that are important in the description of cathodoluminescence. Detailed introductions to solid-state physics are available in the textbooks listed in the bibliography.

2.1. Structure and Bonding

The basic categories of inorganic solids, as distinguished on the basis of their structural order, are crystalline, polycrystalline, and amorphous. In crystalline solids the atoms are arranged in a periodic, regularly repeated three-dimensional pattern. This periodic array of atoms with long-range order is called a *lattice*. Polycrystalline materials are composed of numerous crystalline regions, called *grains*, with different orientation. The region between crystallites in this case is called a *grain boundary*. Amorphous solids posses only short-range order with no periodic structure.

In the crystalline material the entire solid can be recreated by repetitive translation of the so-called primitive cell in three dimensions. For geometrical convenience, it is also possible to choose a larger atomic pattern, a *unit cell*, as a building block of the crystal. The length of the edge of the unit cell is called the *lattice constant*.

Crystalline solids, in principle, can be classified on the basis of their structural symmetry. Although important, such a classification of solids cannot entirely reflect their physical properties. A classification of solids that explains, for example, the electrical and optical properties is based on the electronic energy-band structure of the crystal.

We will first introduce some definitions for the description of the crystalline structure. Many crystals exhibit anisotropy of physical properties, i.e., differences in, for example, electrical and optical properties as a function of crystallographic directions. Thus, for the description of crystalline solids, notations for describing planes and directions in crystals are required.

All crystal structures are produced by repeating an atom or a group of atoms at each point of one of the 14 Bravais space lattices. These all belong to one of the seven systems of axes. The unit vectors along the axes, **a**, **b**, and **c** are called the basis vectors and may be taken as the edges of a unit cell. This unit cell is then translated by integral multiples of the basis vectors to form a lattice. Planes in a three-dimensional lattice are identified by their intercepts along the crystal axes expressed as integral multiples of the basis vectors. The reciprocals of these numbers converted to the smallest set of integers of the same ratio are the *Miller indices* (hkl) for the set of parallel planes. When an intercept along any axis is negative, a bar is placed over that index, for example, ($\bar{h}kl$). Some planes of the cubic system, for example, are shown in Figure 2.1. The set of symmetrically equivalent planes is denoted $\{hkl\}$. Thus, the set of all six cube faces is designated $\{100\}$. Directions in the crystal are expressed by their integral components along the axes, with the notation $[hkl]$. The equivalent directions are designated as $\langle hkl \rangle$. Note that in cubic systems a direction $[hkl]$ is normal to the plane (hkl). This is, however, not so for other crystal systems. In the hexagonal structure the planes are referred to three coplanar axes at 120° to each other and one axis normal to them. The indices in this case are ($hkil$).

The configurations of atoms in many crystalline solids can be represented by a close-packed arrangement of identical spheres. In three dimensions, there are three possible positions for other close-packed planes on top of a first such layer, namely, A, B, or C (see Figure 2.2). This leads to several structures with different stacking sequences. ABCABC... stacking produces the face-centered cubic (f.c.c.) structure of one atom at each point of an f.c.c. Bravais lattice. ABAB... stacking produces the hexagonal close-packed structure based on the simple hexagonal lattice. The crystal structures of the important semiconducting materials are closely related to these but are produced by stacking pairs of planes of atoms vertically above one another, in arrays like those of Figure 2.2. Thus, the diamond cubic structure of Si, for example, has the stacking sequence AαB-

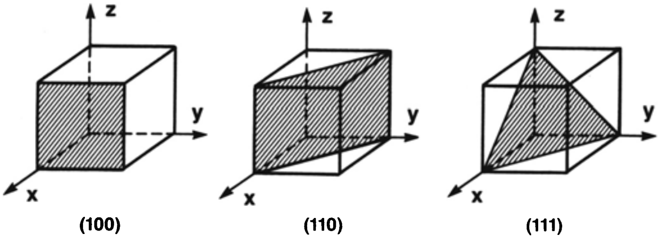

Figure 2.1. Miller indices of some planes in cubic lattices.

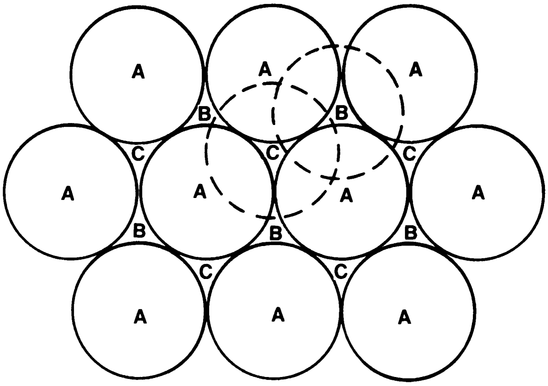

Figure 2.2. A close-packed layer of equal spheres. A, B, and C are three possible stacking positions for successive planes of atoms.

βCγAαBβCγ..., where the roman and greek letter pairs denote vertically placed planes of atoms. The sphalerite or zinc blende structure of, for example, GaAs has the same stacking sequence but now the roman letter planes consist of one element (e.g. Ga), and the greek letter sites are occupied by the other element (As). For brevity the greek letters are sometimes omitted. The wurtzite structure has the stacking sequence AαBβAαBβ.... More complex stacking sequences called *polytypes* are also possible. In the case of ZnS, for example, the zinc blende (sphalerite) structure corresponds to the cubic (often denoted 3C) packing ABCABC.... The wurtzite form corresponds to the hexagonal (often denoted 2H) packing ABABAB.... The polytype 4H can be represented by ABACABAC....

Many semiconductors have the diamond structure, which can be described as an f.c.c. structure with eight atoms in the cubic unit cell. Every atom in this arrangement has four neighbors in a tetrahedral coordination.

The solid state, as mentioned earlier, can be classified on the basis of its structural properties. However, more relevant to our purpose is the classification scheme based on the bonding configurations of atoms.

In a crystal, atoms are held together by a balance between the attractive forces that are dominant at larger interatomic distances and the repulsive forces dominant at smaller distances. Equilibrium between these forces occurs at the interatomic spacing in the crystal. The interatomic forces are quantum mechanical in nature, and they largely depend on the distribution of the outer electrons around the nucleus and whether the solid is composed of one type of atom (such as Si, for example) or more than one type of atom (for example, GaAs or ZnS). There are five basic types of bonding: ionic, covalent, metallic, molecular, and hydrogen types. In some cases it is possible to classify solids by the type of bonding. In many solids, however, the bonding between atoms is of mixed character; for example, the interatomic forces may be partially ionic and partially covalent.

The ionic bond is formed between strongly electropositive and electronegative elements (for example in alkali halides). In such solids electrons are transferred from one atom to another. In contrast, in covalent bonding the electrons are shared between neighboring atoms. In many compounds the electrons are not shared equally between the atoms. This leads to partial ionization and mixed ionic and covalent bonding. There is a range of compounds with continuous transition from ionic, through mixed, to covalent bondings. In the metallic bond the valence electrons are free to migrate between atoms, and thus they are shared by all the atoms in the solid. The bonding in this case is between the positive ions and the negative electron gas. The relatively weak molecular, or van der Waals, bonding is due to the van der Waals attractive force between atoms with closed shells (e.g., inert gas atoms). In this case the attractive force is due to the electric dipoles caused by the vibrating electron cloud. In most cases, this force is overshadowed by one of the stronger forces present. However, for atoms with closed shells (e.g., inert gas atoms), it is the weak van der Waals bonding that holds atoms together in the solid. The hydrogen bond is formed in a compound of hydrogen and strongly electronegative atoms (e.g., oxygen). In this case the hydrogen is positively charged, and it thus can be shared between neighboring atoms or molecules. The luminescent inorganic solids of concern in this book have largely mixed ionic and covalent bondings.

2.2. Energy Levels of Electrons in Solids

The physical processes in solids can be explained by the quantum theory of energy bands. With the formation of a solid, the electron wave functions of constituent atoms overlap. The application of the Pauli exclusion principle in this case leads to the splitting of the discrete energy levels of the isolated atoms into bands of allowed electron levels separated by forbidden gaps. The electron occupation of the highest energy bands (i.e., the valence and conduction bands), which are separated by a (fundamental) energy gap E_g, determines the electrical and optical properties of a solid. Thus, depending on the occupation of these bands and the size of E_g, solids are classified as conductors, semiconductors, and insulators. Solids with partially filled bands are metallic. Solids with a relatively narrow band gap separating a filled valence band and an empty conduction band are semiconductors. Similarly, solids with a wider band gap, a filled valence band, and an empty conduction band are insulators. At elevated temperatures, in the conduction band there will be more thermally excited electrons in a semiconductor than in an insulator.

Important information about the physical properties of crystalline solids is expressed by the electronic energy-band structure. This consists of the relationship between the energy and momentum, as well as the distribution, the density, and the occupancy of allowed states as a function of energy.

The application of a wave approach to free particles leads to a relation between the momentum **p** and the wave vector **k,** where k is related to the wavelength as $k = 2\pi/\lambda$. Since $p = h/\lambda$, the relationship $p = \hbar k$ is obtained. Thus, the energy of free electrons is $E = \hbar^2k^2/2m$.

In quantum mechanics, an electron is described by a wave function ψ satisfying Schrödinger's equation

$$H\psi = E\psi \tag{2.1}$$

where H is the Hamiltonian operator,

$$H = (-\hbar^2/2m)\,\nabla^2 + V(\mathbf{r}) \tag{2.2}$$

E is the energy of the electron, and $V(\mathbf{r})$ is the potential energy distribution, which is zero for a free electron and for an electron inside a potential well, or is a periodic function in the crystalline solid. The physical meaning of ψ is that $|\psi|^2\,dV$ represents the probability of finding an electron in the volume dV. The solution of Schrödinger's equation, with appropriate boundary conditions, leads to quantized energy levels for electrons inside a potential well. In crystalline solids, the periodic potential $V(\mathbf{r})$ applies. The solution of Schrödinger's equation in this case is in terms of the periodic Bloch functions

$$\psi(\mathbf{r}) = u(\mathbf{r})\exp(i\mathbf{k}\bullet\mathbf{r}) \tag{2.3}$$

where $u(\mathbf{r})$ is a periodic function, with the period of the crystal structure, which depends on the value of **k.** Since interatomic distances and the potential energy distribution in real crystals depend on the direction, the $E(\mathbf{k})$ relationship is also a function of the crystallographic orientation. Figure 2.3 presents the $E(\mathbf{k})$ dia-

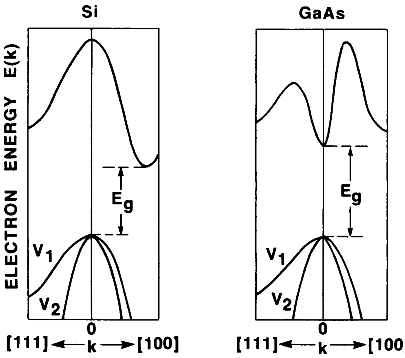

Figure 2.3. The energy bands for Si and GaAs in the [100] and [111] directions. Note that in the valence bands there are both heavy (V_1) and light (V_2) holes.

grams for two crystal directions of Si and GaAs (a more complete description should be visualized in three dimensions). In three dimensions, discontinuities of the bands occur at **k**-values of $\pm n\pi/a$ (where n is an integer) due to Bragg reflection. The locus of these energy-band discontinuities are boundaries in **k**-space enclosing Brillouin zones.

The effective mass m^* of an electron in the periodic potential of the lattice is different from the free-electron mass, and it depends on the curvature of the $E(k)$ relationship; i.e., $m^* = \hbar^2(d^2E/dk^2)^{-1}$.

As can be seen in Figure 2.3, in some cases (e.g., Si) the maximum of the valence band does not occur at the same wave vector **k** as the minimum of the conduction band. The solid in this case is an indirect-gap material. If the band extrema occur at the same wave vector **k** (e.g., GaAs), the solid is a direct-gap material.

In quantum mechanics, a particle may be described in terms of a wave packet of length Δx, which is the resultant of individual waves with different amplitudes and nearly equal wavelengths. The position of the particle is defined so that the probability of finding the particle at the center of the packet is highest. For smaller Δx, the position of the particle is more accurately defined. However, since the range of wavelengths $\Delta\lambda$ in the packet now must be wider, there is greater uncertainty in the momentum Δp. The particle's uncertainties are related by Heisenberg's uncertainty principle

$$\Delta x \, \Delta p \geq \hbar/2 \tag{2.4}$$

which implies that on an atomic scale it is impossible to measure simultaneously the precise position and momentum of a particle.

In a semiconductor containing no impurities or defects (i.e., an intrinsic semiconductor), at temperatures above 0 K some thermally excited electrons are promoted from the valence band to the conduction band. An unoccupied state in the valence band is called a *hole,* and it may be regarded as a positive charge carrier that can contribute to the conduction process. Electronic transitions across the band gap to the conduction band lead to a spontaneous generation of holes in the valence band, and the generated carriers are described as electron-hole pairs. After a random movement through the lattice, the electron in the conduction band encounters a hole and undergoes a recombination transition. The generation of electron-hole pairs and their subsequent recombination is a continuous process, and the average time that carriers exist between generation and recombination is called the *lifetime* of the carrier.

During the spontaneous generation of electron-hole pairs, the concentration n of electrons in the conduction band is equal to the concentration p of holes in the valence band; i.e., $n = p = n_i$, where n_i is the intrinsic carrier concentration. In the steady state, the thermal generation and spontaneous recombination rates, which are temperature-dependent, are equal: $G_i = R_i$.

The availability of charge carriers in the valence and conduction bands is greatly affected by the presence of intentionally introduced impurities in the lattice. In this case, the material is called *extrinsic,* and the process of putting impurities into the lattice is called *doping*. Impurities that contribute electrons to the conduction band are called *donors,* and those that supply holes to the valence band are *acceptors*. Donors are substitutional impurities that have a higher valence than the atoms of the host; thus an electron is donated to the conduction band, which leads to an excess of mobile electrons, and the material is referred to as n-type. Acceptor impurities have a lower valence than the host, which leads to incomplete atomic bonding in the lattice; thus they capture electrons (i.e., supply holes to the valence band), and the material is referred to as p-type.

In an extrinsic semiconductor, electrons are *minority* carriers and holes are majority carriers in p-type material; in n-type material, holes are minority carriers and electrons are majority carriers.

In compound semiconductors, such as the III-V binary compound GaAs, an excess of one of the components may also generate donor or acceptor states. Thus, an excess of Ga atoms would lead to a p-type material; an excess of As atoms, to an n-type material.

The binding energy E_D of the electron to the donor impurity (i.e., the impurity ionization energy) can be estimated by considering an extra electron in the donor atom as a particle with an effective mass m^* moving in the presence of a positive net charge; i.e., the situation is analogous to a hydrogen atom embedded in the dielectric medium of the crystal. Thus, the ground-state binding energy of the extra electron becomes

$$E_D = \frac{13.6m^*}{m\epsilon^2} \qquad \text{(eV)} \tag{2.5}$$

where 13.6 eV is the ionization energy of the hydrogen atom and ϵ is the dielectric constant of the solid. The binding energy is measured relative to the conduction-band level; thus, in terms of the energy-band diagram, donor impurities introduce levels E_d below the bottom of the conduction band E_c so $E_D = E_c - E_d$. The electron orbit around the impurity atom (i.e., the spatial extent of the wave function) can also be estimated. Thus, the radius of the first Bohr orbit becomes $r = (\epsilon m/m^*)a_0$, where a_0 is the radius of the first Bohr orbit of hydrogen. These results indicate that for typical cases, the ionization energies are less than the room temperature energy kT of about 0.026 eV, and values of r are much larger than the atomic diameter. In other words, most such shallow donors are expected to be ionized at room temperature, and the wave functions are expected to extend over many atomic diameters; in other words, the electron is not localized at the impurity.

Similar considerations can be applied to acceptor impurities. In this case it is convenient to describe a positive hole orbiting a negatively ionized impurity atom. The donor and acceptor binding energies are expected to be somewhat different because of the difference in the effective masses of electrons and holes. In the band structure diagram the acceptor impurities introduce levels at energies E_a lying above the top of the valence band, so $E_A = E_a - E_V$ is the *acceptor binding energy*—i.e., the energy required to excite an electron from the valence band to the acceptor energy levels.

If similar concentrations of donors and acceptors are present, one type of impurity will cancel out the effect of the other, and the material is said to be *compensated.*

To summarize, the shallow donor and acceptor impurities we have described produce in the crystal relatively small perturbations that lead to the formation of bound states in the forbidden gap very close to the boundaries of the conduction and valence bands. Thus, they can easily contribute carriers to those bands and eventually control the type and the electrical properties of a material. However, the simple hydrogenic model for impurity levels is not always applicable. In some cases impurities form deep levels in the forbidden gap of a semiconductor. In addition to the impurity-induced deep levels, a wide variety of defects may also give rise to bound states in the forbidden gap. These states usually produce stronger perturbations in the crystal, lie deeper in the gap, and are more localized. The information about these deep centers is crucial in the analysis of luminescent materials, since they usually act as efficient recombination centers or traps and control the carrier lifetime.

Luminescence properties of solids may also depend strongly on isoelectronic impurities. These centers may be formed by replacing one atom of the crystal by another atom from the same group of the periodic table. For example, the substitution of N for P in GaP leads to the formation of a deep localized acceptor level that can trap an electron, and subsequently, through the coulombic attraction, it can also attract a hole. Thus, the isoelectronic trap is an efficient radiative recombination center.

The carrier concentrations in energy bands can be calculated by taking the product of the density of states and the occupation probability of the energy levels. The former, which is defined as the number of states in the given energy interval per unit volume, is given by the parabolic function

$$N(E) = (4\pi/h^3)(2m^*)^{3/2} E^{1/2} \qquad (2.6)$$

and the occupation probability is given by the Fermi–Dirac distribution function

$$f(E) = \frac{1}{1 + \exp\,[(E - E_F)/kT]} \qquad (2.7)$$

where E_F is the Fermi level, the energy for which the occupation probability is 1/2. For holes, the probability of the state being empty is $1 - f(E)$. The carrier concentration in the bands can be derived by integrating the product of the density of states and the occupation probability over the band energy ranges.

In semiconductors, excitations, such as photon or electron irradiation, may lead to the generation of charge carriers in excess of the thermal equilibrium densities. Recombination of electron-hole pairs restores that equilibrium. The rate R at which recombination occurs is proportional to the product of the electron and hole concentrations. So, in general, we may write

$$R = Bn_0p_0 \tag{2.8}$$

where B is a constant and n_0 and p_0 are the equilibrium concentrations of electrons and holes. If Δn and Δp are the excess carrier concentrations, we can write

$$-\frac{d\,\Delta n(t)}{dt} = B[n_0 + \Delta n(t)][p_0 + \Delta p(t)] - Bn_i^2 \tag{2.9}$$

If we assume that $n_0p_0 = n_i^2$ and consider the case of low-level injection (i.e., the excess concentrations are small) for an extrinsic material (for example, p-type), the equation can be simplified to

$$-\frac{d\,\Delta n(t)}{dt} = Bp_0\,\Delta n(t) \tag{2.10}$$

Thus, if the generation process ceases, the original excess carrier concentration $\Delta n(0)$ will decay exponentially:

$$\Delta n(t) = \Delta n(0)\exp(-Bp_0t) = \Delta n(0)\exp(-t/\tau_n) \tag{2.11}$$

where $\tau_n = (Bp_0)^{-1}$ is called the *recombination lifetime* or *minority carrier lifetime*. Similarly, the decay of excess holes in n-type material occurs with decay constant $\tau_p = (Bn_0)^{-1}$. In general, for low-level injection, the carrier lifetime is $\tau = [B(n_0 + p_0)]^{-1}$. In these types of direct recombination, the excess minority carriers decay at the same rate as the excess majority carriers. The analysis of indirect recombination processes (involving traps) in multi-energy-level systems is more complex. These processes will be discussed in the following chapter.

2.3. Defects in Solids

Solids, as most macroscopic objects in nature, contain a wide variety of defects (i.e., deviations from the perfect order in the crystal lattice). First of all, a free surface of even an ideal solid is a defect, containing, for example, dangling bonds. It is essential to begin the theoretical analysis of solids as systems containing atoms in an infinite regular array. After developing such an ideal picture of the solid state, one is left with the task of understanding real solids on the basis of the perturbations that irregularities introduce in the nearly perfectly ordered crystalline structure and the effects that they have on physical properties of the material. General defect categorization schemes have been introduced, and the collective effects of categories of defects on macroscopic properties have to be considered.

The basic categories of defects in solids are point defects (e.g., substitutional and interstitial impurity atoms and vacancies), one-dimensional or line defects (dislocations), two-dimensional or planar defects (e.g., grain boundaries, stacking faults, surfaces), and three-dimensional or volume defects (e.g., voids, defect clusters, inclusions). In addition, the deviation from perfect crystal structure may result from a variety of elementary excitations, such as phonons (quanta of vibrational energy) and excitons (uncharged bound electron-hole pairs). Defects in real solids may also interact and form a myriad of possible combinations. In this section, these defects will be discussed briefly. Excitons, which are of great relevance in the analysis of luminescence processes, are described in the following chapter. For a more detailed discussion of defects in crystalline solids, see Van Bueren (1960), Cottrell (1964), Hirth and Lothe (1968), Henderson (1972), Stoneham (1975), Nabarro (1979–1983), and Hull and Bacon (1984).

Two simple native (or intrinsic) point defects are a *vacancy* (i.e., a site in the lattice with the atom missing) and an *interstitial* (i.e., an atom inserted into a space (interstice) between the sites of the crystal structure; see Figure 2.4). An isolated vacancy in the lattice is termed a *Schottky defect,* and the associated vacancy and interstitial pair is referred to as a *Frenkel defect.* The missing atom in the case of a Schottky defect has migrated to the surface of the crystal or is trapped at an extended defect, such as a dislocation. Although it is not shown in Figure 2.4, since the surrounding atoms in the lattice have to accommodate the defects, localized regions of distortion are formed in the crystal. Foreign (or ex-

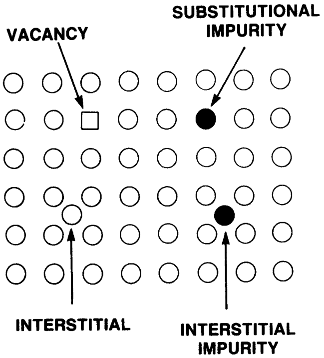

Figure 2.4. Simple native and foreign point defects. For simplicity, the distortion of the lattice around these defects is not shown.

trinsic) point defects are those formed by impurities as shown in Figure 2.4. In some cases, point defects may also form clusters (for example, a vacancy pair) or precipitates of impurity atoms. The presence of vacancies can explain the diffusion of an atom through the solid by its movement to a vacancy. This movement results in a migration of a vacancy in the opposite direction. Note that atomic diffusion may also occur when atoms or ions change their interstitial positions. The equilibrium density of vacancies, n, in a crystal, containing N atoms per unit volume at a temperature T is given by $n = N \exp(-E_V/kT)$, where E_V is the energy of formation of a vacancy (usually of the order of an eV). In compound crystals (AB), an antisite defect may also form if an A atom occupies a B atom site, or vice versa.

In an ionic compound, in order to maintain electrostatic neutrality, a variety of defect complexes (color centers) are formed by the presence of vacancies. The simplest of these is the F-center, which is an electron trapped in a negative-ion vacancy. The center has discrete energy levels. Other color centers, composed of trapped-hole centers and clusters of centers may also form. Electrons may become trapped in clusters of vacancies, which then can be examined by determining the spectroscopic properties of the trapped electrons.

Two elementary types of *dislocation* (Figure 2.5) are an edge dislocation (which can be described as the edge of an extra plane partially inserted into the crystal) and a screw dislocation (which introduces a helical distortion into the crystal). The type and distribution of dislocations present in crystalline materials affect a wide range of properties, such as crystal growth, mechanical strength, and certain electronic and optical properties. Dislocations may be grown-in, for example, when point defects aggregate at some atomic plane. Alternatively, dislocations can be introduced when the stress causes atomic planes to slip past each other at high temperatures during growth or processing. The nature of a dislocation is specified by its (arbitrary) positive line direction **l** and the *Burgers vector* **b**. The definition of the Burgers vector involves executing an atom-to-atom closed loop, called a *Burgers circuit*, in a right-hand sense about an arbitrarily chosen **l**. A corresponding atom-to-atom Burgers circuit in a perfect "reference crystal" will not close. The closure failure, taken in the sense from "finish" atom to "start" atom is the Burgers vector on this standard FS/RH (finish-to-start,

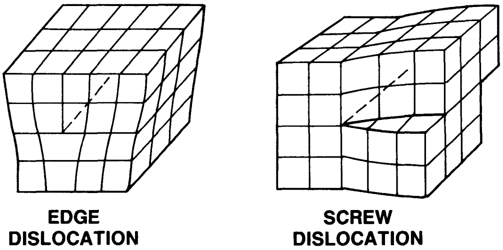

Figure 2.5. A positive edge dislocation and a right-handed screw dislocation.

right-hand) sign convention. Applying elasticity theory to the strain field outside a severely strained core region and integrating halfway out to the next dislocation, an expression for the energy of a dislocation can be obtained. This energy is large, many electron volts per atom length along the line. Hence, dislocations do not occur in thermodynamic equilibrium (unlike point defects, such as vacancies), and large dislocation-free crystals have been produced notably in Si. The elastic energy of a dislocation is also found to be proportional to $|\mathbf{b}|^2$. Thus, the only dislocations that occur are the "unit" dislocations with **b** given by the shortest translation vector of the crystal lattice. For example, $\mathbf{b} = a/2\langle 110\rangle$ for crystals with structures based on the f.c.c. lattice, such as Au, Si, and GaAs. The slip direction for plastic deformation is given by **b**. Two simple geometrical extreme cases can be distinguished, depending on the relation between **l** and **b**. For an edge dislocation, the Burgers vector is perpendicular to the dislocation line; for a screw dislocation, the Burgers vector is parallel to the dislocation line (Figure 2.5). In real solids, dislocations are often intermediate between these two extreme types of defects, and in many materials dislocations are curved. To minimize the total strain energy of the lattice, dislocations interact with one another, which may lead to their annihilation. Point defects also interact with dislocations. This can result in impurity segregation or precipitation at dislocations, which can have a crucial effect on the electrical and optical properties of solids. These interactions may be due to elastic strain fields. In semiconductors and insulators, electrical and chemical bonding interactions are also important. For example, the dangling bonds at the dislocation core may capture electrons from the conduction band of an *n*-type semiconductor and thus lead to the formation of a cylindrical space-charge region around the dislocation. For a review of this field, see Labusch and Schröter (1980). Dislocation densities are 10^4 cm^{-2} or lower in commercial wafers of Si and GaAs semiconductors, for example. However, much higher dislocation densities ($N_D \geq 10^7$ cm^{-2}) may be present, for example, in thin epitaxial films due to the interfacial misfit strain when the layers are deposited on substrates with different lattice constants, and in the cell structure in undoped semi-insulating GaAs, etc. In materials other than semiconductors, dislocation densities are generally high ($>10^6$ cm^{-2}, for example).

In polycrystalline materials, lattice misorientations between the adjoining, randomly oriented crystallites result in *grain boundaries*, which can block the movement of dislocations. When the misorientation between adjacent grains is small, the boundary is called *low-angle* and consists of an array of well-separated dislocations. This representation is valid for angles up to about 20°. For larger angles, when the separation between the dislocations is so small that their core structures begin to overlap, the boundary structure cannot be resolved into dislocations but must be analyzed as a defect in its own right.

As mentioned earlier, various crystalline structures can be described by their stacking sequence of layers in a close-packed arrangement. Thus, the sequence ABCABC... represents the f.c.c. packing, and the ABABAB... corresponds to hexagonal close packing. If the sequences go wrong, say a layer is missing (ABCACABC...) or an extra layer is inserted (ABCACBCABC...) in the cubic case, then a stacking fault is formed. In the hexagonal case, for example, a stacking fault is formed when a layer in the C position is introduced or when a C layer replaces an A or B layer.

Volume defects are formed, for example, from vacancy clusters, which may grow and eventually collapse to form dislocation loops with additional vacancies condensing on them. Impurity atoms and vacancies may also form large three-dimensional aggregates. Some impurities may precipitate into a separate phase in a solid. Additional three-dimensional defects are, for example, cracks, inclusions, and pores.

As will be shown in subsequent chapters, defects play a crucial role in luminescence phenomena. In general, the presence of defects may lead to (1) the introduction of energy levels in the band gap, which may significantly affect the optical properties of the material; (2) a reduced carrier mobility due to increased scattering by defects; and (3) the changes in the recombination rates and mechanisms of excess carriers in luminescence phenomena.

3

Luminescence Phenomena

3.1. Types of Luminescence

Different terms for luminescence are used in optoelectronics semiconductors, inorganic phosphors, and organic molecules. Here we attempt to introduce them in a general form.

When a solid is supplied with a certain form of energy, it may emit photons in excess of thermal radiation. This process is called *luminescence,* and, depending on the source of excitation of the luminescent material, one may categorize the process as, for example, *photoluminescence* (photon excitation), *cathodoluminescence* (excitation by energetic electrons, or cathode rays), *chemiluminescence* (energy supplied by chemical reaction), and *electroluminescence* (excitation by application of an electric field). Another distinction is commonly made between fluorescence and phosphorescence, which differ in the time delay before the emission of photons. After the excitation is stopped, the duration of the emission is determined by the lifetime of the electron transition from one energy level to another. When the emission of photons is due to a direct transition from the excited to the ground state within about 10^{-8} sec, the luminescence is called *fluorescence*. Luminescence that persists after the excitation stops is called *phosphorescence;* materials exhibiting this property are called *phosphors* and are used as powders in fluorescent lamps, cathodoluminescent television screens, etc. The emission may persist from about 10^{-7} sec to minutes and hours in long-persistence phosphors. In such cases, transitions through intermediate metastable states determine the duration of the luminescence after the termination of the excitation. In organic molecules, fluorescence is due to permitted singlet-singlet state transitions, and phosphorescence is due to "forbidden" triplet-singlet transitions.

Luminescence from inorganic phosphors is generally due to the presence of small amounts of impurities known as *activators*. (Activators may also form due to a stoichiometric excess of one of the constituents in the material.) The solubility limit of the activator may be increased by introducing other impurities, called *coactivators,* in the material. Luminescence in semiconductors is generally described in terms of the radiative recombination of electron-hole pairs. This may involve transitions between states in the conduction or valence bands and those in the band gap of the material due to, for example, donors and acceptors. These differences in terminology arose historically, but relate to the luminescence mechanisms. Industrial phosphors were developed not on the basis of the band structure theory but on such semiempirical, crystal defect chemistry concepts as activators and coactivators. The luminescence in traditional phosphors and semiconductors can be distinguished as mainly due to either energy transfer (excitation in phosphors) or charge carrier recombination (in semiconductors) mechanisms, but this distinction does not apply to all cases. For example, rare-earth- and transition-metal-activated luminescence from semiconductors can be of either type (Robbins and Dean, 1978).

The emission of photons in luminescence processes is due to an electronic transition between an initial state E_i and the final state E_f. The energy, or the wavelength, of the emitted photon can be found from the relation

$$h\nu = hc/\lambda = E_f - E_i \tag{3.1}$$

In many wide-band-gap materials, emission of photons occurs in the visible range (about 0.4 to 0.7 μm, corresponding to about 3.1 to 1.8 eV). In many luminescence phenomena light is also emitted at longer wavelengths in the near-infrared region. In the literature, the luminescence results are presented in terms of both wavelength and energy. The wavelength λ (in μm) of a photon is related to the photon energy E (in eV) by $\lambda \cong 1.2398/E$.

3.2. Intrinsic and Extrinsic Luminescence

In inorganic solids light is emitted as the result of electronic transitions between quantum mechanical states differing in energy by less than 1 eV to more than several eV. Luminescence emission spectra can be divided between (1) *intrinsic*, fundamental, or edge emission and (2) *extrinsic*, activated, or characteristic emission. Intrinsic luminescence, which appears at ambient temperatures as a near Gaussian-shaped band of energies with its intensity peak at a photon energy $h\nu_p \cong E_g$, is due to recombination of electrons and holes across the fundamental energy gap, so it is an "intrinsic" property of the material. This edge emission band, arising from essentially conduction-band to valence-band transitions, is produced by the inverse of the mechanism responsible for the fundamental absorption edge. Thus, any change in E_g, due to, say, temperature, crystal structure in polymorphic materials, or high doping concentrations, can be monitored by measuring $h\nu_p$ (see, for example, Davidson, 1977; Datta *et al.*, 1977; Holt and Datta, 1980; Warwick and Booker, 1983).

Energy and (crystal) momentum ($\hbar k$) must be conserved during the electronic transitions. As was mentioned in Chapter 2, when the maximum of the valence band and the minimum of the conduction band occur at the same value of the wave vector **k** (Figure 3.1a), transitions are direct or vertical, and the material is a direct-gap semiconductor (for example, GaAs, ZnS). In materials with a direct gap, the most likely transitions are across the minimum-energy gap, between the most probably filled states at the minimum of the conduction band and the states most likely to be unoccupied at the maximum of the valence band. Radiative recombination between electrons and holes is relatively likely in such transitions. If the band extrema do not occur at the same wave vector **k** (Figure 3.1b), transitions are indirect. For momentum in such an indirect-gap material (for example, Si, GaP) to be conserved, phonon participation is required. Thus, the recombination of electron-hole pairs must be accompanied by the simultaneous emission of a photon and a phonon. Since this requires an extra particle, the probability of such a process is significantly lower compared with direct transitions. Therefore, fundamental emission in indirect-gap semiconductors is relatively weak, especially when compared with that due to impurities or defects.

Band-gap values and types of fundamental transitions for some inorganic solids are given in Table 3.1.

The emission spectra (in both direct and indirect semiconductors), which depend on the presence of impurities, are extrinsic in nature. In phosphor terminology, luminescence emission bands in these cases are "activated" by impurity atoms or other defects, and the emission features are characteristic of the particular activator. Such radiation can be made much more intense than intrinsic CL at ambient temperatures even in direct-gap materials. This is the aim of phosphor technology, and it is the reason for regarding the desired activated emission as characteristic.

When an electron is promoted into the conduction band, the electron and hole become free and they can move independently in corresponding bands. It is

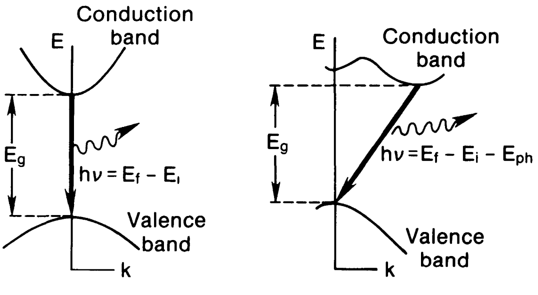

Figure 3.1. The energy transitions in (a) direct- and (b) indirect-gap semiconductors between initial states E_i and final states E_f. For indirect transitions the participation of a phonon (E_{ph}) is required.

Table 3.1. Values and Types of Band Gaps of Some Inorganic Solids*

Inorganic solid	Energy gap E_g (0 K) (eV)	E_g (300 K) (eV)	Type
Ge	0.74	0.66	Indirect
Si	1.17	1.12	Indirect
C (diamond)	5.49	5.47	Indirect
SiC (ZB)	2.68	2.20	Indirect
SiC (6H)	3.04	2.98	Indirect
InP	1.42	1.35	Direct
GaAs	1.52	1.42	Direct
AlSb	1.68	1.58	Indirect
AlAs	2.24	2.16	Indirect
GaP	2.34	2.26	Indirect
AlP	2.50	2.43	Indirect
GaN	3.50	3.36	Direct
CdTe	1.60	1.50	Direct
CdSe	1.85	1.74	Direct
ZnTe	2.39	2.28	Direct
CdS	2.56	2.42	Direct
ZnSe	2.80	2.58	Direct
ZnO	3.44	3.35	Direct
ZnS (ZB)	3.84	3.68	Direct
ZnS (W)	3.91	3.75	Direct

*After Pankove, 1971 and Sze, 1981. ZB, zinc blende; W, wurtzite; and 6H, polytype

possible at low temperatures for electron-hole pairs to form a bound state, an exciton. The coulombic interaction between the pairs, modified by the dielectric constant of the semiconductor, brings their energy levels closer together than the width of the energy gap. Excitonic states, which exist just below the conduction band, are analogous to electronic states in the hydrogen atom. In other words, excitons can exist in a series of bound states in the gap. Excitonic levels are observable at low temperatures at which kT is smaller than the excitonic binding energy, which can be anything from an eV to tenths of an meV, depending on the material. Recombination emission of the excitonic state produces photons of energies, which in most III-V compounds correspond approximately to the band gap of a semiconductor; thus it is an intrinsic process. Some workers prefer the term *near-band-gap* radiation for the intrinsic luminescence band, because excitons and shallow recombination centers may contribute to this emission at room temperature.

A simplified set of radiative transitions that lead to emission in semiconductors containing impurities is given in Figure 3.2. General properties of these transitions will now be discussed briefly.

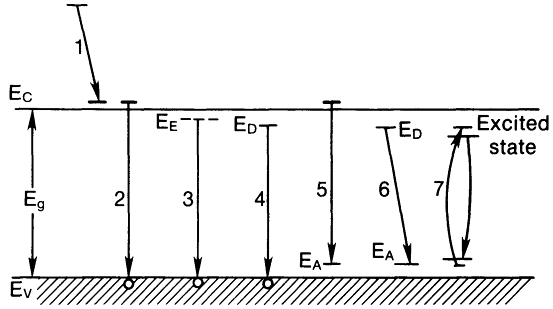

Figure 3.2. Schematic diagram of radiative transitions between the conduction band (E_C), the valence band (E_V) and exciton (E_E), donor (E_D) and acceptor (E_A) levels in a semiconductor.

Process 1 is an intraband transition: an electron excited well above the conduction-band edge dribbles down and reaches thermal equilibrium with the lattice. This thermalization process may lead to phonon-assisted photon emission or, more likely, phonon emission only. The luminescence from microplasma breakdown of Si *p-n* junctions, for example, is due to this mechanism.

Process 2 is an interband transition; this produces intrinsic luminescence. In this case, direct recombination between an electron in the conduction band and a hole in the valence band results in the emission of a photon of energy $h\nu \cong E_g$. Although this recombination occurs from states close to the corresponding band edges, the thermal distribution of carriers in these states will lead, in general, to a broad emission spectrum.

Process 3 is the exciton decay observable at low temperatures; both free excitons and excitons bound to an impurity may undergo such transitions. For bound excitons, one of the charge carriers is localized at a center that can assist in conserving momentum during the transition. This will be especially important in indirect-gap materials. In the literature, these transitions are often denoted with special symbols. Thus, free-exciton recombination is denoted X; recombination of an exciton bound at a neutral donor is $D^\circ X$, of an exciton bound at a neutral acceptor is $A^\circ X$, and of excitons bound to the corresponding ionized impurities are D^+X and A^-X.

Processes 4, 5, and 6 arise from transitions that start and/or finish on localized states of impurities (e.g., donors and acceptors) in the gap; these produce extrinsic luminescence. The recombination processes between free carriers and trapped carriers of the opposite type are known as the *Lambe-Klick model* (process 4 representing donor-to-free-hole transition labeled as $D^\circ h$) and the *Schön-Klasens model* (process 5 representing free-electron-to-acceptor transition labeled eA°), and the donor-acceptor pair (DAP) recombination model (process 6) is known as the *Prener-Williams model* in the phosphor literature. These last three processes account for most of the processes in a wide variety of luminescent materials.

Similar transitions via deep donor and deep acceptor levels can also lead to recombination emission with photon energies well below the band gap. Shallow donor or acceptor levels can be very close to the conduction and valence bands. Thus, to distinguish between shallow impurity transitions and those associated with the intrinsic band-to-band transitions, we must perform measurements at liquid helium temperatures. The energy of the transition in the case of deep levels is much smaller than that of the band-to-band transition. (Ionization energies of donors and acceptors in GaAs and GaP, for example, are given in Tables 3.2 and 3.3.) In wide-band-gap materials, however, transitions associated with deep levels may result in the emission of photons in the visible and near-infrared ranges. An electron in these types of impurity states is highly localized in space; i.e., it has a wave function that extends only to the nearest neighbors. From the Heisenberg uncertainty principle it then follows that if the uncertainty in the position Δx is small, the uncertainty in the momentum Δp must be large. Since $p = \hbar k$, we can write $\Delta k \geq (2\,\Delta x)^{-1}$, and therefore the energy of a deep level extends over a wide range of k-values. Consequently, this allows a direct transition from the impurity level to a wide range of extended states without the participation of phonons. This is especially relevant to indirect-gap materials.

Transition 7 represents the excitation and radiative deexcitation of an impurity with incomplete inner shells, such as a rare-earth ion or a transition metal.

Table 3.2. Ionization Energies of Some Impurities in GaAs at Liquid Helium Temperatures*

Donors (meV)		Acceptors (meV)	
C	6.0	C	26.0
Si	5.8	Si	35.0
Ge	6.1	Ge	41.0
S	6.1	Zn	31.0
Se	5.9	Be	28.0
Te	5.8	Mg	29.0
Sn	6.0	Cd	35.0
O	400, 750	Li	23, 50
		Au	90
		Mn	100
		Ag	110
		Cu	150, 470
		Co	160
		Sn	171
		Ni	210
		Fe	520
		Cr	790

*After Casey and Trumbore, 1970 and Ashen *et al.*, 1975.

Table 3.3. Ionization Energies of Impurities in GaP*

Donors (meV)		Acceptors (meV)		Isoelectronic traps (meV)	
Li	58, 88.3	C	46.4	N	~8
Sn	69	Be	48.7	Bi	~38
Si	82.1	Mg	52	Zn-O	300
Te	89.8	Zn	61.7	Cd-O	400
Se	102.7	Cd	94.3		
S	104.1	Si	202		
Ge	201.5	Ge	257		
O	895.5	Co	410		

*After Bergh and Dean, 1976 and Casey and Trumbore, 1970.

Recombination of electron-hole pairs may occur via nonradiative processes as well, as, for example, for process 1 in Figure 3.2. Examples of nonradiative recombination processes are (1) multiple-phonon emission (i.e., direct conversion of the energy of an electron to heat); (2) the Auger effect, in which the energy of an electron transition is absorbed by another electron, which is raised to a higher-energy state in the conduction band, with subsequent emission of the electron from the semiconductor or dissipation of its energy through emission of phonons (thermalization); this process is especially important for high concentrations of excess charge carriers; and (3) recombination due to surface states and defects. These processes are more difficult to analyze (see Pankove, 1971).

As mentioned earlier, lattice defects can also introduce localized levels in the band gap. Dislocations, for example, may produce both shallow levels due to the elastic strain fields and deep levels associated with dangling bonds. A wide variety of native point defects, such as vacancies and their complexes with impurity atoms, may be present and may introduce a wide range of localized levels in the band gap in binary semiconductors, such as GaAs (see Milnes, 1983).

In a degenerately doped semiconductor, in which the impurity concentration exceeds the value for which the large-radius wave functions of the shallow states begin to overlap, the energy levels broaden into a band. If such a band, for example, is near the top of the valence band, it might even overlap with valence states. The energy gap in such cases depends on the doping concentration, and the photon energy of the previously intrinsic emission will depend on the concentration of impurities (see Pankove, 1971).

3.3. Optical Absorption and Emission

In the fundamental absorption process, a photon excites an electron from the valence band to the conduction band. Energy and momentum must be conserved in this process. Since the photon momentum is small compared with the crystal momentum, the absorption process should essentially conserve the electron momentum (i.e., $\hbar k$). Optical absorption is expressed in terms of the absorption coefficient α, defined by Lambert's law

$$I = I_0 \exp(-\alpha x) \tag{3.2}$$

for the radiation intensity I falling off with distance x through the sample. The absorption coefficient can be expressed as (see Pankove, 1971)

$$\alpha(h\nu) = A\Sigma P_{if} n_i n_f \tag{3.3}$$

where n_i is the concentration of electrons in the initial state, n_f is the concentration of empty energy levels in the final state, P_{if} is the transition probability, and the sum is over all initial and final states. For direct transitions between parabolic conduction and valence bands, the absorption coefficient is described by (see Pankove, 1971)

$$\alpha(h\nu) = A(h\nu - h\nu_0)^{1/2} \tag{3.4}$$

In these expressions $h\nu_0 = E_g$, $h\nu$ and $h\nu_0$ are in eV, α is in cm^{-1}, and $A \approx 2 \times 10^4$. In the absorption edge region in many materials, however, α was found empirically to obey Urbach's rule (Urbach, 1953):

$$\alpha(h\nu) = \alpha_0 \exp[g(h\nu - h\nu_0)] \tag{3.5}$$

The coefficient g is a temperature-dependent parameter for ionic crystals:

$$g = \sigma/kT \tag{3.6}$$

where σ depends on a phonon energy $\hbar\omega_0$:

$$\sigma = \sigma_0\, (2kT/\hbar\omega_0)\tanh(\hbar\omega_0/2kT) \tag{3.7}$$

For covalent semiconductors g was found to depend on the concentrations and the electrical charges of impurities (for a general review of Urbach's rule see Dow and Redfield, 1972). Dow and Redfield (1972) explained the exponential form of absorption edges in terms of internal-electric-field-assisted broadening of the lowest excitonic state. The sources of these internal microfields can vary from material to material and may involve phonons (longitudinal optical and longitudinal acoustic), ionized impurities, dislocations, surfaces, and other defects (Dow and Redfield, 1972). The Dow and Redfield model of internal electrical microfields is not universally accepted, but it does provide a quantitative explanation of most observations on the low-energy tails of absorption edges in a wide range of materials. Their model was also successfully applied, as mentioned before, to describe the shape of the band-to-acceptor emission in lightly doped GaAs:Cd crystals (Dow *et al.*, 1973). However, alternative explanations of Urbach's rule have been proposed (see Dow and Redfield, 1972; Knox, 1983 and references therein). These include, for example, a model of momentary exciton trapping by phonons, proposed by Sumi and Toyozawa (1971), and a model of a thermal fluctuation shift of the band edge, presented by Skettrup (1978). No model, including the Dow-Redfield one, holds for all cases (Knox, 1983). It is very likely that several mechanisms have to be invoked in order to explain the Urbach rule in a wide variety of materials.

As mentioned previously, in indirect-gap materials the maximum energy of the valence band and the minimum energy of the conduction band do not occur at the same wave vector **k.** In such cases, in order to conserve both energy and momentum, transitions involve photons, electrons, and phonons. The latter, in contrast to photons, have low energy but relatively high momentum. Thus, momentum in indirect transitions is conserved via absorption or emission of a phonon with a characteristic energy E_p. It can be shown (see Pankove, 1971) that the absorption coefficient for a transition involving phonon absorption is given by

$$\alpha_a(h\nu) = \frac{A(h\nu - E_g + E_p)^2}{\exp(E_p/kT) - 1} \tag{3.8}$$

The absorption coefficient for a transition involving phonon emission is given by

$$\alpha_e(h\nu) = \frac{A(h\nu - E_g - E_p)^2}{1 - \exp(-E_p/kT)} \tag{3.9}$$

Both phonon absorption and emission are possible for $h\nu > E_g + E_p$, and thus the absorption coefficient is

$$\alpha(h\nu) = \alpha_a(h\nu) + \alpha_e(h\nu) \tag{3.10}$$

The absorption process in indirect-gap materials requires the involvement of an extra particle (phonon) as compared with the direct-gap case. Thus, the probability of the absorption of light (and the absorption coefficient) in indirect-gap materials is much lower than in direct-gap materials. This means that light has to pass a large distance into the material before being absorbed.

At the absorption edge, α may vary in the range between 10^4 and 10^5 cm^{-1} for direct transitions, and it may have values between 10 and 10^3 cm^{-1} for indirect transitions.

In principle, the shapes of the absorption and emission bands of luminescent point defects can be obtained from *configuration coordinate models* (see Klick and Schulman, 1957; Markham, 1959). The basic features of this model are illustrated in Figure 3.3. This is a schematic representation of the effect of the relaxation of the crystal around the center following optical transitions. It represents the center as a "vibronic" (vibrational and electronic) system. Consider the center in its ground state at 0 K. The electron then occupies the $n = 0$ vibrational level of the electronic ground state (lower curve). Transitions to the excited state (upper curve) will occur only from this level. Electronic transitions take place in times much shorter than those required for the relaxation of the positions of neighboring atoms to the excited state configuration. The optical transitions are therefore represented by vertical transitions in configuration coordinate models. This is known as the *Frank-Condon principle*. As can be seen in Figure 3.3, the absorption transition from the midpoint of the $n = 0$ vibrational level carries the electron to a point on the excited electronic state curve corresponding to $m = 8$ (i.e., the eighth vibrational excited state). Projecting the end points of the $n = 0$ state vertically gives the width of the absorption band (i.e., the extreme values of

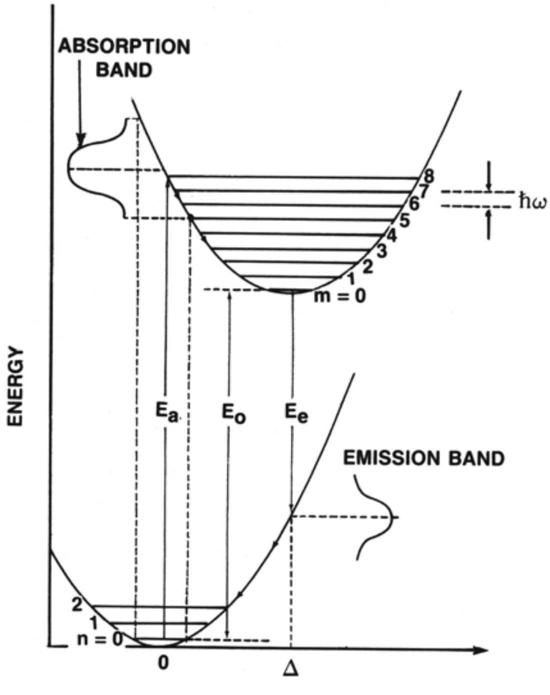

Figure 3.3. The configuration coordinate model for a radiative recombination center involving a mean excitation of eight phonons in the excited state. The breadth of the absorption and emission bands at 0 K are indicated. (After Henderson and Wertz, 1968.)

E_a that can give rise to the transitions from the $n = 0$ vibrational level). Absorption transitions occur with various probabilities from all positions consistent with the spatial extent of the initially occupied vibrational state. The transition energy varies as the luminescence center vibrates throughout the region represented by the horizontal line of the occupied vibrational level in the configuration coordinate diagram. The probability of occurrence of a transition from each value of Q is proportional to $|\psi_n(Q)|^2$, where ψ_n is the oscillator wave function for the nth state. The simplest assumption is that of the harmonic approximation. The maximum probability of transition occurs at the equilibrium position value of Q. Transitions from this point give rise to the peak of the band. The width of the band is defined by the spatial limits of the line representing the initial vibrational state. As the temperature increases, higher and higher vibrational states (of larger n-value) are occupied, giving broader absorption bands. After the excited state has been reached by absorption, the configuration relaxes by emission of phonons (eight in this example) to the $m = 0$ vibrational level. When the electron returns to the ground state, emission of radiation is again a vertical transition corresponding to E_e. The band peak corresponds to the maximum probability in the $m = 0$ state at $Q = \Delta$. Since $E_a > E_e$, there is a spectral shift (known as the *Stokes shift*) between the absorption and emission bands. As the result of the shift of the luminescence bands to lower energies (relative to the absorption bands), the luminescence is not reabsorbed by the material. It can be seen that the greater the number of phonons excited in the transition, the greater will be the Stokes shift. Conversely, the weaker the lattice coupling (i.e., the fewer the phonons), the greater is the amount of spatial overlap of the lowest vibrational states $m = 0$ and $n = 0$. If there is significant overlap of these wave functions, the $m = 0$ state can be reached without the emission of phonons, and a transition can occur to emit a photon of energy $E_0 = E_a$. In this case, the E_0 emission is known as the *zero-phonon-line*.

The probability of an emissive transition between any pair of levels is given by

$$P_{nm} = f|\langle\psi_m|\psi_n\rangle|^2 \tag{3.11}$$

where f is the oscillator strength of the transition and $\langle\psi_m|\psi_n\rangle$ is the overlap integral for the harmonic oscillator wave functions of the two vibrational levels. The overlap integral between the displaced wave functions ψ_m and ψ_n has been evaluated (see Markham, 1959), and the result, which defines the optical line shape at low temperatures, is

$$P_{0m} = e^{-S}S^m/m! \tag{3.12}$$

where S is effectively the number of phonons excited in transitions upward from $Q = 0$ (eight in Figure 3.3) and is known as the *coupling* or *Huang-Rhys factor*. This expression gives the relative intensities of the zero, one, two, etc., phonon

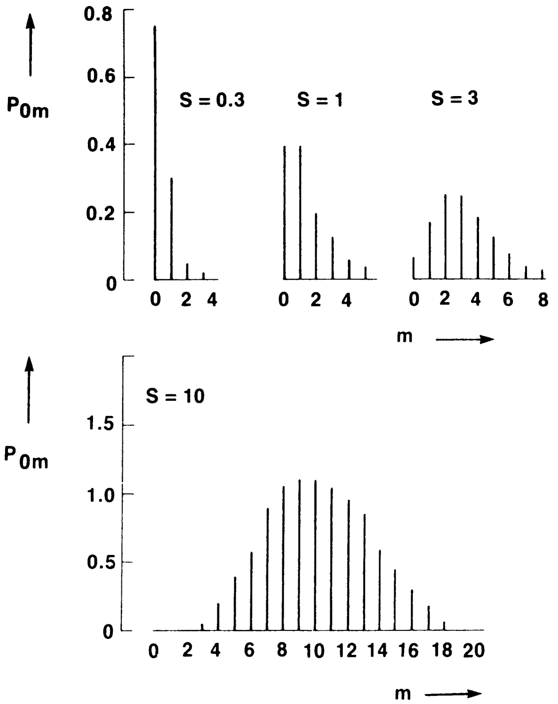

Figure 3.4. Plots of the shape function P_{0m} as a function of m for absorption bands according to equation (3.12) for several values of S. For large S ($S = 10$) the shape is close to the Gaussian band. (After Henderson and Wertz, 1968.)

lines ($m = 0, 1, 2, \ldots$) for transitions after the ground electronic state has relaxed completely. Examples of the optical line shapes derived from equation (3.12) are shown in Figure 3.4, which presents the relative probabilities of phonon lines for several values of the coupling factor S. For small S, the zero-phonon line appears. When S is large, the band shape (the envelope of the lines) approaches that of a Gaussian and the peak occurs at $S = m$.

Sharp zero-phonon lines have been observed from many centers. The narrowness of this line and its relative simplicity make it useful in studies designed to determine the nature of the center by observing the effect of externally applied fields on the emission.

The quantum mechanical configuration coordinate theory of phonon-coupled emission predicts, assuming the harmonic approximation for lattice vibrations, a Gaussian band with peak position (see Klick and Schulman, 1957; Markham, 1959)

$$E_p = A_1 + A_2 \coth(\hbar\omega_0/2kT) \tag{3.13}$$

and full width at half-maximum

$$W(T) = W(0)\,[\coth(\hbar\omega_0/2kT)]^{1/2} \tag{3.14}$$

Here $\hbar\omega_0$ is the energy of the "effective phonon," k is Boltzmann's constant, and T is the temperature. Experimental studies, however, indicated that the shapes of both the intrinsic (edge emission) and extrinsic emission bands in II-VI compounds (Yacobi *et al.*, 1977; Datta *et al.*, 1979a, 1980a) and MgO (Datta *et al.*, 1979b) are not entirely of Gaussian form. At elevated temperatures (above 77 K), these emission bands generally have an asymmetric Gaussian form around the peak, followed on either side by low- and high-energy exponential tails (see Figure 3.5). Thus, the form of the luminescence band can be expressed semiempirically as (see Yacobi *et al.*, 1977)

$$L(h\nu) = L(h\nu_0)\exp[g(h\nu - h\nu_0)^{\beta}] \tag{3.15}$$

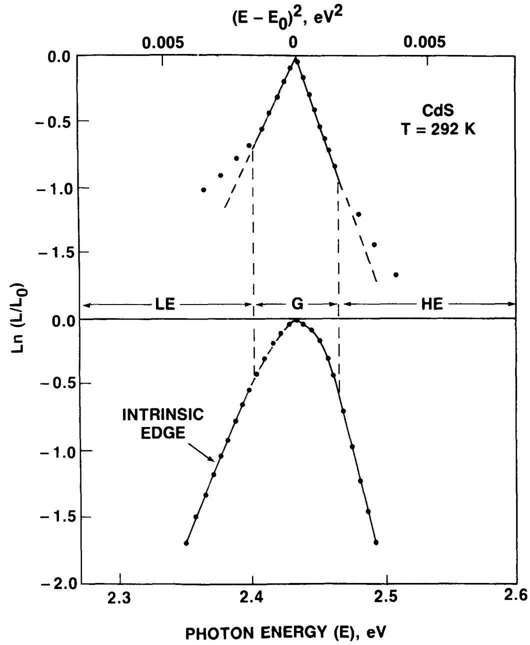

Figure 3.5. Edge emission band data for CdS at room temperature. The straight-line segments in the upper plot show that in region G near the maximum the band has an asymmetric Gaussian form. The straight lines in the lower plot show that in the low-energy (LE) and high-energy (HE) regions the form of the band is exponential. (After Yacobi *et al.*, 1977.)

where L is the intensity, g and β are shape parameters, and $h\nu$ and $h\nu_0$ are the photon energies at a particular wavelength and at the peak, respectively. For the low- and high-energy regions of the band, $\beta = 1$ and exponential tails are obtained, but around the peak $\beta = 2$ and the shape is Gaussian. The slope parameter $g = \sigma_L/kT$ for the low-energy exponential case, $g = -\sigma_H/kT$ for the high-energy exponential region, and $g = -\tau^2$ for the Gaussian ranges of energy. These parameters for some materials are presented in Table 3.4. The relative magnitudes of the corresponding slope parameters give the degree of asymmetry of the emission bands. The numbers quoted in Table 3.4 may be affected by the impurities present in these materials. This might explain the difference in the slope σ_L of the exponential low-energy (LE) region and the half-width H between, for example, ZnS and CdS in the table, since they have similar slopes ($\sigma \approx 2$) at room temperature for exponential absorption edges. Thus, the values in Table 3.4 should not be taken as characteristic of the pure material, since impurities may strongly affect the emission band shape in a manner similar to that found for GaAs (Casey and Kaiser, 1967). The range of fitting of the Gaussian function was found to vary significantly as a function of the structure. For example, as can be seen in Table 3.5, the ranges of validity of the Gaussian function are not as wide in the hexagonal structure of ZnS:Cl than those observed for the cubic structure of that material at the same temperature (Datta *et al.*, 1979a). This could be due to faulting, typical of hexagonal phase material in these platelets, which was observed with a low density even in the best areas selected for the analysis. This faulting may also explain the lower photon emission from the hexagonal structure, compared with the cubic phase. Another possible explanation for the better Gaussian fitting is the fact, derived from electron spin resonance (ESR) results (Schneider *et al.*, 1965), that there are two symmetries for the self-activated center in the hexagonal structure and only one in the cubic phase. This center has been identified as a group VII impurity (for example, Cl) substituted for a S^{2-} ion adjacent to a Zn vacancy, as first proposed

Table 3.4. Band-Shape Parameters (at Room Temperature) According to Equation (3.15) for Edge and Impurity Emissions in Some II-VI Compounds (corrected for spectral response of the CL detection system)*

	E_p (eV)	H (eV)	τ_{LEG} (eV^{-1})	τ_{HEG} (eV^{-1})	σ_L	$-\sigma_H$
ZnS (2H)	3.740	0.10	14.2	17.7	0.38	1.3
ZnS (3C)	3.657	0.11	13.2	18.2	0.40	1.4
CdS	2.432	0.08	19.7	21.7	0.72	1.3
ZnO	3.19	0.15	10.2	12.9	0.31	0.93
ZnS:Cl (2H)	2.634	0.51	2.97	3.61	0.28	0.32
ZnS:Cl (3C)	2.539	0.46	3.87	3.99	0.32	0.33

*After Yacobi *et al.*, 1977; Datta *et al.*, 1979a, 1980a.

Table 3.5. Cathodoluminescence ZnS:Cl (SA) Band-Shape Parameters; Full Width at Half-Maximum H in eV; Slopes τ_{LEG} and τ_{HEG} for Gaussian (G); (LEG) Fraction of the Band Which is Gaussian on the Low-Energy Side, (HEG) Fraction of the Band Which is Gaussian on the High-Energy Side*

Structure	Temperature (K)	H (eV)	τ_{LEG} (eV^{-1})	(LEG) %	τ_{HEG} (eV^{-1})	(HEG) %
	292	0.46	3.87	58	3.99	48
Cubic	200	0.39	4.14	69	4.26	60
	120	0.36	4.68	82	4.76	77
	78	0.35	4.77	87	4.88	79
Hexagonal	292	0.51	2.97	46	3.61	34
	78	0.39	4.18	56	4.54	41

*After Datta *et al.*, 1979a.

by Prener and Williams (1956). At liquid helium temperature, a trapped hole in the excited SA center is fixed at one S^{2-} ion. But at higher temperatures (near 77 K), the hole hops rapidly among the S ions neighboring the Zn vacancy. The ESR results were shown (Schneider *et al.*, 1963) to be consistent with this model: at 77 K, the symmetry of the hole-electron spin-resonance spectrum was indicative of only partial localization on a sulfur orbital. Thus, with increasing temperature, a wave function common to all the bands associated with the vacancy should be considered. This may explain the greater deviation from the Gaussian function description for the hexagonal structure at higher temperatures. The effect of impurities on the band-shape parameters of the self-activated emission in ZnS was also demonstrated by Thomas *et al.* (1984). ZnS samples in that study contained various amounts of Cu contaminants. The temperature behavior of the luminescence peak, as well as the band-shape parameters and the extent of the Gaussian fit to these emission bands, was found to depend strongly on the amount of Cu in the material. Thus, it should be expected that the band-shape analysis will depend strongly on both the type and amount of possible dopants or contaminants.

The temperature variation of both the low-energy slope σ_L and the high-energy slope $-\sigma_H$ for CdS is shown in Figure 3.6. These experimental points cannot be fitted to the function $F \propto (2kT/\hbar\omega_0)\tanh(\hbar\omega_0/2kT)$, which extends the Boltzmann probability distribution of a classical oscillator to low temperatures where the zero-point oscillations of a quantum mechanical oscillator become important and that usually describes the temperature dependence of the slope of absorption edges (Mahr, 1962). More experimental data and careful analysis on other materials will be useful for understanding of these features of luminescence. A significant conclusion of these results is that the harmonic approximation for lattice vibrations seems to be inadequate. More realistic phonon coupling models are required in order to explain these observations.

In early work, Mahr (1962, 1963) and Toyozawa (1959, 1964) proposed a

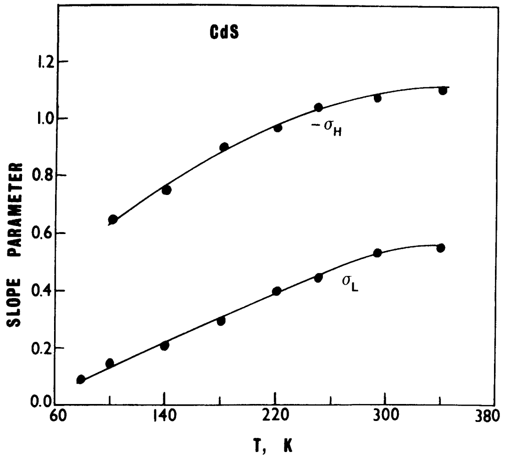

Figure 3.6. Temperature dependence of the slopes σ_L and $-\sigma_H$. (After Yacobi *et al.*, 1977.)

two-mode model for coupling of the electronic transitions to the lattice vibrations in ionic crystals. Both linear and quadratic modes are assumed to interact with the electronic transitions, and this leads to both a Gaussian shape around the maximum (linear interaction) and an exponential function at the edge (quadratic interaction). Keil (1966) later presented quantum mechanical modifications to the semiclassical model proposed by Mahr and Toyozawa. More detailed accounts of configuration coordinate models also predict a variety of band shapes, which are in some cases asymmetric due to the properties of the total vibrational eigenfunctions of the ground and excited states (Markham, 1959).

In some cases, the wide luminescence bands that appear to deviate from a Gaussian shape are composed of several Gaussian bands associated with different transitions (Koschek and Kubalek, 1983). Thus, a knowledge of band shape makes possible a deconvolution procedure for luminescence bands, especially at ambient temperatures, and so is of great importance.

The low-energy exponential tail in the edge emission band corresponds to a similar exponential dependence in the absorption edge that is observable in a wide variety of semiconductors.

The relation between absorption and emission can be derived from the principle of detailed balance (van Roosbroeck and Shockley, 1954), which enables one to calculate the shape of the emission band from the experimentally determined values of the absorption coefficient. The relation between the absorption coefficient $\alpha(h\nu)$ and the equilibrium emission intensity $L(h\nu)$ at a photon energy $h\nu$ was found to be

$$L(h\nu) = \alpha(h\nu)B(h\nu)^2 \,[\exp(h\nu/kT) - 1]^{-1} \qquad (3.16)$$

where $B = 8\pi n^2/h^3c^2$ contains the refractive index n, the speed of light c, and Planck's constant h.

The emission spectrum of GaAs was calculated by using this principle by Casey and Stern (1976) and was found to be in fair agreement with the experimentally determined spontaneous emission band for *p*-type material. Good agreement between experimental and calculated emission spectra was also recently found for $Al_xGa_{1-x}As$ (Swaminathan *et al.*, 1983) (see Figure 3.7).

Dow, Smith, and Lederman (1973) showed that the internal electric microfield model could be employed to account for the shape of the band-to-acceptor luminescence edge in GaAs:Cd. Experimentally, the low-energy tail of the fundamental edge emission band was found to vary exponentially with the photon energy in GaAs (Pankove, 1966; Casey and Kaiser, 1967), CdS and ZnS (Yacobi *et al.*, 1977), and in the photoluminescence excitation spectra of some chalcogenide glasses (Street *et al.*, 1975). In these cases, two distinctive regions of the low-energy tail were found: the higher-intensity intrinsic region and a lower-intensity region where impurities are important. Pankove (1966) and Casey and Kaiser (1967) found in GaAs that the slope parameter in the lower-intensity region of the exponential low-energy tail varied in a simple monotonic way with the carrier concentration, and Yacobi *et al.* (1977) observed the dependence of the slope parameter on temperature in CdS and ZnS crystals. An analogous effect was found for the fundamental absorption edge (Dixon and Ellis, 1961; Casey *et al.*, 1975). Other CL emission parameters in GaAs such as intensity, peak posi-

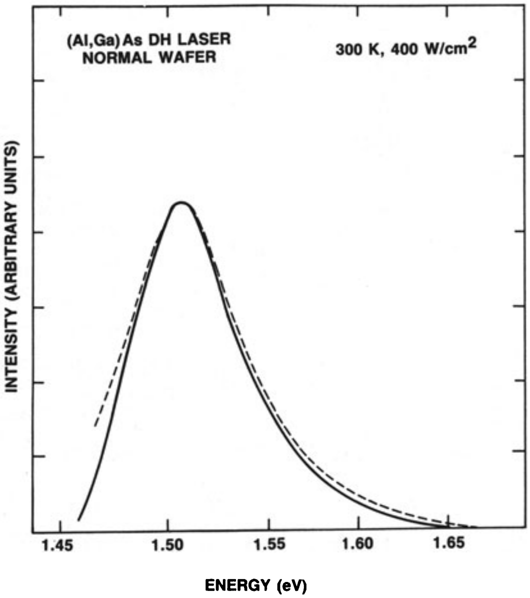

Figure 3.7. The experimental (solid line) and calculated (dashed line) photoluminescence spectra from (Al, Ga)As grown by molecular beam epitaxy. The spectrum was obtained at 300 K, using the 6471 Å line of a Kr laser for excitation at 400 W/cm^2. (After Swaminathan *et al.*, 1983.)

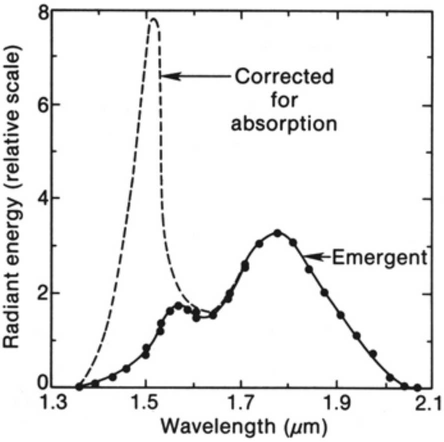

Figure 3.8. Observed luminescence in germanium (solid line), and luminescence obtained by correcting for self-absorption (dashed line). (After Haynes, 1955.)

tion, and half-width have been correlated with the impurity concentration (Cusano, 1964; Pankove, 1966; Casey and Kaiser, 1967); these correlations provide a method of carrier concentration measurement in the semiconductor.

The effect of self-absorption on the shape of the luminescence spectrum should also be considered (see Pankove, 1971; Holt, 1974). For uniform radiative recombination produced per unit depth inside the specimen, the luminescence intensity $L(\nu)$ emitted unidirectionally can be expressed as

$$L(\nu) = (1 - R)\,\frac{L_0(\nu)}{t}\int_0^t e^{-\alpha x}\,dx \tag{3.17}$$

where t is the thickness of the specimen and R is the reflectivity of the exit surface. Hence

$$L(\nu) = (1 - R)L_0(\nu)\,\frac{1 - e^{-\alpha t}}{\alpha t} \tag{3.18}$$

Figure 3.8 shows the effect of correction, using equation (3.18), for the absorption performed for Ge (Haynes, 1955). It is clear that self-absorption virtually eliminates the shorter-wavelength, direct-gap recombination radiation, leaving only the longer-wavelength, indirect-gap recombination band to emerge.

3.4. Luminescence Mechanisms and Centers

The energy levels in the gap of a semiconductor or insulator are categorized as shallow and deep, according to their depth from the nearest band edges. (For discussions of the arbitrariness involved in the definition of deep levels, see the reviews by Neumark and Kosai, 1983 and by Blakemore and Rahimi, 1984.) Deep levels have large capture cross sections for carriers, and they are efficient recombination centers.

As mentioned in Chapter 2, shallow-level centers are relatively simple and can be analyzed by using the effective mass approximation. Another case that is relatively well understood is that of rare-earth ion impurities, and also of transition-metal impurities, which form deep states corresponding to basically sharp levels of the element. This occurs because the electrons in the partially filled *f* and *d* states of rare-earth or transition-metal impurities are screened from the surrounding matrix by the outer electrons of the ion. Thus, they experience only a slight perturbation, which can be described by a crystal field. These types of centers have attracted substantial interest because of their fundamental simplicity and their technological importance due to their strong absorption and emission. For example, Cr ions are the luminescence centers in the ruby laser, and Eu is the luminescence impurity in the red phosphors used in color television (see Chapter 8).

Between these two extremes of shallow centers and the screened atomistic levels of rare-earth and transition-metal impurities fall (deep) levels due to impurities and a wide variety of defects. These defects can be vacancies, interstitials, antisite defects and their complexes, dislocations, stacking faults, grain boundaries, or precipitates. No universal theory, however, is available to account for all these cases. Ligand field theory can be applied in cases in which the atomic levels of the impurity are strongly modified by the surrounding atoms. The shapes of the orbitals of outer valence electrons are strongly modified, and thus the luminescence center is considered as a complex consisting of the impurity atom and its nearest neighbors. The theory appears attractive since it represents intermediate cases between the weakly bound extended states of shallow impurities and the tightly bound inner shell electrons of the rare-earths. The exhaustive study of F-centers in alkali halides, however, provides a good example of the applicability of different models, including the effective mass theory, ligand field theory, and a very simple cubic potential box theory. The latter, for example, correctly accounts for the dependence of the F-band transition energy on the lattice parameter for the alkali halides (Henderson, 1972, 1978). There are also theoretical models that are related to a wide range of possible complexes in compounds containing a number of vacancies and/or interstitials and impurities that can aggregate in various combinations. In such cases, the different possible surroundings for an impurity or defect have different symmetries, which impose selection rules for possible transitions between levels. Thus, some possible complexes can be ruled out on symmetry considerations (Henderson, 1978).

There are three basic processes that determine the luminescence properties of inorganic solids: (1) the absorption of the energy of the incident beam, (2) the transfer of that energy, and (3) the conversion of the energy into photons, i.e., the emission of energy. In addition, important classifications of luminescent systems are (1) those in which the absorption and emission of energy take place in the same center, (2) systems in which the absorption and emission of energy occur in different centers but with no charge transport involved, and (3) systems where luminescence occurs after the transport of charge carriers.

In general, the probability of direct electron-hole recombination is small, and most recombination events occur through levels in the band gap as in the example in Figure 3.9. The electron-hole pair is generated by an incident energetic electron or photon. The carriers dribble down to the band edges within about 10^{-11} to 10^{-12} sec and reach thermal equilibrium with the lattice by the most likely process of emission of phonons. The carriers in the conduction and valence bands can move through the crystal until they are trapped temporarily. By acquiring sufficient energy from the lattice vibrations, an electron, for example, can be reexcited back to the conduction band. The probability of escape is given by the Boltzmann factor $P \propto \exp(-E_t/kT)$, where E_t is the depth of the trap. The coefficient of proportionality, about 10^8 to 10^9 $\sec^{-1}$, is given by $N\sigma_t V_{th}$, where N is the density of states in the band, σ_t is the capture cross section (a measure of the effectiveness of the localized level in capturing excess carriers passing nearby), and v_{th} is the carrier thermal velocity. Thus, the escape probability depends on E_t and on the temperature. At room temperature, electrons can be trapped from seconds to days, depending on E_t. Thus the energy of the incident radiation can be stored in traps, which are responsible for the persistence of phosphors. An electron may eventually encounter a recombination center (i.e., an activator). We can distinguish between traps and recombination centers as follows. If, following the capture of a carrier of one type, the probability of reexcitation is higher than the capture of a carrier of the opposite type, the center is a trap. If the capture of a carrier of one type is followed by a capture of a carrier of the opposite type, it is predominantly a recombination center. In other words, for a trap, the capture cross section of one type of a carrier is much larger than that of the opposite type, whereas a recombination center has a large capture cross section for both types of carriers.

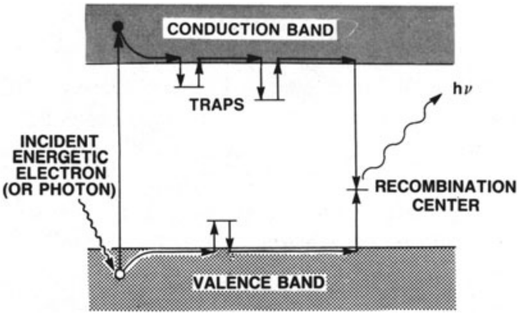

Figure 3.9. Schematic diagram of excitation, trapping, and recombination mechanisms in luminescence with trapping levels for both electrons and holes.

If only one type of recombination center is present, the carrier lifetime is given by $\tau = (N\sigma V_{\text{th}})^{-1}$, where N is the density of recombination centers, σ is the capture cross section of the centers for free carriers, and V_{th} is the carrier thermal velocity. The density of recombination centers generally lies in the range from about 10^{12} to 10^{19} cm^{-3}. Depending on the nature of the Coulomb interaction, capture cross sections range from about 10^{-25} cm^2 (for Coulomb repulsive capture) to 10^{-12} cm^2 (for Coulomb attractive capture). Thus, for a carrier thermal velocity of about 10^7 cm/sec, the lifetime τ of free carriers can vary from about 10^{-14} sec to as long as days.

As mentioned earlier, the information in broad luminescence bands observed above liquid nitrogen temperatures is difficult to interpret. At liquid helium temperatures, however, as the thermal broadening effects are minimized, CL spectra in general become much sharper and more intense. This leads to an improved signal-to-noise ratio and to a more unambiguous identification of luminescence centers (see Figure 3.10). The "edge" (near-band-gap) emission (Figure 3.10a) at liquid helium temperatures is often resolved into emission lines (Figure 3.10b). These can be due to, for example, excitons, free-carrier-to-donor

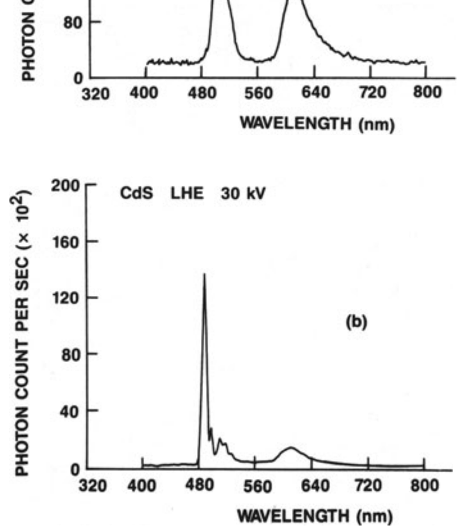

Figure 3.10. Uncorrected CL count-rate spectra from a CdS crystal (a) at room temperature and (b) at liquid helium temperature. There is a change of scale between the two. The near-band-gap emission in (b) has a peak count rate about 4.5 times that of the fundamental band in (a) and is resolved into a series of narrow lines, known as the *edge emission*. The broad impurity peak on the right, in contrast, has the same peak count rate and full width at half-maximum at both temperatures. (After Holt, 1981.)

Table 3.6. Critical-Point Phonon Energies (in eV) for Some III-V Compounds*

Critical-point	Mode	InP	GaAs	GaP
Γ	LO	0.0424	0.0355	0.0486
	TO	0.0398	0.0335	0.0457
L	TO	0.0369	0.0326	0.0468
	LO	0.0312	0.0294	0.0408
	LA	0.0294	0.0257	0.0346
	TA	0.0108	0.0073	0.0085
X	TO	0.0343	0.0319	0.0447
	LO	0.0293	0.0296	0.0385
	LA	0.0286	0.0271	0.0328
	TA	0.0201	0.0095	0.0144

*After Spitzer, 1967 and Stierwalt and Potter, 1967.

(or acceptor) transitions and their phonon replicas (or sidebands), and/or DAP lines.

Phonon replicas are series of lines separated by a phonon energy $\hbar\omega$ (Dean, 1983). Any mechanism giving a sharp emission line may be accompanied by these replicas. In the phonon spectrum, there are transverse and longitudinal phonons in both the acoustic and optical branches. These are denoted as TA (transverse acoustic), LA (longitudinal acoustic), TO (transverse optical), and LO (longitudinal optical). In fact, there are two transverse phonons in both the

Table 3.7. Phonon Energies (in eV) for Some II-VI Compounds*

	ZnO (W)	ZnS (W)	ZnS (ZB)	CdS (W)	CdTe (ZB)
TO (zone center)	—	—	0.039	0.030	0.0174
TO_1 (zone edge)	0.054	0.039	0.037	0.030	0.017
TO_2 (zone edge)	0.052	0.037	—	0.030	—
LO (zone center)	—	—	0.031	0.038	0.021
LO (zone edge)	0.060	0.042	0.026	0.037	0.022
LA (zone edge)	0.030	0.022	0.020	0.019	0.013
TA_1 (zone edge)	0.017	0.011	0.011	0.010	0.008
TA_2 (zone edge)	0.012	0.009	—	0.009	—

*After Ray, 1969. W, wurtzite; ZB, zinc blende.

acoustic and optical branches, and there can be local vibrational modes (characteristic of the center) that may also affect the luminescence spectrum. The phonon energies of some III-V and II-VI compounds, for example, are summarized in Tables 3.6 and 3.7. In general, more than one type of phonon (and in various combinations) may participate in the optical transitions. Edge emission in II-VI compounds was explained by Hopfield (1959), using a model in which a center can emit LO phonons. The observed emission is attributed to radiative recombination via a shallow level E_s that can emit a photon of energy $h\nu = E_g - E_s$, where E_s is the energy depth of the recombination level. The center can also emit one or more phonons, which lead to phonon replicas in the emission spectrum. The energies of the lines thus correspond to $h\nu = E_g - E_s - n\hbar\omega$, where $\hbar\omega$ is the phonon energy (usually LO, although others may be involved).

Line intensities (i.e., photon emission rates) can be derived from the probability of the emission of one or more phonons, which is described by a Poisson distribution. If I_0 is the intensity of the first line at the highest energy due to photon emission with no phonon participation (the second line corresponds to photon emission accompanied by one phonon emission, etc.), then the intensity I_n of the $(n + 1)$st line is

$$I_n = I_0 \bar{N}^n / n! \tag{3.19}$$

where $\bar{N}$ is the average number of phonons emitted in a radiative recombination.

There are two models of excitons. Strongly bound, closely localized excitons are represented by the Frenkel model; weakly bound excitons, by the Wannier-Mott model with a wave function spread over many interatomic distances. Wannier-Mott excitons are usually present in materials with high dielectric constants. At and below liquid nitrogen temperatures these excitonic lines can be resolved from the lower-energy side of the band-gap emission. The energy levels can be described by a hydrogenic-like expression

$$E_n = E_g - E_B / n^2 \tag{3.20}$$

where $n = 1,2,3,\ldots$ is the principal quantum number and E_B is the exciton binding energy (see Figure 3.11 and Table 3.8), $E_B = \mu e^4 / 2\hbar^2\epsilon^2$, where $\mu = m_e m_h / (m_e + m_h)$ is the reduced effective mass and ϵ is the dielectric constant. Frenkel and Wannier-Mott excitons are two limiting models differing in the degree of pair separation. Intermediate separations of electrons and holes are also possible. A detailed discussion of these intermediate cases, as well as the ranges of validity of the Frenkel and Wannier-Mott exciton models and the proper choice of the dielectric constant, is given by Knox (1963). The exciton emission line shapes can be analyzed by using two limits for the phonon-broadened line. For small values of the exciton-phonon coupling constant, a quasi-Lorentzian shape description is valid; for larger coupling constants the line is of Gaussian form (Knox, 1983).

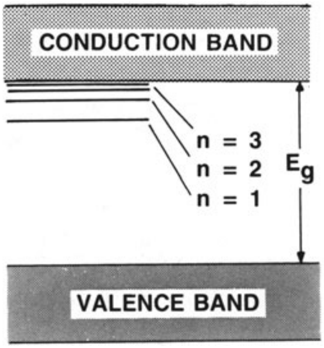

Figure 3.11. Energy levels of excitons in a semiconductor or insulator.

Series of emission lines can also arise from donor-acceptor pairs. An electron captured by a donor (which is positively charged when ionized) recombines with a hole similarly captured by an acceptor. The energy of the donor-acceptor recombination emission depends on pair separation (see Figure 3.12):

$$h\nu(r) = E_g - (E_A + E_D) + e^2/\epsilon r \tag{3.21}$$

where E_A and E_D are the binding energies of the acceptor and donor, respectively, and ϵ is the dielectric constant. The last term arises from the coulombic interaction of the carriers and depends on the pair separation r, which can only have values corresponding to integral numbers of interatomic spacings. Thus, a fine structure, consisting of sharp emission lines, is expected. Two extreme cases are the widely separated (or distant) DAPs and associated (nearest-neighbor) DAPs. For distant DAPs r is large, the last term in equation (3.21) is small, and the discrete lines will form a continuum. Consequently, broad unresolved (distant) DAP bands are observed. For the distant-pair case the static dielectric constant is used, whereas for the associated pair case the optical dielectric constant is used. This equation does not contain the van der Waals term, which may

Table 3.8. Exciton Binding Energies (in meV) of Some Inorganic Solids*

Si	14	CdS	28
InP	4.8	ZnSe	20
GaAs	4.2	ZnS	39
GaP	24	ZnO	59
CdTe	12	BaO	56
CdSe	15	KBr	400

*After Reynolds and Collins, 1981.

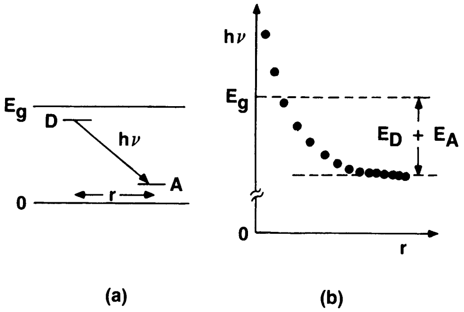

Figure 3.12. Schematic diagram of (a) a donor-to-acceptor transition (r is the pair separation) and (b) the effect of the coulomb interaction on the emission energy $h\nu$. (After Pankove, 1971.)

become important for small r (for more details, see Dean, 1966; Pankove, 1971; Bebb and Williams, 1972).

An interesting feature of the donor-acceptor recombination emission is that at high excitation intensity sharp pair lines are observed, whereas at low excitation power the distant-pair transitions are dominant. This follows from the fact that the recombination rate depends on the pair separation r. The radiative transition probability in this case is

$$P(r) = P(0)\exp(-2r/a) \tag{3.22}$$

where a is the Bohr radius of the less tightly bound center, and $P(0)$, the limiting transition probability as $r \rightarrow 0$, is a constant for all pairs.

A characteristic feature of donor-acceptor recombination is the shift of the peak as a function of the excitation intensity. This follows from the reciprocal dependence of the peak energy $h\nu$ on the pair separation r and the reduction in the transition probability with increasing r. At higher excitation intensities, widely separated pairs will be saturated because of the lower transition probability, and a larger portion of pairs with smaller r are excited and decay radiatively because of their higher transition probability. Therefore, a relative increase in the intensity due to pair transitions with smaller r is expected as the excitation intensity increases. This leads to a shift of the peak to higher energies. A shift of the peak to lower energies can also be observed as the delay after excitation in time-resolved measurements is increased. These features of DAP recombination emission enable one to distinguish it from other recombination processes.

Donor-acceptor pair recombination emission also occurs near the band edge. At low temperatures, however, numerous sharp lines are observable, at least in PL studies, which also distinguishes this emission from other mechanisms. This fine structure can be resolved for pair separations r up to about 50 lattice spacings. The results of low-temperature PL studies of a wide variety of luminescence centers in semiconductors are available in the literature, and the data can help in the identification of emitting centers.

3.5. Recombination Processes

Carriers generated in a semiconductor will undergo diffusion, followed by recombination, including that which gives rise to luminescence. Thus, generation, diffusion, and recombination are important for describing luminescence phenomena. The diffusion of the stationary excess minority carriers for continuous irradiation can be treated in terms of the differential equation of continuity. For electrons in p-type semiconductors this can be written as

$$D\nabla^2(\Delta n) - \Delta n/\tau + g(r) = 0 \tag{3.23}$$

where D is the diffusion coefficient, Δn is the excess minority carrier density per unit volume, τ is the minority carrier lifetime, and $g(r)$ is the generation rate of excess carriers per unit volume. This equation is valid under the conditions that τ is independent of Δn and that the motion of excess carriers is purely diffusive. The former condition is satisfied if Δn is small compared with the majority carrier density p_0 (for p-type material); this low-injection condition can usually be satisfied by using low electron beam currents. The condition that the motion of excess carriers is purely diffusive is valid for sample regions without depletion zones or applied fields.

Recombination centers with energy levels in the gap of a semiconductor are radiative or nonradiative, depending on whether the recombination leads to the emission of a photon or not. These centers are characterized by a rate of recombination $R \propto \tau_r^{-1}$, where τ_r is a recombination time. The carrier diffusion length L is related to the lifetime τ by $L = (D\tau)^{1/2}$, where D is the diffusion coefficient. When competitive radiative and nonradiative centers are both present, the observable lifetime is given by

$$1/\tau = 1/\tau_{rr} + 1/\tau_{nr} \tag{3.24}$$

which can be rewritten as

$$\tau = \tau_{rr}\tau_{nr}/(\tau_{rr} + \tau_{nr}) \tag{3.25}$$

where τ_{rr} and τ_{nr} are the radiative and nonradiative recombination lifetimes, respectively. Here τ_{nr}, in general, is the resultant of several nonradiative recombination processes ($\tau_{nr}^{-1} = \Sigma_i\, \tau_{nri}^{-1}$). The *radiative recombination efficiency* (or internal quantum efficiency) η, which is defined as the ratio of the radiative recombination rate R_{rr} to the total recombination rate R, is, using equation (3.25),

$$\eta = R_{rr}/R = \frac{\tau}{\tau_{rr}} = \frac{1}{1 + \tau_{rr}/\tau_{nr}} \tag{3.26}$$

Hence, $\eta \cong \tau_{nr}/\tau_{rr}$ when, as is often the case, $\tau_{rr} \gg \tau_{nr}$. For a material that contains only one type of radiative and one of nonradiative recombination center, one can write, using $\tau = (N\sigma V_{th})^{-1}$,

$$\eta = \frac{1}{1 + N_{nr}\sigma_{nr}/N_{rr}\sigma_{rr}} \tag{3.27}$$

where N_{rr} and N_{nr} are the densities of the radiative and nonradiative recombination centers, respectively, σ_{rr} and σ_{nr} are the radiative and nonradiative capture cross sections, and V_{th} is the carrier thermal velocity. The rate of CL emission is proportional to η, and equation (3.27) shows that in the observed CL intensity we cannot distinguish between radiative and nonradiative processes in a quantitative manner. It is possible to ensure that $N_{rr} > N_{nr}$ in some cases, but usually $\sigma_{nr} \gg \sigma_{rr}$.

We can describe the temperature dependence of η, which can be written as

$$\eta = P_{rr}/(P_{rr} + P_{nr}) \tag{3.28}$$

where P_{rr} and P_{nr} are the radiative and nonradiative transition probabilities, respectively. The term P_{rr} is independent of temperature, and $P_{nr} \propto \exp(-E^*/kT)$, where E^* is an activation energy. Thus, we can write

$$\eta = \frac{1}{1 + C\exp(-E^*/kT)} \tag{3.29}$$

The surface of a crystal may contain a high density of localized levels in the band gap of the material. Thus, the measured values of the lifetime are effective values determined by the bulk and surface lifetimes:

$$1/\tau_{eff} = 1/\tau_{bulk} + 1/\tau_{surf} \tag{3.30}$$

This result is important in CL analysis of a minority carrier lifetime and in depth-resolved CL studies. Whereas τ_{bulk} depends on the density of recombination centers in the bulk of the material, τ_{surf} is determined largely by the recombination centers on the surface. Surface states arise due to the abrupt change at the surface of the three-dimensional band structure associated with the bulk of the crystal. In addition, impurity atoms and oxide layers present on the surface of the material may also produce discrete energy levels. These lead to a high band-gap density of localized levels near the surface of a material (i.e., surface states). Since to maintain charge neutrality any excess charge in surface states must be compensated by changes in the free-carrier concentration in the crystal, the effect of surface states on the properties of the material may extend substantially below its surface. In pure crystals, τ_{bulk} may be large enough so that surface recombination will dominate. In such a case, the lifetime of the material may depend strongly on surface treatment procedures.

The major electron-hole recombination pathways between the conduction and valence bands involve donor and/or acceptor levels, recombination via deep-level traps, and recombination at the surface. The last two are expected to be nonradiative at any rate in the near-band-gap spectral region. These are competitive recombination processes, the kinetics of which can be analyzed by using Hall-Shockley-Read (HSR) recombination statistics (Hall, 1952; Shockley and Read, 1952). The capture and emission rates of electrons and holes based on recombination through a single dominant type of trap can also be described by HSR recombination statistics, which can be applied to a wide variety of conditions when a single trap dominates the recombination process. From HSR statistics it follows that deeper traps act as efficient recombination centers. In a simple case, when one radiative recombination center is dominant, the luminescence efficiency will depend on the ratio of the radiative recombination lifetime to the nonradiative recombination lifetime [equation (3.26)]. For cases in which a distribution of traps is present, the statistics described by Rose (1963) should be considered. More recent work by Simmons and Taylor (1971) presents statistics for an arbitrary distribution of both the trap levels and trap cross sections. A useful monograph on deep impurity levels and recombination processes in semiconductors is Milnes (1973) (see also Milnes, 1983).

Transitions via recombination centers depend on their occupancy. This is a function of temperature, so the minority carrier lifetime varies with temperature.

In general, CL intensity will depend on the relative probability of radiative recombination and of recombination by all possible mechanisms. As pointed out earlier, there could be several different nonradiative channels present in the material, and equation (3.24) can be rewritten as $\tau^{-1} = \tau_{\mathrm{rr}}^{-1} + \sum_i \tau_{\mathrm{nri}}^{-1}$, where τ_{nri} are the nonradiative recombination times for the operative processes. The recombination times for various processes that are significant in GaAs were analyzed by Kyser and Wittry (1964). These recombination processes are Auger recombination in the host crystal (A-H), Auger recombination at an impurity (A-I), direct band-to-band radiative recombination (D-R), and multiphonon emission at an impurity (MP-I). These calculated recombination times as a function of electron concentration are shown in Figure 3.13. In these calculations it was assumed that (1) the injection level is low (i.e., $n \ll n_0$), except that for the A-H process a high injection level was assumed; (2) Auger recombination in the host crystal (A-H) gives lifetimes $\tau_n = \tau_p = \tau_i(3n_i^2/n^2)$, where n_i is the intrinsic carrier density and the intrinsic carrier lifetime $\tau_i = 10^{19}$ sec at 300 K; (3) in the D-R process $\tau_n = \tau_p = [B(n_0 + p_0 + n)]^{-1}$, where $B = 6.3 \times 10^{11}$ cm^3 sec^{-1} at 300 K; (4) for the impurity controlled processes (A-I and MP-I) an impurity concentration of 10^{16} cm^{-3} and a level 0.5 eV below the middle of the band was assumed. Taking these assumptions (as well as others regarding capture probabilities of recombination processes) into account, Kyser and Wittry pointed out that the calculations plotted in Figure 3.13 should be regarded as order-of-magnitude estimates. They also predicted that similar results would apply for *p*-type material, except that in the MP-I process there might be a different capture probability than that assumed in their calculations, so curve MP-I of Figure 3.13 could be affected. Kyser and Wittry also discussed possible changes in the calculations of Figure 3.13 as the result of varying impurity concentrations.

The results of Figure 3.13 indicate that for $N_0 = 10^{18}$ cm^{-3} (which is close to the optimal doping level for luminescence efficiency) the approximate values of the recombination times for the different recombination processes are $\tau_{A-H} = 10^{-3}$ sec, $\tau_{MP-I} = 10^{-6}$ sec, $\tau_{D-R} = 10^{-8}$ sec, and $\tau_{A-I} = 10^{-10}$ sec. Substituting these values into equation (3.24), where it is assumed that $\tau_{nr}^{-1} = \Sigma_i \tau_{nri}^{-1}$, gives $\tau = 10^{-10}$ sec. Substituting these values of τ and $\tau_{rr} = \tau_{D-R}$ in equation (3.26) shows that only about 10^{-2} of the electron-hole pairs generated in GaAs at room temperature will produce photons. In other words, the internal CL quantum efficiency of *n*-type GaAs (with 10^{18} cm^{-3} carrier concentration) at 300 K is expected to be about 1%.

As mentioned, one of the basic difficulties involved in luminescence characterization is the lack of information on the competing nonradiative processes present in the material. The most widely used technique that complements luminescence spectroscopy for the assessment of nonradiative levels is deep-level transient spectroscopy (DLTS) (Lang, 1974), which is based on the capture and thermal release of carriers at traps. An analogous SEM technique, scanning deep-level transient spectroscopy (SDLTS), was developed by Petroff *et al.* (1977, 1978) for determining both the energy levels and the spatial distribution of deep states in semiconductors. While a voltage bias pulse is used to fill the

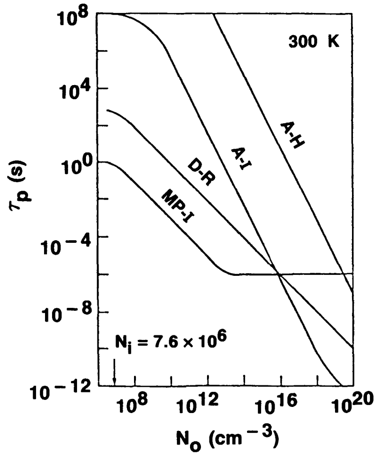

Figure 3.13. Calculated recombination times as a function of electron concentration in GaAs for different processes. These are Auger recombination in the host crystal (A-H), Auger recombination at an impurity (A-I), direct band-to-band radiative recombination (D-R), and multiphonon emission at an impurity (MP-I). (After Kyser and Wittry, 1964.)

traps in the DLTS technique, an electron beam injection pulse is employed in the SDLTS method. Recently, the introduction of a more sensitive detector (Breitenstein, 1982) has made the technique more widely applicable (Heydenreich and Breitenstein, 1985; Breitenstein and Heydenreich, 1989). For more details of the SDLTS technique see Chapter 5.

3.6. Temperature Dependence of Luminescence

Luminescence, like the other optical and electronic properties of semiconductors and the band structure in general, is strongly dependent on temperature. The effects of temperature on both the photon energy and the intensity of the CL emission bands should be considered.

In general, there are two main causes of the temperature dependence of band states in any semiconductor or insulator. First, the band structure must be a function of the crystal lattice spacing, so lattice dilation may be expected to contribute to a change in the energy position of band states. The second contribution is due to electron-phonon interactions. Typically, the dilation contribution, which can be calculated from the thermal expansion and pressure coefficients, amounts to about 20 to 50% of the total temperature dependence of band states (total temperature coefficients range from 10^{-4} to 10^{-3} eV K^{-1}). Several theoretical treatments of the contribution from the electron-phonon interactions are described by Cohen and Chadi (1980).

To account for the phonon contribution to the temperature dependence of the absorption and emission edges, researchers proposed a different approach (Yacobi *et al.*, 1975, 1977, 1980; Samuel *et al.*, 1987) for some II-VI compounds. This approach, which combines the Dow-Redfield theory of the phonon-generated microfields (Dow and Redfield, 1972) and the Franz-Keldysh theory of the electric-field-induced shift of exponential absorption edges, explains the temperature dependence of the absorption and emission edges as due to temperature-dependent phonon-generated microfields. Although this model has been successful in explaining the temperature shifts of the absorption and emission edges in CdS and ZnS (Yacobi *et al.*, 1975, 1977, 1980), the temperature shift of the absorption edge in $Zn_xCd_{1-x}Se$ (Samuel *et al.*, 1987) and that of the first exciton reflection peak in ZnSe and ZnS (Theis, 1977), further studies on other materials will be necessary before the model can be shown to be generally applicable.

For practical applications, the temperature dependence of the band gap can be fitted by the empirical expression (Varshni, 1967)

$$E_g(T) = E_g(0) - bT^2/(T + \Theta) \tag{3.31}$$

where $E_g(0)$ is the energy gap at 0 K, and b and Θ are constants. This expression was found to represent satisfactorily experimental data for a variety of semiconductors. (For b- and Θ-values for some semiconductors, see Pankove, 1971.) More recent and refined values of the fitting parameters for some semiconductors were reported by Thurmond (1975), who showed for GaAs that $E_g(0) = 1.519$ eV, $b = 5.405 \times 10^{-4}$ eV/K, and $\Theta = 204$ K. The use of these values in equation (3.31) gives the dependence shown in Figure 3.14. Temperature shifts of the fundamental CL peak energy can therefore be used to measure temperature gradients in devices such as GaAs and InP Gunn diodes with various bias voltages applied (see Jones *et al.*, 1973; Davidson and Vaidya, 1977).

The temperature dependence of the fundamental CL band intensity in direct-gap semiconductors was considered by Jones *et al.* (1973), who developed a theoretical model based on the van Roosbroeck–Shockley (1954) theory. The total CL output, L_{CL}, can be written as

$$L_{\mathrm{CL}} = \frac{8\pi n}{c^2}\left(\frac{A'}{A}\frac{1}{n_0} + \frac{1}{p_0}\right)\int_{\nu=0}^{\infty} \alpha(\nu)\nu^2 \exp\left(\frac{-h\nu}{kT}\right) Q(\nu)\, d\nu \times \int_{z=0}^{\infty} \Delta p(z) \exp[-\alpha(\nu) z]\, dz \qquad (3.32)$$

where L_{CL} is the photomultiplier output, $\Delta p(z)$ is the excess hole concentration profile (for an n-type semiconductor), $\alpha(\nu)$ is the absorption coefficient, n is the refractive index of the material, c is the speed of light, A'/A is the degeneracy factor, ν is the frequency of the radiation, and $Q(\nu)$ is the quantum efficiency of the detector. The temperature dependence of the CL intensity in a nondispersive experiment can be obtained from this equation provided that $\alpha(\nu)$, p_0, and $\Delta p(z)$ are known as functions of temperature throughout the range of interest. If this information in not available, some simplifying assumptions have to be made. With the assumption that the refractive index n and the factor $\exp[-\alpha(\nu)z]$ do not

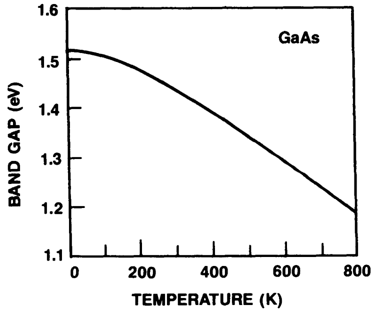

Figure 3.14. The energy gap as a function of temperature for GaAs. The curve was calculated from equation (3.31) using $E_g(0) = 1.519$ eV, $b = 5.405 \times 10^{-4}$ eV/K, and $\Theta = 204$ K.

vary significantly with temperature in the range of interest and because the value of z is relatively small for typical electron beam voltages of 5 to 20 kV, the exponential term was omitted. Thus, the second integral in equation (3.32) can be simplified and rewritten as

$$\int_0^\infty \Delta p(z)dz = g\tau_p \int \psi(z)dz \qquad (3.33)$$

where g is the electron-hole pair generation rate, τ_p is the total lifetime for holes, given by $1/\tau_p = 1/\tau_{rr} + 1/\tau_{nr}$, and $\psi(z)$ is the solution of the diffusion equation for a particular generation function and surface recombination velocity. Being a function of the diffusion length L, $\psi(z)$ is also a function of the temperature. If the detector sensitivity $Q(\nu)$ is constant for all ν, the first integral in equation (3.32) is proportional to $1/\tau_{rr}$. In order to evaluate the integral in equation (3.33), Jones *et al.* considered two types of the generation function. One, the Gaussian function used by Wittry (1958), is $F(z) = F_0 \exp[-a^2(z - z_0)^2]$; the other is a polynomial function $F(z)$ by Everhart and Hoff (1971). Jones *et al.* found that the results of integration, using these two forms of the generation function, were similar, and they used the simpler polynomial function. To obtain the excess minority carrier distribution $\Delta p(z)$, one must use the differential equation of continuity for the diffusion of the excess minority carriers:

$$D_p \frac{d^2 \Delta p}{dz^2} - \frac{\Delta p}{\tau_p} + F(z) = 0 \qquad (3.34)$$

The solution to this equation requires that the boundary condition, which accounts for diffusion of the minority carriers to the surface, be specified as

$$D_p \frac{d \Delta p}{dz} = s \Delta p(0) \qquad (3.35)$$

where s is the surface recombination velocity, and it is assumed that $\Delta p(\infty) = 0$.

The polynomial due to Everhart and Hoff is fitted to $F(z)$ normalized to the Gruen range $R_G = 3.98\mathrm{V}^{1.75}$ μg cm^{-2}. That is, the Everhart-Hoff function is expressed in terms of $y = z/R_G$ and $L_r = L/R_G$. The solution for $\Delta p(z)$ is then $\Delta p(z) = C \exp(-y/L_r)$ for $y \geq 1$. For $0 \leq y \leq 1$, Δp is given by a more complicated expression, which may be evaluated from the boundary condition, given by equation (3.35), by replacing s with the reduced surface recombination velocity $S = s\tau/L$. Substituting these expressions into equation (3.33), we obtain the CL intensity as a function of the reduced range $W = R/\rho L$ for various values of S for the Gaussian and polynomial distributions. The results obtained for both are similar, and for large values of S, which are typical for GaAs over a limited range of

W, the results are approximately proportional to L^{-a}, where a is a constant appearing in the solution of the continuity equation (3.34) for Δp. The excess minority carrier integral can then be written as

$$\int_0^{\infty} \Delta p(z)\, dz = \text{constant} \times g\tau_p L^{-a} \tag{3.36}$$

In this expression, a depends on the range of L and the value of S of interest. Substituting equation (3.36) into equation (3.32) gives

$$L_{\text{CL}} = \text{constant} \times \left(\frac{A'}{An_0} + \frac{1}{p_0}\right) \frac{\tau_p}{\tau_r} L^{-a} \tag{3.37}$$

Using this equation, Jones *et al.* (1973) computed a curve of L_{CL} versus temperature for n-type GaAs ($n_0 = 10^{16}$ cm^{-3}) by substituting expressions for the temperature dependence of the terms L and $A'/An_0 + 1/p_0$, assuming $S \approx 50$ and $0.1 < W < 4.0$, so $a = 0.717$. They also assumed the material had predominantly radiative recombination mechanisms, so $\tau_p \approx \tau_{rr}$ and the temperature dependencies of the lifetimes cancel. The experimental and calculated temperature dependencies, normalized to room temperature, of the total CL emission from an n-type GaAs, shown in Figure 3.15, were in good agreement despite the many simplifications in the model. At low temperatures, specimen degeneracy may invalidate the expression derived for the term $A'/An_0 + 1/p_0$. This may explain the relatively large discrepancy at temperatures below about 200 K.

This analysis of the temperature dependence of CL intensity is applicable to

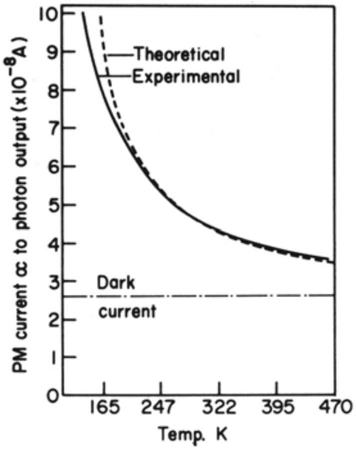

Figure 3.15. Experimental and calculated temperature dependences of the total CL emission from n-type GaAs. (After Jones *et al.*, 1973.)

material with predominantly radiative recombination mechanisms, which led to the elimination of the temperature dependence of the lifetimes. This, however, may not be the case for materials with predominantly nonradiative recombination mechanisms or several competitive recombination channels. In such cases, a more complex model is required.

4

Cathodoluminescence

4.1. Introduction

As mentioned earlier, the mechanisms leading to photon emission in inorganic solids are similar for different types of excitation energy, so cathodoluminescence can be compared with other luminescence phenomena, such as photoluminescence. However, differences associated with the details of the excitation process may arise. Electron beam excitation in general leads to emission by all the luminescence mechanisms present in the material. Excitation-deexcitation centers can be excited, for example, by direct collision or resonant energy transfer from a coactivator. Photoluminescence emission may strongly depend on the excitation energy $h\nu$, which can be used for selective excitation of particular emission processes. Cathodoluminescence analysis of materials, on the other hand, can provide depth-resolved information by varying the electron beam energy (see Chapter 6).

Electron beam excitation may produce orders-of-magnitude greater carrier generation rates than typical optical excitation. This is especially advantageous in studies of wide-band-gap materials, such as diamond. In general, electron energies of up to 100 keV can be used without inducing atomic displacement damage.

Cathodoluminescence analysis enables one to assess various properties of the material with a spatial resolution down to 1 μm or less. For example, (1) spectroscopic CL and monochromatic imaging can be used in the identification and measurement of luminescent center concentrations and distributions, as well as in the determination of the composition of compound materials; (2) electronic properties, such as the carrier diffusion length and surface recombination velocity, can be determined from the dependence of the CL intensity on electron beam voltage, and the minority carrier lifetime can be determined from time-resolved CL measurements; and (3) the concentration and distribution of defects, such as dislocations, can be found from CL maps of the material.

Reviews of CL electron microscopy were provided by Holt (1974), Davidson (1977), Holt and Datta (1980), Pfefferkorn *et al.* (1980), Davidson and Dimitriadis (1980), Booker (1981), Hastenrath and Kubalek (1982), Löhnert and Kubalek (1983), Wittry (1984), Holt and Saba (1985), and Yacobi and Holt (1986). In this chapter, we discuss electron-solid interactions, the basic principles underlying the generation and interpretation of CL signals, the resolution and the detection limit of CL, and artifacts involved in CL analysis. Cathodoluminescence techniques and the characterization of inorganic solids using cathodoluminescence will be discussed in subsequent chapters.

4.2. Interaction of Electrons with Solids

Electron beam–solid interactions, electron energy dissipation, and the generation of carriers in the solid are of great importance for the CL analysis of solids. The bibliography gives several detailed reviews on this subject. In this chapter we present a brief introduction to the subject.

Scattering mechanisms can be divided into elastic and inelastic. The elastic scattering of electrons by the nuclei of the atoms, which are partially screened by the bound electrons, can be analyzed by using the Rutherford model. The total relativistic Rutherford scattering cross section is given by

$$\sigma = (5.21 \times 10^{-21}) \left(\frac{Z}{E}\right)^2 \frac{4\pi}{\delta(\delta + 1)} \left(\frac{E + m_0c^2}{E + 2m_0c^2}\right)^2 \qquad (4.1)$$

where Z is the atomic number of the scattering atom, E is the energy of electrons in keV, and δ is a screening parameter:

$$\delta = (3.4 \times 10^{-3})\, Z^{0.67}/E \qquad (4.2)$$

The angle θ for a particular scattering event can be obtained from the probability for elastic scattering into a particular angular range (0 to θ), which can be derived from equation (4.1) (see Newbury *et al.*, 1986.) Thus, a relationship obtained from the probability distribution is

$$\cos\theta = 1 - \frac{2\delta R}{1 + \delta - R} \qquad (4.3)$$

where R is a uniformly distributed random number ($0 \leq R \leq 1$). The relativistic correction in equation (4.1) can be ignored for electron energies of less than about 50 keV, i.e., for most SEM work. At higher energies, the relativistic correction to the cross section is significant and should be applied. The Rutherford scattering model is fairly accurate for electron energies from about 20 to 50 keV for solids of low to intermediate atomic numbers. The more exact Mott elastic scattering cross section should be used instead for low electron energies and for solids with high atomic numbers (see Kotera *et al.*, 1981).

Inelastic scattering can be described by the Bethe expression for the mean rate of energy loss per segment of distance S traveled in the solid as

$$\frac{dE}{dS} = -2\pi e^4 N_A \frac{\rho Z}{EA} \ln\left(\frac{1.166E}{J}\right) \tag{4.4}$$

where e is the electronic charge, N_A is Avogadro's number, ρ is the density, A is the atomic weight, E is the mean electron energy, and J is the mean ionization potential. The latter is the average energy loss per interaction (for all possible energy loss processes) and is given by

$$J = (9.76\, Z + 58.5\, Z^{-0.19})\, 10^{-3}\ (\text{keV}) \tag{4.5}$$

For low electron energies ($E < 6.34$J), the empirical modification to the Bethe expression by Rao-Sahib and Wittry (1974) should be used.

The elastic scattering of electrons by atoms gives rise to high-energy backscattered electrons and, in the SEM, to atomic number contrast and diffraction effects (channeling patterns) in the emissive mode. Inelastic interaction processes result in a wide variety of useful signals in an electron probe instrument: secondary electron emission, generation of electron-hole pairs, cathodoluminescence, characteristic *x*-rays, Auger electrons, and thermal effects, including electroacoustic (thermal wave) signals. The incident electron undergoes a successive series of elastic and inelastic scattering events in the material. As the result of these scattering events within the material, the original trajectories of the electrons are randomized. The (Gruen) range of the electron penetration is a function of the electron beam energy E_b,

$$R_e = (k/\rho)\, E_b^{\alpha} \tag{4.6}$$

where ρ is the density of the material, k depends on the atomic number of the material and is also a function of energy, α depends on the atomic number and on E_b (see Everhart and Hoff, 1971). An important method of dealing with the electron beam energy dissipation in the solid is that of Monte Carlo trajectory simulation. This is used in x-ray microanalysis computations, for example, and it was also successfully applied to electron-beam–induced current (EBIC) imaging by Joy (1986), but it has not been applied to CL at this writing. Alternatively, analytical approximations can be used, which we will discuss first, followed by basic principles of Monte Carlo simulation.

The total length of an individual electron "random walk" trajectory can be obtained from equations (4.4) and (4.5) and is known as the *Bethe range*. The effective depth to which energy dissipation extends is known as the *Gruen, electron beam,* or *penetration range,* and it is much smaller. It is given by expressions such as equations (4.6) to (4.8).

One can estimate the so-called generation volume (or excitation volume) in the material. According to Everhart and Hoff (1971),

$$R_e = (0.0398/\rho)\, E_b^{1.75}\ (\mu\text{m}) \tag{4.7}$$

where ρ is in g/cm^3 and E_b is in keV. This result was derived for the electron energy range of 5 to 25 keV and atomic numbers $10 < Z < 15$. A more general expression derived by Kanaya and Okayama (1972) was found to agree well with experimental results in a wider range of atomic numbers (see Goldstein *et al.*, 1981). The range according to Kanaya and Okayama is

$$R_e = (0.0276A/\rho Z^{0.889})\, E_b^{1.67}\ (\mu\text{m}) \tag{4.8}$$

where E_b is in keV, A is the atomic weight in g/mol, ρ is in g/cm^3, and Z is the atomic number. Figure 4.1 shows a comparison of the electron generation range calculated according to the Everhart–Hoff and Kanaya–Okayama models for

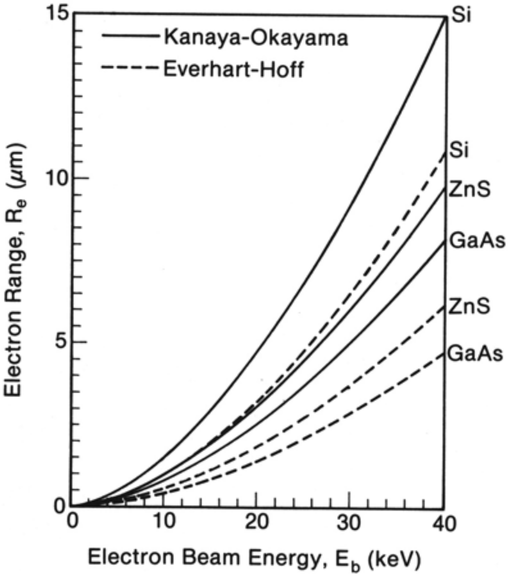

Figure 4.1. The electron beam range R_e in various materials as a function of electron beam energy E_b, calculated from the Kanaya–Okayama and Everhart–Hoff models.

several materials. In view of its wider applicability and good agreement with experimentally derived data, it appears that the Kanaya–Okayama model is more appropriate for quantitative SEM analysis of inorganic solids. In principle, the diffusion of minority carriers can increase the excitation volume, but the observed spatial resolution in both CL and EBIC is approximately equal to R_e. This is largely due to the rapid fall in the diffused carrier density of the form $r^{-1}\exp(-r/L)$ [as will be shown in equation (4.15)]. The dissipated energy density in the generation volume is also concentrated up toward the beam impact point, as we shall see.

The shape of the generation volume depends on the atomic number, varying from a pear shape for a low-atomic-number material, through a spherical shape for $15 < Z < 40$, to hemispherical for larger atomic numbers. One of the fundamental differences between CL and PL is that, whereas a photon generates only one electron-hole pair, one 20-keV electron, for example, can generate thousands of electron-hole pairs in the excitation volume, which is usually several microns in diameter. It is also important to emphasize the difference in the excitation volumes of the thin target and the bulk sample (see Figure 4.2).

The generation factor (i.e., the number of electron-hole pairs generated per incident beam electron) is given by

$$G = E_b(1 - \gamma)/E_i \tag{4.9}$$

where E_b is the electron beam energy, E_i is the ionization energy (i.e., the energy required for the formation of an electron-hole pair), and γ represents the fractional electron beam energy loss due to the backscattered electrons. The ionization energy E_i is related to the band gap of the material, $E_i = 2.8E_g + M$, where $0 < M < 1$ eV depending on the material, and is independent of the electron

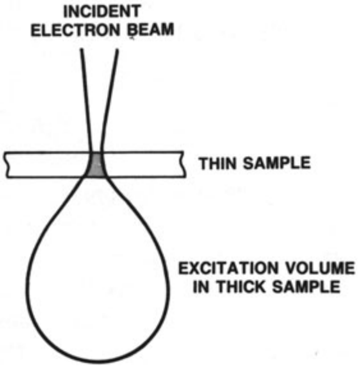

Figure 4.2. Schematic illustration of the volumes analyzed in a thin specimen and a bulk sample.

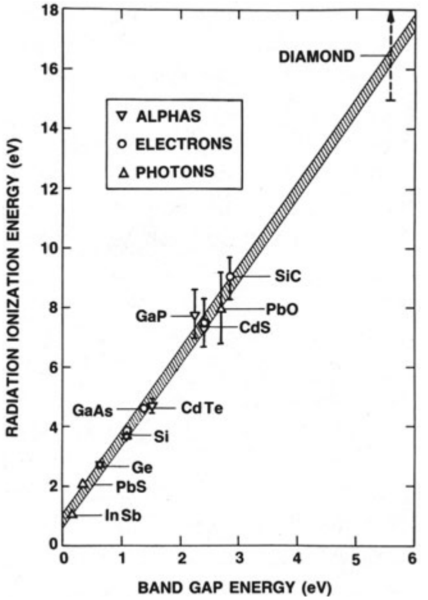

Figure 4.3. The effective ionization energy (i.e., the average energy required for the generation of an electron-hole pair) for incident radiation as a function of the band-gap energy E_g. (After Klein, 1968.)

beam energy (Klein, 1968) (see Figure 4.3). For later data, leading to the same essential conclusion, see Ehrenberg and Gibbons (1981).

The local generation rate of carriers is

$$g(r, z) = \langle g \rangle \, GI_b/e \tag{4.10}$$

where $\langle g \rangle$ is the normalized distribution of the ionization energy in the generation volume, I_b is the electron beam current, and e is the electronic charge. The local generation rate has been determined experimentally for silicon by Everhart and Hoff (1971), who proposed a universal depth-dose function $g(z)$, which can be expressed as

$$g(z) = 0.60 + 6.21z - 12.40z^2 + 5.69z^3 \tag{4.11}$$

(More generally, this polynomial is written in terms of the normalized depth $y = z/R_e$.) This function, shown for different electron beam energies in Figure 4.4, represents the number of electron-hole pairs generated per electron of energy E per unit depth and per unit time.

In many applications, knowledge of the carrier generation distribution is important. Three approximations that have been often used are the point source, the uniform sphere, and the Gaussian (or a modified Gaussian) distribution func-

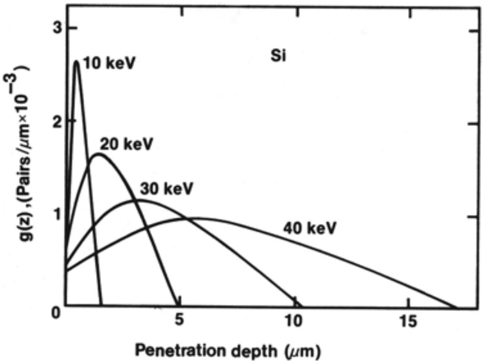

Figure 4.4. The depth-dose curves for Si. These curves were calculated using a universal depth-dose function *g(z)*, which represents the number of electron-hole pairs generated by one electron of energy *E* per unit depth and per unit time. (After Everhart and Hoff, 1971.)

tions (see Figure 4.5). The actual pear-shaped distributions observed experimentally in gases (Cohn and Caledonia, 1970) and in resists (Shimizu *et al.*, 1975) are in a good agreement with Monte Carlo calculations of the energy dissipation in solids. The Gaussian models of the type $F(z) = F_0 \exp[-a^2(z - z_0)^2]$ appear to provide a good approximation (Wittry, 1982; Donolato and Venturi, 1982). A nearly Gaussian representation of the type $g(r,\theta) \propto \exp(-r^2/a^2)\cos\theta$ was also considered for the calculation of carrier density distributions (Davidson and Dimitriadis, 1980). An example comparing the distribution of the carrier generation by a focused electron beam on (a) the uniform generation sphere and (b) the Gaussian approximation is shown in Figure 4.6. In this case, the distance scale is normalized to the electron range R_e, and r and z are the radial distance from the electron beam axis and the depth coordinate, respectively. Figure 4.6b shows the generation as contours of equal ionization rate, and Figure 4.6a provides com-

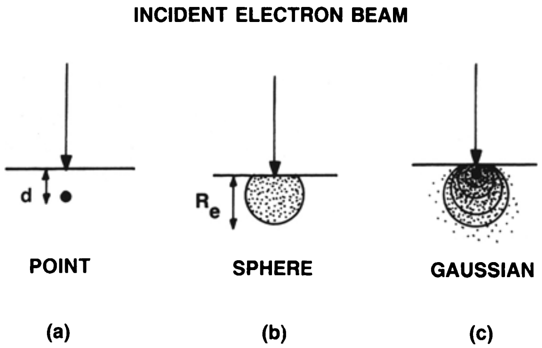

Figure 4.5. Schematic diagram of generation distributions for point source, generation sphere, and Gaussian distribution function. (After Davidson and Dimitriadis, 1980.)

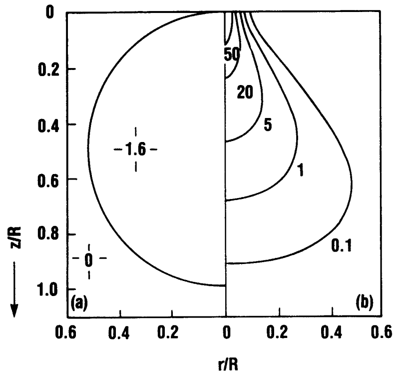

Figure 4.6. Comparison of the distribution of carrier generation by a focused electron beam according to (a) the uniform generation sphere and (b) the Gaussian approximation with $d/R = 0.05$, where d is the electron beam diameter (i.e., the probe size) and R is the electron range. (After Donolato and Venturi, 1982.)

parison with the uniform generation sphere with the same total generation as in Figure 4.6b.

In Monte Carlo electron trajectory calculations, each electron can undergo elastic and inelastic scattering, and it can be backscattered out of the target. The path of an electron is calculated in a stepwise manner; i.e., each electron travels a small distance S in a straight line between random scattering events. At each step, the type of the scattering event (i.e., elastic or inelastic) and the appropriate scattering angle are chosen by using random numbers R. The angular scattering events are due to elastic interaction, and the energy loss is continuous. The step length S is derived from

$$S = -\lambda \ln(|R|) \tag{4.12}$$

where λ, the mean free path, can be obtained from the total scattering cross section

$$\lambda = A/(N_A \rho \sigma) \tag{4.13}$$

where N_A is the Avogadro number, ρ is the density of the material, and σ is the total scattering cross section given by equation (4.1). The energy loss along the trajectory is calculated by equation (4.4) until the energy falls below the value at which an electron can no longer cause ionization. The Monte Carlo method can also compute γ, the backscatter coefficient for any particular case. This is done by dividing the number of backscattered electrons by the total number of calculated trajectories. A few trajectories calculated by the Monte Carlo method do not represent the electron beam–solid interaction volume. The latter can be progressively visualized by plotting larger numbers of electron trajectories. An example is shown in Figure 4.7, where plots of (a) 10 trajectories, (b) 50 trajectories, and (c) 100 trajectories of 20-keV electrons in ZnS clearly illustrate the

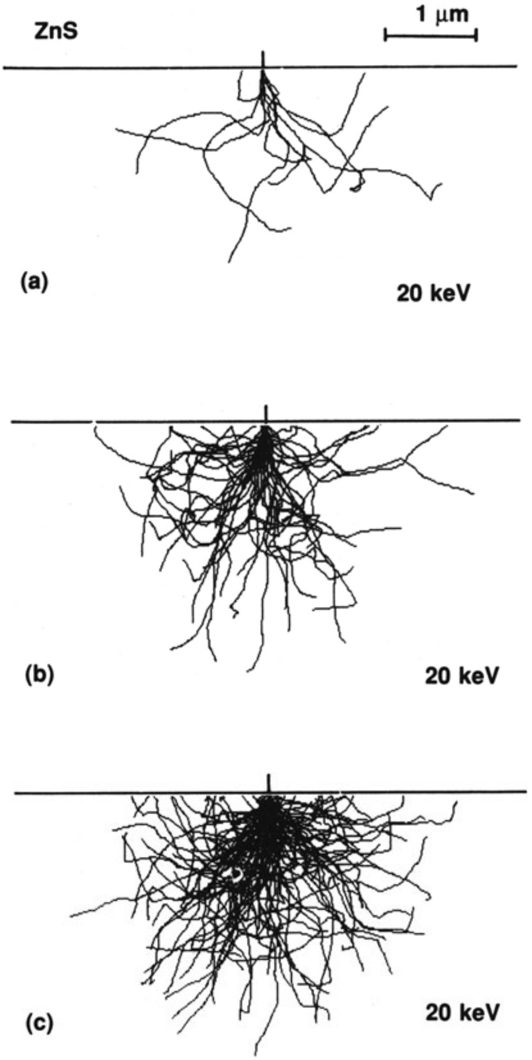

Figure 4.7. Trajectories of (a) 10, (b) 50, and (c) 100 electrons of 20 keV calculated by the Monte Carlo method for ZnS.

effect of the number of electron trajectories on the visualization of the interaction volume. In order to achieve statistical significance in Monte Carlo computations, about a thousand trajectories have to be calculated. The Monte Carlo calculation can also be used for the visualization of the effect of the electron beam energy on the interaction volume, as in Figure 4.8, which presents Monte Carlo calculations of 100 electron trajectories of (a) 10 keV, (b) 20 keV, and (c) 30 keV in

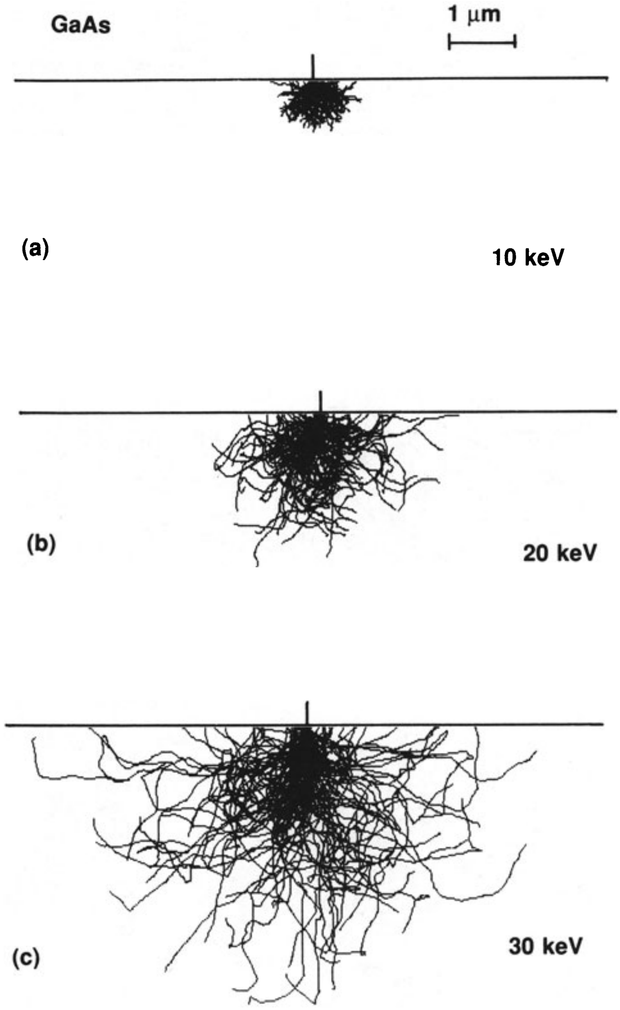

Figure 4.8. Trajectories of 100 electrons of (a) 10 keV, (b) 20 keV, and (c) 30 keV calculated by the Monte Carlo method for GaAs.

GaAs. Similarly, useful illustrations of the interaction volume as a function of such parameters as thickness, tilt, and atomic number of the specimen can be obtained.

Monte Carlo calculations indicate that the boundaries of the generation volume are not well defined. It is also observed that the density of electron trajectories varies significantly and that the energy dissipation (obtained from experiments in polymethylmethacrylate) is not uniform (see, for example, Figure 4.9).

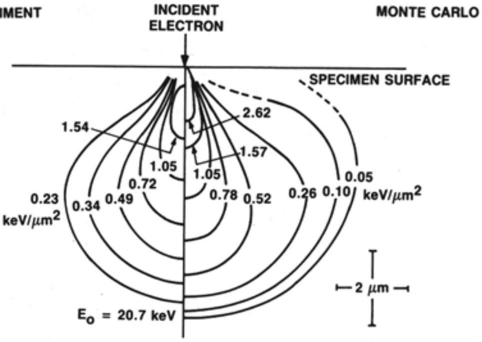

Figure 4.9. Energy dissipation profiles for a low-atomic-number solid (polymethylmethacrylate) as a function of depth, as obtained experimentally by the etching technique and as calculated by Monte Carlo simulation. (After Shimizu *et al.*, 1975.)

Thus, single values for the generation volume obtained from equations (4.7) or (4.8) are only approximations. Contours of equal energy dissipation determined experimentally and calculated by the Monte Carlo method are in good agreement (see Figure 4.9), and they indicate that a substantial fraction of energy dissipation occurs in a small volume near the electron beam impact point.

4.3. Formation of the Cathodoluminescence Signal

The CL intensity, i.e., the number of photons emitted per unit time, can be derived from the overall recombination rate, $\Delta n(r)/\tau$, by noting that only a fraction, $\Delta n(r)\eta/\tau$, recombines radiatively. The radiative recombination efficiency, $\eta = \tau/\tau_{rr}$, is given by equation (3.26). Thus, assuming a linear dependence of the CL intensity, L_{CL}, on the stationary excess carrier density, Δn, which can be verified by measuring the dependence of L_{CL} on electron beam current I_b, we can express the total CL intensity as

$$L_{CL}(r) = \int_V f \frac{\Delta n(r)}{\tau_{rr}} \, d^3r \tag{4.14}$$

where τ_{rr} is the radiative recombination lifetime and f is a function containing correction parameters of the CL detection system and factors that account for the fact that not all photons generated in the material are emitted (due to optical absorption and reflection losses). To analyze the generation of the CL signal, we need to know the excess minority carrier density $\Delta n(r)$. The solution of the continuity equation [see equation (3.23)] for an arbitrary generation function presents a challenging problem (Löhnert and Kubalek, 1983, 1984), since no analytical expression for this function is available. The solution of the continuity equation can be greatly simplified by considering a point source or a sphere of uniform generation. For a spherically symmetric distribution far from a point source, the solution of the continuity equation is

$$\Delta n(r) = C\,\frac{\exp(-r/L)}{r} \tag{4.15}$$

where C is a constant and $L = (D\tau)^{1/2}$ is the minority carrier diffusion length. For a source of finite size, assuming that the generation rate is a constant g_0 inside a spherical excitation volume and zero elsewhere, the solution is (Kyser and Wittry, 1964)

$$\Delta n(r) = \frac{A\exp(-r/L) + B\exp(r/L)}{r} + \tau g_0 \tag{4.16}$$

where A and B are constants. It can be shown that $A = -B$ if the flow of carriers out of a sphere equals the number of carriers generated inside this volume per second minus the number of carriers lost per second by recombination. Thus, equation (4.16) can be expressed as

$$\Delta n(r) = \frac{C\sinh(r/L)}{r} + \tau g_0 \tag{4.17}$$

where C is a constant. It can be shown, by differentiating, that the value of r at which Δn is a maximum is $r = 0$. At this electron beam impact point $\Delta n = C/L + \tau g_0$.

In principle, both the point source solution [equation (4.15)] and the expression for the sphere of uniform generation [equation (4.17)] can be used to obtain information on the CL intensity from $L_{\mathrm{CL}} \propto \Delta n/\tau_{\mathrm{rr}}$.

The depth distribution of $\Delta n(z)$ for a point source solution [equation (4.15)] can be obtained by rewriting this solution and assuming that the total number of carriers generated per second is GI_b/e (where I_b is the electron beam current and e is the electronic charge):

$$\Delta n(z) = \frac{GI_b}{2\pi eD}\int_0^\infty \frac{\exp(-\sqrt{\xi^2 + z^2/L})}{\sqrt{\xi^2 + z^2}}\,2\pi\xi\,d\xi = \frac{GI_bL}{eD}\exp\left(\frac{-z}{L}\right) \tag{4.18}$$

where the integration is over the x-y plane and ξ is a radial coordinate in the plane of the layer so that $r^2 = \xi^2 + z^2$. Assuming again that the CL intensity is proportional to the excess carrier concentration Δn, we have that the luminescence intensity due to radiative recombination in a layer of thickness dz at a depth z is

$$L_{\mathrm{CL}}(z)\, dz \propto \frac{\Delta n}{\tau_{\mathrm{rr}}} \propto \frac{G I_b L \exp(-z/L)\, dz}{e \tau_{\mathrm{rr}} D} \tag{4.19}$$

The actual number of photons generated per second at a depth z can be derived by noting that $L^2 = D\tau$:

$$L_{\mathrm{CL}} = f_D f_A f_R \frac{G I_b \tau}{e \tau_{\mathrm{rr}}} \tag{4.20}$$

or, alternatively, by noting that $\eta = \tau/\tau_{\mathrm{rr}}$:

$$L_{\mathrm{CL}} = f_D f_A f_R\, \eta \frac{G I_b}{e} \tag{4.21}$$

where f_D is a constant factor that accounts for such parameters of the CL detection system as the overall collection efficiency of the light collector, the photomultiplier (or solid-state detector) quantum efficiency, the transmissive efficiency of the monochromator, and the signal amplification factor (see Chapter 5). In this equation, f_A and f_R are factors that account for absorption and internal reflection losses. The absorption loss factor f_A arises from a decrease in intensity of the form $\exp(-\alpha d)$, where α is the absorption coefficient and d is the length of the photon path in the interior of the material. This correction factor can be derived for the point source model as follows:

$$f_A = \frac{L_{\mathrm{CL\ (obs)}}}{L_{\mathrm{CL\ (gen)}}} = \frac{\int_0^\infty L_{\mathrm{CL}}(z) \exp(-\alpha z)\, dz}{\int_0^\infty L_{\mathrm{CL}}(z)\, dz} = \frac{1}{1 + \alpha L} \tag{4.22}$$

where L_{CL} is the CL intensity and L is the minority carrier diffusion length.

The factor f_R, which accounts for the refraction and total internal reflection, can be derived (Reimer, 1985) by using Snell's law $n_1 \sin\theta_1 = n_2 \sin\theta_2$, where n_1 and n_2 are refractive indices of two media and θ_1 and θ_2 are the angles made by incident and refracted rays with the normal to the surface. When $\theta_2 = 90°$, the critical angle of total internal reflection $\theta_1 = \theta_c$ is given by $\sin\theta_c = n_2/n_1$. For normal incidence ($\theta_1 = \theta_2 = 0$) the reflected intensity is

$$R = \left(\frac{n-1}{n+1}\right)^2 \tag{4.23}$$

where it was assumed that $n_1 = n$ for a given material and $n_2 = 1$ for vacuum. For nonnormal incidence and unpolarized light, equation (4.23) is valid to a first-order approximation over $0 < \theta_1 < \theta_c$. Although luminescence is generated isotropically, only the small fraction inside a cone of semiangle θ_c will escape. The fraction f_R of the total generated signal that leaves the medium is (note that $\sin\theta_c = 1/n$) (Reimer, 1985)

$$\begin{aligned} f_R &= (1-R)\frac{1}{4\pi}\int_0^{\theta_c} 2\pi \sin\theta_1 \, d\theta_1 \\ &= \left[1 - \left(\frac{n-1}{n+1}\right)^2\right] \frac{n - \sqrt{n^2-1}}{2n} \end{aligned} \tag{4.24}$$

where $2 < n < 4$ for typical materials (see Table 4.1). For example, for $n = 3$, $f_R \cong 2\%$; i.e., the CL intensity can be significantly reduced by internal reflection losses. It is important to know what happens to the major part of the CL that is totally internally reflected. Is it lost by absorption, or does it emerge to be detected after repeated reflections? In the latter case, ghost peaks may be formed in the emission spectrum. Precautions must then be taken to prevent the detection of multiply reflected CL (Warwick and Booker, 1983; Warwick, 1986) (see Section 4.7).

In CL microscopy studies (i.e., in obtaining CL images) it is important to remember that factors f_A, f_R, and η may all depend on coordinate r; i.e., they may be spatially dependent and thus lead to CL contrast. This may occur, for example, in the case of strongly inhomogeneous samples and/or specimens with rough surfaces or multilayer structures (with thickness variations), which may lead to local variations in optical absorption and reflection losses. Local variations in η may be caused by the myriad of possible factors affecting both the radiative and nonradiative processes. The latter is often the objective of CL analysis, and it is essential in CL images to distinguish between the variations in η and those due to local variations in optical losses. In addition to these contributions to CL contrast, variations in the generation factor G will also be expected in regions of samples or devices containing various metalization layers, for example.

Table 4.1. Refractive Indexes (n) of Some Crystals*

Crystal	n
Si	3.44
InP	3.37
GaAs	3.40
GaP	3.37
CdTe	2.75
CdS	2.50
ZnSe	2.62
ZnO	2.02
ZnS	2.40
SiC	2.68
Al_2O_3	1.76
SiO_2	1.55
$LiNbO_3$	2.31
$SrTiO_3$	2.49
$BaTiO_3$	2.40

*After Pankove, 1971 and Kingery *et al.*, 1976.

In addition to the loss mechanisms outlined here, the observed luminescence efficiency varies with such factors as temperature, the presence of defects (e.g., dislocations), particular dopants and their concentrations, the specifics of the recombination process (e.g., whether it is a monomolecular or bimolecular process), and the presence of internal electric fields. The need to account for these factors makes the use of CL intensity as a quantitative characterization tool difficult. In this context, since $L_{CL} \propto \eta$, in the observed CL intensity we cannot distinguish between radiative and nonradiative processes in a quantitative manner [see equation (3.27)]. This is one of the most difficult issues in quantitative CL analysis.

Nonradiative surface recombination is an additional loss mechanism of great importance, especially for materials such as GaAs. This effect, however, can be minimized by increasing the electron beam voltage V_b to produce a greater electron penetration range. Analytically, surface recombination can be expressed by the appropriate boundary condition for diffusion to the surface

$$s\,\Delta n = D \left. \frac{\partial \Delta n}{\partial z} \right|_{z=0} \tag{4.25}$$

where s is the surface recombination velocity (in cm/sec). The solution of the continuity equation with this boundary condition was derived by van Roosbroeck (1955) for the one-dimensional case as

$$\begin{aligned}\Delta n = \frac{G\tau}{2e(\pi d)^2 L} \int_0^{R_e} \Bigg\{ & \exp\left[\frac{-|z - z_s|}{L}\right] \\ & - \frac{S - 1}{S + 1} \exp\left[\frac{-(z + z_s)}{L}\right]\Bigg\} g(z_s)\, dz_s \end{aligned} \qquad (4.26)$$

where $S = s\tau/L$ is the (dimensionless) reduced surface recombination velocity and $g(z_s)$ is the source depth distribution of excess carriers per unit depth. The results of calculations using equation (4.26) are illustrated in Figure 4.10, which shows how the depth-dose distribution $g(z)$ is affected by surface recombination and the diffusion length. In this plot, the extreme values of $S = 0$ (solid lines) and $S = \infty$ (dashed lines) were used. They represent the specimen surface as a perfect reflector and as a perfect sink, respectively. The effect of surface recombination is evident from this plot: in addition to the reduced pair density near the surface, it also leads to lower total level of excitation. Note that the effect of surface recombination is diminished for large bulk recombination (i.e., for small diffusion length L). It can also be seen that for large z ($z/R > 1$), the pair density decreases as $\exp(-z/L)$, which results in straight lines in this semilogarithmic plot.

The density of minority carriers lost by surface recombination can be obtained by differentiating equation (4.26) with respect to z_s and setting $z = 0$:

$$\Delta n_s = \frac{S}{S + 1} \int_0^{\infty} \exp\left(\frac{-z_s}{L}\right) g(z_s)\, dz_s \qquad (4.27)$$

Equation (4.27) indicates that the loss due to surface recombination increases with $S/(S + 1)$ and decreases as $\exp(-z_s/L)$ if the generation range is increased and/or the diffusion length is decreased.

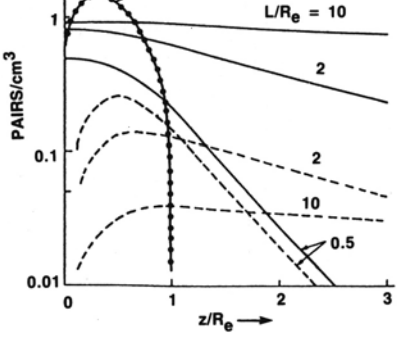

Figure 4.10. A plot of the generation rate $g(z)$ as a function of the reduced depth z/R. Different diffusion lengths were assumed for both $S = 0$ (solid lines) and $S = \infty$ (dashed lines).

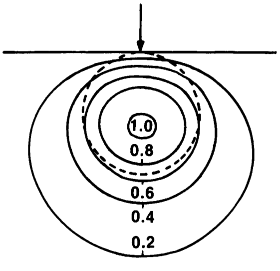

Figure 4.11. The distribution of excess minority carriers for $L = S = \infty$ displayed as curves of equal carrier density. The dashed curve represents the generation sphere. (After Donolato, 1978.)

These results provide important relationships between the electronic parameters L and S and the generation rate $g(z)$. This one-dimensional case can be useful in experiments with defocused electron beam. For a focused beam condition and the simplified case of spherically uniform generation, calculations (Donolato, 1978) show a rapid decrease in the minority carrier concentration with distance. This is illustrated, for example, in Figure 4.11 for $L = S = \infty$. Although the distribution of excess minority carriers in this particular case is nearly spherical (because the surface is a perfect sink), it can be seen that the decrease in the density of the minority carriers as a function of distance is faster than exponential. This finding means that the minority carrier density is highest (and most relevant) inside a volume of the same order of magnitude as that corresponding to the electron generation range (i.e., the volume corresponding to the dashed circle

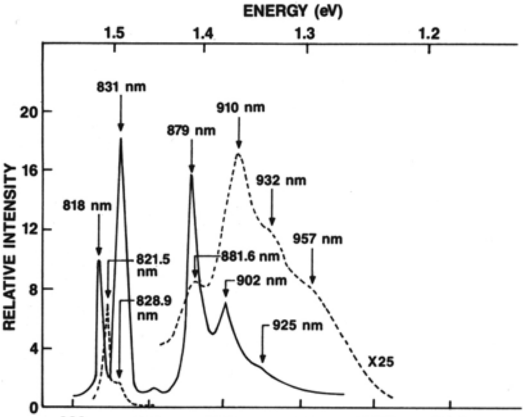

Figure 4.12. Comparison of the photoluminescence spectrum at 4.2 K (solid line) with the cathodoluminescence spectrum at 30 K (dashed lines) for GaAs:Cr heat-treated in H_2 for 1/2 h at 800°C. (After Yin and Wittry, 1983.)

in Figure 4.11). This implies that the resolution of the CL image should not depend significantly on the diffusion length L (Donolato, 1978). It has been found experimentally that it does not, as mentioned.

Some possible differences between PL and CL were discussed in the introduction. Differences between PL and CL spectra may also arise due to differences in their sampling depth. Such an example for GaAs:Cr is illustrated in Figure 4.12. In these experiments (Yin and Wittry, 1983), PL and CL spectra were obtained under various experimental conditions of temperature and electron beam characteristics (in the case of CL). However, the results indicated that the observed differences were caused not by a difference in injection level or specimen temperature in these experiments, but by a difference in the depth analyzed. Irradiation of a sample with the 40-keV electron beam generates excess carriers to a depth of several microns (See Figure 4.13). However, the penetration depth ($1/e$ distance) of the visible light in the PL measurements in this case is only about 0.25 μm (assuming $\alpha \approx 4 \times 10^4\ \text{cm}^{-1}$). In the calculations of the excess carriers in these cases it was assumed that the reduced surface recombination velocity is $S = 50$, the carrier diffusion length is 0.76 μm, and in the CL case the excess carrier generation was assumed to be Gaussian. The excess carrier distributions, shown in Figure 4.13, will be affected by possible gradients in the concentration of electrically active impurities and/or defects that could cause electric field–induced carrier drift in addition to carrier diffusion (Yin and Wittry, 1983).

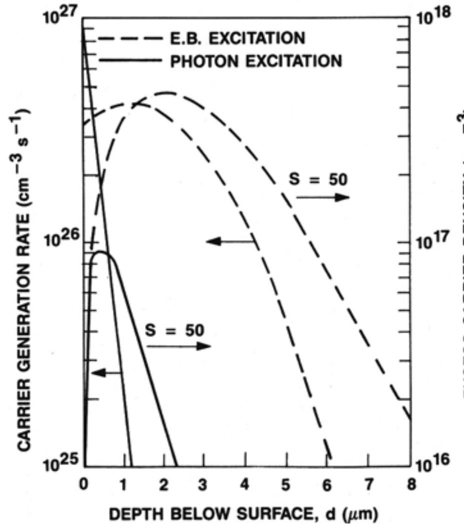

Figure 4.13. Carrier generation rates and equilibrium carrier densities as a function of the sampling depth for photon excitation (solid lines) and electron beam excitation (dashed lines). For electron beam excitation, $V_b = 40$ kV, $J = 2$ A/cm^2, $z_0 = 0.65$ μm, $L = 0.76$ μm, $D_p = 3$ cm^2/s. For optical excitation, $\alpha = 4 \times 10^4$ cm^{-1}, $G_{\text{op}} = 10^{27}$/cm^3 s at the surface, $L = 0.76$ μm. (After Yin and Wittry, 1983.)

4.4. Dependence of Cathodoluminescence on Excitation Conditions and Materials Properties

In general, the dependence of CL brightness on the electron beam current and voltage is of the form

$$L_{\mathrm{CL}} = f(I_b)\,(V - V_0)^m \tag{4.28}$$

where V_0 is a "dead voltage" and $1 \leq m \leq 2$. Naturally, this relationship is of great importance for CL phosphor applications, and many reports on phosphors were published. However, only a few similar studies on semiconductors have been reported.

Early analytical models of cathodoluminescence in semiconductors were provided by Kyser and Wittry (1964), Wittry and Kyser (1966, 1967), and Rao-Sahib and Wittry (1969). For direct, intrinsic recombination in GaAs, Kyser and Wittry (1964) provided a description of the recombination process as a function of excitation conditions, and the main conclusions are as follows. The CL intensity is proportional to the excess carrier generation rate g ($g \propto I_bV_b$). For constant V_b, the dependence of CL intensity on the electron beam current may shed some light on the dominant type of transition. As discussed earlier, L_{CL} is proportional to $g\tau_{\mathrm{nr}}(\tau_{\mathrm{rr}} + \tau_{\mathrm{nr}})^{-1}$, where $g = GI_b/e$. From the Wittry-Kyser model it follows that for $\tau_{\mathrm{rr}} \ll \tau_{\mathrm{nr}}$, when radiative recombination is dominant, the CL intensity should be proportional to the beam current only. For $\tau_{\mathrm{nr}} \ll \tau_{\mathrm{rr}}$, when nonradiative recombination is dominant, the low- and high-excitation cases have to be considered separately. In the former case, the CL intensity should be proportional to the equilibrium carrier concentration n_0 and to the beam current, whereas at higher excitation levels the CL should be proportional to I_b^2 and independent of n_0 (provided that τ_{nr} does not depend on n_0). Experimental results (Kyser and Wittry, 1964) were in general agreement with these predictions for the case in which nonradiative recombination is dominant and the excitation level is low. They were unable, however, to reach sufficiently high beam currents to observe the predicted dependence on the square of the current. The measurements of relative intensity as a function of the free-carrier concentration showed the expected linear dependence, although the scatter between experimental points was fairly large. Kyser and Wittry (1964) reported that CL intensities in some samples of the same high carrier concentration varied by up to two orders of magnitude. Spatial variations in CL intensity (see Chapter 6) indicate that differences in purity and crystalline perfection of the material may predominate over the carrier concentration in determining the CL efficiency. Wittry and Kyser (1967) also pointed out that the CL intensity may depend on g^m, where $m \geq 1$, and if m does not remain constant due to changes in the occupation of recombination centers, a different treatment has to be developed. To the best of our knowledge this has not yet been done.

The dependence of the CL intensity on the electron beam voltage was calculated by Wittry and Kyser (1966, 1967), who concluded that it could be explained by invoking a "dead layer" of thickness d at the surface. This layer, where radiative recombination is absent, was interpreted as being due to the existence of a space-charge depletion region, which is caused by the pinning of the Fermi level by surface states. By assuming that only nonradiative recombination occurs in the dead layer and noting that the luminescence intensity is proportional to the net excess carrier concentration, the CL efficiency in this case (neglecting absorption) can be written as

$$\eta_{\mathrm{CL}} = \left[\int_{d}^{R_e} g(z_s)\, dz_s - \frac{S}{S+1} \int_{d}^{R_e} g(z_s) e^{-(z_s-d)/L}\, dz_s \right] \Big/ \int_{d}^{R_e} g(z_s)\, dz_s \tag{4.29}$$

These results, calculated by Wittry and Kyser (1967) for a Gaussian approximation to $g(z_s)$, are shown in Figure 4.14, under the assumptions of no dead layer (Figure 4.14a) and a dead layer of thickness $d = 0.1L$ (Figure 4.14b), as a function of the reduced electron range R_e/L (absorption is not included). These plots indicate that for CL excitation, a threshold electron beam energy would be required in order to penetrate the dead layer. Experimental measurements (Wittry and Kyser, 1967) for electron beam voltages between 5 and 50 kV were fitted to this model to obtain values for the diffusion length L, the reduced surface recombination velocity S, and the reduced dead layer depth d/L. However, as they remark, caution must be exercised in this type of fitting, since equally good agreement can be obtained for various choices of these parameters (Wittry and Kyser, 1967).

The condition of a linear dependence of L_{CL} on I_b is not always valid. In p-type GaAs, for example, a superlinear dependence was observed (Rao-Sahib and Wittry, 1969), i.e., $L_{\mathrm{CL}} \propto I_b^m$, where m, which is a function of both I_b and V_b, lay between 1 and 2. The analysis outlined here would not be applicable in this case. This problem was treated by Rao-Sahib and Wittry (1969), who modified the theoretical curves and the experimental method. In their analysis, a Gaussian distribution of electron beam–excited carrier generation with depth was assumed, and solutions for the excess carrier density were obtained with and without the assumption of the existence of a dead layer. The solutions given by Rao-Sahib and Wittry (1969) are also based on the assumptions that the total carrier generation is invariant for constant electron beam power (i.e., for $I_bV_b =$

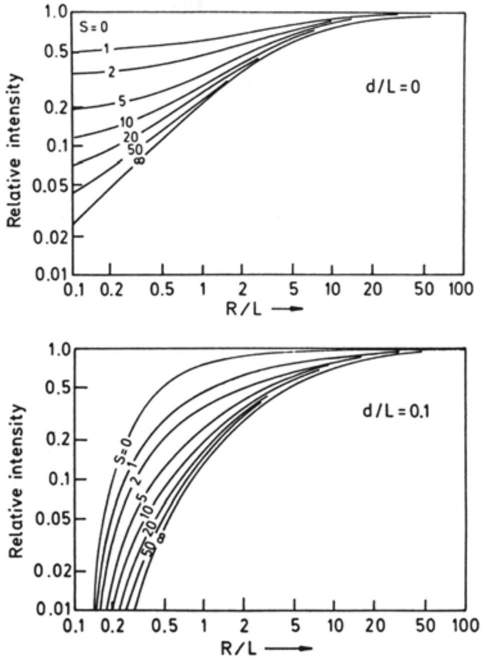

Figure 4.14. The calculated cathodoluminescence intensity for n-type GaAs as a function of the reduced electron range R_e/L and reduced surface recombination velocity S, assuming (a) no dead layer and (b) dead layer of thickness $d = 0.1L$. (After Wittry and Kyser, 1967.)

constant) and for focused and defocused electron beams (provided that the excess carrier distribution in planes parallel to the surface can be ignored). Taking into account the dependence $L_{\mathrm{CL}} \propto I_b^m$, one can write, in terms of the steady-state carrier density,

$$L_{\mathrm{CL}} \cong \int_0^\infty [\Delta n(u)]^m \, du \tag{4.30}$$

where $u = \rho z/R_e$, ρ is the density of the material, and R_e is the electron range. Using the solutions derived by Rao-Sahib and Wittry for $m = 1$, we can evaluate the integral analytically. When $m \neq 1$, the integral must be evaluated numerically. This was done for several different values of m, d/L, and S. However, no agreement could be obtained between the theoretical calculations and experimental results for a finely focused electron beam for $m \neq 1$. In fact, the good agreement obtained for n-type GaAs occurred because $m \cong 1$ and was independent of I_b and V_b. The mathematical solution for the three-dimensional case with a nonlinear response is fairly difficult, and therefore Rao-Sahib and Wittry (1969) used experimental conditions that approximate one-dimensional diffusion. This was accomplished by using a large-diameter electron beam (180 μm)

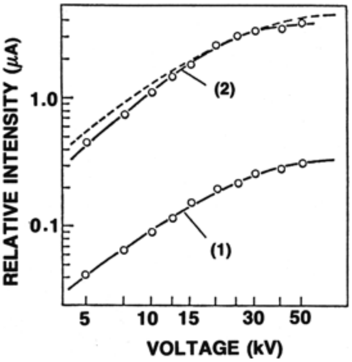

Figure 4.15. Comparison of theoretical calculations and experimental results for p-type GaAs using a broad electron beam. Curve 1 is calculated for $m = 1.0$, $d/L = 0.033$, and $S = 10$, fitted to the experimental results at a power level of 5×10^{-3} W. Curve 2 is calculated for $m \approx 1.2$, $d/L = 0.033$, and $S = 10$, fitted to the experimental results at a power level of 50×10^{-3} W. Curve 2 is also compared with curve 1 (the dashed curve) normalized at 30 kV. (After Rao-Sahib and Wittry, 1969.)

and monochromator slit settings to select the signal from a small area (27 × 27 μm) on the specimen surface. Consequently, good agreement (see Figure 4.15) was obtained between the calculated curves for $m = 1.0$ and $m = 1.2$ and experimental values for beam powers of 5×10^{-3} W and 50×10^{-3} W, respectively, giving consistent values for d/L, S, and L. Thus, the authors showed that these latter parameters can be derived in both n- and p-type GaAs by using their method of voltage dependence of cathodoluminescence. This approach is phenomenological, and it does not explain the nonlinearity of the relationship between L_{CL} and I_b. For specimens with high radiative recombination efficiencies it is possible to measure CL intensities over a wide range of the electron beam power levels, i.e., for a wider range of different values of m. This should reduce the range of choice of values of d/L and S for which consistent values of L are obtained by this method of fitting the experimental results to calculated curves.

The method of Wittry and Kyser (1967) was later applied by Casey and Jayson (1971) to the case of GaP doped with Zn and O. In this material, the radiative recombination mechanism for efficient red emission requires the presence of a Zn acceptor and a donor oxygen atom on nearby lattice sites. When they occupy adjacent sites, an electrically neutral complex is formed; this acts as a deep electron trap that can attract a hole to form a bound exciton. This can then decay radiatively. At high excitation levels, the Zn-O luminescence centers become filled with captured minority carriers. As the centers are filled, the excess minority carriers recombine nonradiatively in the bulk or at the surface, which results in a slower than linear increase of CL intensity with increasing excitation. As mentioned earlier, the calculated curves obtained by Wittry and Kyser were valid for $m = 1.0$ (i.e., $L_{\mathrm{CL}} \propto I_b$). Casey and Jayson (1971) showed that although L_{CL} had a sublinear dependence on I_b for a focused electron beam, a linear dependence was obtained for the case of nonfocused electron beam excitation

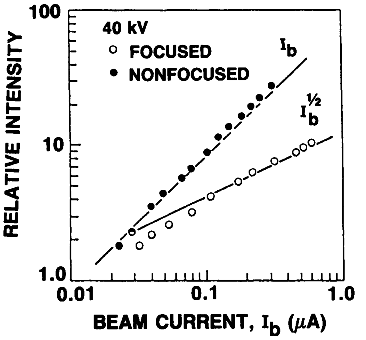

Figure 4.16. The variation in relative cathodoluminescence intensity for GaP (doped with Zn and O) at 40 kV for a focused electron beam of diameter 0.5 μm and for a nonfocused beam. (After Casey and Jayson, 1971.)

(see Figure 4.16). Cathodoluminescence intensity was measured by using a nonfocused electron beam and a constant beam power for electron beam voltages between 5 and 40 kV. The experimental results were fitted to one of the curves of Wittry and Kyser (1967) (see Figure 4.17); since the curves were calculated for GaAs (Wittry and Kyser, 1967), the value of the diffusion length was corrected for GaP. Thus, values of $L_n = 0.5 \pm 0.2$ μm, $S = 5 \times 10^5$ cm sec^{-1}, and $d = 0.025$ μm were derived. These were within the range of values obtained on similar material by using photoexcitation.

As mentioned earlier, the effect of self-absorption on the emergent CL spectrum may be significant. Kyser and Wittry (1964) used the effect of self-absorption to explain the differences between the CL spectra of *p*- and *n*-type GaAs and the injection electroluminescence (EL) spectrum observed on passing a forward current through a *p*-*n* junction in GaAs (see Figure 4.18). The peak intensity for the injection EL occurred at a longer wavelength than the CL peaks from both *p*- and *n*-type material. (Some differences in peak intensity and half-width between *n*- and *p*-type GaAs were also noted.) The difference between injection EL and CL was attributed to self-absorption: for EL, which is generated all over the *p*-*n* junction plane normal to the surface scanned, a large fraction of

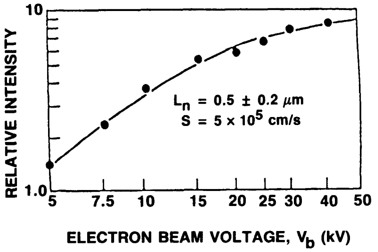

Figure 4.17. Relative cathodoluminescence intensity as a function of electron beam voltage for constant beam power. The experimental points are fitted to a calculated curve of Wittry and Kyser (1967) for the values of the parameters shown. (After Casey and Jayson, 1971.)

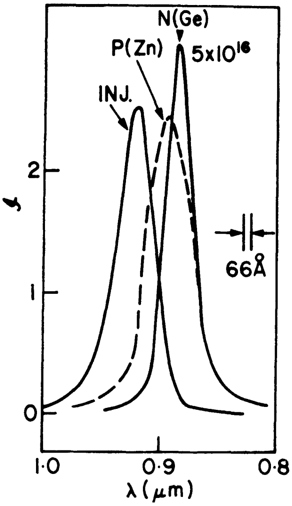

Figure 4.18. The observed spectra of cathodoluminescence (electron beam current is 1.0 μA and beam voltage is 30 kV) for *p*- and *n*-type GaAs compared with the electroluminescence spectrum from injection at a *p*-*n* junction using a current density of about 15 A cm^{-2}. (After Kyser and Wittry, 1964.)

the radiation originates at greater depths than does the CL. The differences can be explained analytically as follows. If L_0 is the constant EL intensity produced per unit depth of the junction, the absorption correction factor for the injection EL can be expressed as

$$\frac{L_{\mathrm{EL\ (obs)}}}{L_{\mathrm{EL\ (gen)}}} = \frac{L_0 \int_0^t \exp(-\alpha z)\, dz}{L_0 t} \tag{4.31}$$

where L_{EL} is the EL intensity, and t is the thickness of the material and hence the maximum depth of any point on the *p*-*n* junction below the surface. Thus, for injection we obtain

$$\frac{L_{\mathrm{EL\ (obs)}}}{L_{\mathrm{EL\ (gen)}}} = \frac{1 - \exp(-\alpha t)}{\alpha t} \tag{4.32}$$

The absorption correction factor for the CL intensity, on the other hand, can be written (for the point source model) as

$$\frac{L_{\mathrm{CL\ (obs)}}}{L_{\mathrm{CL\ (gen)}}} = \frac{\int_0^\infty L_{\mathrm{CL}}(z) \exp(-\alpha z)\, dz}{\int_0^\infty L_{\mathrm{CL}}(z)\, dz} = \frac{1}{1 + \alpha L} \tag{4.33}$$

where L_{CL} is the CL intensity, and L is the minority carrier diffusion length. Thus, for $L \ll t$, the injection EL spectrum is expected to be affected more by absorption than is the CL spectrum.

Self-absorption can also explain charge collection current observations in *p-n* junctions in GaAs scanned normal to the barrier. In this case, in *n*-GaAs, the charge collection current (I_{cc}) is composed of two exponential terms, one of which is the minority carrier diffusion term

$$I_{cc} = A_1 \exp(-X/L_1) + A_2 \exp(-X/L_2) \qquad (4.34)$$

where A_1 and A_2 are constants, X is the distance of the beam impact point from the *p-n* junction, and L_1 is the minority carrier diffusion length. The second term was suggested by Wittry and Kyser (1965) to be due to infrared CL photons that reach the junctions and are absorbed there, producing electron-hole pairs that contribute to I_{cc}. Comparison with Lambert's law of absorption indicates that $L_2 = 1/\alpha$. They, however, pointed out the discrepancy between the experimental value for the effective infrared absorption coefficient derived this way ($\alpha_{\text{eff}} = 300\ \text{cm}^{-1}$) and the absorption coefficient for the wavelength of the CL emission peak ($\alpha_p = 1500\ \text{cm}^{-1}$). This analysis was further refined by Holt and Chase (1973), who showed that this discrepancy could be removed by considering the effect of self-absorption over the varying distance X through the material. This leads to continuous changes of the position of the CL peak and the value of the absorption coefficient. By calculating the modified spectra for a series of values of X, Holt and Chase (1973) derived corresponding values of α_{eff} for each X and found good agreement between the calculated values of α_{eff} and $\alpha = 1/L_2$ obtained from charge collection current measurements.

The analysis of recombination for materials like GaAs, in which $\tau_{rr} \cong \tau_{nr}$, has also shown that the effect of reabsorbed recombination radiation (RRR) has to be considered (Von Roos, 1983) for a material with high doping levels. This effect, i.e., repeated emission and absorption in the bulk of the semiconductor, will essentially diminish the contribution due to the radiative recombination process, and the total recombination rate will depend on τ_{nr} only.

4.5. Interpretation of Cathodoluminescence

As mentioned earlier, the interpretation of CL cannot be unified under a simple law.

The information in the peak of the fundamental or edge emission band ("intrinsic" CL at ambient temperatures) is relatively easy to interpret because $h\nu \cong E_g$ and the variation of E_g with materials parameters and external perturbations is comparatively well understood. However, the information in the broad "extrinsic" CL bands (which arise from transitions that start and/or finish on localized states of impurities in the gap) observed above liquid nitrogen temperatures is difficult to interpret because of the lack of any generally applicable theory for the wide variety of possible types of luminescence centers and radiative recombination mechanisms. Experimentally, thermal broadening can be minimized by using liquid helium temperatures at which CL spectra will generally consist of a series of sharp lines corresponding to transitions between well-defined energy levels. These processes can then be identified with particular CL emission phenomena, such as excitonic lines, phonon replicas, and DAP lines.

The influence of defects, of the surface, and of external perturbations, such as temperature, electric field, and stress, have to be considered in the analysis of CL spectra. For example, the luminescence intensity can depend strongly on dislocation densities, defect concentrations, including their configuration and depth from the surface of the sample, and the internal electrical fields. Further possible complications are electron beam-induced contamination at the surface of the specimen and beam-induced defects.

The difficulties involved in accounting for all these factors make the use of the total CL intensity as a quantitative characterization tool difficult, although not impossible. With, for example, time-resolved CL (Steckenborn *et al.*, 1981ab; Bimberg *et al.*, 1985ab, 1986) one can determine the minority carrier lifetime and the recombination cross sections of donors and acceptors and obtain information on competitive recombination channels. Nonradiative channels can, in principle, be analyzed by using scanning deep-level transient spectroscopy (SDLTS) (Petroff and Lang, 1977). Correlations between dopant concentrations and the peak energies, half-widths, and slopes of the exponential tails of the relevant emission bands in intentionally doped standards would be more practical and reliable as means for the quantitative assessment of the carrier concentration at this juncture (Cusano, 1964; Pankove, 1966; Casey and Kaiser, 1967; Gatos *et al.*, 1981). Even in this case one would have to account for the effect of defects on the luminescence efficiency η of the material. For example, the effect of dislocations on η of light-emitting devices was considered by Roedel *et al.* (1977) (see also Lax, 1978; Yamaguchi *et al.*, 1986), who found that η was related to the dislocation density N_D as follows:

$$\frac{\eta}{\eta_0} = \frac{1}{1 + L_0^2 \pi^3 N_D / 4} \tag{4.35}$$

where L_0 is the minority carrier diffusion length, and η_0 is the efficiency without dislocations (see Figure 4.19). Thus, in quantitative analyses of luminescence intensities it is important to know the defect densities.

Despite all these difficulties, one has to begin somewhere. Warwick (1987) proposed the so-called MAS corrections (in analogy with the *ZAF* correction procedure for x-rays) to obtain, for example, quantitative impurity concentrations from CL band intensities. MAS stands for corrections for the effects of mixed-

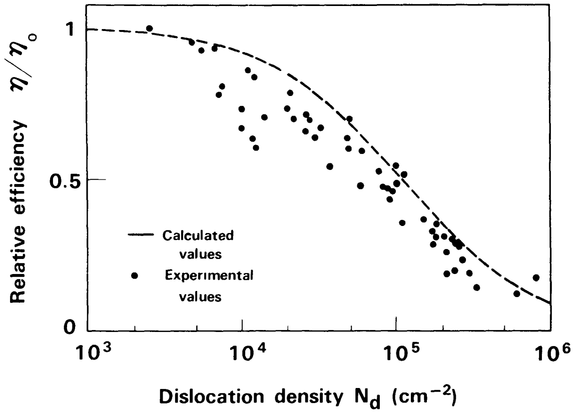

Figure 4.19. Electroluminescence efficiency (from Roedel *et al.*, 1977) as a function of dislocation density for GaAs light-emitting diodes. The dashed line represents the efficiency calculated using $\eta/\eta_0 = 1/(1 + L_0^2\pi^3 N_d/4)$.

level injection, absorption, and surface recombination. Because of the presence of competitive recombination channels in most luminescence phenomena, the luminescence intensity is not a simple function of the impurity concentration, but it also depends on the minority carrier lifetime (Warwick, 1987), which is determined by the combined effect of all the channels in parallel. Thus, measurements of both the luminescence intensity and the luminescence time decay will be required. The mixed-level injection correction is necessary because the excess carrier density is greater than the ionized impurity concentration near the electron probe, and less than it further away. In addition to the MAS corrections, a (total internal) reflection (and refraction) correction should also be included in the CL analysis, thus leading to the MARS set of corrections.

The previous chapter reviewed some theoretical models that are helpful in further developments of quantitative CL analyses. As mentioned earlier, compared with electron probe microanalysis (EPMA), quantitative CL is in its infancy, and major problems in quantitative CL analysis are the lack of data concerning the competing nonradiative processes and the various factors that affect the emitted CL intensity. The difficulties involved in the quantitative analysis of CL intensities can be circumvented by CL band-shape analysis (Cusano, 1964; Pankove, 1966; Casey and Kaiser, 1967; Chapter 6). The effects of temperature and carrier concentration on such band-shape parameters as the peak energy and the half-width of the CL emission of InP were demonstrated by Gatos *et al.* (1981). Using the fact that the band gap and, hence, the intrinsic band peak energy decreases with increasing temperature, they also established the temperature increase of the InP surface with increasing electron beam current. Davidson and

Rasul (1977) similarly measured the operating temperature distributions in GaAs and InP Gunn diodes.

To summarize, the development of the CL mode as a quantitative analytical tool requires the solution of difficult problems. The CL signal can depend on so many physical parameters that no unified theory is in sight. As mentioned earlier, CL quantitative analysis would require knowledge of, for example, the recombination cross sections, the minority carrier lifetime, self-absorption, surface recombination and defect concentrations. Therefore, no correction method for CL intensities, analogous to the *ZAF* corrections in x-ray analysis, has been developed yet. Development of MARS-type correction methods, together with the refinement of such techniques as time-resolved CL and SDLTS, and the use of carefully characterized standards should provide a viable approach for the development of quantitative CL analysis. X-ray microanalysis developed as a useful tool more through the discovery of semiempirical relations between impurity concentration and readily observable spectral parameters than through any advances in fundamental understanding. This also appears to be the pattern of early developments in quantitative CL microcharacterization.

4.6. Spatial and Spectral Resolution and the Detection Limit

The spatial resolution of the CL mode of the scanning electron microscope is affected by the electron probe size, the size of the generation volume, which is related to the beam penetration range in the material, and the minority carrier diffusion. Additional factors such as a low signal-to-noise ratio, vibrations, and electromagnetic interference may degrade the resolution in practice.

A minimum signal-to-noise ratio is required for each mode of the SEM. This depends on detector sensitivities and electronic system noise levels. This determines the minimum signal intensity necessary to get pixel brightnesses above the noise level or reliable data for processing. A certain beam power will be necessary in order to excite that level of signal in any given specimen.

The size of the electron beam decreases with the decrease of the beam current and the increase of the beam voltage (see Goldstein *et al.*, 1981). Also note that, for the same beam current and beam voltage, the probe diameter for a tungsten (W) filament is about twice as large as the diameter obtained using a lanthanum hexaboride (LaB_6) gun. For the latter, for example, the electron probe diameter for a 30-kV beam is about 40 Å for an electron probe current of 10^{-11} A, increasing to about 250 Å for $I_b = 10^{-9}$ A and to about 3000 Å for $I_b = 10^{-6}$ A. As mentioned earlier, for lower electron beam energies, the probe size is larger. For example, for a 10-kV beam, the probe diameter of the LaB_6 filament is about 60 Å for $I_b = 10^{-11}$ A, increasing to about 350 Å for $I_b = 10^{-9}$ A and to about 5000 Å for $I_b = 10^{-6}$ A. For a W filament, the probe sizes for given probe energies and currents are about twice as large. (For more details, see Goldstein *et al,* 1981.)

In practice, at low electron beam currents, the spatial resolution is determined basically by the size of the excitation volume necessary to satisfy the signal-to-noise ratio requirement. Increasing the electron beam energy improves the signal-to-noise ratio, but it also produces a larger excitation volume. For larger values of the electron probe current (about 10^{-7} A and greater), the incident beam diameter becomes large, comparable to that of the generation volume. In most inorganic solids, a CL spatial resolution of the order of 1 μm can be achieved.

As mentioned earlier in this chapter, Donolato (1978) pointed out that the minority carrier density is large only in a region commensurate to the generation range. Thus, the CL spatial resolution in most cases is essentially equal to the generation range and is not affected significantly by the minority carrier diffusion length (see Figure 4.11).

For low electron beam currents, an improved spatial resolution may be expected in samples with strong self-absorption of light from greater depths within the specimen. In such a case, most of the signal arises from the narrower region of the generation volume (see Figure 4.2) just below the specimen surface.

It is also possible to improve the CL spatial resolution by limiting the minority carrier diffusion. This can be achieved by using time-resolved imaging (see Bimberg *et al.*, 1988), which allows CL observations in different short time windows (in the l-ns range) that limit the diffusion of the minority carriers. Another method of limiting the minority carrier diffusion is *Lorentz force carrier confinement* (Wada *et al.*, 1988), which is based on the principle that a magnetic field applied to a sample leads to the confinement of minority carriers in a spiral orbit (i.e., cylindrical confinement), which can be of smaller radius than the minority carrier diffusion length.

The spectral resolution in CL measurements depends on the luminescence efficiency of the material, its temperature, and the CL detection system sensitivity. It is to be expected that for most materials at elevated temperatures, between about liquid nitrogen and room temperatures, the spectral resolution is specimen-limited, since signal maximization requires a larger than optimal monochromator slit-width. Luminescence lines become more intense and narrower at liquid helium temperatures, and the spectral resolution is then mainly dependent on the slit-width of the monochromator.

The sensitivity of CL analyses was demonstrated to be in some cases at least 10^4 times better than that attainable by x-ray microanalysis. In other words, impurity concentrations as low as 10^{14} cm^{-3} can be detected. In PL (and arguably CL as well) in the most favorable cases of strongly luminescent impurities that emit at energies undisturbed by other emission or absorption mechanisms in the host material, it should be possible to detect impurities down to 10^{12} cm^{-3} (Dean, 1982).

4.7. Artifacts

Spurious signals in CL analyses may arise, for example, from luminescent contaminants, from incandescence from the electron gun filament reaching the detector or from scintillations caused by backscattered electrons striking components of the CL systems. Many of these background contributions may be eliminated by chopping the electron beam and detecting the CL signal with a lock-in amplifier.

An artifact in the CL emission spectrum, a ghost CL peak in InP, was reported by Warwick and Booker (1983) and by Warwick (1986). This was due to the rays that are totally internally reflected before emerging from the specimen after self-absorption. This mechanism of the ghost peak was established by using aperture disks, that blocked such rays reaching the light collector. It was demonstrated that by varying the effective field of view of the light collector, the artifacts (ghost peaks) in the low-temperature CL spectra could be controlled (see Figures 4.20 and 4.21). As shown in Figure 4.20a, light that propagates along the paths for rays *A* and *B* may reach the light collector. Most of the light generated in the material cannot exit directly to the detection system due to its total internal reflection and/or its being directed away from the top specimen surface. Only a few percent of the generated light leaves the specimen along paths like ray *A*. Thus, light that propagates along paths like ray *B* may be expected to contribute significantly if it reaches the collector. Since the absorption edge of this material is at an energy close to the 1.415-eV donor-related peak (i.e., at 1.414 eV at liquid helium temperatures), a majority of photons with energies near 1.415 eV

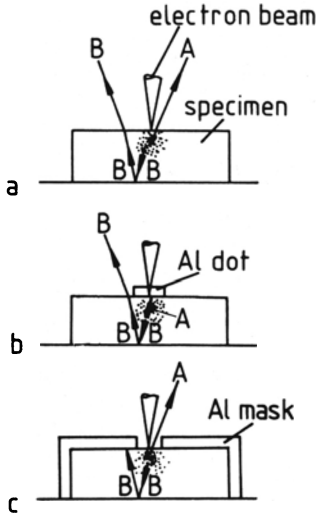

Figure 4.20. (a) Standard specimen with no mask. Rays *A* and *B* reach the collection optics, and the corresponding CL spectrum (denoted *S*) is shown in Figure 4.21. (b) Dot mask specimen; only ray *B* reaches the collector, and the corresponding spectrum (denoted *D*) is shown in Figure 4.21. (c) Hole mask specimen; only ray *A* reaches the collector, and the corresponding spectrum (denoted *H*) is shown in Figure 4.21. (After Warwick, 1986.)

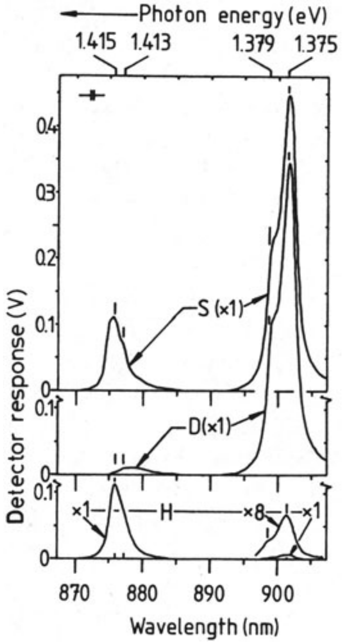

Figure 4.21. 10-K CL spectra of undoped InP from a standard specimen, spectrum *S* (see Figure 4.20a); from a dot mask specimen, spectrum *D* (see Figure 4.20b); and from a hole mask specimen, spectrum *H* (see Figure 4.20c). (After Warwick, 1986.)

will be absorbed. The low-energy tail of this luminescence band and the acceptor-related emission bands at 1.379 eV and 1.375 eV, however, occur at such energies that the absorption coefficient is sufficiently small to allow a significant fraction of the light traveling along paths like that of ray *B* to be emitted (Warwick, 1986).

In these experiments, the effect of the rays that are totally internally reflected before emerging from the specimen was determined by first obtaining the luminescence spectrum from a standard sample (see Figure 4.20a). In this case, a large fraction of the light in rays such as *B*, which are reflected from the bottom and side surfaces, can leave the top surface of the specimen within the field of view of the light collector, giving rise to the spectrum *S* in Figure 4.21. Subsequently, to correlate the features of the spectrum with particular types of ray paths, a sample was used with a 0.25-μm-thick Al mask, which effectively limited the field of view of the collector (see Figure 4.20b). Although transparent to 20-keV electrons, the Al film blocked luminescence emission. An Al dot 100 μm in diameter, centered at the electron beam impact point, resulted in allowing only the light in rays like *B* to reach the collector. The corresponding luminescence spectrum is denoted *D* in Figure 4.21. Comparison of spectra *S* and *D* reveals that the intensity of the 1.375-eV peak, which is due to the recombination of electrons bound to shallow donors with holes bound to Zn_{In} acceptors, and the

1.379-eV peak, which is due to the recombination of free electrons with holes bound to Zn_{In} acceptors, are nearly the same. The intensity of the 1.415-eV peak, on the other hand, is significantly reduced in spectrum *D*. In spectrum *S* a shoulder is also observable at 1.413 eV. The latter corresponds to the remaining low-energy portion of the 1.415-eV peak, following selective absorption along paths like *B* (see Figure 4.20). The path length of rays like *A* is significantly smaller, and thus little selective absorption is expected. To allow only light that has followed direct paths like ray *A* into the collector, they used a hole mask (see Figure 4.20c) that covered the whole surface, except for a hole 50 μm in diameter centered on the electron beam impact point. The corresponding spectrum is denoted *H* in Figure 4.21. In the spectrum, no shoulder at 1.413 eV is observable, the intensity of the 1.415-eV peak is nearly the same as that in spectrum *S* (i.e., the standard specimen), and the intensities of the 1.379-eV shoulder and 1.375-eV peak are reduced significantly in comparison to those in spectrum *S*. These experiments indicate that rays like *A* (see Figure 4.20) account for nearly all of the intensity of the 1.415-eV peak but provide only a small contribution to the intensities of the 1.379-eV shoulder and 1.375-eV peak. Rays like *B*, on the other hand, account for all of the intensity of the 1.413-eV shoulder and most of the intensities of the 1.379-eV shoulder and 1.375-eV peak. Thus, the shoulder at 1.413 eV is an artifact due to the admittance of light along paths like ray *B*, and it is not related to any recombination mechanism. Also, these results indicate that the intensities of luminescence features at lower energies are greatly affected by the admittance of light that traveled long distances before emission, for example, along ray *B*. It was concluded that using large-field-of-view (a commonly used value is of the order of 1 mm in diameter) light collection optics may lead to significant changes in the luminescence intensities and some features of the shapes of the luminescence bands. A field of view less than 50 μm is required in order to prevent this type of artifact (Warwick and Booker, 1983; Warwick, 1986).

Changes in the luminescence intensity, the luminescence band shape, and the value of the luminescence peak energy may also be expected with the correction of spectra for the overall detection system response characteristics (Steyn *et al.*, 1976; Datta *et al.*, 1977, 1979a). This issue will be discussed in Section 7.3.3.

Prolonged electron beam irradiation may also cause significant changes in the CL intensity, which should be considered in quantitative analyses. It is especially difficult to quantify observations if the signal continues to change over an hour, for example, so the stabilities of the excitation, the detector, and the material are all important. Electron irradiation can lead to quenching or enhancement of the CL signal. In ZnS, for example, dark regions in CL observations were associated with possible electron beam charging of vacancies (see Holt and Saba, 1985), whereas in Si Myhajlenko *et al.* (1983a) observed electron beam annealing–induced enhancement of the infrared CL intensity (see Figure 4.22). The electron beam–induced sample heating was estimated by Myhajlenko *et al.*

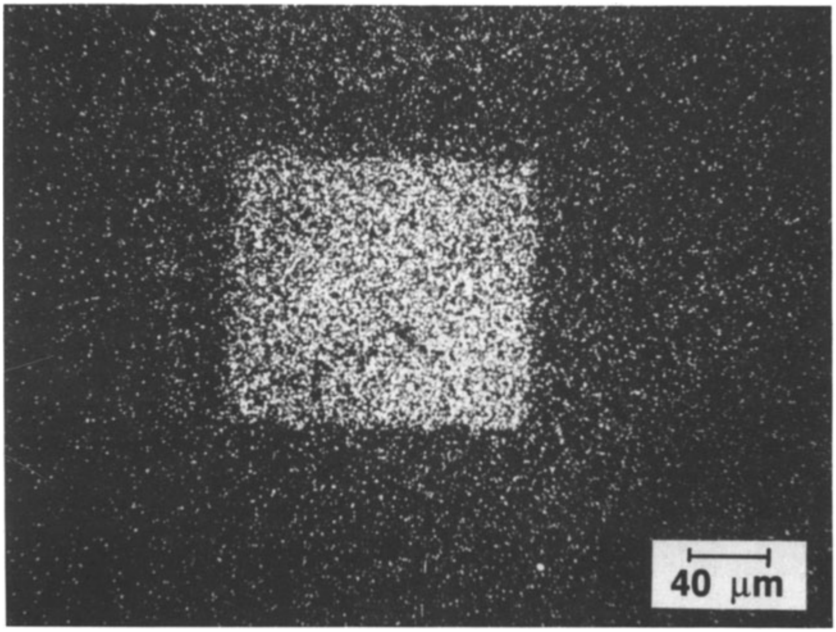

Figure 4.22. CL micrograph of ion-implanted silicon showing a bright region (i.e., luminescence recovery) resulting from electron beam annealing. (After Myhajlenko *et al.*, 1983a.)

(1983a) on the basis of the Vine-Einstein (1964) model, which predicts the steady-state maximum temperature rise from

$$\left(\frac{P}{a}\right)_{\text{eff}} = 4.27 \int_{T_{\text{substrate}}}^{T} k(T)dT \qquad (4.36)$$

where P is the beam power (in W), a is the spot radius (in cm), $k(T)$ is the thermal conductivity (in W cm^{-1} K^{-1}), and $(P/a)_{\text{eff}}$ is the effective beam power corrected for penetration. For excitation with a 30-kV, 10-μA beam and a spot diameter of 3 μm, a temperature rise of about 150 K was obtained for a substrate temperature of 300 K, and a rise of about 30 K was obtained for a substrate temperature of 100 K.

Caution should be exercised during CL contrast observations on defects. Balk *et al.* (1976) reported contrast inversion at a single dislocation in Se-doped GaAs by increasing the electron beam current from about 10^{-6} to about 10^{-5} A. This was explained as being due to the localized heating effect at higher beam currents, which leads to enhanced nonradiative recombination and a decrease of the CL signal.

Prolonged electron bombardment often leads to surface contamination of the specimen. The deposition of a film, which consists primarily of polymerized hydrocarbons, is caused by the electron bombardment of the adsorbed molecules of the pump oil, etc. Adsorbed molecules from the earlier sample preparation steps may also contribute to the contamination. Replacement of the diffusion pump by a turbomolecular pump may alleviate the problem significantly, as can liquid-nitrogen-cooled shields around the specimen and careful handling of the specimen prior to its insertion to the vacuum chamber.

The analysis of nonconducting samples requires special care due to specimen charging. A conductive thin coating will reduce the charging, but it will also significantly reduce the emitted luminescence intensity. The charging effects in uncoated samples can be largely minimized by using lower electron beam energies, provided that the CL signal can be detected. Altering the scan speed can also help by optimizing (1) the time available for the charge to leak away before the beam returns and (2) the heating effects that may increase the local conductivity.

Misinterpretation of the images obtained with a scanning electron microscope in general can arise through reliance on subjective judgments. Difficulties can arise through preconceived expectations, selective memory, etc. Computer-aided image processing and the application of statistical tests should alleviate the difficulties. For analyses, spectral correction prior to imaging will also be required. A detailed description of these issues was provided by Newbury *et al.* (1986).

The size of the electron beam dissipation volume increases with the beam voltage V_b. Therefore, for a given electron beam current I_b, an increase in V_b results in a reduction in the electron beam energy dissipated per unit volume. In contrast, an increase in I_b, at a given V_b (i.e., an increase in the number of electrons dissipated in the same volume) leads to a corresponding increase in the electron beam energy dissipated in that volume. Thus, a general rule for the minimization of electron beam damage would be *maximizing* V_b *and minimizing* I_b so that a usable CL signal is obtained, and *using the fastest line and frame speeds* that provide sufficient interline scan separation at a given magnification (Giles, 1975). Modern frame stores with signal averaging greatly improve the signal-to-noise ratio and make it possible to use lower beam powers. Signal averaging over repeated spectral scans has a similar effect. With a frame store it also becomes possible to examine an image at leisure with the beam chopped, so damage and contamination do not continue. These effects therefore less seriously limit CL studies than it was once thought they would.

5

Cathodoluminescence Analysis Techniques

In this chapter we describe CL systems that are used for materials characterization.

Early systems for examining cathodoluminescence were based on a CRT design, shown schematically in Figure 5.1. The basic elements of the device, which is a highly evacuated glass tube, are the electron gun, the deflection plates, and the fluorescent screen. The electron gun consists of a cathode, control grid, and focusing and accelerating anodes. Electrons ("cathode rays") emitted from the cathode, which is raised to a high temperature by the heater, are accelerated to the anode, which is maintained at a high positive potential relative to the cathode. A narrow beam of electrons passes through a small hole in the anode and then travels to the fluorescent screen, which is coated with the phosphor layer that emits light at the point of impact of the electron beam. The brightness of the spot on the screen is regulated by the control grid, which determines the number of electrons that arrives at the anode. The size of the irradiated spot on the fluorescent screen is controlled by the focusing anode. The electrons can be deflected vertically and horizontally by an electric field when they pass between the pairs of vertical and horizontal deflection plates. The electrostatic deflection plates mounted inside the tube lead to a relatively small screen. Larger viewing screens used in television receivers are achieved by using magnetic deflection coils mounted outside the vacuum tube. In a television receiver, the bright spot is rapidly rastered over the screen. When the electron beam intensity is altered according to the incoming signal (i.e., the electromagnetic wave received from the transmitting antenna) at the control grid, the variations in intensity of the electron beam cause variations in the intensity of visible light emitted by the phosphor layer. This leads to the pattern (or image) formation seen on a television screen. In the latter case, a medium-persistence phosphor is chosen to minimize flicker, while allowing depiction of rapid change in the picture. During the electron bom-

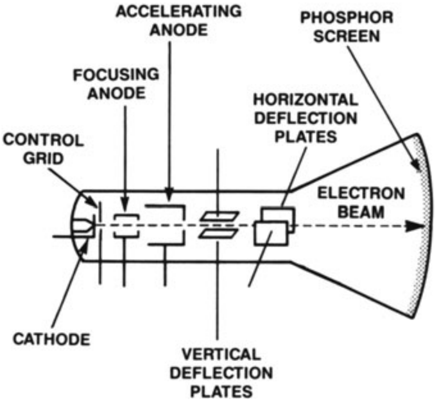

Figure 5.1. Schematic diagram of a cathode-ray tube (CRT).

bardment of the phosphor screen, the light emission is accompanied by the emission of secondary electrons as well. Therefore, to avoid charging of the screen, the inner walls of the tube are coated with a conductive layer (e.g., graphite) that is held at anode potential. The phosphor screen, which consists of phosphor granules several microns in size, may also be coated with a thin electron-transparent layer of aluminum evaporated on the side of the electron impact. Besides preventing a charge buildup, this layer also acts as a mirror that reflects light emitted toward the interior of the tube and directs it toward the observer. In cathode-ray oscilloscopes, the voltage applied to the horizontal deflecting plates increases linearly with time to move the electron beam and the bright spot at constant velocity to provide a time base. The signal of interest is applied to vertical deflection plates, so its waveform can be determined. In applications requiring the simultaneous display of various signals, CRTs in oscilloscopes are equipped with multiple independent electron guns. In color displays, three electron guns slightly inclined to each other and the shadow mask are used so that the three electron beams excite only their respective phosphor dots in the patterns of three dots corresponding to three primary additive colors of blue, green, and red. A wide range of colors can be synthesized from variations in the relative luminescence from the three dots by varying the excitation intensities. To summarize, the electron beam can be readily controlled by electric or magnetic fields in a CRT-based instrument. This fact, together with the continuing progress in the phosphor technology, gives this instrument the capacity to display such large amounts of information so rapidly that no other display technology can as yet compete.

Optical microscopes with electron gun attachments (i.e., the optical CL microscope), which were developed several decades ago, are based on a CRT design with the glass side of the screen being replaced by the specimen stage of the optical microscope (see Section 5.4). Such instruments, often referred to as *luminoscopes,* are being used, for example, in mineralogy. In current designs, a small vacuum chamber may be fitted to a regular optical microscope.

Currently, there are two basic types of CL analysis systems. One is based on electron microscopes, scanning electron microscopes (SEMs), scanning transmission electron microscopes (STEMs), or TEMs equipped with CL detecting attachments. Using CL-SEM enables one to obtain CL images and display, for example, defect maps. There are significant differences between SEM and STEM-based systems and between these and systems attached to a TEM. By far most CL attachments are on SEM instruments because of the larger chambers and the ease of installing larger collection systems. The other approach employs a simple high-vacuum system containing an electron gun for the excitation of a material; no scanning capability is provided, so no image of a sample can be obtained; thus it is limited to spot mode CL only. The use of large-area, high-power electron beams gives high CL intensity and thus makes high-spectral-resolution analysis possible. In general, spatial and spectral resolutions vary inversely. In this type of CL analysis system, other optical measurements and/or processing of the sample are also possible. The main application of such systems is in depth-resolved CL studies.

The electrooptical systems and other components of electron microscopes are described in several books listed in the bibliography. Here, we review the basic principles and systems of electron microscopy.

The modes available in the SEM provide a variety of information about a sample. The secondary electrons are used for topographic information and voltage contrast, and the backscattered electrons provide atomic number contrast. Backscattered electrons can also be used for structural analyses of solids (channeling patterns). X-rays provide information on the composition of the sample. The CL and charge collection (CC) modes are complementary techniques for the analysis of optical and electronic properties of semiconductors and insulators. In TEMs and STEMs, the transmitted and elastically scattered electrons provide microstructural information from images and crystallographic information from diffraction patterns. The inelastically scattered transmitted electrons provide information on composition using electron energy loss spectroscopy (EELS).

5.1. Cathodoluminescence Scanning Electron Microscopy

5.1.1. Principles of Scanning Electron Microscopy

The basic principle of a SEM is analogous to the coupling of two CRTs. One "tube" (the microscope) contains a sample. The other CRT is used as a display instrument.

The two main components of a SEM (Figure 5.2) are (1) the electron optical column, which includes the electron gun, the electromagnetic lenses, and the specimen chamber, and (2) a display and operating unit. Either a thermionic electron gun or a field emission gun is used. The thermionic gun may contain a tungsten or a lanthanum hexaboride (LaB_6) cathode. This heated cathode is maintained at a high negative potential relative to the Wehnelt cylinder, and an anode is maintained at earth potential. The potential may usually be varied from less than 1 kV to 40 kV, thereby providing various beam powers and electron penetration depths in the material. The field emission electron gun consists of a pointed cathode (a single-crystal tungsten tip) and two anodes. A voltage applied between the cathode and the first anode regulates the field strength at the tungsten tip and causes the emission of electrons, which are subsequently accelerated by the second anode voltage. The advantages of the field emission electron source are the higher brightness, which makes possible a smaller probe size for a given (small) beam current, and a smaller energy spread. The brightness of the field emission source of about 10^9 A cm^{-2} sr^{-1} is two orders of magnitude higher than that of the LaB_6 thermionic source and three orders of magnitude higher than that of the tungsten thermionic filament. The electron probe size of the field emission source is smaller than those of the thermionic sources, and it may be as small as 20 Å for a beam current of 10^{-11} A or less. The service life of the field emission source, which depends on the operating vacuum, is in excess of 1000 h. This should be compared with the service lives of several hundred hours for the LaB_6 thermionic source and up to about 50 hours for the tungsten filament. The

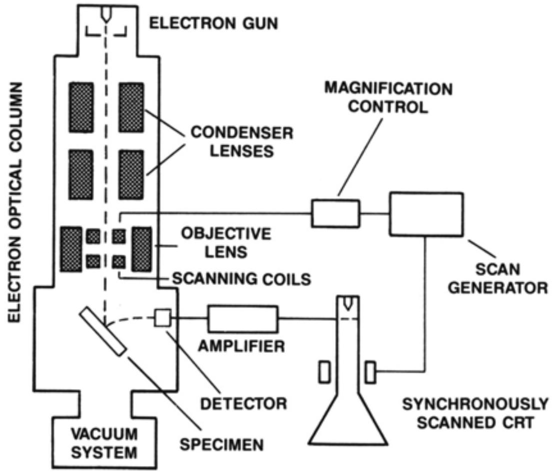

Figure 5.2. Schematic diagram showing the basic components of a scanning electron microscope (SEM).

operating vacuum required, however, is also higher for the field emission source: better than about 10^{-7} Pa (1 Pa $\approx 10^{-2}$ torr) compared with 10^{-5} Pa for the LaB_6 source and 10^{-3} Pa for the tungsten filament. The inability of field emission guns to produce the larger beam currents obtainable from thermionic guns is a major drawback when low-efficiency CL materials have to be studied.

Usually two condenser and one objective electromagnetic lenses are used to form a fine electron beam and focus it onto the specimen surface. For the emissive mode, the electron probe size can be made as small as 50 Å for a tungsten thermionic filament, or about 30 Å for a LaB_6 filament, and 20 Å (or less) for a field emission electron source. Scanning coils, placed in the bore of the objective lens, deflect the beam so that the electron spot scans line by line a square raster (similar to the raster on the television screen) over the specimen surface. The standard television picture is currently made of 525 (in America) or 625 (in Europe) horizontal lines, but the rasters in the SEM may contain from 100 to more than 1000 horizontal lines. The latter value is used for obtaining a micrograph, in which case the scanning rate is much lower than in television sets. (At this writing there are efforts under way to develop the so-called high-definition television sets with more than twice the number of lines currently used.)

A variety of signals are produced as a result of the dissipation of the electron beam energy in the sample into other forms of energy, which can then be detected and turned into an electrical signal by a suitable detector (or transducer). The electrical signal is amplified and fed to the grid of the synchronously scanned display CRT. The amplified (video) signal modulates the brightness of the CRT and produces an image of the specimen. The raster scan of the electron spot over the specimen surface results in a one-to-one correspondence between picture points on the display CRT screen and points on the specimen. Thus, the variations in the strength of the particular signal being detected result in variations in brightness on the CRT screen, i.e., contrast on the micrographs. The image magnification is the ratio of the size of the square area scanned on the display CRT and the size of the area scanned on the specimen. The magnification is varied by varying the currents in the SEM scanning coils (the magnification is increased when the currents in the scanning coils are reduced). Modern SEMs have magnifications that are continuously variable from 10× to 300,000×. Usually, the SEM is equipped with two display CRTs, or a split-screen CRT, so that signals that provide complementary information can be displayed simultaneously.

Different forms of physical energy from the electron bombardment of the sample are used as signals for the modes of operation of the SEM. Thus, (1) emitted electrons produce signals for the emissive mode; (2) x-rays are the basis of electron probe microanalysis (EPMA); (3) transmitted electrons (in thin samples) form the signals for (scanning) transmission electron microscopy; (4) ultraviolet, visible, and near-infrared photons are the basis of the CL mode, and (5) CC currents or voltages are the signals of the CC or conductive mode. In addition, a thermal wave, electroacoustic mode has emerged recently as a new SEM technique for the analysis of thermal, mechanical, and electronic properties of materials.

5.1.1.1. The Emissive Mode

The emissive mode is the most widely used SEM technique. Three types of emitted electrons, which provide different information, can be selected for detection by appropriate detectors. *Secondary electrons* emitted with energies less than 50 eV provide topographical contrast with much better resolution and depth of field than do optical microscopes. They can also provide important information (contrast) on local electric and magnetic fields that are present in the material and that affect the energy and direction of emission of the low-energy electrons. Voltage contrast with high-frequency stroboscopy is especially useful for the analysis of large-scale integrated circuits. Secondary electrons originate from material within about 50 Å of the specimen surface. Emitted electrons with energies close to that of the incident primary electron beam are called *backscattered,* and they originate from within a micrometer of the specimen surface. These electrons provide atomic number contrast, since regions of higher atomic number backscatter more primary electrons. Thus, this type of contrast provides qualitative information on compositional uniformity. Areas that appear brighter correspond to the regions with a larger average atomic number. Backscattered electrons can also provide, under appropriate operating conditions, crystallographic information due to electron channeling. This arises because the backscattered electron yield varies as the angle of incidence of the scanned electron beam passes through the Bragg angle to crystal lattice planes. That is, selective channeling of primary electrons between the crystal planes at specific incidence angles can lead to SEM pictures consisting of series of bands and fine lines. These pictures are called *electron channeling patterns* (ECPs), and they depend on the crystal structure and orientation of the material. Electron channeling patterns can be obtained from selected small areas of the specimen by rocking the incident electron beam at the site of interest. Orientation changes across grain boundaries, for example, can give rise to channeling contrast in backscattered electron images. Finally, Auger electrons emitted from about the top 10 Å of the material have energies characteristic of the elements of the material. Auger electron spectroscopy (AES) and scanning Auger microscopy provide a useful surface analytical mode in ultrahigh vacuum electron probe instruments.

5.1.1.2. The X-Ray Mode

As mentioned in the introduction, the basis of the x-ray mode or EPMA is Moseley's law, which relates the energy of an x-ray emission line to the atomic number ($h\nu \propto Z^2$). Two types of spectroscopic detection are used in this mode. Wavelength-dispersive spectrometers (WDS) give the highest elemental resolution, but are slower than energy-dispersive spectrometers (EDS). The latter have a poorer elemental resolution, but can detect a wide range of the elements simultaneously. In both these methods, the relative arrival rates of characteristic x-ray photons from different elements is a measure of their concentrations in the electron-excited volume. To determine actual percentage composition, we apply a set of corrections. These so-called *ZAF* corrections are iterative corrections for the atomic number *Z*, which affects the efficiency of characteristic x-ray emission, for the absorption *A*, which reduces the count rate for element *Y* if element X absorbs its characteristic x-ray photons, and for fluorescence *F*, which increases the count rate for element Y if it absorbs x-ray photons and reemits them at its own characteristic energy. In modern EDS instruments, *ZAF* corrections are performed by microcomputers and software supplied by the manufacturers. In this mode, in addition to quantitative "point analyses," micrographic displays of the distribution of particular elements ("x-ray maps") can be obtained. It is essential in these measurements to make sure that experimental conditions correspond to the assumptions built into the *ZAF* correction procedures. In the most favorable cases of heavy elements (provided no complications arise due to the presence of other elements that emit photons at energies close to those of the elements of interest), the x-ray mode can detect down to about one part in 10^4, i.e., to about 10^{18} atoms cm^{-3}. The spatial resolution of such an analysis is about 1 μm.

5.1.1.3. Transmitted Electrons

In relatively thin specimens (of the order of 1000 Å), transmitted electrons can be detected and analyzed. These electrons contain information related to the crystal structure and defects in the material. The signal can be amplified and processed by detectors that are incorporated in STEMs. The transmitted electrons have energies that depend on the thickness and the structure of the specimen. Energy losses characteristic of the elements present can be analyzed, and this method (i.e., EELS) can be used for compositional analysis. Such analyses are useful with electron energies greater than about 100 keV; i.e., it will be applicable to STEMs or TEMs but not to SEMs.

5.1.1.4. The Thermal Wave, Electroacoustic Technique

The thermal wave, electroacoustic technique is a recent addition to the SEM modes (Cargill, 1980; Rosencwaig and White 1981; Rosencwaig, 1982). It uses a chopped electron beam to produce intermittent heating. Spherical heat waves spread from the heated volume and are damped out. The thermal expansion and contraction produce propagating acoustic waves with the chopping frequency. These ultrasonic waves can be detected by piezoelectric transducers, and devices of piezoelectric materials such as GaAs and InP will self-detect. The spatial resolution is several microns in metals and about a micron in semiconductors (Balk, 1988). Contrast arises from variations in the thermal and elastic features, semiconductor properties such as doping levels or electrical barriers, and ferroelectric or ferromagnetic domains (Balk, 1988).

The electroacoustic signal in semiconductors was also shown to be useful in the analysis of defects and doping striations in, for example, heavily doped GaAs (Bresse and Papadopoulo, 1987, 1988).

The CC mode and the relatively new technique of scanning deep-level transient spectroscopy (SDLTS) provide the most relevant complementary information for CL analysis, and these techniques are discussed next.

5.1.1.5. The Charge Collection Mode

In the charge collection or conductive mode, three types of signals (see Figure 5.3) can be distinguished. The first case, shown in Figure 5.3a, is the *specimen current* (sometimes referred to as the *absorbed electron current*) flowing from the incident electron beam to earth via the specimen. If I_b is the electron beam current, I_s is the specimen current, and I_e is the total emissive current (i.e., backscattered, secondary, and Auger electrons), we can write $I_b = I_s + I_e$. The second case (Figure 5.3b) is that in which the signal is a current flowing in a closed loop between two contacts in the absence of any external voltage source. Such a charge collection current will flow if electron irradiation generates a potential difference between the contacts. This is called an *electron voltaic effect*. In the third case (Figure 5.3c) external biasing is applied and charge collection current variations are obtained as the beam scans, if the conductivity is nonuniform,

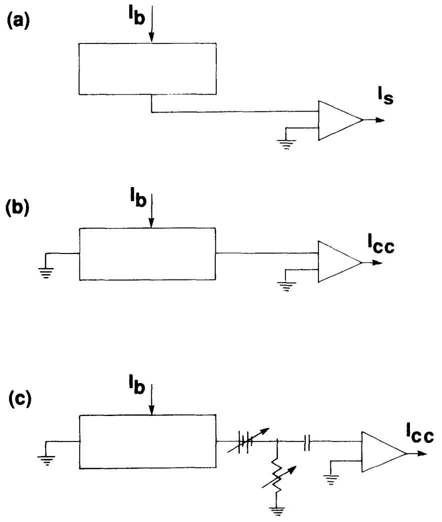

Figure 5.3. Schematic illustration of the three basic types of charge collection (or conductive) mode signal. (a) The specimen (or the absorbed electron) current flowing from the incident electron beam to earth via the specimen. (b) The signal is a current flowing in a closed loop between two contacts in the absence of any external voltage source; in this case, the charge collection current (I_{cc}) will flow only if the specimen exhibits electron-voltaic effects to generate potential differences between the contacts and drive currents round the external circuit. (c) Under external bias, charge collection currents will flow. Variations (contrast) will be obtained even in the absence of electron-voltaic effects, as the beam scans, if the conductivity is nonuniform. This is referred to as β-conductivity.

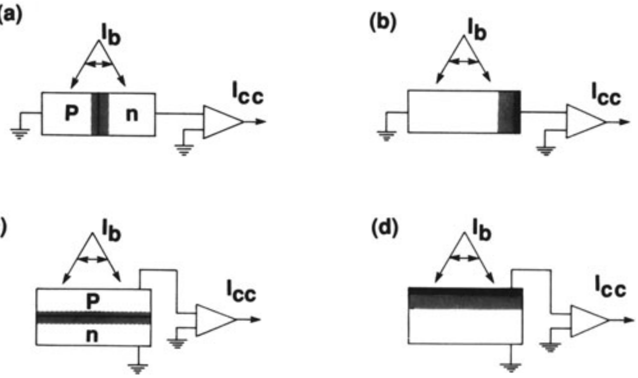

Figure 5.4. Schematic illustration of charge collection geometries. Parts (a) and (b) show perpendicular *p-n* junction and Schottky barrier geometries, respectively. Parts (c) and (d) show planar *p-n* junction and Schottky barrier geometries, respectively.

even in the absence of electron-voltaic effects. This case is often referred to as β-*conductivity.* The term "electron beam–induced current (EBIC)" is sometimes used indiscriminately for CC signals, but it should only be applied to the second case, i.e., electron-voltaic effect signals (true EBIC uses the short-circuit current).

The standard charge-collection arrangements, illustrated schematically in Figure 5.4, are the planar and perpendicular (edge-on) geometries for *p-n* junctions and Schottky barriers. The depletion zones in these cases are indicated by shaded regions.

The CC mode requires the formation of contacts and the presence of a rectifying junction or an externally applied electric field. The CL mode, however, can be applied to as-grown material as well as to devices. In many cases, these two modes provide related information. The CC mode is more commonly used in cases of low-luminescence-efficiency materials, such as Si. Thus, most work on the SEM microcharacterization of extended defects in Si was done with the CC mode.

The EBIC technique is used in studies of *p-n* junction and Schottky barrier characteristics, as well as in the analysis of extended defects such as dislocations. The charge collection contrast in a SEM image is due to variations in charge collection efficiency that may arise from recombination at defects. In these measurements, electron-hole pairs generated in the depletion zone, or within minority carrier diffusion range of it, are separated by its electric field, and the charge collection current (I_{cc}) is measured in the external circuit. Two types of signal used are the EBIC and the electron beam–induced voltage (EBIV). In the former case, the short-circuit current of a device is measured at zero bias. The signal, amplified with a low-input-impedance amplifier, modulates the intensity of the video display. In the second method (the EBIV), the open-circuit voltage is measured across the diode by a voltmeter with high input impedance (hundreds of megohms).

Analytically these two cases can be described as follows. The electron beam irradiation of a device (i.e., *p-n* junction, Schottky barrier, or a heterojunction) produces a charge-collection current $I_{cc} = \eta_{cc} G I_b$ that flows in the direction opposite to the forward-biased barrier diode current (where G, the generation factor, is the number of electron-hole pairs produced per incident electron and η_{cc}, the charge collection efficiency, is the fraction of the pairs that is separated by the built-in field). The externally observed EBIC signal current is

$$I = I_{cc} - I_d = I_{cc} - I_0 \, [\exp(eV/nkT) - 1] \tag{5.1}$$

where I_d is the diode current, I_0 is the saturation current, and n is the ideality factor for the barrier. When $I = 0$, the open-circuit voltage (i.e., EBIV signal) is measured:

$$V_{oc} = (nkT/e) \ln(1 + I_{cc}/I_0) \tag{5.2}$$

Using the EBIC technique in the configurations shown in Figure 5.4, we can derive various semiconductor parameters: for example, the minority carrier diffusion length and lifetime, the surface recombination velocity, and the width and depth of depletion zones (for details, see Holt, 1974; Davidson, 1977; Van Opdorp, 1977; Davidson and Dimitriadis, 1980; Schick, 1981; Leamy, 1982; Holt and Lesniak, 1985; Holt, 1989; also see the Oxford "Conferences on Microscopy of Semiconducting Materials," Institute of Physics Conference Series, Vol. 60, 67, 76, 87). The minority carrier diffusion length L is derived from the dependence of I_{cc} on the distance x of the SEM electron beam away from the junction in the geometries of Figures 5.4a,b. The simple expression $I_{cc}(x) = I_0 \exp(-x/L)$, in which surface recombination is neglected, is sometimes used. Even if surface recombination is negligible, other complications can arise. For example, as mentioned in Section 4.4, Wittry and Kyser (1965) found two exponential terms in the variation of EBIC with distance from a *p-n* junction in GaAs on the *n* side. This was shown to be due to (1) short-range collection of minority carriers by diffusion and (2) long-range self-detection of infrared photons by the junction; i.e., it was due to infrared CL photons reaching the junction and being absorbed there and contributing electron-hole pairs to the charge-collection current (Wittry and Kyser, 1965; Holt and Chase, 1973). Lesniak *et al.* (1984) found a similar form of EBIC line-scan profile in π-p-n^+ Si photodiodes (π is low-doped *p*-type). The two exponential decays on the π-p side occur because the minority carrier diffusion length in the π-region was larger than that in the *p*-layer. To obtain minority carrier lifetimes, one measures the charge collection decay as a function of time when a stationary electron beam is blanked. This type of measurement requires a fast beam-blanking device. In both diffusion length and lifetime measurements, the effects of injection level, finite source size, and surface recombination have to be considered. However, in the planar Schottky barrier configuration (Figure 5.4d), the surface is within the depletion zone. Thus, surface recombination can be disregarded. Wu and Wittry (1978) demonstrated that such a method can be used to measure small carrier diffusion lengths (about 0.5 μm) with high accuracy and spatial resolution.

Donolato (1983) proposed measuring the minority carrier diffusion length and surface recombination velocity by evaluating the first moment of two EBIC profiles at different electron beam energies. Using this method, he obtained an equation containing only the minority carrier diffusion length, which can be easily derived, followed by the determination of the surface recombination velocity by substitution. The important advantage of this method is that no fitting of the experimental results to a two-parameter theory is required (see Donolato, 1983, and references therein).

EBIV measurements can also provide device quantities. For example, the open-circuit voltage (V_{oc}) saturation value, reached for high beam powers, occurs at the flat-band condition to give the diffusion potential V_D of the junction. Huang *et al.* (1982) used the EBIV technique to measure the Schottky barrier height Φ_B (which is contained in the standard expression for I_0). This method is especially valuable for the *in situ* analysis of the changes of silicide Schottky barrier heights as a function of annealing (Huang *et al.*, 1982). It gives, however, a weighted average value of the barrier height. To obtain spatial resolution in such measurements, one must use an EBIC method (Gibson *et al,* 1985).

The CC mode can be also used for determining the doping concentration for a *p-n* junction or a Schottky barrier. It involves measuring the depletion width as a function of the reverse bias. Then, from the well-known relationship between depletion width, reverse bias, and doping concentration, the latter can be obtained (MacDonald and Everhart, 1965; Schick, 1981, 1985; Holt and Lesniak, 1985). Schick (1981) demonstrated that the spatial resolution of the depletion width measurements as a function of the reverse bias can be improved by differentiating EBIC line scans.

Jakubowicz (1986, 1987) and Jakubowicz *et al.* (1987) applied both CC and CL techniques to the analysis of extended defects in semiconductors. These results will be discussed in Chapter 6.

5.1.1.6. Scanning Deep-Level Transient Spectroscopy

Another important complementary technique to CL analysis is SDLTS, developed by Petroff, Lang, *et al.* (1977, 1978). It is especially important since it complements CL spectroscopy for the assessment of nonradiative levels. As mentioned earlier, a fundamental difficulty in quantitative luminescence analysis is the lack of information on competing nonradiative processes. Thus, SDLTS in conjunction with the CL mode may become crucial to the efforts directed at quantification of CL analysis.

SDLTS is a derivative of the deep-level transient spectroscopy (DLTS) technique (Lang, 1974), which is based on the capture and thermal release of carriers at traps. A voltage bias pulse is used to fill the traps in the DLTS technique, whereas an electron beam injection pulse is employed in the SDLTS method. In a SEM the SDLTS technique lets us determine the energy levels and the spatial distribution of deep states in semiconductors. The introduction of capacitance meters of higher sensitivity has made the technique more widely applicable (Breitenstein, 1982; Breitenstein and Wosinski, 1983; Breitenstein and Heydenreich, 1983, 1985, 1989; Heydenreich and Breitenstein, 1985, 1986).

The principle of SDLTS is the pulsed-electron-beam-induced filling of the deep levels. After each excitation pulse, the deep levels are in a nonequilibrium state. The thermal emission of the captured carriers restores the thermal equilibrium, and if the levels are located in the space-charge region of a *p-n* junction or a Schottky barrier, the relaxation process will lead to a measurable current transient or transient in the capacitance of the system. The rate of decay depends on the energy of the deep level and the temperature. Thus, two different signals, current transient or capacitance transient, can be used in SDLTS measurements. By measuring the time constant of the transients as a function of the excitation pulse repetition rate (i.e., rate window) at different temperatures, one can derive the energy level and the concentration of deep levels in the material. An important distinction between capacitance transient and current transient SDLTS is that in the former, one can distinguish between electron and hole traps from the sign of the signal that is independent of the rate window, whereas with current transients the sign of the signal that depends on the rate window is the same for electrons and holes. In SDLTS the beam is pulsed in such a manner that it is on for several microseconds and off for about 10 μsec. In the on state, the electron beam–induced increase in the electron-hole pair density will change the trap occupation level. This occupation will be restored due to thermal excitation in the off state.

In this technique, levels are excited by a pulsed electron beam (Figure 5.5). By selecting a given energy level corresponding to a defect center in the material by setting an appropriate temperature and rate window and scanning the pulsed electron beam over the specimen surface, we can obtain the spatial distribution of the level. Conversely, keeping the pulsed electron beam stationary and varying the temperature (for example, between −150° and 300°C), we can obtain a DLTS spectrum.

The main disadvantage of this method is the sensitivity problem. In SDLTS measurements, to obtain a high spatial resolution (about 1 μm), we must excite a very small area. Therefore, for the same sample, a typical SDLTS signal is several orders of magnitude smaller than the standard DLTS signal. Also, the

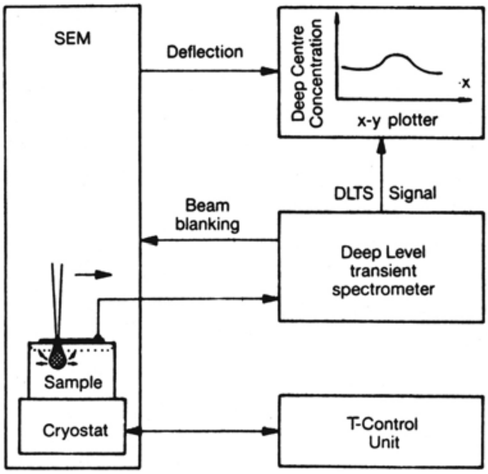

Figure 5.5. Schematic illustration of the basic components of an SDLTS system. (After Breitenstein and Heydenreich, 1985.)

SDLTS measurement is generally fairly complex, involving, in addition to the control of the SEM parameters, monitoring such SDLTS parameters as the rate window, sample temperature, filling pulse length, and bias. Thus, a microcomputer-based system is desirable (Breitenstein and Heydenreich, 1985; Heydenreich and Breitenstein, 1986).

An SDLTS image is illustrated in Figure 5.6, which presents both the EBIC image (Figure 5.6a) and the SDLTS map (Figure 5.6b) of an n-GaAs (Au)

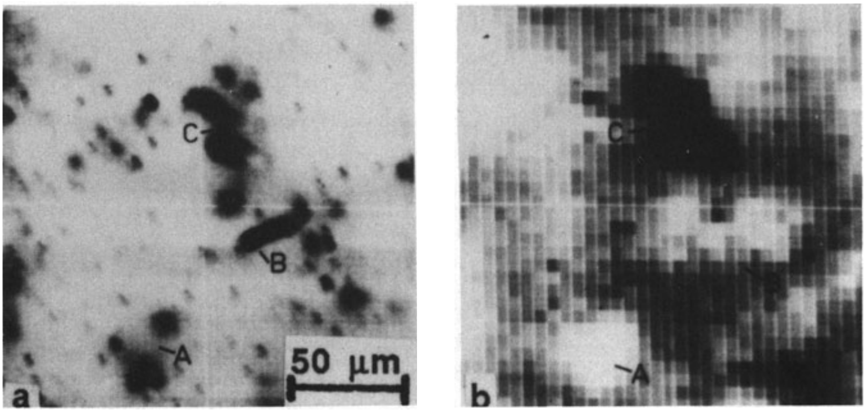

Figure 5.6. (a) EBIC image and (b) SDLTS image of an n-GaAs (Au) Schottky diode containing a 400-meV hole trap level. Dark areas in the SDLTS image indicate a low trap concentration. (After Breitenstein and Heydenreich, 1985.)

Schottky diode containing a 400-meV hole trap level (the so-called A-level) (Breitenstein and Heydenreich, 1985). This center is thought to be associated with a Ga_{As} antisite defect (i.e., a Ga atom on an As lattice site). The EBIC image (Figure 5.6a) reveals many dark dots, which are probably related to dislocations. In the EBIC image there are also several larger dots (for example, one denoted A). This type of defect appears to be accompanied by an increase of the SDLTS signal in the vicinity (bright contrast in the SDLTS image corresponds to a higher concentration of the A-level in this case). In the extended dark region C in the EBIC image, however, the SDLTS image indicates a much lower A-level concentration in that vicinity. Breitenstein and Heydenreich (1985) explained these observations as follows. The material under investigation was grown under Ga-rich conditions, favoring Ga_{As} antisite defect formation. If the defects in the vicinity of region C are local Ga precipitates or act as sites for gettering Ga atoms, the excess of Ga around these defects is reduced, so Ga_{As} antisite defect formation is not favored anymore. This leads to much lower A-level concentration and significantly reduced SDLTS signal. Breitenstein (1987) also demonstrated the usefulness of the SDLTS technique in the current detection mode in conjunction with applied reverse bias to image inhomogeneous distributions of various deep-level defects in semi-insulating GaAs.

A modification to the SDLTS technique, called *scanning double deep-level transient spectroscopy* (SDDLTS), was applied by Woodham and Booker (1987) to the analysis of dislocations in silicon. In this method, the defect traps throughout the diode area are filled by a bias pulse, as in the conventional DLTS method. By medium-energy electron irradiation of a small area, some of the traps are emptied, and thus the dislocations from the irradiated area do not contribute a signal to the subsequent capacitance transient. The signal component corresponding to the electron-irradiated area is obtained by subtracting the reduced signal (due to electron irradiation) from the signal with no irradiation.

In summary, SDLTS is an important complementary technique to CL analysis for the assessment of nonradiative levels. The availability of the SDLTS technique in conjunction with the CL mode may become crucial to the efforts directed at quantification of CL analysis of semiconductors.

5.1.2. Cathodoluminescence Detection Systems

Cathodoluminescence detector designs differ in the combinations of components used. For details, see Holt (1981) or Trigg (1985). The collection efficiencies of the systems vary from several percent for a photomultiplier tube (PMT) with collection lens, through tens of percent for PMTs equipped with light guides, to about 90% for systems containing ellipsoidal mirrors coupled directly to a monochromator. We can make two basic distinctions. One is between dispersive (spectroscopic) and nondispersive systems. The other is between ambient and cryogenic temperature designs. The shape of the collecting mirror (if present), the type of the detector system used, and other choices of components result in CL systems optimized for different applications. In many applications, such as studies of phosphors and minerals, simple noncryogenic systems may be sufficient. In semiconductors, useful qualitative information may be obtained by using relatively simple panchromatic or monochromatic systems operated at room temperature only. For detailed quantitative studies of defects and dopants in semiconductors, however, it is necessary to use high-efficiency light-collection, dispersive systems capable of sample cooling, preferably to liquid helium temperatures.

The essential requirement of CL detection system designs are a high efficiency of light collection, transmission, and detection. A schematic diagram of a typical early CL detection system for the visible range is presented in Figure 5.7. The signal from the photomultiplier (PM) can be used to produce micrographs or spectra. For a constant monochromator setting and a scanning electron beam condition, monochromatic micrographs can be obtained. When the monochromator is stepped through the wavelength range of interest and the electron beam is stationary or scans a small area, spectral information can be derived. When the grating of the monochromator is bypassed, photons of all wavelengths fall on the photomultiplier giving the panchromatic (integral) CL signal.

In many cases of CL in semiconductors, the signal is weak. Thus, to avoid using high electron beam power for stronger CL signals, we need an efficient system to collect the emitted light and transmit it with minimum loss to the light detector. There have been many reports on the designs and applications of various light collection systems. The early development of CL collection systems is summarized by Giles (1975 and references therein). Later developments of efficient light-collection systems are described by Davidson and Rasul (1976) and Myhajlenko (1984).

The basic features of the evolution of light collectors of increasing efficiency are shown in Figure 5.8. The fraction of the light collected depends, first, on

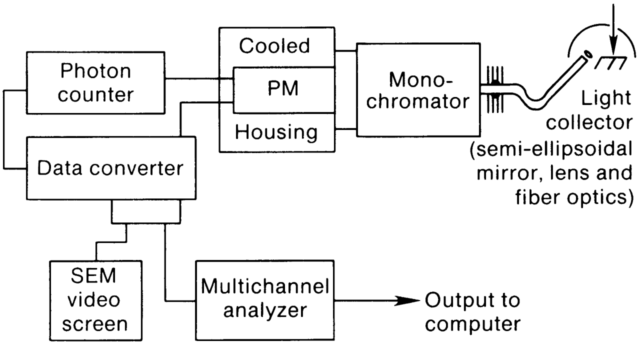

Figure 5.7. Schematic diagram of a typical early CL detection system for the visible range.

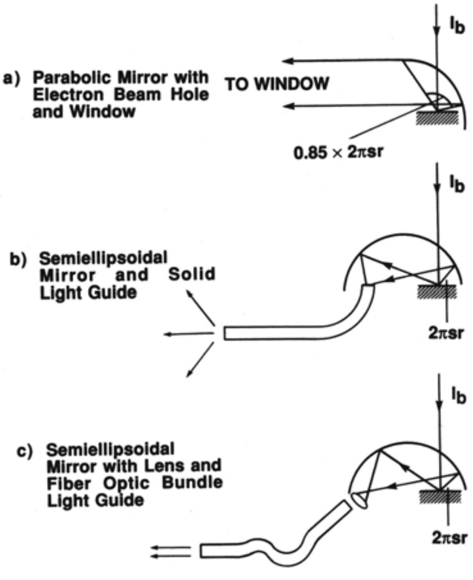

Figure 5.8. The evolution of light collectors of increasing efficiency. (a) Parabolic mirror with electron beam hole and window (Bond *et al.*, 1974). (b) Semiellipsoidal mirror and solid light guide (Hörl and Mügschl, 1972). (c) Semiellipsoidal mirror with lens and fiber-optic bundle light guide (Carlsson and van Essen, 1974). (After Steyn *et al.*, 1976.)

the fractional solid angle subtended by the collector at the emitting point on the specimen surface. This can vary from about 20% in the collection employing a parabolic mirror on one side of the specimen (Muir *et al.*, 1971), through an estimated 80–90% for the larger parabolic mirror collector (Bond *et al.*, 1974) (see Figure 5.8a), to about 100% collection of the CL by the semiellipsoidal mirror of Hörl and Mügschl (1972) (Figure 5.8b) and Carlsson and van Essen (1974) (Figure 5.8c). The disadvantage of the collector using a solid light guide is the difficulty in collimating or reducing to a point focus, light that is spread over a solid angle of 2π *sr*. This problem is solved by using a microscope objective lens and a fiber-optic bundle (Figure 5.8c). These are so arranged that the light is collimated before it enters the fiber bundle, which is also gradually altered along its length from circular (to match the lens) to rectangular (to match the entrance slit of the monochromator).

A variety of other CL collectors and modifications to those illustrated in Figure 5.8 have been reported, but it will be sufficient to describe the semiellipsoidal mirror and a fiber-optic guide shown in Figure 5.9 (Steyn *et al.*, 1976). In this design, the electron beam is incident on the sample at the first focus of a semiellipsoidal mirror, which concentrates the emitted light through the second focus of the mirror where it is collimated by a lens and transmitted via a fiber-optic guide into the entrance slit of the monochromator. Light with a narrow range of wavelengths then falls on the photomultiplier, the output of which is a train of pulses corresponding to the incident photons. The output of the photon counter, which provides noise rejection and amplification, can then be fed

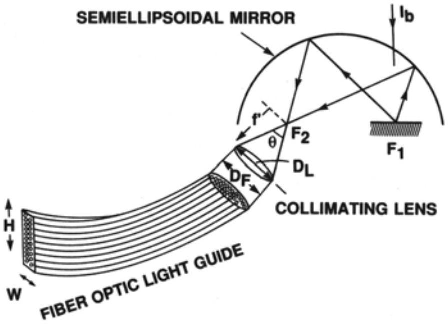

Figure 5.9. The semiellipsoidal light collector. (After Steyn *et al.*, 1976.)

through a video amplifier to a cathode-ray oscilloscope to produce CL images, or it can be subjected to computer analysis. This design was optimized by Steyn *et al.* (1976), who considered the diameter of the fiber bundle, the choice of the lens and its orientation, and the eccentricity of the mirror ellipsoid. Since the CL signal is fed into the rectangular slit of the monochromator, for maximum signal throughput at minimum bandwidth (which depends on the slit width), the criterion

$$HW = \pi D_F^2/4 \tag{5.3}$$

should be satisfied, where H and W are the height and minimum width of the monochromator slit.

The lens is used to collect light over as large an angle as possible from a point corresponding to the second focus of the ellipsoidal mirror and to collimate the beam that should fill the fiber bundle. Thus, the diameter of the lens, D_L, should satisfy the criterion

$$HW = \pi D_L^2/4 \tag{5.4}$$

and the lens must be positioned one focal length, f', from the second focus (Figure 5.9). The relationship between the angle of the cone, Θ (from which the lens collects light), and the diameter and focal length of the lens is

$$\Theta = 2 \tan^{-1}(D_L/2f') \tag{5.5}$$

Each ray of light emitted from the specimen is concentrated into a cone with its apex at the second focus of the semiellipsoidal mirror. For maximum collection efficiency, the convergence cone of the light must be matched to the acceptance cone of the lens. This can be achieved by optimizing the ellipticity of the mirror, and calculations show that the collecting lens should be tilted about 45° toward the specimen (Steyn *et al.*, 1976). The choice of the ellipticity of the semiellipsoidal mirror was found to depend on the area to be examined (Steyn *et al.*, 1976). For high collection efficiencies, large ellipticity mirrors are better. However, in these cases, the area from which light is efficiently collected is very small (about 10–100 μm on a side). Thus, the general criterion is that for the spectral analysis of points (or very small areas), mirrors with maximum ellipticity should be used, whereas for CL imaging of larger areas lower ellipticities are required.

For samples with planar surfaces oriented horizontally, the emitted CL intensity will be greatest in the vertical direction and fall off with angle of emission Θ from the vertical approximately as $\cos \Theta$. Thus, the bottom edge of the mirror, as well as a portion of the mirror on the side of the lens away from the first specimen focus, could be removed without significant degradation of the light-collection efficiency, to allow secondary electron imaging.

Steyn *et al.* (1976) represented the number of pulses per second recorded by the detection system, R, as

$$R(\lambda) = Q(\lambda)E(\lambda)F(\lambda)\,[1 - A(\lambda)]\,N(\lambda) \tag{5.6}$$

where N is the number of photons of wavelength λ generated per second in the interior of the material, $1 - A$ is the fraction of the photons that escape from the specimen (i.e., A is the fraction lost due to, for example, self-absorption and internal reflection), F is the fraction of the emitted photons collected and transmitted to the monochromator entry slit, E is the transmissive efficiency of the monochromator, and Q is the PM quantum efficiency (i.e., the ratio of the number of PM pulses produced to the number of photons of wavelength λ incident on the photocathode per unit time). The overall collection efficiency $F(\lambda)$ of the light collector was measured by using a small incandescent bulb, which was initially placed at the first focus of the mirror (i.e., the position normally occupied by the specimen) and then moved to the entrance slit of the monochromator. Then, the collection efficiency was calculated from the equation (Steyn *et al.*, 1976)

$$F(\lambda) = \frac{C_R(\lambda)}{P_R(\lambda)}\,\frac{P_M(\lambda)}{C_M(\lambda)} \tag{5.7}$$

where C_R and C_M are the count rates obtained with the bulb positioned at the mirror and at the monochromator, respectively, and P_R and P_M are the powers radiated into the entry aperture of the mirror and the monochromator for wavelengths between λ and $\lambda + \delta\lambda$ (Steyn *et al.*, 1976).

5.1.3. Detectors

The choice of a detector is important in CL measurements. Photomultipliers are the most efficient detectors in the visible range, and most recent CL work was performed with them, although increasing use of solid-state detectors and Fourier transform spectrometry (FTS) for detecting luminescence in the infrared is being reported. Koschek and Kubalek (1985b) describe the properties of various detectors for CL measurements.

Photomultipliers are classified according to type of photocathode. S20 photomultipliers (multialkali photocathodes) detect UV and blue light efficiently, but their response drops to zero in the red region. S1 photomultipliers (Ag-O-Cs photocathodes) have a low efficiency in the red region only, but this extends to longer wavelengths than can be detected by S20 devices. GaAs:Cs-photocathode PMTs have relatively high and nearly constant efficiencies throughout the visible range. Representative sensitivity curves for these types of PMTs are presented in Figure 5.10. The wavelength response may also depend on the optical transmission of the envelope material. Thus, S20 photomultipliers can be extended to shorter wavelengths by using UV glass or fused silica envelope materials. There are two basic PM configurations: (1) the end window type with semitransparent photocathode, which operates at higher voltages and has higher gains and quantum efficiency, and (2) the side window type with solid photocathode, which is usually smaller and operates at lower voltages. For low signal levels, the preferable PMTs are the end window type, for which two types of signal acquisition can be used: (1) integrating the signal into an average current, or (2) counting the individual pulses, which allows digital processing of the data. Cooling photomultipliers reduces the dark current. Thermoelectric cooling (to −20° or

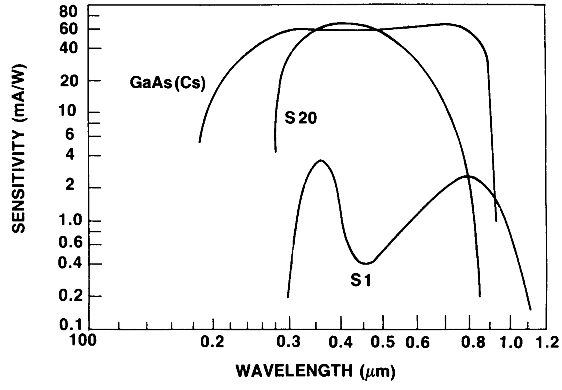

Figure 5.10. The spectral sensitivity of three types of photomultipliers.

−30°C) is sufficient, since the minimum possible dark current is then reached. The time response of photomultipliers can be as small as 1 nsec.

In many applications with low signal levels, the signal-to-noise ratio is improved by using phase-sensitive lock-in amplification with synchronized electron beam chopping (Balk and Kubalek, 1973).

For low-CL signal levels, it is advantageous to use photon counting techniques. In addition to improving the signal-to-noise ratio, this technique gives the CL information in digital form, so multichannel analyzers can be employed to record CL spectra numerically. The spectra can subsequently be transmitted to a computer for analysis. The sensitivity of the digital signal makes it preferable for monochromatic imaging, although analog signals provide images of better quality and are more suitable for panchromatic CL work.

There are two methods of acquiring CL spectra: sequential and simultaneous. In the sequential method, the electron beam is usually stationary, the transmitted wavelength is varied, and the amplified detector signal is recorded as a function of wavelength. In the simultaneous acquisition method, the photomultiplier is replaced by a silicon intensified target (SIT) vidicon camera (Löhnert *et al.*, 1979, 1981), and an optical multichannel analyzer (OMA) is used. Each line of the silicon target responds to a particular wavelength of the spectrally dispersed light from the monochromator. Thus, the whole spectral range of interest is detected simultaneously, and the signal is integrated by the multichannel analyzer. The spectrum acquisition time in this case is much shorter than in the sequential method. This is especially advantageous in studies of electron beam–sensitive materials.

Solid-state detectors can be used for transmission CL (TCL) and emission CL (ECL) infrared panchromatic microscopy (Vale and Greer, 1977; Chin *et al.*, 1979a–c; Cocito *et al.*, 1983; Marek *et al.*, 1985; Yacobi and Herrington, 1986). In these cases, Si and/or Ge solid state detectors are positioned inside the SEM vacuum chamber either below the specimen (TCL) or above it (ECL). Unless filters are used, panchromatic CL is obtained. A more recent design for ECL

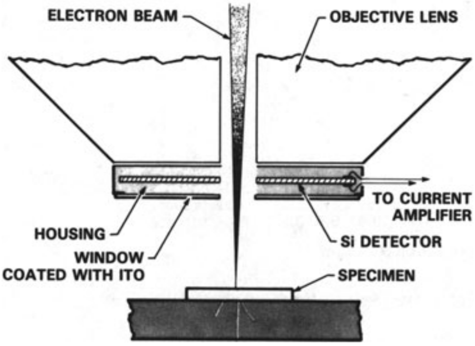

Figure 5.11. Schematic arrangement of a doughnut-shaped Si detector attached to the pole piece of the objective lens in the SEM. (After Marek *et al.*, 1985.)

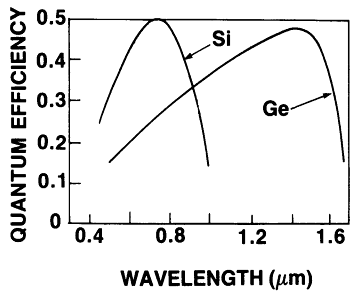

Figure 5.12. Quantum efficiency as a function of wavelength of Si and Ge photodetectors.

imaging utilizes a doughnut-shaped Si detector mounted on the pole piece of the objective lens (essentially replacing the backscatter detector) (Marek *et al.*, 1985), as shown in Figure 5.11. In this design, the glass cover of the photodetector blocks backscattered electrons that could also contribute to the detector signal.

Solid state detectors that are suitable for luminescence in the spectral range between about 0.5 and 4 μm are made of Si, Ge, PbS, InAs, and InSb. Quantum efficiency curves for Ge and Si are given in Figure 5.12. The detectivity of a Si detector is usually higher by more than an order of magnitude than that of a Ge detector. The sensitivity curves of PbS, InAs, and InSb are progressively shifted further into the infrared, but the detectivities are significantly reduced compared with that of the Si detector. In most cases, lowering the temperature, generally to the liquid nitrogen point, improves the sensitivity of the detector (Figure 5.13).

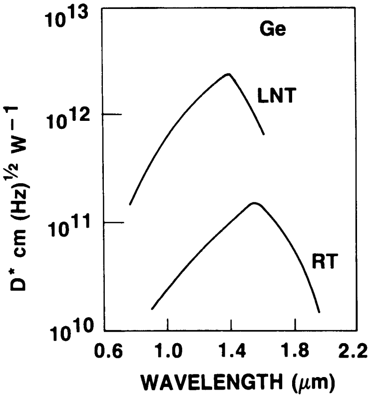

Figure 5.13. Effect of the operating temperature on the specific detectivity of a Ge photodetector.

However, in some cases it is preferable to use thermoelectric cooling to about 200 K. For example, in the PbS detector the detectivity increases upon cooling, but so does the response time and the optimum is reached at about 200 K. Similarly, thermoelectric cooling should be adequate for InAs detectors. The time response of solid state detectors may vary, depending on the type, between about 0.1 and 10 nsec.

Infrared CL detection methods are necessary in investigations of semiconductors with energy gaps below the detection range of photomultipliers. Although photoconductive and photovoltaic semiconductor detectors can be used with monochromators, the optimal method in the infrared range is FTS based on the Michelson interferometer (Davidson *et al.*, 1981; Myhajlenko *et al.*, 1984; Saba and Holt, 1985). Figure 5.14 is a schematic diagram of such an instrument. The light to be analyzed is collimated, and the parallel beam falls on a beam splitter that, ideally, transmits 50% of the beam to the fixed plane mirror and reflects 50% to the moving mirror. Subsequently, the two beams are reflected back to the splitter and recombine. The moving mirror introduces an optical path difference between the two arms of the interferometer, so the phase difference varies sinusoidally with the position of the moving mirror. The period of the variation depends on the wavelength of the radiation, and the interferogram encodes the intensity of each wavelength. The interference pattern is transduced by a photodetector, and the spectrum is obtained by Fourier-transforming the interferogram. The advantages of FTS over dispersive spectroscopy are the improvements in the signal-to-noise ratio and in the optical throughput. With this method, panchromatic micrographs can be recorded when the light bypasses the interferometer to reach the detector; monochromatic micrographs can be obtained by inserting suitable filters in the bypassing light path.

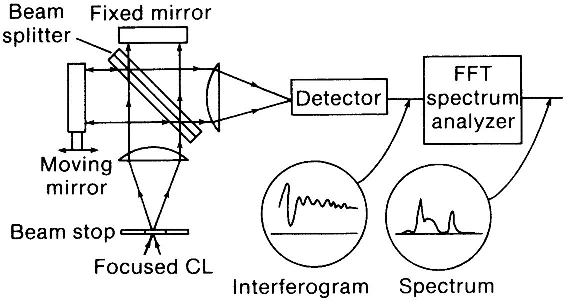

Figure 5.14. Schematic diagram of an infrared CL detection system utilizing a Fourier transform spectrometer. (After Davidson *et al.*, 1981.)

5.1.4. Calibration of the Cathodoluminescence Detection System

The correction of luminescence spectra for the detector system response characteristics is desirable for both qualitative and quantitative CL analyses.

An example of the calibration of the detection system for its spectral response characteristics was provided by Steyn *et al.* (1976) for the system shown in Figures 5.7 and 5.9 and equation (5.6). The transmissive efficiency of the monochromator was not calibrated separately. Instead, the combined performance of the monochromator and photomultiplier, $Q(\lambda)E(\lambda)$, was obtained. For this purpose, a standard tungsten lamp was run at a specific color temperature at a known distance from the monochromator input slit. From the lamp temperature, the number of photons leaving the tungsten filament can be calculated by using Planck's equation. The color temperature T is determined from the standardized calibration graph against current. The number of photons incident on the monochromator input slit, $N_I(\lambda)$, can be calculated from the number of photons leaving the source and the known geometry. The monochromator-photomultiplier response factor is then given by

$$Q(\lambda)E(\lambda) = R(\lambda)/N_I(\lambda) \tag{5.8}$$

where $R(\lambda)$ is the observed count rate. Thus by measuring $R(\lambda)$ and calculating $N_I(\lambda)$, we obtain the performance factor $Q(\lambda)E(\lambda)$. Finally, combining the mirror system collection efficiency and the monochromator-photomultiplier response factor gives the overall detection system response factor QEF. The emission spectrum is obtained as

$$[1 - \mathrm{A}(\lambda)]\, N(\lambda) = R(\lambda)/Q(\lambda)E(\lambda)F(\lambda) \tag{5.9}$$

which is in units of the number of photons emitted per unit time in the resolution interval $d\lambda$.

The overall detection system response factor, QEF, as a function of wavelength, using an S20-response PMT, is presented in Figure 5.15. These data can be stored in the computer as a polynomial and used to correct the observed count rate spectra to obtain the true CL emission spectra. The spectra are often plotted as a function of photon energy ($h\nu$) instead of wavelength. This conversion requires a λ^2 correction term to be applied to the spectral count rate. The spectra in this case represent the number of photons emitted per unit time in a constant-energy resolution interval. Calibration curves of the light-collection system incorporating different monochromators were also obtained (Steyn *et al.*, 1976).

The importance of correcting spectral data, especially for broad emission bands, will be demonstrated in Chapter 7.

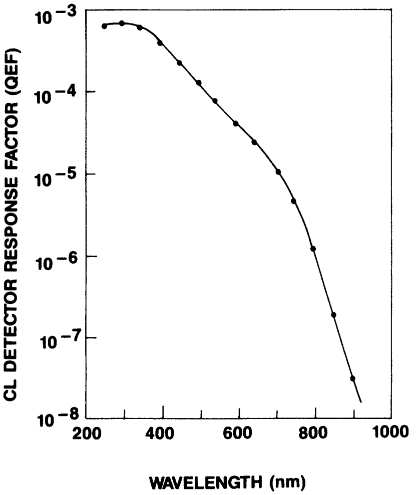

Figure 5.15. The calibration curve of the CL detection system that is shown in Figures 5.7 and 5.9. The detector response factor (*QEF*) is the fraction of photons emitted from the specimen that result in a pulse in the photon counter. (After Datta *et al.*, 1979a.)

5.1.5. Low-Temperature Cathodoluminescence

In the CL mode, the major advantages of cooling the sample, especially to liquid helium temperatures, are (1) that the CL spectrum is sharpened into lines and series of lines corresponding to transitions between well-defined energy levels; (2) there are significant increases in CL intensity, i.e., in signal strength for many CL mechanisms; and (3) the rate of electron bombardment damage in electron beam–sensitive materials is reduced.

The value of low temperatures in increasing the intensity and decreasing the width of emission bands ultimately into quantum mechanical line series has already been emphasized. A number of liquid helium stages for CL-SEM mode studies have been reported (De Mets *et al.*, 1974; Hörl and Roschger, 1980; Davidson *et al.*, 1981; Holt, 1981; Löhnert *et al.*, 1981; Steckenborn *et al.*, 1981a and b).

The increased intensity obtained at liquid helium temperatures can radically improve the signal-to-noise ratio, and thus, the quality of monochromatic micrographs, and make it possible to observe spectral phenomena not accessible at higher temperatures (Holt, 1981).

A liquid helium system is currently available commercially, based on a continuous-flow liquid helium cryostat (Holt, 1981). Cooled thermal shielding reflects heat radiation. A system of mirrors and a lens or a tapered metal tube transmits the light to the port in the side of the specimen chamber and, subsequently, to the entrance slit of a monochromator.

5.1.6. Time-Resolved Measurement Systems

The time-resolved CL technique was found very useful in the assessment of semiconductors. Smaller values of the lifetime τ can be measured with the CL technique than with EBIC, since in the latter case the depletion-zone capacitance imposes frequency limitations. The technique enables direct mapping of relaxation times in the material.

Analogous to the methods for CL spectra, there are sequential and simultaneous methods of time-resolved CL measurements. In sequential time-resolved analysis, the specimen is excited by an electron beam pulse. It is important to ensure (1) that the electron excitation pulse is sufficiently long to establish a dynamic equilibrium in the material and (2) that the decay time of the excitation pulse is significantly shorter than the carrier lifetime. Electron excitation pulses with variable pulse lengths to below 50 psec can be obtained by electrostatic beam blanking (Menzel and Kubalek, 1979). Signal acquisition from the (fast) photomultiplier can be achieved by a microprocessor-controlled boxcar integrator system (Steckenborn, 1980; Steckenborn *et al.*, 1981a,b) or by the single-photon counting method (Rasul and Davidson, 1977b). For the simultaneous acquisition of CL decay times, a streak camera is used as a time-resolving photodetector in conjunction with an optical multichannel analyzer (Hastenrath *et al.*, 1980, 1981). The single-photon counting method can be used also in the latter case (Hastenrath and Kubalek, 1982). The streak camera transforms the temporal luminescence intensity distribution into a lateral brightness distribution on the camera phosphor screen. Subsequently, the intensity distribution is detected by an SIT vidicon camera and processed by a multichannel analyzer. Under computer control, such a system can be used for lifetime mapping measurements. The simultaneous acquisition method offers better time resolution and the possibility of detecting all the CL decay rates simultaneously in a very short time (several seconds).

A block diagram of a CL-SEM system for time-resolved measurements described by Bimberg *et al.* (1985a,b) is shown in Figure 5.16. Electron pulses of rise and decay times ≤ 200 psec with widths variable between 1 nsec and 10 μsec and a repetition rate of 1 kHz to 1 MHz are used for excitation. A liquid helium cryostat allows the temperature to be varied from 5 to 300 K. The pulse generator triggers both the beam blanking unit and a photon counting system via a delay line. The pulse-height distribution is evaluated by a computer-controlled multichannel analyzer, and the data are stored on a magnetic tape. This allows simultaneous acquisition of 14 spectra taken at different times relative to the start of the exciting pulse.

An example of an 800-nsec electron pulse excitation is shown in Figure 5.17. Up to 14 time windows, indicated by hatched regions, can be simultaneously set during the onset of the CL, the quasi-equilibrium, and the CL de-

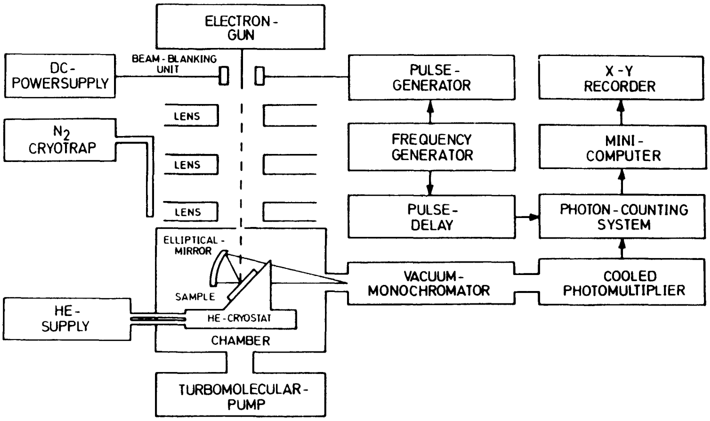

Figure 5.16. Schematic diagram of a liquid helium CL-SEM system for time-resolved studies. (After Bimberg *et al.*, 1985a.)

cay. Advantages of such a system, in comparison with a time-resolved photoluminescence system with similar time resolution, are as follows (Bimberg *et al.*, 1985a). First, the depth-resolved capability of the electron beam excitation (from a few nanometers to several micrometers) allows predominantly surface or bulk excitation. Second, the excitation pulse width can be varied by several orders of magnitude without affecting the pulse rise and decay time, and therefore the temporal resolution of the system does not depend on the pulse width. Third,

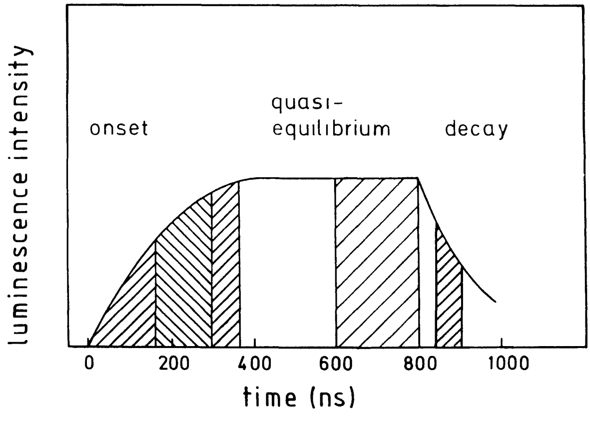

Figure 5.17. Schematic CL response to a 800-nsec electron pulse; time windows that are simultaneously set during the onset, quasiequilibrium, and decay portions of the CL profile are indicated by the hatched regions under the curve. (After Bimberg *et al.*, 1985a.)

scanning CL decay measurements can be used for carrier lifetime mapping. Moreover, such a system is essential for the analysis of lifetimes in a complex system containing more than two levels (one initial and one final state). Comparing several decay spectra covering the wavelength range of interest in such a system would allow the interpretation of results in multilevel systems (Bimberg *et al.*, 1985a).

5.2. Cathodoluminescence Scanning Transmission Electron Microscopy

Transmission electron microscopy is the most powerful technique for the observation and identification of defects in crystals. Together with the CL and EBIC techniques, TEM is invaluable for directly correlating the structure of individual defects to their physical properties. Thin specimens (about 1000 Å) are required, however, for TEM analysis. The signals are therefore lower than are attainable from bulk samples in SEM analysis. In addition, since the volumes analyzed are small, unless they are carefully selected or the observations are repeated in different regions, the results may be atypical.

Figure 5.18 is a schematic diagram of a transmission electron microscope. The electron optical column contains condenser lenses to control the electron illumination of the sample, and objective, intermediate, and projector lenses that produce either the micrograph or the diffraction pattern on the fluorescent screen. In such a conventional transmission electron microscope (CTEM), the image of

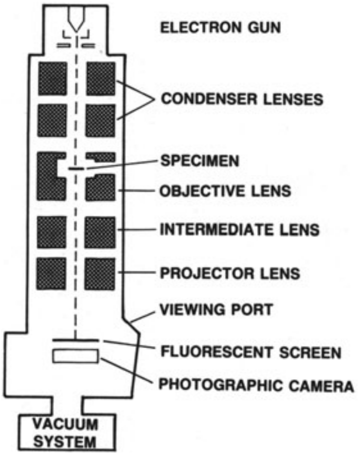

Figure 5.18. Schematic diagram of a transmission electron microscope.

the entire illuminated region of the specimen is projected on the fluorescent screen or on a photographic plate.

Unfortunately, two techniques are known as STEM. The first, sometimes referred to as "dedicated" or field emission gun (FEG) STEM, uses special ultrahigh vacuum field emission gun SEMs. The much higher brightness source in the FEG makes it presently (1989) possible to focus the necessary 10^{-11} A of beam current into a probe 5 nm in diameter. As the beam scans a raster over the thin specimen, the electrons transmitted through the thin specimen are detected by an electron spectrometer. This signal is used to video-modulate a synchronously scanned CRT to produce the STEM micrograph.

The second form of STEM is possible in TEMs with scanning facilities (called TEMSCANs by one manufacturer). These facilities make possible not only STEM video imaging but also, with appropriate detectors above the specimen, emissive, CL, and x-ray mode observations. The advantage of this system is that, due to the very limited lateral beam spreading in the thin specimen, the spatial resolution is much better than in (bulk) CL-SEM. The disadvantage is the low intensity of CL that can be excited in such a small volume. The performance of this CL-STEM instrument is nevertheless impressive (Steeds, 1989).

Petroff *et al.* (1977, 1978, 1980) and Pennycook *et al.* (1977, 1980) have developed CL collection systems in dedicated STEMs. This enables a direct correlation to be made between the structure and physical properties of any defect.

In one of the dedicated STEM designs shown in Figure 5.19 (Petroff *et al.*, 1978), an elliptical mirror is used for light collection. Transmission of the CL uses two planar mirrors and an optical fiber. The signal, taken out of the micro-

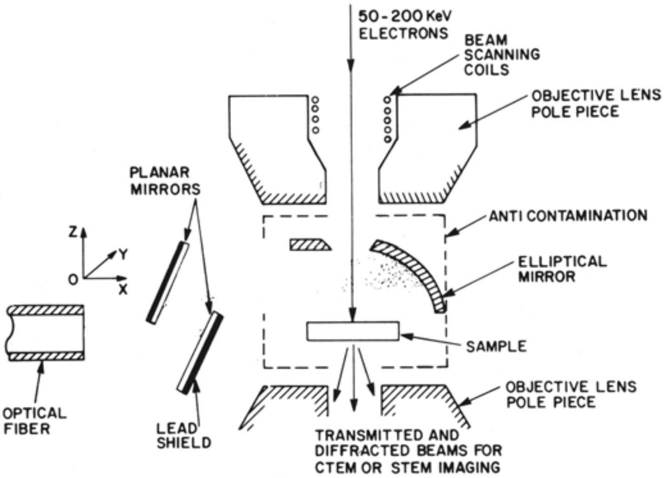

Figure 5.19. Schematic diagram of a CL-STEM system. The distance between the two halves of the objective pole piece is 8 mm. (After Petroff *et al.*, 1978.)

scope column by the optical fiber, is passed through a monochromator and detected by a photomultiplier or a solid-state detector. The CL system can be manipulated to bring the focal point of the mirror and the sample into coincidence. This arrangement also allows for the simultaneous STEM analysis of the microstructure.

In another dedicated STEM design, Pennycook *et al.* (1977, 1980) employed a hemispherical reflector placed on the electron-entrance side of the specimen. The reflector also served as the specimen holder. The light-collection efficiency in such a design is lower than for an ellipsoidal mirror. However, this type of collector can provide fairly uniform light-collection efficiency over a scan of about 1 mm, which is an order of magnitude or more larger than for an ellipsoidal mirror. Also, careful mirror alignment is not required as for an ellipsoidal mirror. The light collected by the hemispherical reflector is directed into a tapered silver tube positioned at one side of the transmitted electron beam. The use of a tapered tube compresses the angular range of light before it enters a solid quartz light guide to be transmitted through a window to the detector.

For infrared CL studies, Graham *et al.* (1987) used a Fourier transform infrared (FTIR) spectrometer in conjunction with the ellipsoidal mirror positioned above the specimen (Yamamoto *et al.*, 1984). In this design, light collected by the ellipsoidal mirror is collimated and transmitted to the FTIR spectrometer and subsequently detected by a germanium photodiode.

5.3. High-Vacuum Nonscanning Cathodoluminescence Systems

Cathodoluminescence systems with no scanning capability are relatively simple but are nevertheless powerful characterization tools, especially for the analysis of interfaces and ion-implanted materials, because of their ability to obtain depth-resolved information.

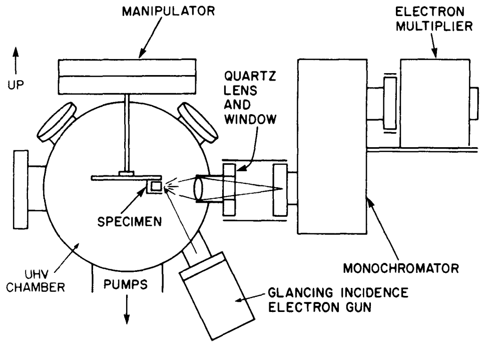

Figure 5.20. Schematic arrangement of an ultrahigh vacuum nonscanning CL system. (After Brillson *et al.*, 1985.)

Such a system consists of a high-vacuum chamber with optical ports and a port for an electron gun. The electron beam is incident at small glancing angles at energies usually between a few hundred eV and several keV in order to obtain information from the near-surface region only.

The system in Figure 5.20 was described and used for the analysis of metal-semiconductor interfaces by Brillson *et al.* (1985) (see also Viturro *et al,* 1986). This system has a chamber with a base pressure of 5×10^{-11} torr. A sample is positioned at the common focal point of both a glancing incidence electron gun and the optical detection system. The CL signal is focused by a quartz lens inside the chamber and transmitted through a quartz window into the monochromator. In order to avoid light emitted from the electron gun filament, the electron beam is chopped and a photomultiplier or a solid-state detector is used with a lock-in amplifier.

5.4. Optical Cathodoluminescence Microscopes

These instruments couple electron gun attachments to optical microscopes (Sippel, 1968). Such an instrument essentially uses the glass side of the screen of a suitably manufactured CRT as the specimen stage of an optical microscope.

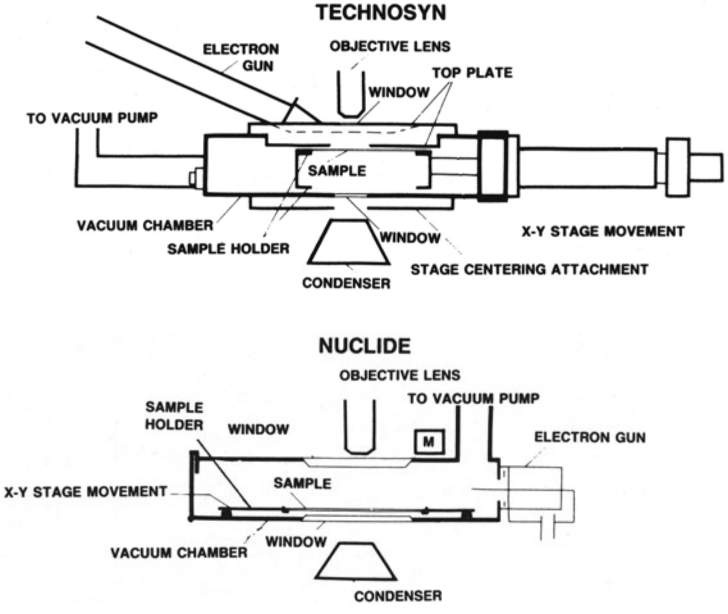

Figure 5.21. Schematic diagrams of cross-sectional views of the basic components of two currently available stages (Nuclide model ELM-2a and Technosyn model 8200) for optical CL microscopes. (After Barker and Wood, 1987.)

Although such a system has a limited spatial resolution, it is widely used in the analysis of minerals (Hagni, 1987).

The basic components of currently available commercial stages (made by Nuclide and Technosyn) are similar. These include a small vacuum chamber with windows, an X-Y stage movement, and a cold-cathode electron gun (see Figure 5.21). The difference between the two stages is in the method of directing the electron beam onto the sample. One design (Technosyn) uses an electron gun aimed at the sample, which is centered on the optical axis of the microscope; the other (Nuclide) employs magnets to deflect the electron beam. More details, together with a comparison of the advantages and disadvantages of these two stages, are given by Barker and Wood (1987). In these systems, the electron energy is between 3 and 30 keV, the electron beam current is between 0.4 and 0.9 mA, and the electron probe size is between about 1 and 10 mm.

An additional accessory, an x-ray detector attachment, was developed by Marshall *et al.* (1987) for the luminoscope (Nuclide). Elemental compositional analysis using this instrument, in addition to the CL capability, provides a simple but powerful characterization tool for studies of minerals.

6

Applications

This section reviews general features of the CL assessment of electronic properties of inorganic solids. Cathodoluminescence applications to the main classes of luminescent materials will be discussed in subsequent chapters.

6.1 Defect Contrast and Spectroscopy Studies

Characterization of the electrically active defects in semiconductors is important for device applications, and the CL and EBIC modes of the SEM are frequently used for this purpose. The CL mode is a contactless method and so is of value for the assessment of starting material. It thus may help to identify problems associated with processing steps that cause device failure. In CL imaging of defects, contrast is due to the enhanced recombination at irregularities in the crystal lattice. For a material with $\tau_{nr} \ll \tau_{rr}$ (nonradiative transitions are dominant), equation (3.25) gives $\tau \cong \tau_{nr}$, and if there are any spatial variations in η due to variations in *radiative lifetime only,* contrast would be expected in the CL mode but not in the EBIC mode, since there is no spatial variation in τ. Cathodoluminescence contrast can also arise due to variations in *nonradiative lifetime* when either τ_{rr} = constant or $\tau_{nr} \ll \tau_{rr}$. In such cases, the contrast in CL and EBIC should be similar.

In recent years, the dislocation-induced electronic levels in the gap and their effects on electrical and optical properties have attracted increasing fundamental interest (Lax, 1978; Labusch and Schröter, 1980; Farvacque *et al.*, 1983; Marklund, 1983; Hutson, 1984; Veth and Teichler, 1984). Cathodoluminescence studies have contributed to elucidating the recombination properties of dislocations (Petroff, 1981; Dupuy, 1983; Löhnert and Kubalek, 1984; Myhajlenko *et al.*, 1984; Holt and Saba, 1985). It appears that dislocations may introduce two types of levels in the gap: (1) narrow energy bands near the middle of the gap, which are associated with dangling bonds, and (2) shallow levels, which are introduced by the localized deformation potential due to the elastic strain field of dislocations. Several reviews have also described the mechanisms of CL defect contrast in semiconductors (Schiller and Boulou, 1975; Davidson, 1977; Booker, 1981; Löhnert and Kubalek, 1983, 1984; Holt and Saba, 1985; Jakubowicz, 1986, 1987; Steeds, 1989). An analysis of the contributions of point defects, dislocations, the surface, and the interface between epitaxial film and substrate to the nonradiative recombination in GaP was presented by Werkhoven *et al.* (1978/79).

6.1.1. Dislocation Contrast Studies

An important question in analyzing dislocation contrast is whether the recombination is due to the inherent structure of the dislocation (e.g., dangling bonds or reconstructed dangling bonds in the dislocation core) or, e.g., due to a Cottrell atmosphere of point defects around the dislocation. Experiments suggest that both dislocation core effects and Cottrell atmospheres are involved in dislocation CL contrast (Davidson, 1977; Davidson and Dimitriadis, 1980; Dupuy, 1983; Holt and Saba, 1985). As mentioned earlier, caution is necessary in CL observations of dislocations, as Balk *et al.* (1976) reported CL contrast inversion at a single dislocation in Se-doped GaAs by increasing the electron beam current from $\sim 10^{-6}$ to $\sim 10^{-5}$ A. This was explained as being due to localized heating leading to enhanced nonradiative recombination and a decrease of the CL signal.

Dislocations in the CL mode appear as dots when viewed end on (e.g., threading dislocations) or as lines (e.g., misfit dislocations). When viewed end on, several different forms of dislocation contrast have been observed: *dark dot, bright dot,* and *dot-and-halo* contrast. Dot-and-halo contrast was first reported in CL images of Te-doped GaAs by Kyser and Wittry (1964); in CL images by Casey (1967), and in charge collection images by Holt and Chase (1968). Investigation of dot-and-halo contrast in Se-doped GaAs by Balk *et al.* (1976) supported the conclusions of Shaw and Thornton (1968) that the contrast is mainly due to variations in the doping concentration around dislocations. As noted by Shaw and Thornton (1968) and Chase and Holt (1973), in some Te-doped GaAs only dark dot contrast is observed without surrounding bright halos.

Examples of dark dot and dot-and-halo contrast are shown in Figure 6.1 for GaAs doped with Te concentration of 10^{17} cm^{-3} (Figure 6.1a) and 10^{18} cm^{-3} (Figure 6.1b). In the GaAs matrix, away from the dislocations, there is a higher concentration of dark dots, thought to be due to precipitate-like microdefects that act as nonradiative centers (Fornari *et al.*, 1985). In some cases, a white dot contrast due to dislocations has also been observed (Shaw and Thornton, 1968; Chin *et al.*, 1984). This was explained by Chase and Holt (1973) in terms of the dependence of CL intensity on the dopant concentration (Figure 6.2). If a specimen contains the average Te concentration indicated by the open circle (numbered 2) in Figure 6.2a, it will exhibit the corresponding luminescence intensity over most of its surface area. Segregation of Te atoms to a dislocation will increase the Te concentration near the dislocation line to some value, such as that indicated by

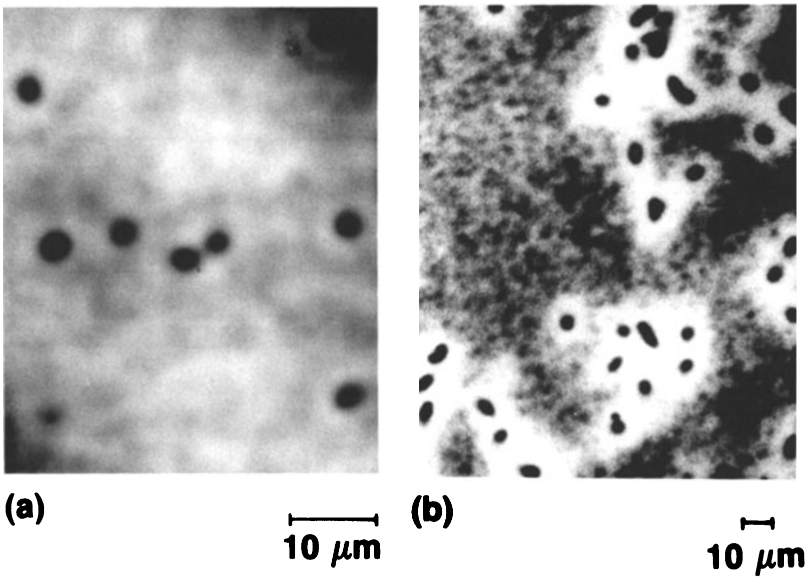

Figure 6.1. CL micrographs of Te-doped GaAs. (a) "Dark dot" dislocation contrast in GaAs doped with a Te concentration of 10^{17} cm^{-3}. (b) "Dot and halo" dislocation contrast in GaAs doped with a Te concentration of 10^{18} cm^{-3}. Note also the contrast due to precipitate-like microdefects in the GaAs matrix.

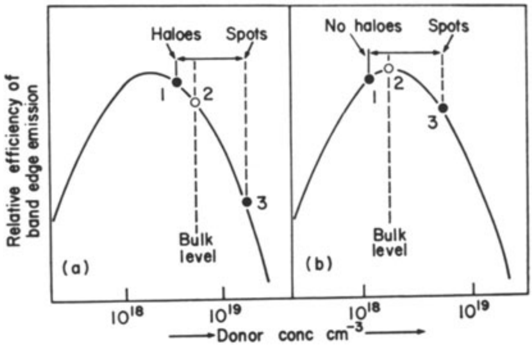

Figure 6.2. Relative efficiencies for radiative recombination in Te-doped GaAs at 300°C. (After Cusano, 1964.) Compositions are indicated that could give rise to (a) the dot and halo contrast and to (b) dark dot (without halo) contrast. Points 1, 2, and 3 in each case indicate the relative efficiencies for the depleted region, the bulk material, and the dislocation spot, respectively. (After Holt and Chase, 1973.)

the solid circle numbered 3, and it will reduce the local luminescence intensity producing the dark dot in the CL image. This will denude a region round the dislocation line, reducing the concentration to a lower value such as that indicated by the solid circle numbered 1. This will increase the CL intensity in this region and result in a bright halo. As shown in Figure 6.2b, if a specimen has an average Te concentration near the peak of the curve of CL intensity versus impurity concentration (i.e., the optimal doping concentration), it will have its luminescence intensity reduced in both the higher concentration dislocation region (solid circle 3) and in the surrounding reduced concentration denuded volume (solid circle 1). Schematic diagrams of the detailed form of the expected dislocation contrast in the cases shown in Figure 6.2, as well as in the case of the average Te concentration being well below the optimal value, are illustrated in Figure 6.3 (Shaw and Thornton, 1968).

A different mechanism, however, may be responsible for the observed dot-and-halo contrast in substrate quality GaP (Davidson *et al.*, 1975; Darby and Booker, 1977). In this case, the contrast may result from the effect of dislocation gettering in reducing the local concentration of *nonradiative* centers, leading to local CL enhancement.

Striation contrast is also due to variation of CL efficiency across the sample. Impurity growth striations are bands of varying impurity concentration resulting from temperature fluctuations during crystal growth (Wittry and Kyser, 1964; Casey, 1967; Shaw and Thornton, 1968). The results presented in Figure 6.2 indicate that the contrast in Te-doped GaAs, showing growth striations in CL images, could correspond to the bright bands having either higher or lower Te concentrations, as compared to the darker bands, depending on whether the average concentration is lower or higher, respectively, than the optimal level. Wittry

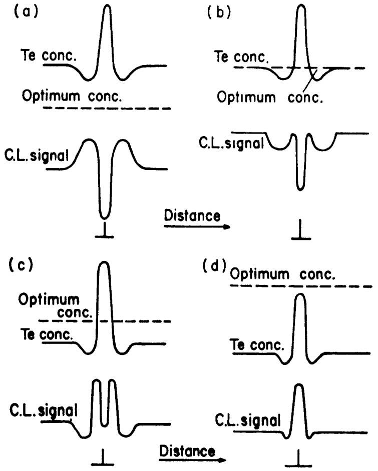

Figure 6.3. Schematic diagrams of the redistribution of Te occurring at dislocations and the corresponding CL signal when (a) the optimal concentration is below the bulk concentration; (b) the optimal concentration equals the bulk level; (c) the optimal level is above the bulk level but below the peak level; and (d) the optimal level is above the peak level. (After Shaw and Thornton, 1968.)

(1966) showed, for example, that in the GaAs samples he studied, the brighter regions had the lower Te concentrations by comparing the CL results with Te concentrations obtained from x-ray microanalysis. On the other hand, Shaw and Thornton (1968) observed cases in which the brighter striations corresponded to both higher Te concentrations and lower Te concentrations than the average. This was deduced by comparing CL observations with infrared absorption results for the same area. By comparing their results with the data of Cusano (1964), Shaw and Thornton estimated that the dopant concentrations across striations varied between 10 and 40% at levels of 4×10^{18} cm^{-3}. The nonuniform distribution of Ge in LEC InP was investigated, using CL spectra, by Warwick and Booker (1983), who observed doping striations as bright and dark bands separated by about 25 μm.

Booker (1981), Löhnert and Kubalek (1984), and Holt and Saba (1985) reviewed the analysis of CL contrast produced by dislocations. The CL contrast was defined as

$$C_{CL} = (L_{CL} - L_{CLD})/L_{CL} \qquad (6.1)$$

where L_{CL} is the CL intensity away from a defect and L_{CLD} is the CL intensity at the defect. Löhnert and Kubalek (1984) analyzed defect CL contrast in semiconductors by using an extension of Donolato's model for the EBIC contrast of dislocations. The dislocation was treated as a cylinder of radius R_0 with a uniform CL quantum efficiency $\eta_d < \eta$. The generation function was represented by a point source. Numerical calculations were performed for a threading dislocation orthogonal to a surface of infinite recombination velocity (Figure 6.4). An expo-

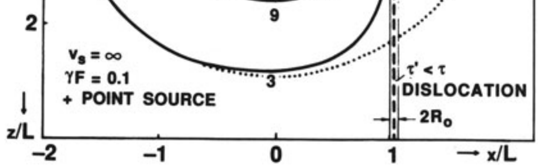

Figure 6.4. Isoconcentration profiles of excess carrier density under the electron beam impact point. The dotted curves represent the case in the absence of the dislocation (the dislocation is indicated by a vertical dashed line) and the continuous curves represent the case when the dislocation is present as shown. (After Löhnert and Kubalek, 1983.)

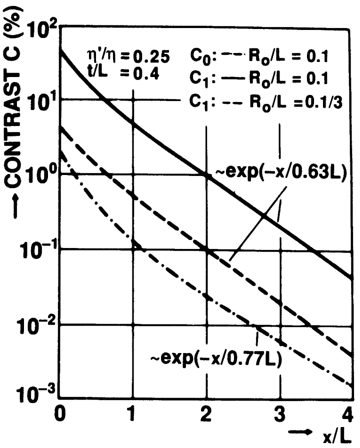

Figure 6.5. The fall in the calculated CL contrast with distance from the dislocation relative to the carrier diffusion length. R_0 is the radius of the cylinder round the dislocation. (After Löhnert and Kubalek, 1983.)

nential decay of the CL contrast with distance from the dislocation was obtained for $x \geq 2L$ (Figure 6.5). These calculations were shown to be in a good agreement with the experimental observations of the dark dot dislocation contrast in GaP. Since the decay constant of the CL contrast (i.e., $0.63L$) is linked to the minority carrier diffusion length L, CL line scans across threading dislocations provide a contactless method for the measurement of L. Löhnert and Kubalek (1984) concluded that the crucial factor for CL contrast formation is the reduction of the excess carrier density due to enhanced nonradiative recombination at the dislocation rather than the reduction of the CL quantum efficiency around the defect.

This work was extended by Jakubowicz (1986) and Pasemann and Hergert (1986), who provided a theoretical background (and experimental data) for simultaneous measurement of the CL and EBIC contrast of a defect. The basic mechanisms of contrast formation, as well as the spatial resolution, of these techniques are the same. However, there are also specific differences in the signal formation. In the CL case, the number of photons (which are generated in the whole volume around the defect) that travel from greater depths will be reduced due to internal absorption; in the EBIC case, the signal is measured in one plane only (i.e., the Schottky contact) (Jakubowicz *et al.*, 1987). Thus, the differences between the images of these two modes can be employed in order to obtain information about the shape and position of defects in the semiconductor.

Jakubowicz presented analytical solutions for both the EBIC (Jakubowicz, 1985a) and CL (Jakubowicz, 1986) contrast from an individual pointlike defect. The defect is characterized by an effective radius γa, where a is the actual radius and γ $(0 \leq \gamma \leq 1)$ is the strength of the defect (for details, see Jakubowicz, 1985a). The treatment of the CL contrast includes the influence of surface recombination and internal optical absorption. The CL contrast can be expressed as (Jakubowicz, 1986)

$$C_{\mathrm{CL}} = f_1(\delta, S, L, H) f_2(\alpha, S, L, b, h, H) \tag{6.2}$$

where

$$f_1 = \frac{\delta}{1 + \frac{1}{2}\delta[(1 - S)/(1 + S)](L/H)e^{-2H/L}} \tag{6.3}$$

and

$$f_2 = \left(\frac{e^{-b/L}}{b/L} + \frac{1 - S}{1 + S} F \frac{e^{-b/FL}}{b/L}\right)\left(\frac{e^{-\alpha H} - [(S + \alpha L)/(1 + S)]e^{-H/L}}{e^{-\alpha h} - [(S + \alpha L)/(1 + S)]e^{-h/L}}\right) \tag{6.4}$$

In these expressions, $\delta = (\gamma a/L)\exp(\gamma a/L)$, $F = (1 + 4Hh/b^2)^{-1/2}$, S is the surface recombination velocity, L is the minority carrier diffusion length, α is the absorption coefficient, H and h are the depths of the defect and the point source, respectively, and b is the distance between the source and the defect (Figure 6.6). The function f_1 relates the CL contrast to the defect strength and the materials and geometrical parameters; generally the CL contrast is a nonlinear function of the defect strength. The function f_2 describes the materials properties and the geometry of the system. The same geometry was used by Jakubowicz (1985a) to analyze the EBIC contrast C_{EBIC} for pointlike defects. In many cases, the surface recombination rate is much higher than the bulk recombination rate. Since in a Schottky EBIC configuration the surface recombination velocity is infinitely high, the CL and EBIC geometries become identical. Thus, by substituting $S = \infty$ into equation (6.2) [i.e., in equations (6.3) and (6.4)], we obtain a simple

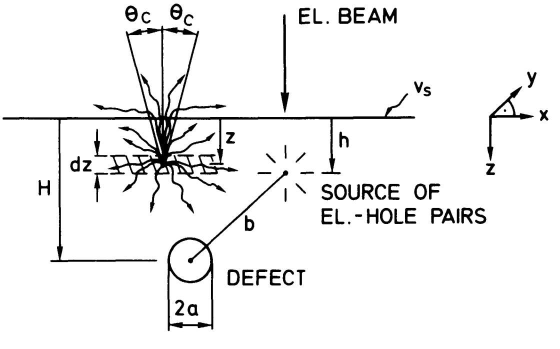

Figure 6.6. The geometrical configuration of the Jakubowicz model. (After Jakubowicz, 1986.)

relationship between the CL and EBIC contrast for a pointlike carrier source and a pointlike defect:

$$C_{\mathrm{CL}} = C_{\mathrm{EBIC}}\sigma \tag{6.5}$$

where C_{EBIC} is the EBIC contrast derived by Jakubowicz (1985a) and

$$\sigma = (1 - e^{-h(\alpha - 1/L)})/(1 - e^{-H(\alpha - 1/L)}) \tag{6.6}$$

Equation (6.6) indicates that σ in the simple case of a pointlike source and a pointlike defect depends mainly on their depths, i.e., on the geometry, and thus one can separate the contribution of the defect configuration to the contrast from that caused by local changes in recombination properties. It follows from this equation that if $H > h$ then $C_{\mathrm{CL}} > C_{\mathrm{EBIC}}$, and if $H < h$ then $C_{\mathrm{CL}} < C_{\mathrm{EBIC}}$. When $H = h$ or $\alpha \gg 1/L$, the CL and EBIC contrasts are equal. These suggest a method of measuring the depth of the defect, H, by comparing C_{CL} and C_{EBIC} at any distance from the defect (provided that the optical absorption coefficient α, the carrier diffusion length L, and the electron beam penetration depth h are known). Another important feature of this correlation between the CL and EBIC contrast is that σ is independent of the defect strength. In other words, if σ remains constant, any variations in C_{CL} or C_{EBIC} are caused by variations of the defect strength. Extending this analysis to dislocations, we see that if, during the electron beam scanning along a defect, σ remains constant and C_{CL} and C_{EBIC} vary, this is due to local variation of the recombination properties; variations in σ, on the other hand, would indicate changes in the depth of a dislocation segment.

Jakubowicz (1986) carried out numerical calculations for an inclined dislocation intersecting the surface of a semi-infinite semiconductor at an angle β (Figure 6.7). The electron beam was assumed to move in the plane $y = 0$. The source of electron-hole pairs was approximated by a uniform generation sphere with diameter equal to the electron range. The dislocation was divided into small spheres with the radius r of the dislocation. The CL contrast was calculated by integrating the analytical solution for a pointlike defect over the dislocation length. Thus, CL contrast profiles of dislocations of various geometries can be simulated, even with local variations of the recombination rate along the defect. This model neglects the carriers generated inside the dislocation cylinder, where, because of the electric field associated with the defect, the analysis should involve a drift component. The latter, however, can be disregarded if the size of the excitation volume is much larger than the dislocation diameter. Calculated CL and EBIC contrast profiles for three values of the angle β are presented in Figure 6.8. As expected, for $\beta = 90°$, symmetrical CL and EBIC curves with the maxima at $x = 0$ are obtained (Figure 6.8a). At each beam position C_{CL} is larger than C_{EBIC} because the major contribution to the contrast comes from the portion of

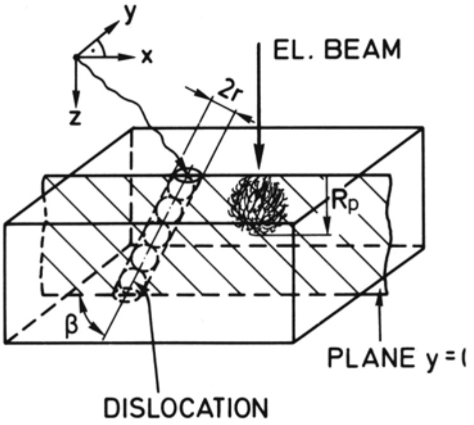

Figure 6.7. A dislocation at an angle β to the surface of a semi-infinite semiconductor. (After Jakubowicz, 1986.)

the dislocation located below the excitation volume. For $\beta = 60°$ and $\beta = 30°$, however, the maxima of the CL and EBIC contrast profiles appear at different beam positions (Figures 6.8b,c). Thus, the details of CL and EBIC images may appear to be displaced for $\beta < 90°$, with this effect becoming more distinctive for decreasing β.

The results for σ as a function of beam position are presented in Figure 6.9. Note that the smallest value of σ corresponds to beam positions close to the dislocation. Jakubowicz (1986) also found that the displacement between the CL and EBIC images depends on the optical absorption coefficient (Figure 6.10) and on the surface recombination velocity (Figure 6.11). The dependence of the displacement on the optical absorption coefficient indicates that the monochromatic CL image may exhibit better resolution than the panchromatic image (Jakubowicz, 1986). These results are valid when both the CL and EBIC contrast are due to enhanced nonradiative recombination at the defect (i.e., dark dot contrast).

If, however, radiative recombination also affects the CL contrast, the analysis may become more complex. For example, in some cases, the CL contrast may change inversely to the EBIC contrast with variations in a particular radiative recombination process. As mentioned earlier, in some cases the CL contrast may consist of spatially resolved bright and dark regions around the defect (i.e., dot-and-halo contrast). In this context, note that, depending on the excitation level, reversal of both CL and EBIC contrast signs was reported (Jakubowicz, 1987, and references therein). More experimental and theoretical work is required to sort out the myriad of possible cases of recombination processes at dislocations and complexes of point defects and dislocations.

A method similar to that of Jakubowicz (1986) was proposed by Pasemann and Hergert (1986), who considered a dislocation lying parallel to the surface at a particular depth.

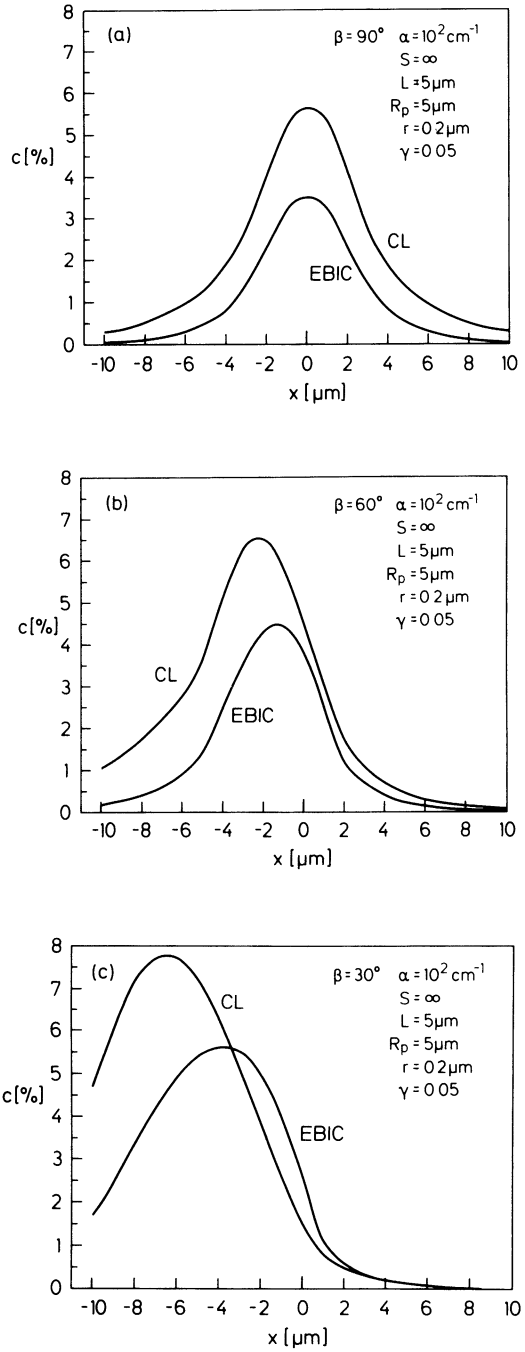

Figure 6.8. Calculated CL and EBIC contrast profiles for a straight semi-infinite inclined dislocation lying in the plane $y = 0$ at different angles β to the surface and intersecting the surface at the center of the coordinate system: (a) $\beta = 90°$; (b) $\beta = 60°$; (c) $\beta = 30°$. (After Jakubowicz, 1986.)

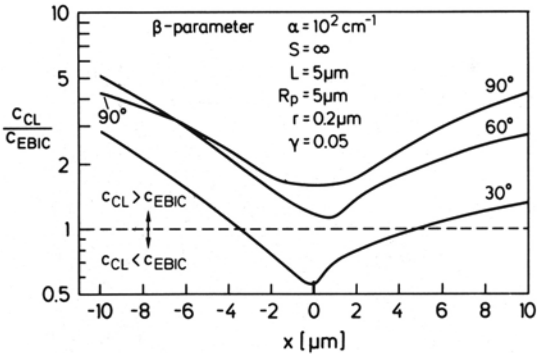

Figure 6.9. Dependence of $\sigma = C_{\mathrm{CL}}/C_{\mathrm{EBIC}}$ on the beam position for angles $\beta = 90°$, $\beta = 60°$, and $\beta = 30°$. (After Jakubowicz, 1986.)

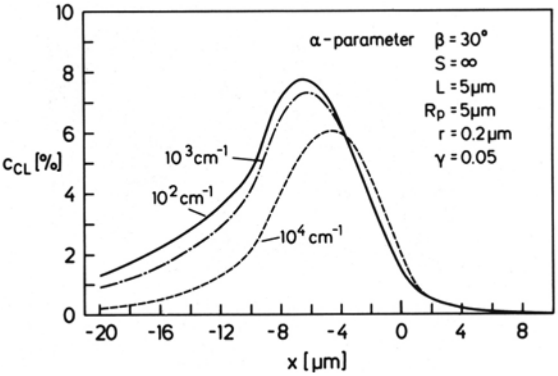

Figure 6.10. Calculated CL contrast profiles for different values of the optical absorption coefficient α. (After Jakubowicz, 1986.)

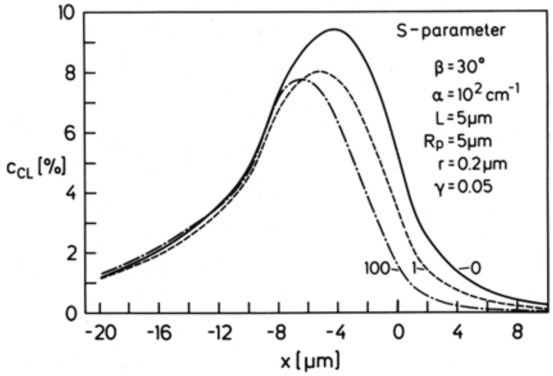

Figure 6.11. Calculated CL contrast profiles for different values of the surface recombination velocity S. (After Jakubowicz, 1986.)

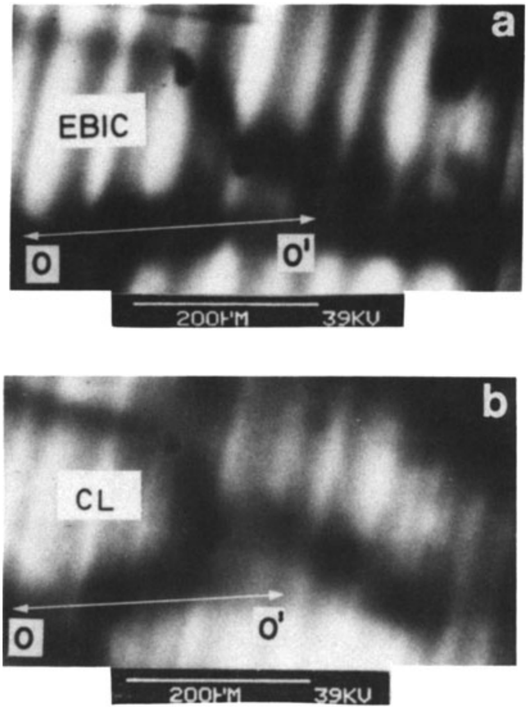

Figure 6.12. EBIC and CL images of the same area of a Sn-doped GaAs specimen. (After Jakubowicz *et al.*, 1987.)

Jakubowicz *et al.* (1987) and Bode *et al.* (1987) compared experimental observations of the combined CL and EBIC contrast at nonradiative dislocations with calculations based on the model of Jakubowicz (1986). Simultaneous CL and EBIC contrast measurements on dislocations were performed on Si-doped and Sn-doped (doping level about 10^{17} cm^{-3}) bulk GaAs crystals and also on

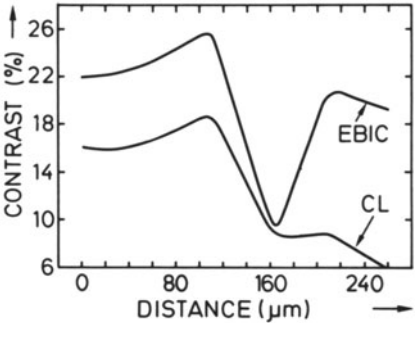

Figure 6.13. EBIC and CL contrast as functions of the electron beam position [measured along the line $O - O'$ (see Figure 6.12)]. (After Jakubowicz *et al.*, 1987.)

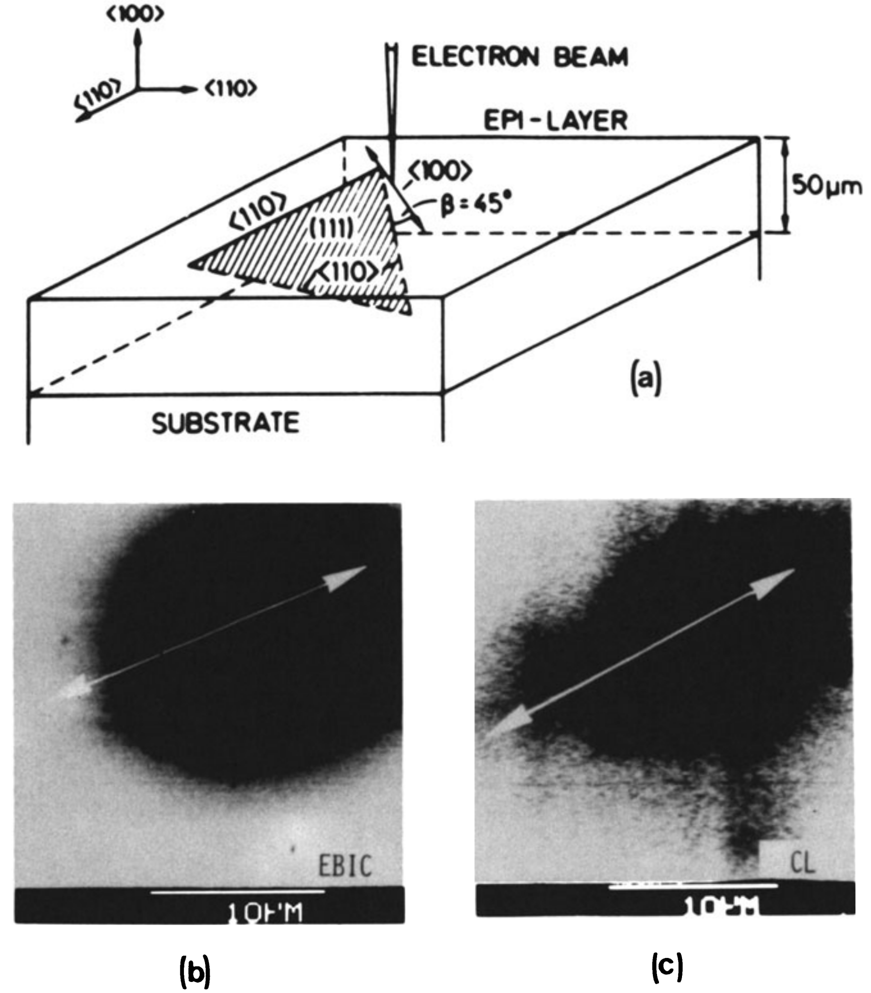

Figure 6.14. (a) The geometry of the stacking fault in an epitaxial GaAs layer used for experiments; (b) experimental EBIC micrograph; (c) experimental CL micrograph from the same area as in (b). (After Bode *et al.*, 1987.)

undoped GaAs liquid-phase epitaxial (LPE) layers. Figure 6.12 presents CL and EBIC images of the same area of Sn-doped GaAs. The bright and dark bands are dopant striations, and the dark irregular regions are associated with nonradiative dislocations. Despite the visual similarities between the CL and EBIC images, differences are clearly revealed in the contrast profiles [measured along the line

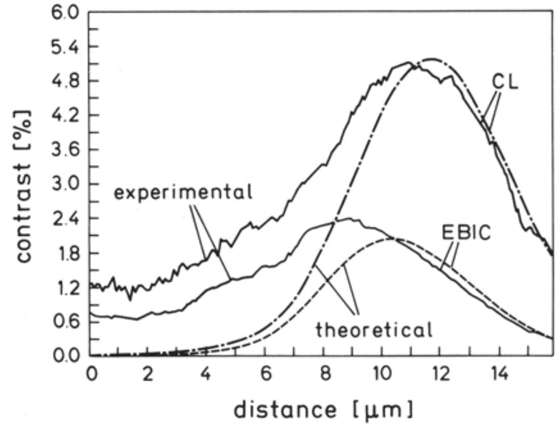

Figure 6.15. Experimental and calculated CL and EBIC contrast profiles. The experimental line scans were taken along the white lines shown in Figure 6.14. The parameters used in the calculations are: surface recombination velocity, $S = \infty$; carrier diffusion length, $L = 2.5$ μm; range of primary electrons, $R_p = 5.6$ μm; radius of dislocation, $r = 0.2$ μm; optical absorption coefficient, $\alpha = 1500$ cm^{-1}. (After Bode *et al.*, 1987.)

O-O' (shown in Figure 6.12)] shown in Figure 6.13, confirming qualitatively the behavior expected from the model. Quantitative comparison between experimental CL and EBIC results and calculations was performed on a stacking fault in a 50-μm-thick GaAs epitaxial layer grown on a (100) GaAs substrate (Bode *et al.*, 1987; Jakubowicz *et al.*, 1987). The stacking fault lay in the (111) plane with the

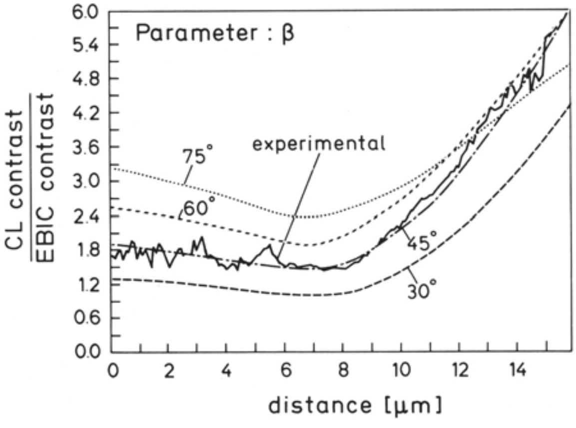

Figure 6.16. Experimental and calculated ratios of CL and EBIC contrast profiles (see Figure 6.15). The calculations were performed for different angles β between dislocation and surface. (After Bode *et al.*, 1987.)

bounding, electrically active dislocations in the ⟨110⟩ directions. The CL and EBIC profiles were obtained with the electron beam scanned along the projection of one of these directions onto the surface (Figure 6.14a). Figures 6.14b,c present experimental EBIC and CL micrographs. The displacement between these images indicates the change of depth of the dislocation with position. Figures 6.15 and 6.16 show the experimental and calculated CL and EBIC contrast profiles and their ratio. The calculated contrast ratio is presented for different inclination angles β between the dislocation and the surface. Parameters used in the calculations are listed in the caption of Figure 6.15. It is evident from Figure 6.16 that the best fit is obtained for $\beta = 45°$, which is in fact the angle of the ⟨110⟩ direction of the dislocation with the (100) plane of the surface that was used in the experiments. In comparison with this agreement between the experimental results and calculations for the ratios (Figure 6.16), the CL and EBIC experimental contrast profiles show only a qualitative agreement with the calculated curves (Figure 6.15). This is explained by the fact that, though both the CL and EBIC contrast profiles depend on the defect strength, the ratio $C_{\mathrm{CL}}/C_{\mathrm{EBIC}}$ is independent of the recombination strength (Jakubowicz *et al.*, 1987). The recombination strength of a defect varies with excitation conditions, and thus it depends on the defect depth and, hence, on the electron beam position. Although this effect was not considered in the calculations, qualitatively both the shape of the CL and EBIC contrast profiles and the displacement between them are well matched to the experimental curves. These results demonstrated that simultaneous CL and EBIC measurements can effectively be used to determine (1) the orientation, shape, and depth of a dislocation in the material, and (2) the local recombination properties of dislocations.

6.1.2. Determination of Dislocation Densities

Cathodoluminescence is a valuable tool for the determination of dislocation distributions and densities in semiconductors (Booker, 1981; Dupuy, 1983). This is relatively simple, since electrically active dislocations are directly revealed in the CL mode. Reliable measurements of dislocation densities up to about 10^6 cm^{-2} can be made with the CL image. It is also possible to derive densities up to about 10^7 cm^{-2} if the conditions for obtaining small dislocation image widths are met by, for example, minimizing the electron beam probe size and the size of the carrier generation volume. [The dislocation image width also depends on the carrier diffusion length (Figure 6.5), the specimen configuration, and the defect geometry.] In high-dislocation-density areas, it is preferable to use CL line scans to ensure that all the defects are counted. In heteroepitaxial structures, such as GaAs layers grown on Si, dislocation densities higher than 10^7 cm^{-2} may be present. In such cases, although dislocations can be identified, density determinations would be unreliable.

6.1.3. Recombination at Dislocations

Recent studies have demonstrated the usefulness of the CL mode in the analysis of the luminescence properties of individual dislocations. Petroff *et al.* (1977, 1978, 1980, 1981, 1984) and Pennycook *et al.* (1977, 1979, 1980) utilized CL attachments to a scanning transmission electron microscope (STEM), and Booker *et al.* (1979) and Myhajlenko *et al.* (1984) used CL and TEM for the analysis of the structure and the electronic properties of defects in several semiconductors. Petroff *et al.* (1980) observed carrier recombination at misfit dislocations at a $Ga_{1-x}Al_xAs_{1-y}P_y$/GaAs interface (Figure 6.17). By comparing the STEM, CL, and EBIC images, they observed that the sessile edge dislocation (marked D1) did not give EBIC or CL contrast, unlike the other dislocations

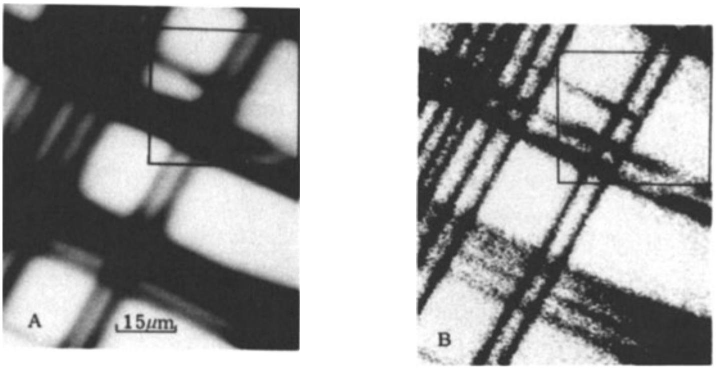

EBIC CL λ - 790nm

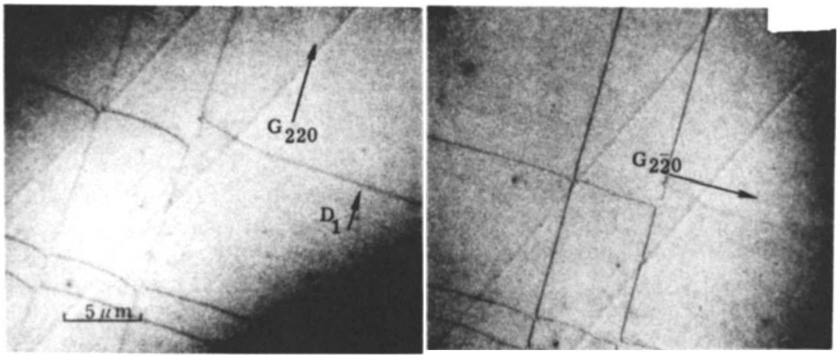

STEM

Figure 6.17. (a) EBIC, (b) CL and STEM micrographs of a misfit dislocation network in $Ga_{1-x}Al_xAs_{1-y}P_y$ epitaxial layers. D_1 in the STEM micrograph is a sessile edge dislocation that does not give EBIC and CL contrast, unlike the other dislocations, which are all 60° type. (After Petroff *et al.*, 1980.)

which are all 60° type (Petroff *et al.*, 1980). In order to explain the absence of carrier recombination at the edge dislocation, Petroff *et al.* (1980) proposed a model of dislocation core reconstruction with no dangling bonds. On the other hand, Fitzgerald *et al.* (1988) studied AlGaAs/InGaAs/GaAs heterostructures and concluded that edge dislocations are stronger nonradiative recombination sites than are 60° dislocations at AlGaAs/InGaAs and InGaAs/GaAs interfaces.

A CL study of molecular beam epitaxy (MBE)-grown double-heterostructure GaAs/$Ga_{1-x}Al_xAs$ layers revealed the dependence of dislocation contrast on photon energy (Petroff, 1981). From the monochromatic CL micrographs it was deduced that some of nonradiative centers, which appear as dark dots at 1.513 eV (the donor-bound exciton, $D^{-o}X$ emission), behave as radiative centers at photon energies between 1.498 and 1.508 eV. The latter were identified with point defects (giving rise to a defect bound exciton luminescence) concentrated around the dislocations that originate in the substrate.

Simultaneous CL and TEM studies of individual dislocations and dislocation tangles in ZnSe and InP were reported by Myhajlenko *et al.* (1984) and Batstone and Steeds (1985). Luminescence at 2.60 eV (*Y*-band) and 2.52 eV (*S*-band) in ZnSe were related to dislocations with an indication that in the case of the *Y*-band impurity-dislocation associations are involved. Some of these results for organometallic chemical vapor deposition (OMCVD) Al-doped ZnSe films grown on GaAs substrates are presented in Figures 6.18 and 6.19, which show the CL spectra acquired from a dislocation tangle and corresponding monochro-

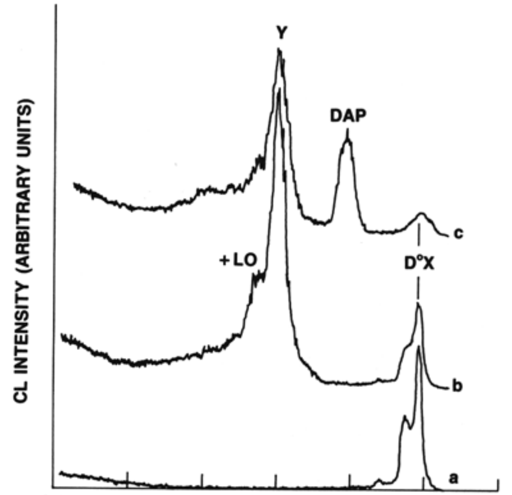

Figure 6.18. CL spectra (30 K) acquired from a dislocation tangle in Al-doped ZnSe: (a) electron probe away from tangle; (b) and (c) probe on tangle. (After Batstone and Steeds, 1985.)

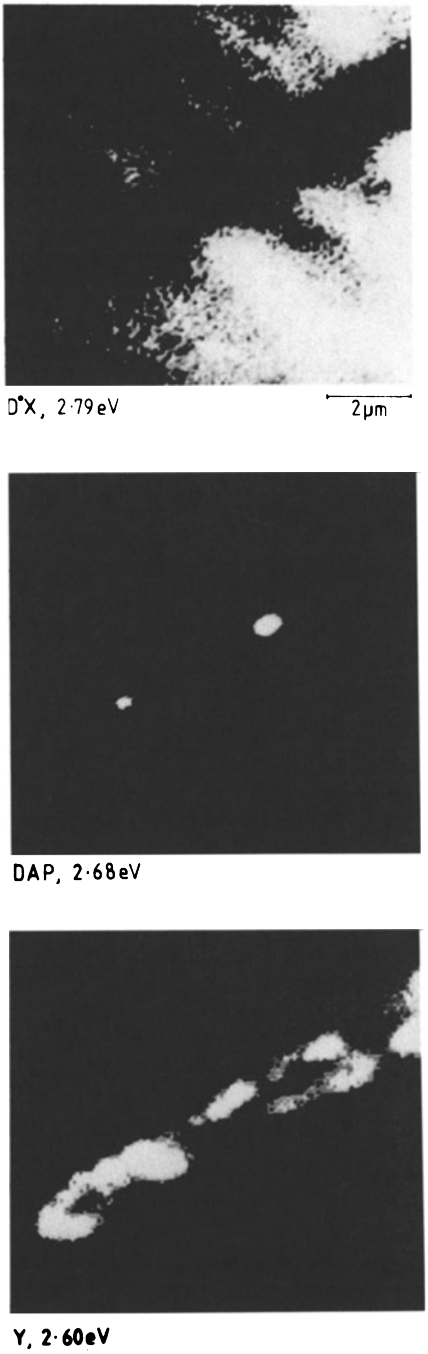

Figure 6.19. Monochromatic CL images from a dislocation tangle in Al-doped ZnSe (compare with Figure 6.18). (After Batstone and Steeds, 1985.)

matic CL images. The donor-bound exciton (D^oX) emission at 2.79 eV and the free exciton (FE) (1*s*-2*s*) emission at 2.78 eV were reduced in the dislocation tangle region, the *Y* emission was localized along the tangle (see the top and bottom micrographs of Figure 6.19). The donor-acceptor pair (DAP) emission at 2.68 eV originated from local regions in the tangle (see the middle and bottom micrographs in Figure 6.19). The quenching of exciton emission in the vicinity of dislocations could result from, for example, the dislocation core or imperfections at the core (i.e., kinks), strain fields, and impurities or point defects around the dislocation core (Batstone and Steeds, 1985). Although exciton quenching was also observed at screw dislocations in heat-treated InP crystals (Figure 6.20), no dislocation-induced emission band was detected in this material (Hutchinson and Myhajlenko 1984; Myhajlenko *et al.,* 1984). In this case (see Figure 6.20), the high-energy peak at 1.42 eV (denoted X) is attributed to a mixture of donor-bound and free exciton transitions; the peak at 1.38 eV (denoted *e*A) is a mixture of donor-acceptor and free-bound-acceptor transitions, with associated LO-phonon replicas; and the deep transition (referred to as band *C*) is thought to be related to lattice nonstoichiometry (Myhajlenko *et al.,* 1984).

The direct correlation of the CL observations and TEM images of single dislocations in diamond have revealed luminescence at energies less than the band gap at individual dislocations (Pennycook *et al.,* 1980). No correlation of the CL with dislocation type (i.e., screw dislocation and 60° dislocation) was

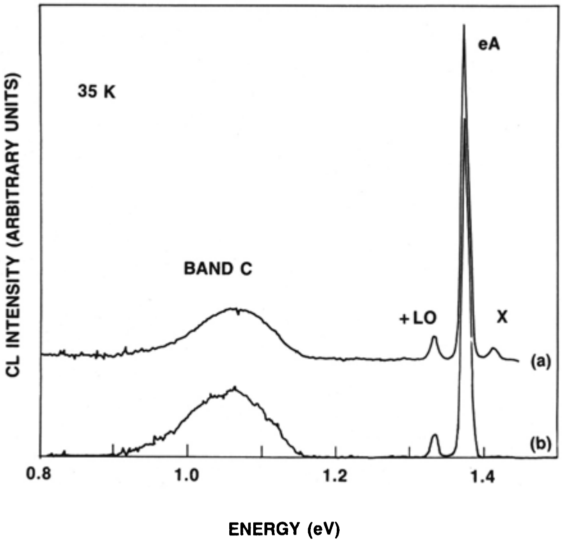

Figure 6.20. CL spectra (35 K) from bulk as-grown InP: (a) away from the dislocation; (b) at the dislocation. In the latter case, note the absence of the exciton (X) transition. (After Myhajlenko *et al.*, 1984.)

found. Cathodoluminescence variations along dislocations were also observed and explained as being due to local dissociation into partial dislocations or due to varying impurity segregation along the dislocation line (Pennycook *et al.*, 1980). In CL and polarization studies of individual dislocations in diamond (Yamamoto *et al.*, 1984), a broad [0.416-eV full-width, half-maximum (FWHM)] emission at 2.85 eV was found to be polarized along the dislocation. By eliminating several possible mechanisms, the emission was attributed to donor-acceptor pairs arranged along the dislocation core (Yamamoto *et al.*, 1984). As will be discussed in Section 7.1, CL due to dislocations has also been observed in deformed silicon at energies less than band gap (Graham *et al.*, 1987).

Recent advances in time-resolved CL measurements provide useful means for the determination of minority carrier lifetimes at and away from a dislocation (Section 6.2).

6.1.4. Transmission Cathodoluminescence Studies of Defects

A relatively new technique of transmission infrared CL has also emerged for the study of defects in semiconductors (Chin *et al.*, 1979a,b,c, 1980; Gaw and Reynolds, 1981; Cocito *et al.*, 1983). In this method, a solid-state detector is placed underneath the specimen so that the transmitted luminescence is detected. A detector may also be placed above the specimen, and in that case emission CL (ECL) is obtained. Despite the spectroscopic limitations of this transmission CL (TCL) technique, it provides a simple means for identifying defects in semiconductors, measuring the dislocation density, and it may also reveal additional defects that are beyond the range of the primary electrons (Figure 6.21). In the double-heterostructure (InP/InGaAsP/InP) sample, shown in Figure 6.21, the vertical and diagonal lines observed in the TCL image (but not visible in the secondary electron or ECL images) are probably stacking faults or dislocations at the interface between the InP layer and the InGaAsP layer (Chin *et al.*, 1979b).

6.1.5. Plastic Deformation and Dislocation Motion Studies

Cathodoluminescence microscopy can be used for studies of the influence of plastic deformation on the luminescence properties of semiconductors (Esquivel *et al.*, 1973, 1976; Davidson *et al.*, 1975) and for *in situ* studies of stress-induced motion of dislocations in semiconductors (Maeda *et al.*, 1981, 1983; Maeda and Takeuchi, 1981, 1983).

A CL study of plastically deformed GaAs was reported by Esquivel *et al.* (1973). GaAs has the sphalerite crystal structure, which exhibits polarity in the [111] directions. Consequently, there are two types of dislocations in sphalerite-structure materials. For dislocations with an edge component, the two types are described as α- and β-type dislocations. The former are those in which the atoms with dangling bonds along the edge of the extra half-plane are of the lower-val-

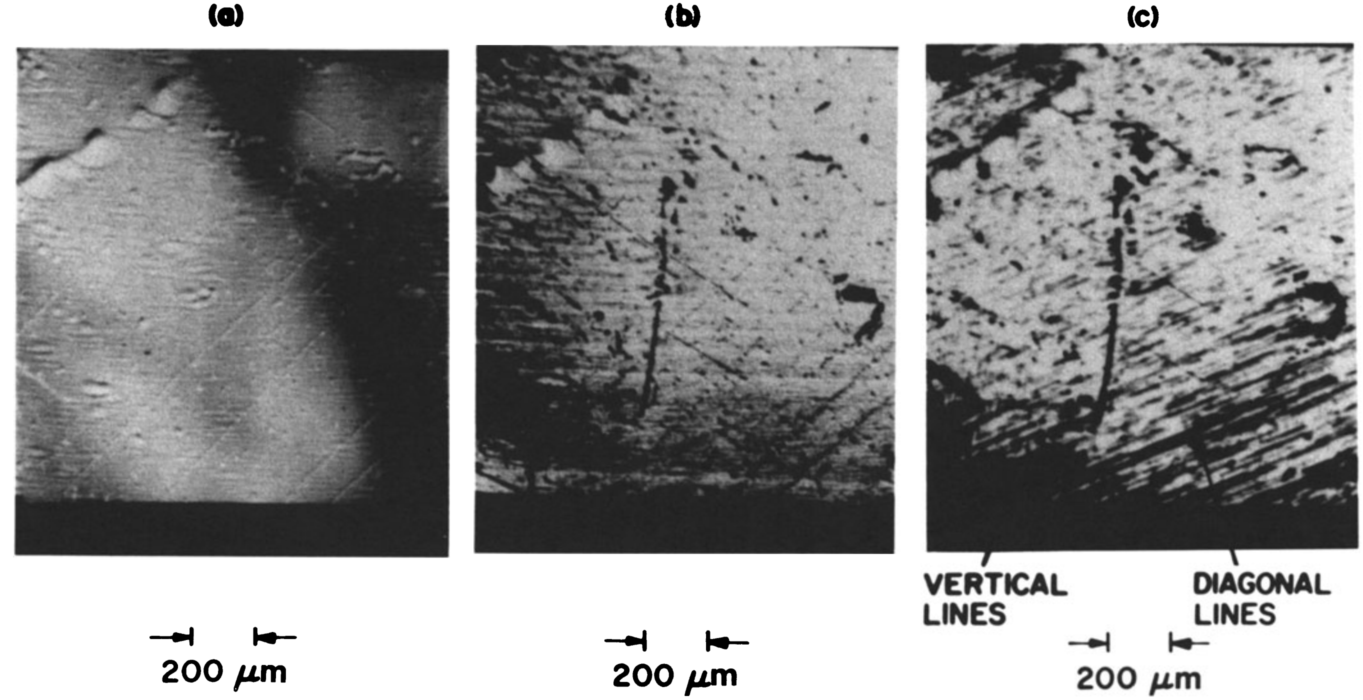

Figure 6.21. Growth lamellae, hillocks, and surface scratches in a double heterostructure (InP/InGaAsP/InP) wafer: (a) secondary electron image; (b) emission CL image of the region in (a); (c) TCL image of the region in (a). (After Chin *et al.*, 1979b.)

ence element (i.e., Ga in the present case). β-Dislocations have As atoms with dangling bonds at the core (Holt, 1962). These dislocations can be studied by bending bars of the material in two opposite senses, one of which introduces α-dislocations and the other, β-dislocations. (The α- and β-characters of the dislocations are interchanged if they belong to the glide, not the shuffle, set, so care is needed in interpreting the results.) Results obtained by Esquivel *et al.* (1973) are illustrated in Figure 6.22. The orientations used are shown in Figures 6.22a,b. Both undoped and Te-doped (10^{17} cm^{-3}) specimens were bent in both senses to radii resulting in about 5×10^6 cm^{-2} and 10^7 cm^{-2} each of α- and β-dislocations. (The initial dislocation density was about 10^3 to 10^4 cm^{-2}). Figures 6.22e,f are infrared CL micrographs revealing checkered patterns, as well as a subsurface flaw in Figure 6.22f, in the heavily deformed areas labeled 1 in Figures 6.22a,b. No such features of plastic deformation were observed in optical, transmission infrared micrographs (not shown) or in the secondary electron images of the same areas shown in Figures 6.22c,d. It was suggested that the dark dots (~3 μm in diameter), one of which is indicated by an arrow in Figure 6.22e, were related to dislocations lying on the (111) slip planes. In the specimen in Figure 6.22e, a count of these dots gave a dislocation density of 5×10^6 cm^{-2} whereas the density calculated from the radius of curvature of the bend was 8×10^6 cm^{-2}.

Löhnert and Kubalek (1983) investigated CL in plastically deformed silicon using low electron beam currents (~100 nA). They concluded that the additional features in the CL spectrum of plastically deformed Si were due to dislocation-induced radiative states in the gap.

Studies of several optoelectronic devices established that the cause of their rapid degradation during operation was fast multiplication of dislocations through their motion (Maeda *et al.*, 1983, and references therein). Quantitative measurements of the effect of electron beam irradiation on dislocation motion in III-V compounds were presented by Maeda and Takeuchi (1981, 1983) and Maeda *et al.* (1983), who explained the effect in terms of recombination-enhanced defect motion. Measurements of the dislocation velocity were performed by using CL in a scanning electron microscope equipped with a bending attachment for *in situ* observations of dislocation motion in the material. In contrast to the chemical etching technique, the CL-SEM technique proved invaluable in such studies, since it makes possible accurate and repeatable measurement of dislocation velocity on the same specimen as a function of temperature, applied stress, and irradiation intensity, which were all varied independently (Maeda and Takeuchi, 1981, 1983; Maeda *et al.*, 1983). Dislocation velocities were measured by recording sequential CL micrographs and evaluating the distance traveled by the dislocation during the application of the load (CL micrographs were recorded after significantly reducing the applied load).

An example of the dislocation motion in *n*-GaAs is shown in Figure 6.23, which is a sequential series of CL-SEM TV images of a moving dislocation glid-

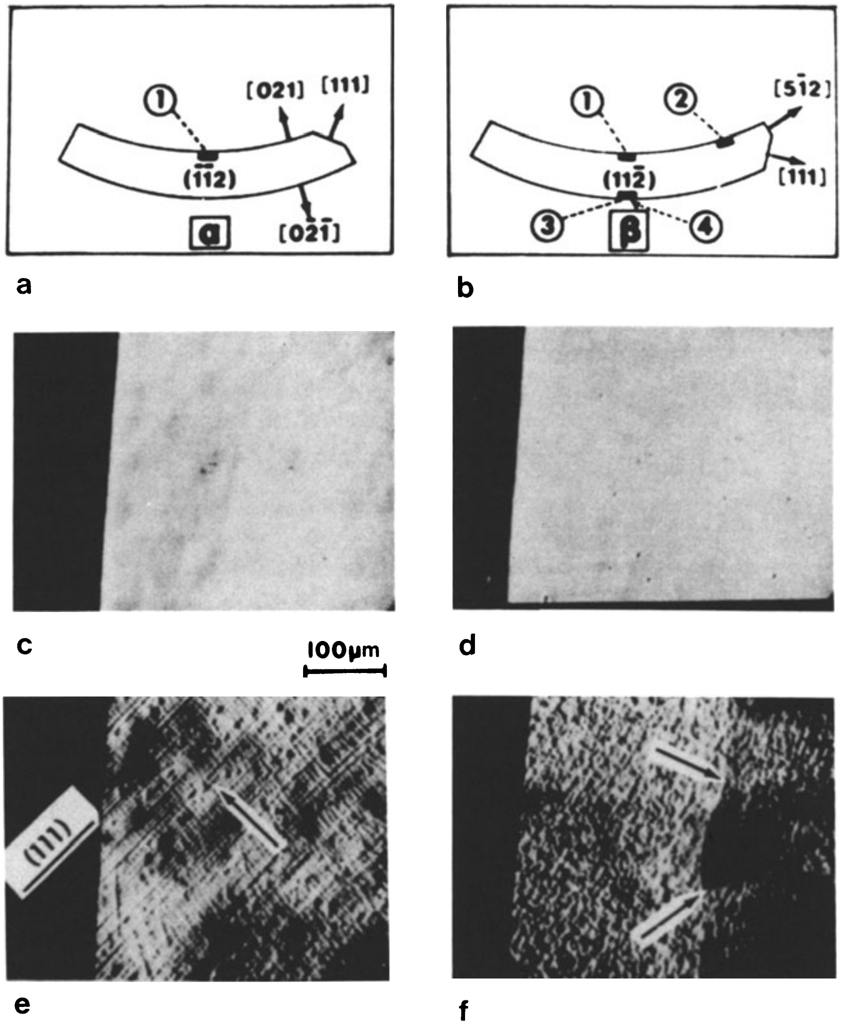

Figure 6.22. (a) and (b) are schematic diagrams of the orientations of the specimens deformed in four-probe bending in order to introduce an excess of α or of β dislocations in GaAs. Areas (1) and (2) are the areas examined. (c) and (d) are secondary electron emission micrographs of area 1 on crystals bent as in (a) and (b), respectively. (e) and (f) are infrared CL micrographs of the same area 1 as in (c) and (d), respectively. The arrow in (e) points to black dots associated with the intersection of dislocation lines with the $(\bar{1}\bar{1}2)$ surfaces. The trace of the (111) slip plane on the $(\bar{1}\bar{1}2)$ surface is also indicated. In (f) the arrows point to a subsurface flaw. (After Esquivel *et al.*, 1973.)

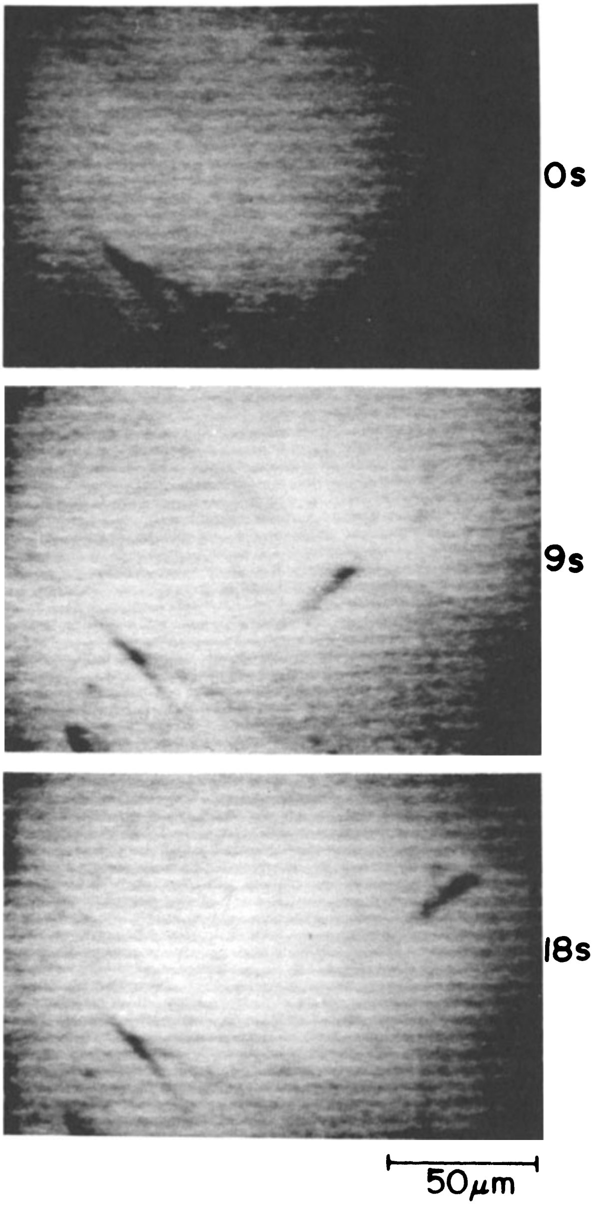

Figure 6.23. CL-SEM TV images of a moving dislocation in *n*-GaAs. (After Maeda and Takeuchi, 1983.)

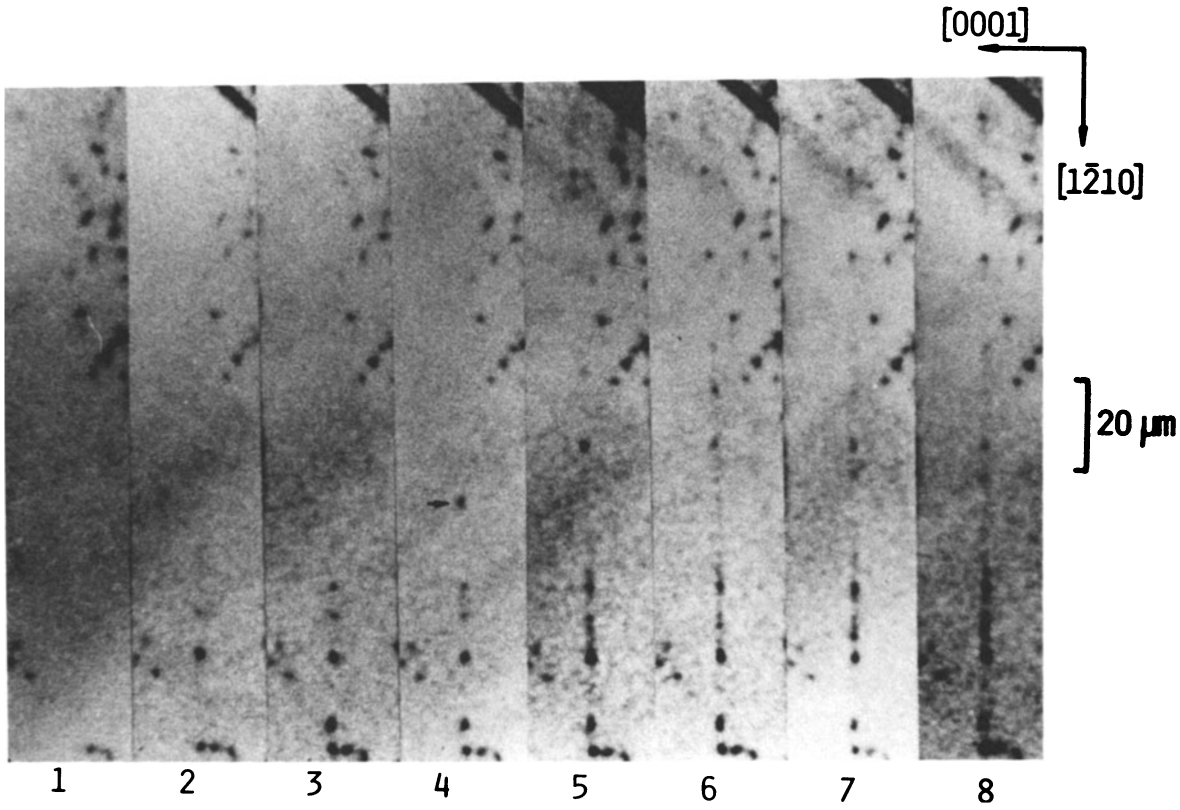

Figure 6.24. Sequential development of dark spots along a slip trace in CdS deformed at 345 K. (After Maeda *et al.*, 1981.)

ing under an applied load. The dislocation in this sequence always appears dark, indicating that nonradiative recombination occurs consistently. By referring to the results of Petroff *et al.* (1980), who found that the dislocations giving dark contrast in CL are dissociated into Schockley partials, Maeda and Takeuchi (1983) concluded that the gliding dislocations in their observations are dissociated in the moving state. Similar CL-SEM studies of dislocation motion were also performed on some II-VI compounds (Maeda *et al.*, 1981). In this case, with the application of stress, CL observations indicated an increasing density of dislocations, most of which did not change their positions (see, for example, Figure 6.24), leading to the conclusion that dislocations are immobilized following motion from the source with a high velocity (Maeda *et al*, 1981).

6.2. Time-Resolved Cathodoluminescence

In time-resolved CL, a CL decay time is measured by employing a beam-blanking system and a fast detector (for a review, see Hastenrath and Kubalek, 1982). If the decay of the luminescence intensity $L(t)$ is exponential, i.e.,

$$L(t) = L(0)\exp(-t/\tau) \tag{6.7}$$

a CL decay time can be obtained that is affected by surface recombination. The measured values are effective lifetimes (Shockley, 1950):

$$1/\tau_{\text{eff}} = 1/\tau_{\text{bulk}} + 1/\tau_{\text{surf}} \tag{6.8}$$

Hence, observations of the variation of a CL decay time as a function of electron beam energy (and thus electron penetration range) make possible calculations of both the minority carrier lifetime and the surface recombination velocity. Hastenrath and Kubalek (1982) analyzed such CL measurements to derive the surface recombination velocity S from $S = L_p(\tau_{\text{eff}}^{-1} - \tau_0^{-1})$, where L_p is the hole diffusion length, and τ_{eff} and τ_0 are the effective lifetime and bulk lifetime, respectively. They found this value of S was well within the typical range of values of surface recombination velocity for GaAs.

A theoretical analysis presented by Boulou and Bois (1977) considered the influence of various excitation factors and materials parameters on CL decay. They used the difference in the shape of the decay with short and long excitation pulses for the determination of both the surface recombination velocity and bulk minority carrier lifetime in GaP. Jakubowicz (1985b) presented a theoretical analysis of transient CL for a focused electron beam with the conclusion that the initial part of the decay depends on the surface recombination velocity, the excitation range, and the absorption coefficient, whereas at longer times, the near-exponential decay is controlled by the bulk lifetime.

Cathodoluminescence decay measurements can be utilized for carrier life-

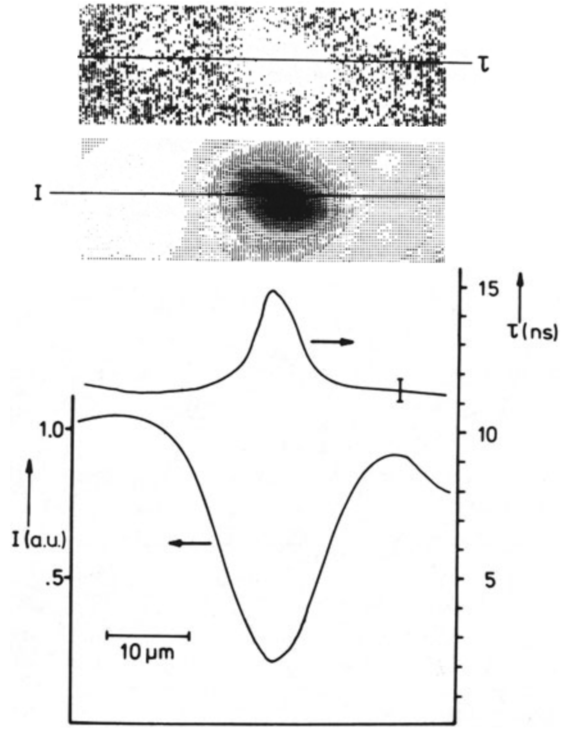

Figure 6.25. Lifetime τ and intensity *I* values measured round a dislocation and displayed as maps and line scans at 50 K for GaAs doped with Se. (After Steckenborn *et al.*, 1981a.)

time mapping, as shown, for example, in Figure 6.25 (Steckenborn, 1980; Steckenborn *et al.*, 1981a,b). This can be achieved by using a microprocessor-controlled boxcar integrator system for data acquisition (Steckenborn, 1980; Steckenborn *et al.*, 1981a,b) or computer-controlled CL acquisition with an optical multichannel analyzer (Hastenrath *et al.*, 1981). It is somewhat puzzling that in the case of GaAs:Se (4×10^{16} cm^{-3} doping level) the lifetime at the dislocation increases while CL intensity decreases (see Figure 6.25; Steckenborn *et al.*, 1981a,b). A contradictory result was obtained in GaAs:Se (1.6×10^{18} cm^{-3} doping level) by Hastenrath and Kubalek (1982), who observed a decrease of both the lifetime and CL intensity at the dislocation. The observations of Steckenborn *et al.* (1981a,b), shown in Figure 6.25, may be explained by assuming that in their case τ_{rr} increases near the dislocation and $\tau_{nr} \approx$ constant [see equations (3.25) and (3.26)].

Cathodoluminescence decay analysis was also applied recently to Si (Cumberbatch *et al.*, 1981; Davidson *et al.*, 1981; Myhajlenko *et al.*, 1983a,b) to measure the carrier lifetimes at and away from grain boundaries in that material.

One such observation in Si, shown in Figure 6.26, is of particular interest. In this ribbon silicon, minority carrier lifetimes derived from CL decay rates at various grain boundaries (Figure 6.26) are significantly different, indicating that some boundaries are electrically more active than others (Myhajlenko *et al.*, 1983b). Time-resolved luminescence in these experiments was obtained by using the delayed coincidence technique, which is especially useful in materials with weak luminescence (Myhajlenko and Ke, 1984).

In general, the minority carrier lifetime measured near a dislocation can be described as

$$\frac{1}{\tau_{\text{eff}}} = \frac{1}{\tau_{\text{bulk}}} + \frac{1}{\tau_{\text{surf}}} + \frac{1}{\tau_d} \tag{6.9}$$

where τ_d corresponds to recombination at dislocations. Examples of the determination of the minority carrier lifetime at single dislocations in GaP using CL decay measurements were provided by Rasul and Davidson (1977a,b), Davidson and Rasul (1977), and Dimitriadis *et al.* (1978). Figure 6.27 shows examples of CL decays obtained away from a dislocation with electron beam voltages (V_b) of 15 and 25 kV, and obtained at the dislocation with V_b = 25 kV. It is evident that, although the CL intensity is substantially reduced with decreasing V_b due to surface recombination, the minority carrier lifetime measured away from a disloca-

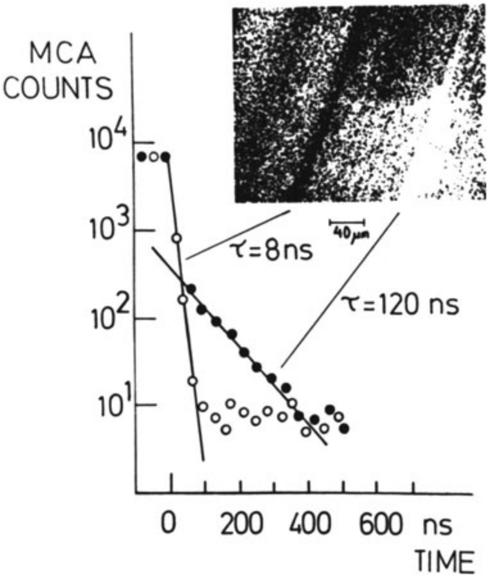

Figure 6.26. Minority carrier lifetimes derived from CL decay rates in ribbon silicon at grain boundaries with different electrical activities. (After Myhajlenko *et al.*, 1983b.)

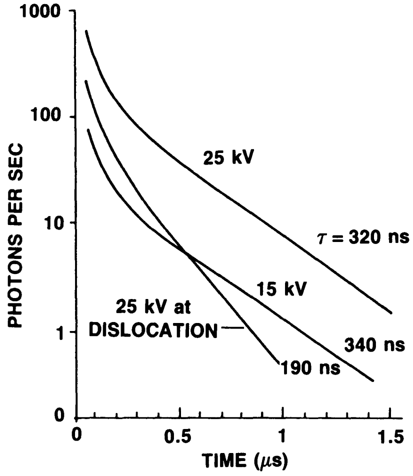

Figure 6.27. Minority carrier lifetimes derived from CL decay rates in GaP away from a dislocation for electron beam voltages of 15 and 25 kV, and at a dislocation for beam voltage of 25 kV. (After Rasul and Davidson, 1977b.)

tion has remained nearly the same. A significant decrease in the carrier lifetime, however, was observed at the dislocation (Rasul and Davidson, 1977b).

The value of this technique for the study of the kinetics of the recombination of nonequilibrium carriers in GaAs and GaAs quantum wells was demonstrated by Bimberg *et al.* (1985a,b, 1986). Their results illustrate the power of time-resolved CL in elucidating the distribution of competing recombination channels and determining such important parameters as the charge carrier capture cross sections of ionized donors and acceptors. The lifetimes of nonequilibrium carriers in their different band and impurity states were analyzed, and capture cross sections were subsequently derived from the lifetimes. Thus, cross sections of conduction-band-acceptor transitions, and of hole capture by ionized acceptors (carbon and tin) and of electron capture by ionized donors were derived. During the experiments, CL spectra and transients were found to depend strongly on pulse lengths up to 1 μsec. The capture cross sections for electrons and holes of ionized donors and acceptors were derived from these luminescence onset results. Further analysis of the decay from a metastable excited state as a function of excitation intensity, temperature, and doping, using pulse lengths of ~ 1 μsec, provided additional information for the interpretation of recombination kinetics. The excitation-pulse-length dependence of the CL spectra in both *n*- and *p*-type GaAs is shown in Figure 6.28. Luminescence peaks from the free exciton X, from the donor- and acceptor-bound excitons (D^0X, D^+X, A^0X), from the acceptor-tin-bound exciton (Sn^0X), from free-electron-acceptor recombination (eA^0), and from donor-acceptor pair recombination (D^0A^0) are present. It is evident from this figure that the spectral distribution of the emission depends on the length of the exciting pulse. (No analogous observations were reported in time-resolved PL experiments using pulsed lasers, since the width of a laser pulse cannot be adjusted independently of its rise and decay time. As pointed out by Bimberg *et al.* (1985a), the failure to consider the effect of the shape of the exciting laser pulse on quantities derived from luminescence transients may lead to erroneous conclusions.)

Figure 6.28 shows that long pulses excite more recombination processes than do short excitation pulses. For example, 2-nsec excitation of the *n*-GaAs does not produce features related to the presence of neutral acceptors, and in *p*-GaAs it does not produce features related to the presence of neutral donors. These results indicate that, for the specific doping levels used, the capture of free minority carriers into bound states requires a longer time than does excitation (Bimberg *et al.*, 1985a). The dependence of the luminescence spectra on excitation pulse length can be used to derive the capture times of free holes into acceptor ground states (Bimberg *et al.*, 1985a). This can be achieved by fitting the experimental data on the time dependence of the luminescence intensity (Figure 6.29) to an analytical expression containing the hole-capture time (Bimberg *et al.*, 1985a). Subsequently, using the relationship between the carrier lifetime τ and the capture cross section for free carriers, σ, i.e., $\tau = (N\sigma V_{\text{th}})^{-1}$, one can derive the hole capture cross section of acceptors. Thus, Bimberg *et al.* (1985a) obtained the values of the capture cross section of Sn and C. Using this technique, Bimberg *et al.* (1985a) were able to analyze in detail the kinetics of the

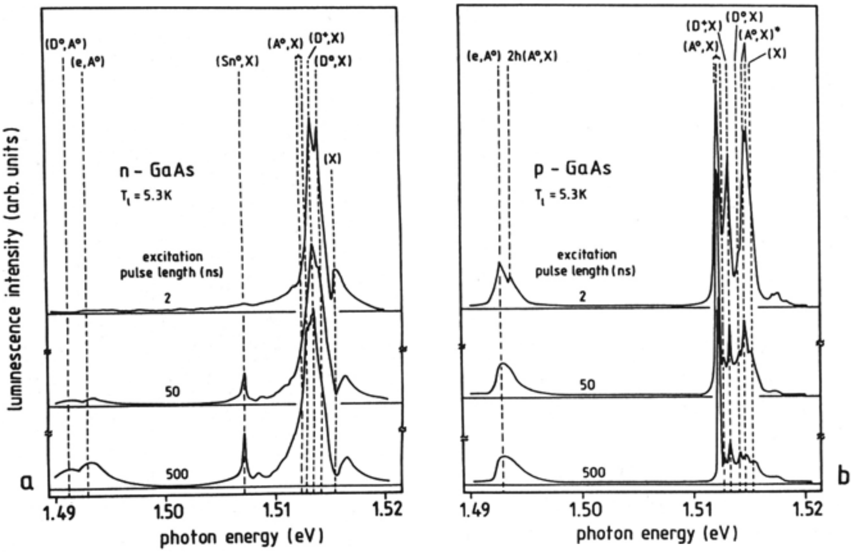

Figure 6.28. CL spectra of (a) highly Sn-doped *n*-type GaAs, and (b) high-purity *p*-type GaAs. The value of the excitation pulse length (2, 50, or 500 nsec) is indicated for each spectrum. (After Bimberg *et al.*, 1985a.)

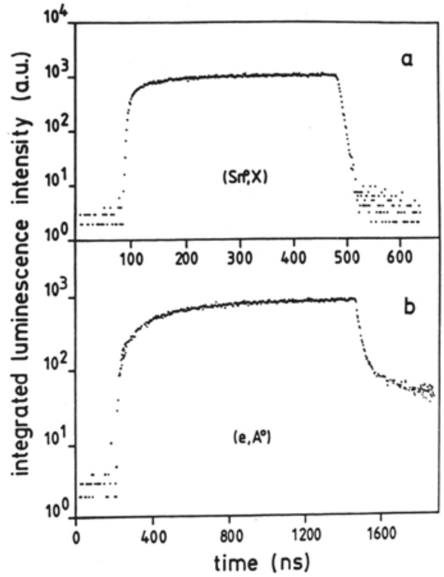

Figure 6.29. Time dependence of luminescence intensity of the (a) (Sn^0,X) emission in Sn-doped GaAs and (b) (e,A^0) luminescence in a nominally undoped n-type sample. A^0 is the effective-mass acceptor carbon. (After Bimberg *et al.*, 1985a.)

capture and recombination processes of nonequilibrium carriers in a variety of n- and p-type GaAs samples.

6.3. Depth-Resolved Cathodoluminescence

Depth-resolved information obtained from the CL analysis of inorganic solids is one of the most attractive features of this technique as compared with PL analysis. Nondestructive depth resolution in CL analysis is obtained by varying the range of electron penetration (which depends on the electron beam energy; see Chapter 4) in order to excite luminescence from different depths of the material. This technique is particularly useful for studying ion-implanted materials. In this case, since the penetration depth of ions with energies between about 50 and 300 keV are comparable with the penetration range of electrons with energies between about 1 and 20 keV, the analyses can be performed by using commercial SEMs or relatively simple dedicated systems for depth-resolved studies. This technique provides information on the redistribution of impurities and lattice damage defects during annealing of ion-implanted samples. This, in conjunction with the (lateral) spatial resolution available in a SEM, in principle, allows three-dimensional mapping of impurities and defects in the material. Such studies are often performed by using a constant total electron-hole pair injection rate (i.e., constant electron beam power I_bV_b) to obtain greater signals from shallower depths at low energies (Norris *et al.*, 1973, 1977; Norris and Barnes, 1980). In some cases, to maintain a constant level of excitation at the surface of the sample and keep the relative peak of the electron-hole pair density at a constant level (compare with Figure 4.4, which represents the relative density of electron-hole pairs for a constant electron-beam current I_b), we keep the ratio $I_b V_b / R_e$ constant in depth-resolved CL measurements. This method is useful for comparing electron-hole pair profiles with calculated profiles of implanted ion concentration as a function of penetration depth (Norris *et al.*, 1973; Pierce and Hengehold, 1976).

Caution must be exercised during depth-resolved CL measurements, since a strong dependence of the CL spectra on injection level for a constant excitation depth may be expected (Norris *et al.*, 1973). In GaAs, for example, CL measurements indicated that at high injection levels the band-to-band emission was dominant, but at low injection levels it was substantially quenched due to the competition between a small density of impurity-related recombination centers and those corresponding to the edge emission (Norris *et al.*, 1973). However, careful analysis of both the depth-resolved and injection-level dependencies of the CL spectra should allow one to determine depth distributions of the luminescence centers (Norris *et al.*, 1973).

Most depth-resolved studies can be performed in relatively simple high-vacuum systems equipped with an electron gun. Although these nonscanning systems are unable to provide a mapping capability, they are, nevertheless, powerful tools for analyses of ion-implantation-induced defects and metal-semiconductor interfaces. These CL studies demonstrated, for example, that implantation-induced damage in the material may occur beyond the projected ion range of implants. This finding has important implications for the fabrication of ion-implanted devices. Such a case is illustrated in Figure 6.30, which presents the depth-resolved CL spectra of a 100-keV Xe^+-implanted In-doped CdTe sample that was etched to a depth of about 1400 Å. The presence of the implantation-induced 1.2-eV band in this case indicates that the defects associated with that band are present at depths of several thousand angstroms beyond the projected ion range (Norris *et al.*, 1977). Also note that the appearance of the implantation-induced band at 1.2 eV is accompanied by quenching of the "native" luminescence in CdTe at about 1.4 eV. (This native luminescence is believed to be due to transitions involving defect-impurity complexes.) These results were explained as being primarily due to Te vacancies, which are responsible for the anomalously deep introduction of both the 1.2-eV centers and those that cause quenching of the native luminescence. Similar anomalous (postrange) implantation-induced introductions of defects were also observed in other compound semiconductors. It was suggested that this process may be due to the interaction of ionization with the dynamic stresses or phonon flux effects during ion implantation (Norris *et al.*, 1977; Norris and Barnes, 1980).

Brillson *et al.* (1985) and Viturro *et al.* (1986), employing the ultrahigh-vacuum CL system described in Chapter 5, used CL depth-resolved analysis in characterizing subsurface metal-semiconductor interfaces (see also Brillson,

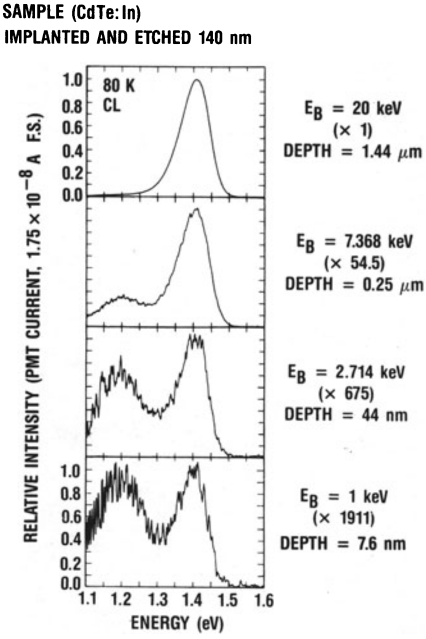

Figure 6.30. CL spectra (at 80 K) of 100-keV Xe^+-implanted and etched In-doped CdTe as a function of the electron beam energy. Note that the implantation-induced 1.2-eV band appears in this sample, even though it was etched to a depth of about 1400 Å, which indicates its presence at depths beyond the projected ion range of 1100 Å. (After Norris *et al.*, 1977.)

1985; Viturro *et al.*, 1987a,b; Brillson and Viturro, 1988; Viturro *et al.*, 1988a). For example, Figure 6.31 shows CL spectra of UHV-cleaved CdS before and after 50 Å Cu deposition and pulsed laser annealing (Brillson *et al.*, 1985). The deposition of Cu produces only a weak peak at about 1.27 eV, in addition to band-edge emission at 2.42 eV. Pulsed laser annealing with an energy density of 0.1 J/cm^2 leads to an intense (relative to band-edge emission) peak at 1.28 eV, which can be related to Cu_2S compound formation (Brillson *et al.*, 1985). In contrast to the Cu case, similar experiments with Al layers indicated the formation of bulk defects due to lattice damage (Brillson *et al.*, 1985). These results indicate that this CL technique can be effectively used in the analysis of chemical interactions at metal-semiconductor interfaces that produce new interfacial phases.

Viturro *et al.* (1986) investigated the formation and evolution of interface states for various metals deposited on InP and GaAs. CL spectra in these studies reveal the energy levels that are localized at the interface. The energy distributions of the interface states were found to depend on the particular metal, the semiconductor, and the semiconductor's surface morphology. For example, Figure 6.32 illustrates the changes in the CL spectra of InP with the deposition of various metals. In these cases, the CL spectrum of clean InP exhibits one peak at 1.35 eV corresponding to near-band-gap transitions. Deposition of Au on *n*-InP (Figure 6.32a), which leads to new peaks at 0.8 and 0.96 eV, reduces the relative CL intensity at higher energies with increasing thickness of the deposited layer.

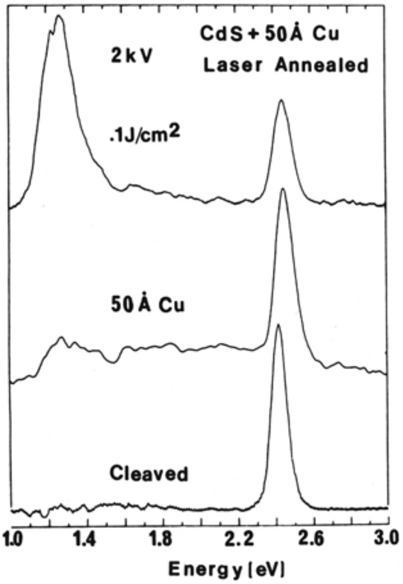

Figure 6.31. CL spectra of UHV-cleaved CdS before and after *in situ* deposition of 50 Å of Cu, and after *in situ* laser annealing with an energy density of 0.1 J/cm^2. The electron beam voltage is 2 kV. (After Brillson *et al.*, 1985.)

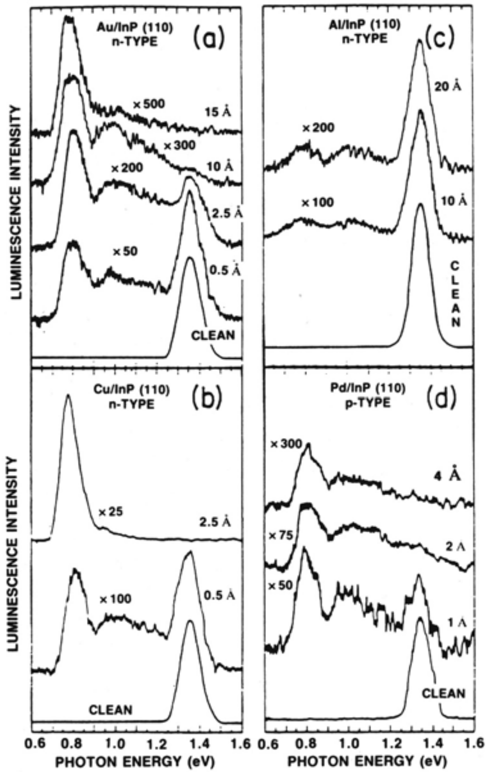

Figure 6.32. CL spectra of (a) Au, (b) Cu, and (c) Al on clean, mirrorlike *n*-InP (110), and (d) Pd on clean, mirrorlike *p*-InP (110) as a function of metal layer thickness. (After Viturro *et al.*, 1986.)

In comparison with Au, interface states due to Cu deposition on *n*-InP (Figure 6.32b) evolve faster with the layer thickness. Deposition of Al on *n*-InP (Figure 6.32c), on the other hand, does not cause a significant relative reduction in the near-band-gap emission. The low energy emission is again observed for Pd deposition on *p*-InP (Figure 6.32d), but the near-band-gap emission is reduced. The metal-deposition-induced reduction in the near-band-gap emission in all these cases can in part be due to electron beam attenuation by the metal layer and the formation of a surface dead layer. Increasing band bending, which depends on the particular metal, and the widening of the surface space-charge region reduces bulk radiative recombination (Wittry and Kyser, 1967). The changes in the near-band-gap CL intensity were found to correlate with the metal-deposition-induced Fermi-level movement measured by photoemission. This explains the relatively strong reduction in near-band-gap emission due to the deposition of Au, Cu, and Pd, which cause large Fermi-level movement and correspondingly large band bending. Aluminum deposition, on the other hand, causes smaller band bending and a smaller reduction in the near-band-gap emission. The observed metal-deposition-induced emission peaks were thought to be due to metal indiffusion and semiconductor outdiffusion, leading to the formation of defect complexes that are responsible for the interface states. The observed CL results were also found to be consistent with the Schottky-barrier heights of different metals on these semiconductors (Viturro *et al.* 1986). Thus, low-energy CL spectroscopy studies can reveal metal-deposition-induced interface states that are distributed over a wide energy range. The results obtained by Viturro *et al.* (1986) support the models of rectification that involve charge transfer to discrete levels due to chemical interaction between semiconductor and metal. Their results contradict models that predict no significant differences for different metals and that involve no discrete levels in the band gap (Viturro *et al.*, 1986; Brillson and Viturro, 1988).

More examples of depth-resolved CL studies will be presented in the following chapter.

6.4. Microcharacterization of Electronic Properties

Cathodoluminescence microcharacterization of semiconductors in an electron microscope constitutes the determination of various electronic properties with a high spatial resolution. Several types of CL analysis can be employed to derive semiconductor properties. These will be outlined next.

6.4.1. Measurement of the Carrier Concentration

The carrier concentration in direct-gap semiconductors (such as GaAs) can be derived by two CL methods. One applies when the radiative recombination rate is proportional to the carrier concentration. Then, if the nonradiative recom-

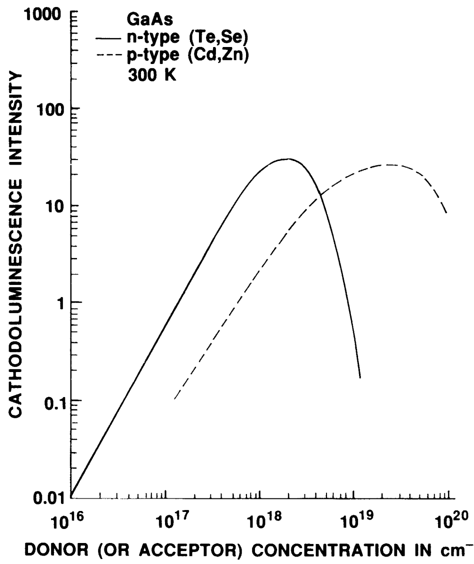

Figure 6.33. Dependence of CL intensity on doping in GaAs. (After Cusano, 1964.)

bination rate remains constant (or does not change significantly) with doping, the CL intensity will vary directly with doping. The variation in GaAs (Figure 6.33), reported by Cusano (1964), demonstrated that in the doping range between about 10^{17} and 10^{18} cm^{-3} the luminescence intensity increases linearly with doping. Thus, in this range the doping concentration of an unknown sample can be derived from calibrated CL measurements.

The second method of carrier concentration measurement is based on work of Casey and Kaiser (1967), who studied the CL emission spectrum of *n*-type GaAs. They demonstrated that the band-shape parameters, i.e., the slope of the low-energy tail of the CL emission band, the peak energy, and the half-width of the CL band (Figure 6.34) vary with doping as shown in Figures 6.35, 6.36, and 6.37. Thus, measurement of these parameters can be used to determine the doping concentration. This method is particularly sensitive to doping concentrations greater than 10^{18} cm^{-3}. The luminescence intensity as a function of doping in *n*-type GaAs (Figure 6.33) varies linearly up to about 10^{18} cm^{-3}, so the band-shape parameter method is especially valuable for doping concentrations greater than 10^{18} cm^{-3}. Electrical measurements provide the number of free charge carriers, which in *n*-type material is given by the density of donors minus the density of acceptors. If there is a significant density of acceptors, the semiconductor is (partially) compensated. Both donors and acceptors affect CL, so the emission band for compensated material has a shape different from the uncompensated material of the same carrier density shown in Figure 6.34. Casey and Kaiser

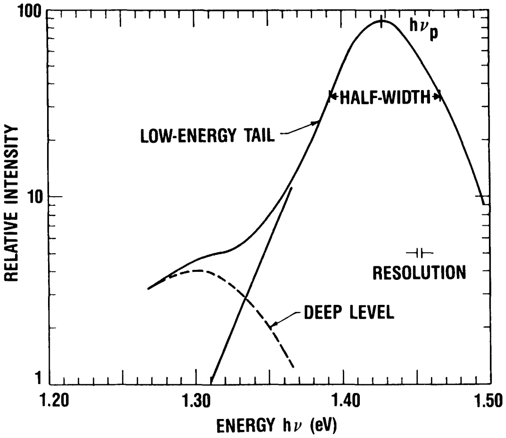

Figure 6.34. Typical CL emission spectrum for *n*-type GaAs (carrier concentration 1.75×10^{18} cm^{-3}). The electron beam voltage was 40 kV, and the electron beam current was 0.3 μA. (After Casey and Kaiser, 1967.)

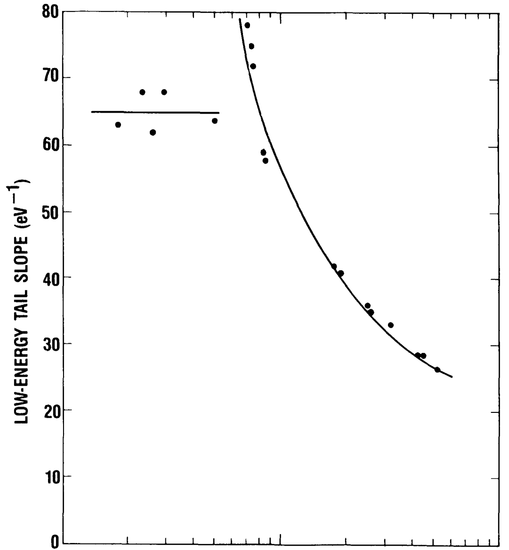

Figure 6.35. The dependence of the slope of the low-energy tail of the CL emission band, defined in Figure 6.34, on the free-carrier concentration in *n*-type GaAs. (After Casey and Kaiser, 1967.)

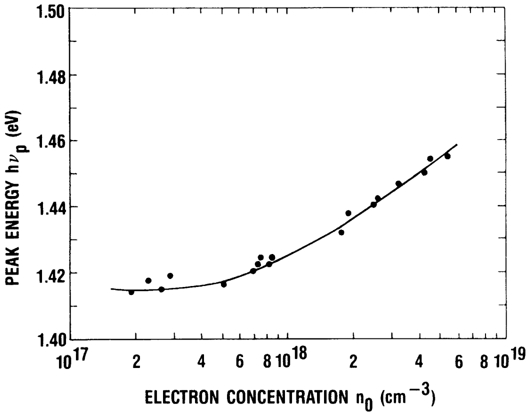

Figure 6.36. The dependence of the CL emission peak energy on the free-carrier concentration in *n*-type GaAs. (After Casey and Kaiser, 1967.)

(1967) demonstrated that in compensated samples, the peak position is too low for the value of the free-electron concentration indicated by the half-width, and the low-energy-tail slope is much less than that corresponding to the half-width value of the free-electron concentration. Thus, the band-shape parameter method also provides means to detect the presence of acceptors in *n*-type GaAs. As noted

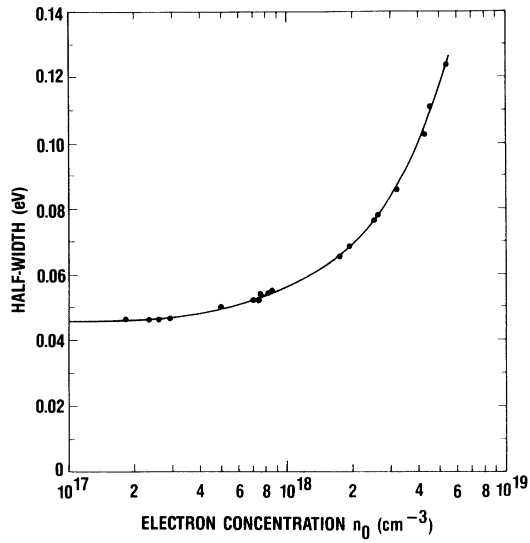

Figure 6.37. The dependence of the half-width of the CL band (see Figure 6.34) on the free-carrier concentration in *n*-type GaAs. (After Casey and Kaiser, 1967.)

by Casey and Kaiser (1967), of the three spectral band-shape parameters, the low-energy-tail slope is the least reliable because of the distortion of the low-energy tail caused by the presence of deep levels (Figure 6.34). Also, for lightly doped material, errors can be introduced in measuring the slopes, which are steep. Casey and Kaiser (1967) noted that this method should be also applicable to *p*-type GaAs. However, because of the larger effective mass of holes, the concentration at which the spectral band-shape begins to depend on the acceptor concentration would be about an order of magnitude higher (Casey and Kaiser, 1967). The latter was demonstrated by Pankove (1966) to be true for *p*-type GaAs (Zn-doped with carrier concentration between 3×10^{16} and 1.2×10^{20} cm^{-3}).

Gatos *et al.* (1981) demonstrated in *p*-type InP that the half-width of the CL emission band can be used for the determination of the carrier concentration and its inhomogeneities between about 10^{17} and 10^{19} cm^{-3}.

6.4.2. Measurement of the Minority Carrier Diffusion Length

As outlined in Section 4.4, the dependence of the CL intensity on the electron beam voltage (Wittry and Kyser, 1966, 1967; Rao-Sahib and Wittry, 1969) can be used to derive values of the diffusion length L and the reduced surface recombination velocity S. As mentioned in Section 6.1, Löhnert and Kubalek (1983) suggested a method of evaluating the minority carrier diffusion length from CL line scans across localized nonradiative defects. This is possible, since the exponential decay constant of the CL contrast with distance from the dislocation is linked to the minority carrier diffusion length.

6.4.3. Measurement of the Minority Carrier Lifetime

The minority carrier lifetime can be determined from CL decay time measurements by employing electron beam blanking and a fast detector. In general, the measured values are effective lifetimes. Both the minority carrier lifetime and the surface recombination velocity can be derived from measurements of the CL decay time as a function of electron beam energy. Time-resolved CL techniques and typical examples of measurements of carrier lifetimes at and away from defects in various materials were described in Section 6.2.

6.4.4. Measurement of CL Spectra for the Analysis of Luminescence Centers, the Composition, and the Sample Temperature

Cathodoluminescence spectroscopy can be used for the analysis of point defects (and their complexes) in semiconductors. An example of such a study was provided by Wakefield *et al.* (1984b), who observed in epitaxial InP an emission line at 1.359 eV together with many phonon replicas (Figure 6.38 and Table 6.1). This spectrum was found in epitaxial InP grown by both MBE and MOCVD (metal-organic chemical vapor deposition) under growth conditions that give rise to phosphorus deficiency in the epilayers (Wakefield *et al.*, 1984b). Duncan *et al.* (1984) reported a closely corresponding PL spectral line series in bulk *n*-type LEC InP that had been heated in a vacuum at 900°C for 6 h. Using optical measurement techniques, Duncan *et al.* (1984) showed that the line at 1.36 eV is due to the recombination of an exciton bound to a deep neutral donor (D^0X). This emission has been observed only in phosphorus-deficient InP, and it was suggested therefore that the 1.36 eV emission is related to a complex involving a phosphorus vacancy (Wakefield *et al.*, 1984b). Myhajlenko (1984) measured the CL spectrum (at 45 K) of LEC InP annealed at 750°C for 15 min. In addition to a near-band-edge line due to excitons bound to shallow impurities and a DAP line with LO-phonon replicas, a deep-level band at 1.06 eV was observed and ascribed to a phosphorus vacancy complex (Myhajlenko, 1984).

In indirect-gap materials (such as GaP), edge emission is weak since phonon participation is required. Luminescence is enhanced by doping such materials with luminescent centers. In GaP these are, for example, Zn-O donor-acceptor pairs or N isoelectronic traps. Spatial variations in nonradiative recombination due to defects make it difficult to measure dopant concentrations from luminescence intensity. The preferred method of measurement in this case is that of variations in the luminescence spectrum with dopant concentration. For example, in N-doped GaP, the luminescence peak photon energy gradually shifts with N concentration (Davidson, 1977). Furthermore, the ratio of the intensities of certain peaks in the spectrum varies significantly with variations in N concentration. Thus, these features of the CL spectrum can be used to determine N concentration in GaP (Rasul and Davidson, 1977a).

In ternary III-V compounds the band gap may vary quantitatively and from direct to indirect as a function of composition. The composition of such ternary

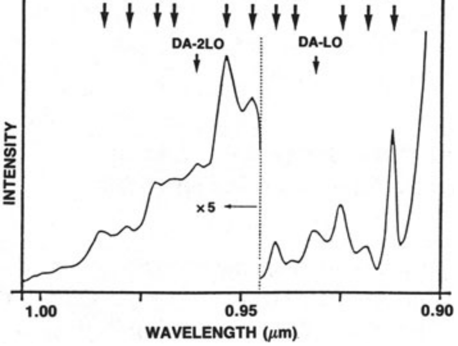

Figure 6.38. Liquid helium temperature CL spectrum of epitaxial InP (grown at 600°C by MOCVD) showing a series of phonon replicas of a line at 1.359 eV. For the identification of the emission lines see Table 6.1. (After Wakefield *et al.*, 1984b.)

Table 6.1. Observed Lines in a Liquid Helium CL Spectrum of InP*

Line	Energy (eV)	Assignment
	1.376	*D-A* pair (Zn)
A	1.359	$D^{\circ}X$
B	1.350	$D^{\circ}X$-TA
C	1.340	$D^{\circ}X$-LA
	1.331	*D-A* pair-LO
D	1.322	$D^{\circ}X$-TO
E	1.317	$D^{\circ}X$-LO
		$D^{\circ}X$-Loc
F	1.308	$D^{\circ}X$-TA-Loc
G	1.299	$D^{\circ}X$-LA-Loc
	1.290	*D-A* pair-2LO
H	1.282	$D^{\circ}X$-TO-Loc
I	1.276	$D^{\circ}X$-LO-Loc
		$D^{\circ}X$-2Loc
J	1.268	$D^{\circ}X$-TA-2Loc
K	1.259	$D^{\circ}X$-LA-2Loc

*After Wakefield *et al.*, 1984b. Phonon designation: TA, transverse acoustic; LA, longitudinal acoustic; TO, transverse optic; LO, longitudinal optic; Loc, local mode. Symbols of lines are as in Figure 6.38.

compounds can be derived from measurements of the peak position of the fundamental (intrinsic) band in the CL spectrum, which depends on the composition. For example, Marciniak and Wittry (1975) reported observations of CL in $GaAs_{1-x}P_x$ alloys. From the variation of the peak energy of the CL intensity maximum with x, they determined the crossover composition ($x \approx 0.51$) for direct and indirect transitions in these alloys (Figure 6.39). In luminescent devices, the composition x does not exceed the crossover value since the luminescence efficiency in the indirect-gap material is significantly reduced. This method can also be used to determine the composition x of $Ga_xAl_{1-x}As$ layers in heterojunction systems containing multiple epitaxial layers of GaAs and $Ga_xAl_{1-x}As$ with carefully selected x and n- and p-type doping. Such layers, grown on GaAs substrates, are used in GaAs/$Ga_xAl_{1-x}As$ double-heterostructure laser diodes. The presence of multiple layers, each 1 μm or less in thickness, makes it difficult to determine the composition by other analytical techniques. On the other hand, the CL emission spectra of the GaAs and $Ga_xAl_{1-x}As$ layers consist of well-separated bands at room temperature. Thus, the measurement of the position of the CL emission peak, which depends on x, makes it possible to derive the composition and its possible variations (Steyn *et al.*, 1976). This method can also be applied to the analysis of graded layers in $GaAs_{1-x}P_x$ devices grown on GaAs substrate (Davidson, 1977; Davidson and Rasul, 1977). The CL contrast due to

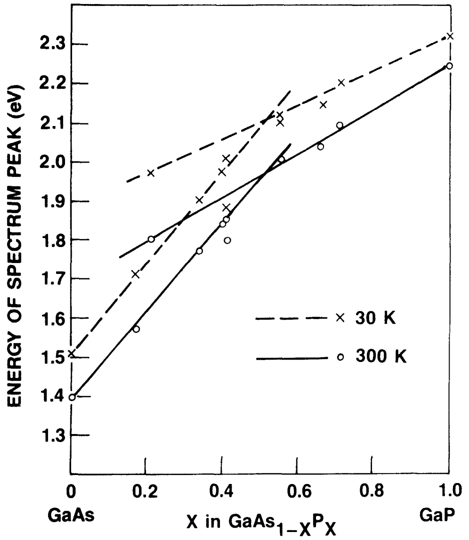

Figure 6.39. Peak energy of the intrinsic CL spectral band as a function of crystal composition in $GaAs_{1-x}P_x$. The data were taken at 30 and 300 K with an electron beam voltage of 50 kV. (After Marciniak and Wittry, 1975.)

local variations in alloy composition of $Al_xGa_{1-x}As$ layers grown on GaAs was explained by Levin and Ladany (1978) as being due to the changes in the band structure with x.

As outlined in Section 3.6, the band structures of solids in general are strongly dependent on temperature. In most materials, the band gap decreases with increasing temperature (Figure 3.14), so CL intrinsic emission peaks are expected to shift to lower energies. Thus, this property of the CL emission can be used to measure operating temperatures in various regions of devices. A demonstration of this method for a GaAs Gunn diode was provided by Davidson and Vaidya (1977). In principle, CL intensity, which is strongly dependent on temperature (see Section 3.6), can also be used to determine the device operating temperature. However, it should be kept in mind that CL intensity measurements are more sensitive to the stability of the system, contamination of the specimen, and various external perturbations.

It is possible to investigate energy levels deep in the band gap by using infrared to modulate CL (Lin and Wittry, 1976). The energy levels are deduced from the wavelength dependence of the modulation. The variations in the CL are caused mainly by changes in recombination mechanisms due to the infrared excitation of carriers from either the valence band to the deep levels or the deep levels to the conduction band. In addition to these processes in the bulk of the material, the nonradiative surface recombination rate and the recombination rates via the centers in the space-charge region will also be affected by changes (due to illumination) in the surface potential (Lin and Wittry, 1976). Examples of the IR-induced modulation of CL intensity in Cr-doped GaAs and undoped GaAs are presented in Figures 6.40 and 6.41, respectively. Lin and Wittry (1976) proposed that the IR-induced modulation of the band-edge CL is caused by changes in the rates of recombination via intermediate levels in the band gap. For the Cr-doped GaAs (Figure 6.40) they assumed the presence of two acceptor centers at $E_{t1} = E_c - 0.77$ eV (fast recombination centers) and $E_{t2} = E_c - 0.48$ eV (slow recombination centers). The value of E_{t2} was obtained from the peak in the spectrum at 1.02 eV, although it was also considered that the peak at ΔI_c may actually lie at higher photon energies than $E_c - E_{t2}$. Lin and Wittry (1976) proposed that the E_{t1} center had a larger electron capture cross section than that of the E_{t2} center, and vice versa for the hole capture cross section. During the excitation, the E_{t1} centers are mostly filled with electrons and the E_{t2} centers are mostly empty. The 0.77-eV threshold was attributed to the onset of infrared excitation of electrons from the E_{t1} level to the conduction band, leading to an increase of excess electron density Δn and decrease of recombination via this level. When the energy of the infrared radiation reaches about 1.02 eV, electrons can be transferred from the valence band to the E_{t2} level and additional holes may become trapped at the E_{t1} center, resulting in an increase in recombination via the E_{t1} levels and a decrease in recombination via the E_{t2} centers. Thus, with further increase in the energy of the infrared radiation (beyond 1.02 eV), ΔI_c begins to decrease. As pointed out by Lin and Wittry (1976), the measured change of I_c may be caused also by modulation of the nonradiative surface recombination rate and the recombination rates through impurity centers in the space-charge region. For undoped GaAs (Figure 6.41), the existence of three deep levels was assumed at $E_c - 0.92$ eV (donor), $E_c - 0.77$ eV (acceptor), and $E_c - 0.69$ eV (acceptor) (Lin and Wittry, 1976). By varying the excitation conditions during their experiments, Lin and Wittry (1976) concluded that to obtain high sensitivity of the infrared modulation, the electron beam voltage and the electron beam current should be minimized.

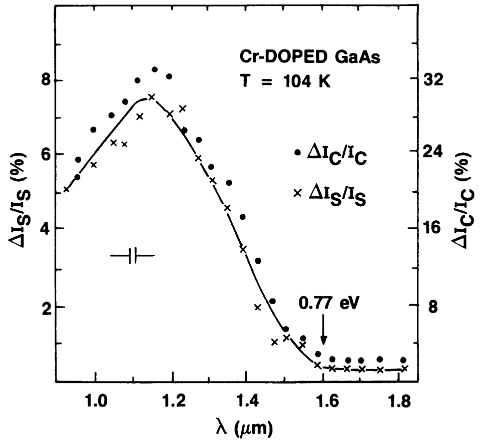

Figure 6.40. Infrared-induced relative increases in CL intensity $\Delta I_c/I_c$ and in specimen current $\Delta I_s/I_s$ as a function of wavelength for Cr-doped GaAs. (After Lin and Wittry, 1976.)

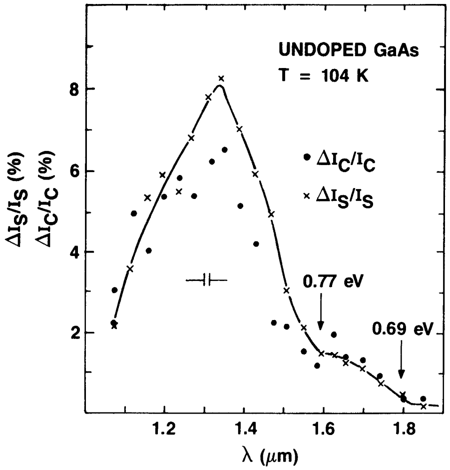

Figure 6.41. Infrared-induced relative increases in CL intensity $\Delta I_c/I_c$ and in specimen current $\Delta I_s/I_s$ as a function of wavelength for undoped GaAs. (After Lin and Wittry, 1976.)

Cathodoluminescence microscopy (i.e., monochromatic and/or panchromatic CL images) together with CL spectroscopy can be effectively used for (1) analyzing defects (such as dislocations) and measurements of their densities, (2) analyzing impurity segregation, and (3) studying semiconductor devices, e.g., locating electrostatic inhomogeneities and measuring the depletion zones. Some examples of these applications of CL were outlined in preceding sections, and others will be presented in the following chapters.

Several reports have appeared in the literature of combined CL and EBIC measurements on GaAs and GaP diodes. Wittry and Kyser (1965) reported that the CL intensity and the charge collection (CC) current varied inversely during line scans across *p-n* junctions in GaAs. This is explained by the fact that the CC current is produced due to the separation (by the junction field) of electron-hole pairs generated by the electron beam. The CL intensity is reduced correspondingly, since the separated electron-hole pairs cannot recombine to produce photons. The measurement of the CL and CC signals from the same device was applied to GaP electroluminescent (EL) diodes by Calverley and Wight (1970), who demonstrated that there was an inverse relationship between the maximum EL efficiency of GaP red-emitting diodes and the so-called CL-CC shift. The latter is defined as the displacement between the midpoints of the CL drop and the CC peak produced as the beam scans across a *p-n* junction normal to the surface. A similar correlation between the CL-CC shift and the device efficiency of GaP diodes was obtained by Holt *et al.* (1973). However, Hackett *et al.* (1972) found no CL-CC shifts at all, which suggests that correlation occurrence depends on possible materials differences arising from differing starting materials (Holt *et al.*, 1973).

7

Semiconductors

Most work in the CL characterization of semiconductors was devoted in recent years to III-V and II-VI compounds. These compounds found applications in a wide variety of electronic and optoelectronic devices. The group IV materials, Si and Ge, although the first and the most important used in semiconductor technology, have indirect energy gaps of about 1 eV, which limits both the optical applications and optical characterization of these materials. Many of the III-V and II-VI materials, however, have direct gaps with greater widths corresponding to visible photon energies.

Semiconductors are grown as bulk crystals or as epitaxial films. Bulk crystal wafers are used as substrates for epitaxial layers, and the properties of the substrates have a major effect on the growth and properties of these epitaxial layers. Increasingly complex epitaxial multilayer structures are presently used in devices. Such materials require characterization by methods with both spectroscopic and spatial resolution, such as CL-SEM.

7.1. Group IV Materials

SEM characterization of silicon using the EBIC mode has found wide application. However, CL studies on Si are more limited because of the low luminescence efficiency of Si and the relatively low sensitivities of detectors in the wavelength range above 1.1 μm. Davidson *et al.* (1981), Cumberbatch *et al.* (1981), and Myhajlenko *et al.* (1983a,b), however, demonstrated the progress made possible by a specially constructed scanning CL microprobe for CL transient measurements in deriving minority carrier lifetimes (see, for example, Figure 6.26). They obtained CL images and spectra, as well as CL decay measurements at various defects (see, for example, Figures 4.22 and 6.26). However, the high electron beam currents used ($\sim$ 10 μA) in these studies lead to significant electron beam–induced heating of the material; another undesirable effect associated with high excitation is the high excess carrier generation rate (Cumberbatch *et al.*, 1981; Myhajlenko *et al.*, 1983a,b). Löhnert and Kubalek (1983) obtained CL images and spectra at lower electron beam currents. Panchromatic CL micrographs were recorded at 80 K by using an electron beam current of about 1 μA (at 30 kV beam voltage), and CL spectra were obtained with even lower beam currents (of the order of 100 nA). Löhnert and Kubalek (1983) obtained CL spectra at 80 K from plastically deformed silicon with a dislocation density of 10^9 cm^{-2}, and they concluded that the features in the CL spectrum around a wavelength of 1.5 μm are associated with dislocations.

CL-STEM observations of infrared emission due to dislocations in deformed silicon were reported by Graham *et al.* (1987). Figure 7.1 presents a CL spectrum obtained at 23 K from dislocations in a thick (opaque to 120-keV electrons) region of deformed silicon. The discrete luminescence bands due to dislocations in silicon were labeled as D1 (0.812 eV), D2 (0.875 eV), D3 (0.934 eV), and D4 (1.000 eV) by Drozdov *et al.* (1976), and D5 (≈0.953 eV) and D6 (≈1.0126 eV) by Sauer *et al.* (1985). The photoluminescence intensity of the D1–D4 lines as a function of temperature was investigated by Suezawa *et al.* (1983) (see also references therein), who interpreted their results by invoking two types of traps, shallower levels (hole traps) in the range between 4 and 12 meV derived from the valence band by the deformation potential of a dislocation, and deeper levels in the range between 0.16 and 0.35 eV below the conduction band associated with electron traps due to the antibonding states of reconstructed bonds at the dislocation core. Luminescence in this model is due to recombination between carriers trapped by these types of levels, and different lines are attributed to different types of dislocations (Suezawa *et al.*, 1983). Chew *et al.* (1985) correlated transmission electron microscopy observations with low-tem-

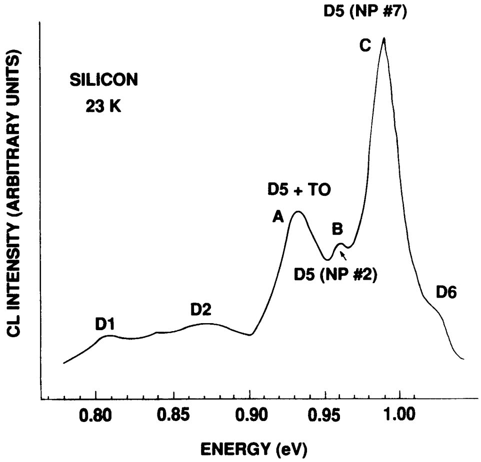

Figure 7.1. A STEM CL spectrum (at 23 K) obtained with a 120-keV electron beam from dislocations in a "thick" region of deformed silicon. Peaks A, B, and C are all tentatively related to D5, although there is some ambiguity about the precise identification of these peaks. NP#2 and NP#7 stand for no-phonon lines 2 and 7, respectively, identified in PL data. (After Graham *et al.*, 1987.)

perature (10 K) CL results to investigate Si layers grown by molecular beam epitaxy on single-crystal Si substrates, and they have concluded that the 1.05-eV luminescence was caused by the presence of grown-in stacking faults and that the D4 (0.99 eV) luminescence was localized and related to topographical defects. Sauer *et al.* (1985) suggested that lines D1–D4 are associated with relaxed dislocations, line D5 is associated with straight dislocations, and D6 is due to stacking faults. Photoluminescence measurements under uniaxial stress also revealed that D1 and D2 originate from tetragonal defects in random orientation relative to ⟨100⟩ directions, whereas D6 originates from triclinic centers that are preferentially oriented (Sauer *et al.*, 1985). It was concluded from these studies that impurities and point defects are not responsible for these lines, dislocations themselves are the active recombination centers, dangling bonds are not involved (Suezawa *et al.*, 1983), and D3–D6 defects are closely related; in addition, D1 and D2 centers could be due to deformation-produced point defects in the strain field of dislocations (Sauer *et al.*, 1985). By comparing their results (see Figure 7.1) with those available in the literature, Graham *et al.* (1987) definitely identified the peaks D1, D2, and D6. The prominent peaks labeled *A*, *B*, and *C* were thought to be associated with line D5, although there was some ambiguity about precise nature of these peaks (Graham *et al.*, 1987). It is possible that the ambiguity could be removed by the deconvolution of these peaks (i.e., A, B, and C) and by correcting the data for the spectral response characteristics of the optical detection system. Both of these are known to affect luminescence spectra (see Sections 5.1.4 and 7.3.3).

The investigation of amorphous semiconductors evolved into a new research field with the discovery a decade ago of the effect of hydrogen passivation of the defects in amorphous silicon. Hydrogenated amorphous silicon has attracted increasing interest in recent years in a variety of applications, such as photovoltaics, electrophotography, vidicons, field-effect transistors, high-speed detectors, threshold switching, and memory devices (see Pankove, 1984). The PL technique is widely used for characterization of amorphous semiconductors (Street, 1976). A wide variety of electron probe instruments is also utilized for structural and chemical analyses of these materials. However, recent experiments (Pankove, 1984) indicated that hydrogenated amorphous silicon does not exhibit CL. This is explained (see the review by Schade in part B of Pankove, 1984) by a mechanism of formation of electron beam–induced defects in *a*-Si:H. These defects, which are thought to be created by the breaking of weak bonds, act as nonradiative centers that reduce the luminescence efficiency. The formation of electron beam–induced defects in hydrogenated amorphous silicon can be observed in the charge collection mode (Yacobi, 1985). These results indicate that for typical SEM operating conditions, rapid generation of defects would be expected (See Figure 7.2; Yacobi and Herrington, 1985), which would prevent obtaining useful luminescence data.

Silicon carbide (SiC) has attracted increasing interest in a variety of applica-

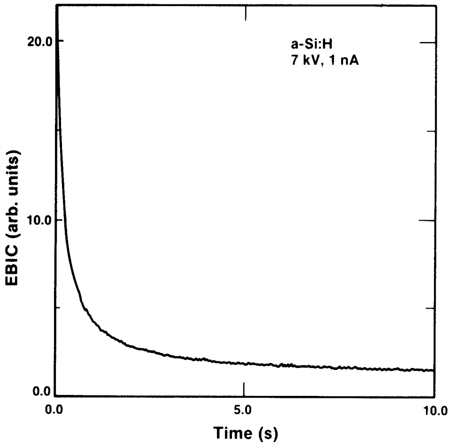

Figure 7.2. Decay of the EBIC signal of a p-i-n hydrogenated amorphous silicon device under continuous irradiation by a 7-keV electron beam of 1 nA. (After Yacobi and Herrington, 1985.)

tions. This is an indirect-gap material with a band gap depending on the polytype. Thus, for example, zinc blende structure SiC has a band gap of 2.2 eV at room temperature, and the 6H-polytype has a band gap of about 3 eV (see Table 3.1). The latter is especially attractive for blue light-emitting diode (LED) applications, since *n*- and *p*-type doping can be obtained. The electrical properties of SiC also make this material very attractive for use in high-temperature electronic devices and in high-power and high-speed devices. A problem is the high growth temperature. Fortunately, epitaxial SiC layers can be obtained at lower temperatures. Typical deposition temperatures for chemical vapor deposition (CVD) are around 1800°C, although temperatures as low as around 1400°C were reported. Epilayers that are not intentionally doped typically exhibit *n*-type conductivity. For *p*-type doping, trimethylaluminum (TMA) or triethylaluminum (TEA) are used. Yoshida *et al.* (1984) used TEA for aluminum doping of 6H-SiC, and their measurements of the CL (at 77 K) and electrical properties indicated that the aluminum doping concentration can be controlled by the flow rate of TEA. Figure 7.3 presents the CL spectrum of an aluminum-doped 6H-SiC epitaxial layer grown on a 6H-SiC crystal substrate. The peaks in the CL spectrum could be ascribed to free-to-acceptor (A) and donor-to-acceptor (B and C) transitions and their phonon replicas. For this, they took the excitation band-gap energy to be 3.022 eV, the free-exciton binding energy to be 78 meV, the ionization energies of nitrogen donors to be 100 meV for hexagonal-like sites and 155 meV for cubiclike sites, and of aluminum acceptors to be 239 and 249 meV for *h* and *c* sites, respectively; the LO-phonon energy was taken to be about 100 meV. The CL measurements indicated that the peak intensities increased with increasing TEA flow rate (Yoshida *et al.*, 1984).

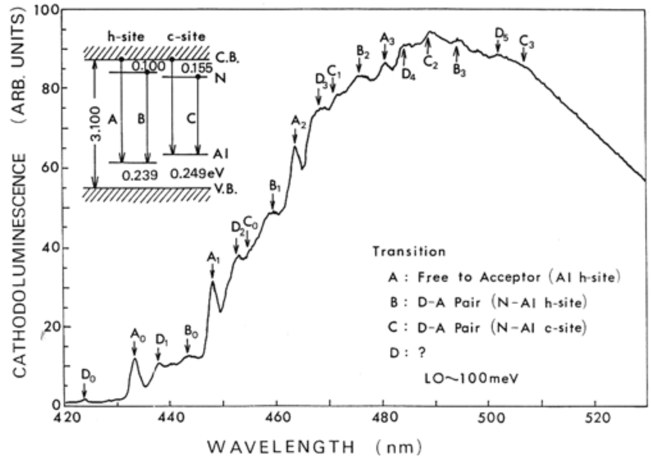

Figure 7.3. CL spectrum (at 77 K) of a 6H-SiC epilayer doped with aluminum using triethylaluminum (TEA) (6×10^{-6} atm). The inset shows the nitrogen donor and the aluminum acceptor levels in 6H-SiC crystal. (After Yoshida *et al.*, 1984.)

7.2. III-V Compounds

The III-V compounds are important for a wide variety of both majority and minority carrier device applications. These materials crystallize with a high degree of stoichiometry, and most of them can easily be obtained *n*- and *p*-type. These materials are used in a variety of optoelectronic devices for the detection or generation of radiation.

As can be seen from Table 3.1, some of these compounds are direct-band-gap materials, whereas others have an indirect band gap. In luminescent devices, in order to obtain transitions leading to visible radiation, the band gap of the material must be $E_g \geq 2$ eV. Indirect-gap materials with larger band gaps are not expected to be such efficient luminescence emitters, in principle, as direct-gap materials, although properly doped GaP, for example, exhibits efficient donor-acceptor (Zn-O) pair red electroluminescence in LEDs. To obtain direct-gap materials with band gaps greater than 2 eV, a variety of ternary alloys have been developed. For example, in the $GaAs_{1-x}P_x$ alloys, the transition from direct to indirect gaps occurs at $x = 0.45$, and a band gap of 2.0 eV. The ternary alloy systems of major interest are GaAsP, InGaP, and GaAlAs. In the $In_xGa_{1-x}P$ system, the transition from a direct to an indirect gap occurs at $x = 0.3$ and a band gap of 2.2 eV. In $Ga_xAl_{1-x}As$, the direct band gap of about 2 eV corresponds to

$x = 0.6$. All these alloys can be obtained with either n- or p-type doping and can be used in devices, such as LEDs.

GaN is a direct-gap material with a band gap of 3.36 eV at room temperature, and thus it is potentially very attractive as an emitter of blue light and possibly other colors as well. The snag, however, is that, in common with other wide-band-gap materials, GaN can only be obtained n-type. (The n-type behavior is believed to be due to a nitrogen vacancy.) Although the incorporation of various dopants does not lead to p-type material, characteristic luminescence in the blue (Zn), green (Cd), yellow (Li), and violet (Mg) spectral regions can be obtained.

7.2.1. Uniformity Characterization

With the demands for higher speed (compared with Si), integrated circuits, injection lasers and other optoelectronic devices, III-V compounds, and especially GaAs have attracted increasing interest. Uniformity of electronic properties is essential for device applications of these materials. This requirement led to numerous CL studies of these compounds in the last decade.

For high-performance GaAs integrated circuits, uniformity of field-effect transistor (FET) parameters, such as threshold voltage (V_{th}) across a wafer is essential. Such devices may be fabricated by direct ion implantation into a semi-insulating (SI) substrate obtained by the liquid-encapsulated Czochralski (LEC) growth technique. (The SI property is thought to be a result of compensation of shallow acceptors by the deep donor intrinsic center EL2, which is believed to be related to the $\mathrm{As}_{\mathrm{Ga}}$ antisite defect.) Several reports demonstrated that the threshold voltage of GaAs devices fabricated on LEC-grown SI substrates are affected by the dislocations in the walls of the cell structure characteristic of SI GaAs (Nanishi *et al.*, 1982; Honda *et al.*, 1983; Miyazawa *et al.*, 1983; Wang and Bujatti, 1984; Miyazawa and Hyuga, 1986). Furthermore, Chen *et al.* (1984) showed the dependence of the threshold voltage on the residual carbon concentration; and Miyazawa and Ishii (1984), Dobrilla *et al.* (1985), and Miyazawa and Wada (1986) concluded from their observations that the dislocation proximity effect on the threshold voltage is correlated with the local EL2 density. As noted by Dobrilla *et al.* (1985), the often-reported dislocation proximity effect on the threshold voltage may be the result of a dislocation being a source or sink for point defects. This is consistent with the report by Winston *et al.* (1984), who observed no correlation between the threshold voltage and FET proximity to a dislocation, as well as with observations by Dobrilla *et al.* (1985) on some of their samples.

Uniformity detection in III-V compounds was demonstrated to be one of the most useful and practical microcharacterization capabilities of the CL-SEM technique. Cathodoluminescence microscopy and spectroscopy have been used also for the analysis of semiconductor devices (Bakker *et al.*, 1980; Davidson and

Rasul, 1977; Chin *et al.*, 1980; Miyazawa *et al.*, 1983, 1984) and of the nonuniformity of the dopant distribution in materials such as InP (Warwick and Booker, 1983), $Ga_{1-x}In_xP$ (Kaniewski *et al.*, 1981) and GaP (Menniger *et al.*, 1978).

Examples of the power of CL in uniformity characterization of SI GaAs were reported by Kamejima *et al.* (1982), Chin *et al.* (1984), Wakefield *et al.* (1984a), Warwick and Brown (1985), and Warwick *et al.* (1985). Kamejima *et al.* (1982) correlated CL and secondary ion mass spectrometry (SIMS) line scans in undoped LEC SI GaAs and observed cellular dislocation structures (see also Clark and Stirland, 1981; Stirland *et al.*, 1983) and the segregation of oxygen, chromium, silicon, and carbon at these dislocations. Nonuniformity of the electrical properties derived from scanning leakage current measurements was also observed by Kamejima *et al.* (1982).

Wakefield *et al.* (1984a) used spectroscopic CL at liquid He temperatures to characterize undoped LEC SI GaAs. The luminescence spectrum consists of two peaks at 1.494 eV due to the residual carbon acceptors and 1.514 eV associated with shallow donors or bound excitons (Figure 7.4). The intensities of these lines, derived from spectra measured inside the cells and at the cell walls (dislocation tangles), vary significantly. Figures 7.5a,b present plots of the CL intensity of the 1.494-eV and the 1.514-eV peaks measured across a 5-mm-wide strip. These figures demonstrate that relative to the 1.514-eV emission, luminescence due to the carbon impurities (i.e., the 1.494-eV peak) varies substantially more across the wafer. Monochromatic CL micrographs recorded using the carbon (1.494-eV) emission peak clearly demonstrate the segregation of carbon to the dislocation walls (Figure 7.6). This leads to the increase in the intensity of the

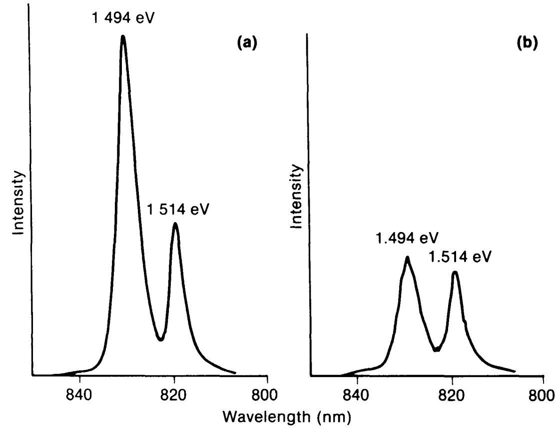

Figure 7.4. Liquid He CL spectra from (a) a bright area and (b) an adjacent dark area in semi-insulating GaAs. (After Wakefield *et al.*, 1984a.)

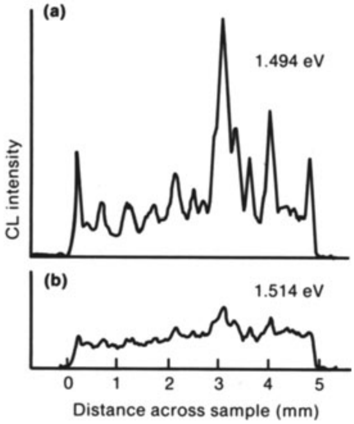

Figure 7.5. Liquid He CL intensity line scans across a 5-mm strip of a semi-insulating GaAs at the photon energies of (a) 1.494 eV due to residual carbon and of (b) 1.514 eV associated with shallow donors or bound excitons. (After Wakefield *et al.*, 1984a.)

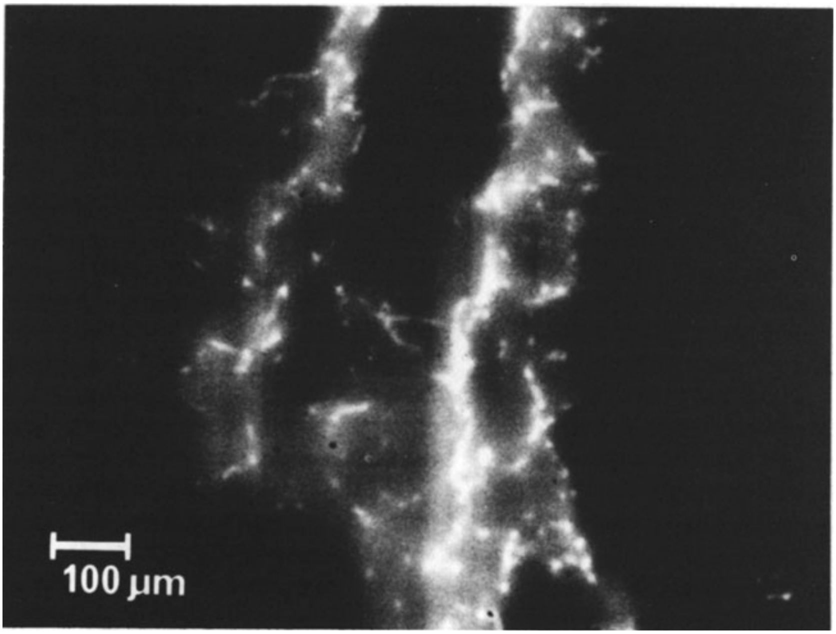

Figure 7.6. Liquid He monochromatic CL micrograph of a cell boundary in semi-insulating GaAs using the 1.494-eV emission due to residual carbon. (After Wakefield *et al.*, 1984a.)

carbon CL (Wakefield and Davey, 1985). Dark spots along the dislocation walls were not observed by Wakefield *et al.* (1984a), but were seen in the later work of Warwick *et al.* (1985). The major conclusion of these studies is that inhomogeneous distribution of impurities may lead to nonuniform electrical transport in the material, which would be undesirable for such applications as GaAs integrated circuits (Warwick *et al.*, 1985). Voltage contrast observations on these samples also indicated that there are inhomogeneities in the resistivity due to the cellular dislocation network.

Similar effects were reported by Chin *et al.* (1984), who compared the uniformities of Cr-doped and undoped LEC SI GaAs with undoped SI material grown by the horizontal gradient freeze (HGF) technique. Whereas dot-and-halo contrast at the dislocation cell walls was observed in LEC GaAs in CL images, localized bright regions with no apparent cellular dislocation structure were observed in HGF crystals. Bright contrast in these observations was explained as being due to impurity gettering effects at dislocations, which lead to an increase in radiative as compared to nonradiative recombination at the dislocation core. It was concluded that HGF GaAs is more uniform than LEC material.

Cathodoluminescence observations by Warwick and Brown (1985), who used cooled PbS and Ge detectors for liquid He CL imaging of deep levels in undoped LEC SI GaAs, confirmed the segregation of the dominant intrinsic defect EL2 (which may be an As_{Ga} antisite-related defect) from the cell interior to the dislocation cell walls. Figure 7.7 presents a reflection x-ray topograph (Figure 7.7a) and the 1.51-eV CL image (Figure 7.7b) of the same area of a sample. The x-ray topograph reveals that dislocations are arranged in both linear and cellular arrays. In Figure 7.7, a cell wall is labeled *W*, a cell center *C*, and a linear array *L*. The 1.51-eV CL band, which was used for monochromatic CL imaging, is assumed to be due to recombination of free holes at neutral shallow donors. Figure 7.7 demonstrates that the dislocation arrays in the x-ray topograph correspond to the bright walls in the CL image. Figure 7.8 shows a magnified CL image (recorded at 1.51 eV) of an area containing a cell wall. In this figure, dark spots correspond to dislocations (one of them is labeled *D* in Figure 7.8a), which have a lower 1.51-eV CL intensity than do the surrounding cell walls (labeled *W*). In Figure 7.8a, a line trace of the 1.51-eV CL intensity profile through the cell wall is also recorded. While no significant variation of the 1.51-eV intensity was detected inside the cell (i.e., between the points labeled *C* and *X*), the ratio of the intensity in the cell wall (at point *W*) to the intensity in the cell interior (at, e.g., points *C* or *X*) was about 8 to 1 (Warwick and Brown, 1985). The CL spectra recorded in the near-band-edge wavelength range for both the cell wall (*W*) and the cell center (*C*) are shown in Figure 7.9a. Two peaks at 1.51 eV and 1.49 eV are observed in the spectra for both the cell wall and the cell interior. The 1.49-eV band was assumed to be due to a mixture of DAP recombination and free-electron recombination at carbon acceptors. Contrary to the results of

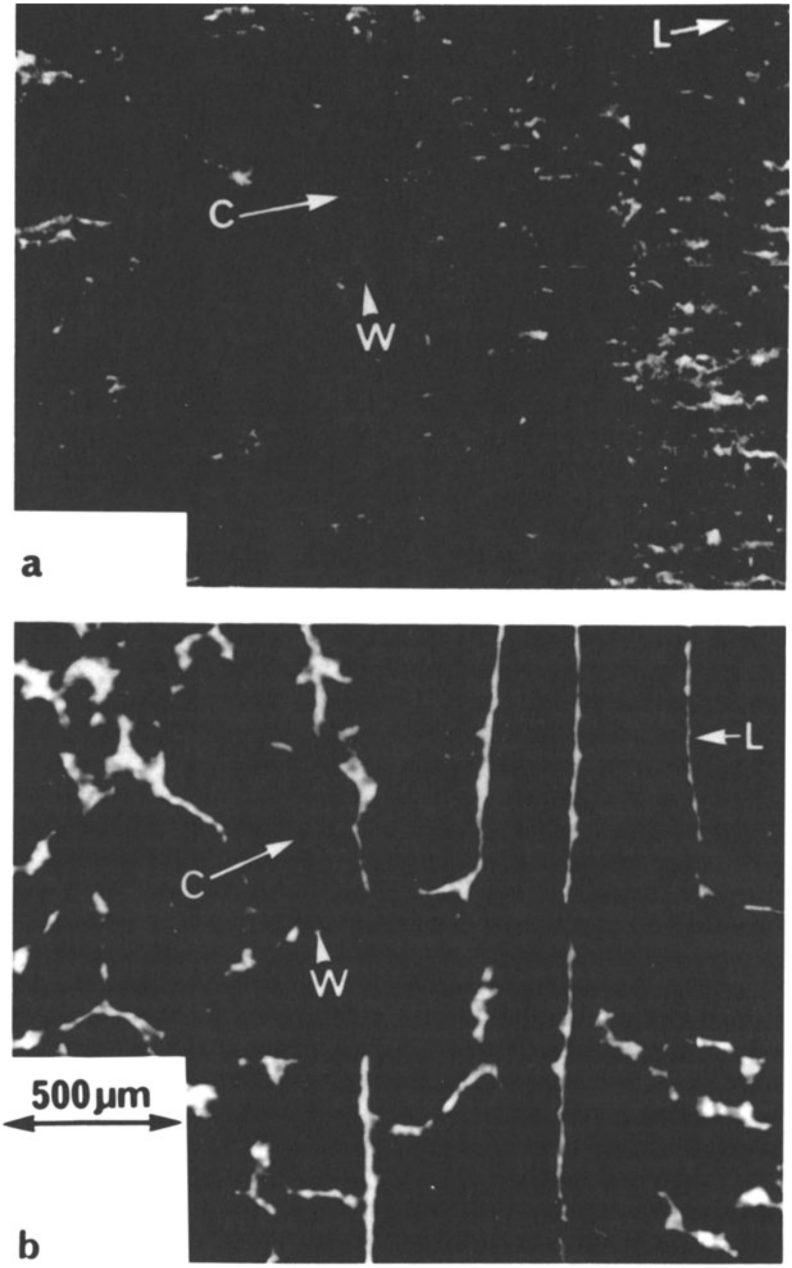

Figure 7.7. (a) Reflection x-ray topograph of the cellular dislocation arrays in undoped semi-insulating GaAs. (b) 1.51-eV CL-SEM image (recorded at a sample temperature of about 10 K) of the same area as (a). (After Warwick and Brown, 1985.)

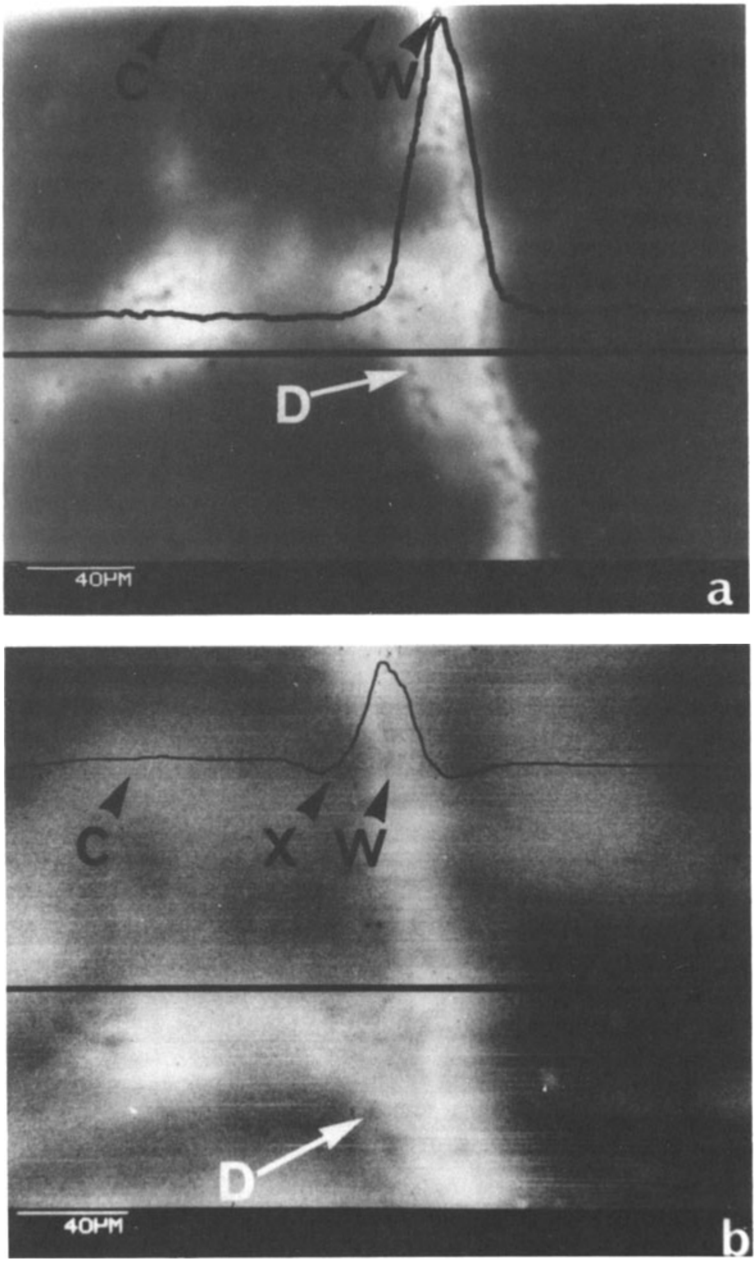

Figure 7.8. (a) 1.51-eV CL image (sample temperature is about 10 K) of an area containing a cell wall at higher magnification; the 1.51-eV line trace through points *C*, *X*, and *W* is overlaid with the zero-signal base line. (b) 0.68-eV CL image of nearly the same area as (a); the 0.68-eV line trace through points *C*, *X*, and *W* is overlaid with the zero-signal base line. (After Warwick and Brown, 1985.)

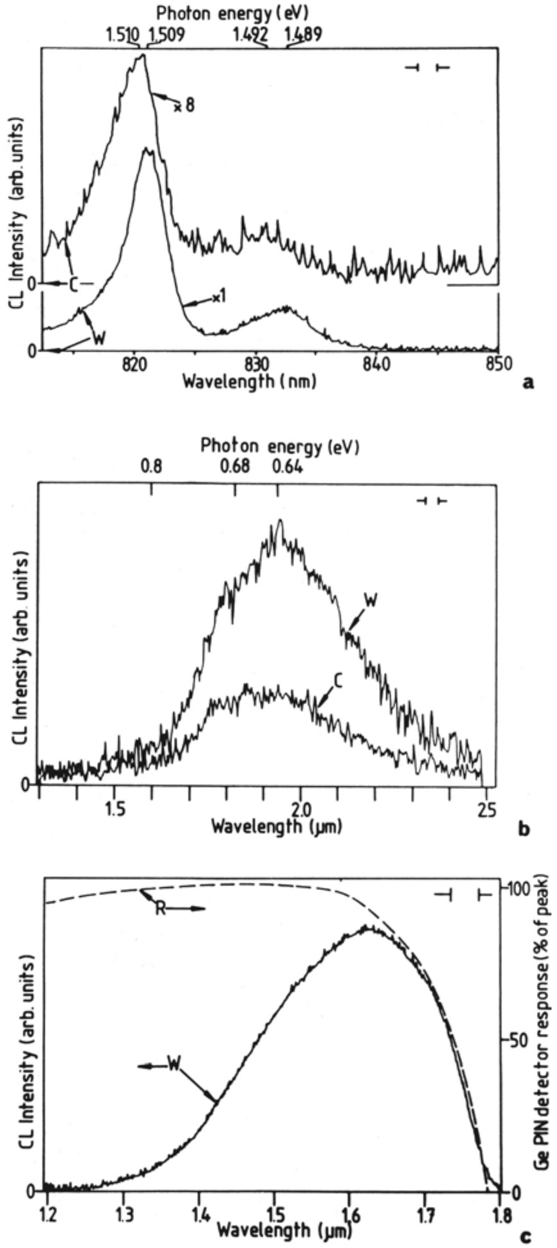

Figure 7.9. (a) Near-band-edge CL spectra from point *C* and point *W* of Figure 7.8. (b) Deep-level CL spectra from these points; PbS detector. (c) High-energy part of the deep-level spectrum from point *W* of Figure 7.8 (Ge detector) with the Ge detector response curve (*R*). (After Warwick and Brown, 1985.)

Wakefield *et al.* (1984a) (Figures 7.4–7.6), the ratio of the intensity of the 1.49-eV band to that of the 1.51-eV band in the cell wall and in the cell interior remained constant. As pointed out by Warwick and Brown (1985), this discrepancy could be due to the differences in excitation conditions used by these two groups of researchers. Figure 7.8b is a CL image and line trace through points *C, X,* and *W* obtained by using the 0.68-eV CL peak, which is assumed to be due to hole capture by neutral EL2 centers. The 0.68-eV line trace shows a contrast feature of reduced intensity (labeled *X* in Figure 7.8b) near either side of the cell wall (*W*). Each zone of lower 0.68-eV intensity is about 20 μm wide. Figure 7.9(b) shows the deep-level spectra (using a PbS detector) for the cell wall (*W*) and the cell center (*C*); and Figure 7.9c presents the CL spectrum (using a Ge detector) from the cell wall (*W*) together with the Ge detector response curve (trace *R*). In this context, note that the 0.68-eV intensity map (Figure 7.8b) was recorded with the Ge detector, which is sensitive to photons of energy greater than 0.69 eV. However, since the 0.68-eV band is broad, the high-energy portion of it is detected (Warwick and Brown, 1985). From the analysis of their data, Warwick and Brown (1985) concluded that there was lower concentration of EL2 in zone *X* than in the cell center. In other words, it appears that EL2 segregates from the cell interior to the dislocations. The attractive force between the EL2 centers and the dislocations in such a process could be the result of strain field interactions and electrostatic attraction (Warwick and Brown, 1985). These results demonstrate that dislocation arrays in undoped SI GaAs getter the EL2 centers rather than generate them (Warwick and Brown, 1985).

The uniformity of SI GaAs for device applications can be improved by, for example, indium doping, to reduce the grown-in dislocation densities (Barret *et al.*, 1984), and by heat treatment (Miyazawa *et al.*, 1984; Chin *et al.*, 1985; Kasahara *et al.*, 1986; Ding *et al.*, 1987). Chin *et al.* (1985) observed, using CL microscopy, a contrast reversal in a SI undoped bulk GaAs crystal with annealing at 800°C for 30 h. In other words, dislocation-free cell interiors have a higher luminescence efficiency than do the cell walls. They also found that the improved CL uniformity of annealed material was a result of an increase in CL efficiency of the dislocation-free cell interior rather than a decrease in the CL efficiency of the cell walls. Chin *et al.* (1985) concluded from their studies that improvements in the CL uniformity of annealed SI LEC GaAs are due to a diffusion process that involves As vacancies. Similar effects of contrast reversal and improved device characteristics were observed by Ding *et al.* (1987) in SI LEC GaAs substrates after an extrinsic gettering treatment, which consisted of mechanical damage on the backside of the wafer followed by a low-temperature heat treatment (typically at 500°C for 24 h) with the front side of the wafer capped for protection. Comparing their results with those of Chin *et al.* (1985), Ding *et al.* (1987) concluded that the gettered species may be related to As. An important conclusion of these studies is that heat treatment can significantly change the electrical properties of LEC GaAs with no corresponding change in the dislocation density distribution. It appears that the electrical properties of LEC GaAs are predominantly influenced by the concentration and distribution of intrinsic point defects and/or impurities that often correlate with the dislocation distribution in this material because of the gettering effect of the dislocations. Heat treatment alters this correlation so that device parameters are no longer affected by the dislocation distribution.

As mentioned in Sections 5.1.3 and 6.1, TCL and ECL using Si and Ge solid-state detectors can be effectively used for investigating defects in semiconductors. Although such studies provide no spectroscopic data, important information on CL uniformity of the material can be obtained with this relatively simple method. Such uniformity studies using TCL (and ECL) were reported in GaAs (Chin *et al.*, 1979a; Fornari *et al.*, 1985; Marek *et al.*, 1985), in InP (Chin *et al.*, 1979b,c), in InGaAsP/InP double heterostructures (Chin *et al.*, 1979b; Cocito *et al.*, 1983), in GaAlAs/GaAs double heterostructures (Chin *et al.*, 1980), and in InGaAs/InP single heterostructures (Franzosi *et al.*, 1986). These studies demonstrated the usefulness of TCL and ECL as nondestructive techniques for imaging defects in semiconductors.

CL uniformity studies in Mg-doped epitaxial GaN layers grown on sapphire substrates were reported by Liu *et al.* (1977), who found that CL properties of the layers depend strongly on Mg concentrations. Cathodoluminescence spectra of Mg-doped GaN layers for Mg source temperatures of 428°C and 510°C are shown in Figure 7.10. A summary of their CL results and data on layer resistivity as a function of Mg source temperature is presented in Figure 7.11. These results revealed that in GaN with increasing Mg concentrations, the CL peak shifts to longer wavelengths and the CL band broadens. Liu *et al.* (1977) also found that with increasing Mg concentration, when Mg fully compensates the native donors (which is indicated by an abrupt increase in resistivity), the CL intensity is quenched. They proposed that these effects were caused by the increased density

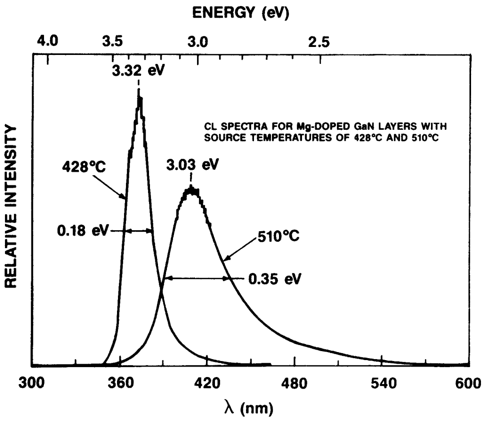

Figure 7.10. CL spectra for Mg-doped GaN epitaxial layers with Mg source temperatures of 428°C and 510°C. (After Liu *et al.*, 1977.)

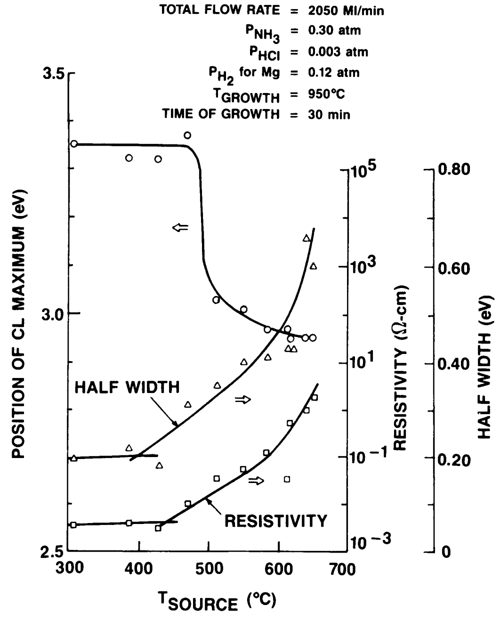

Figure 7.11. Peak energy and width at half-maximum of the CL band of epitaxial GaN and layer resistivity as a function of Mg source temperature. (After Liu *et al.*, 1977.)

of predominantly nonradiative recombination centers due to the Mg deep-level impurities. Using these effects of Mg concentration on the CL, Liu *et al.* (1977) found that the Mg tended to segregate at the low-angle boundaries separating faceted areas which had lower Mg concentrations. The presence of various conducting grains embedded in the insulating matrix of the doped layer explained the large leakage currents in the I-V characteristics of the metal-insulator–*n*-type semiconductor (MIN) EL GaN diodes. Cathodoluminescence and SIMS studies of Al-doped GaN epitaxial layers revealed significant three-dimensional nonuniformities in the distributions of Al and N_2 in both single-crystalline and polycrystalline layers (Monemar and Lagerstedt, 1979). In the latter case, an increase in doping was observed at the grain boundaries.

7.2.2. Recombination at Dislocations

As mentioned in Section 6.1, the work of Petroff *et al.* (1977, 1978, 1980, 1981, 1984) demonstrated the power of CL combined with STEM to relate the recombination properties of individual dislocations to their crystallographic structure. For example, the lack of carrier recombination at a sessile edge dislocation at a $Ga_{1-x}Al_xAs_{1-y}P_y$/GaAs interface was explained on the basis of a reconstructed core model (see Figure 6.17; Petroff *et al.*, 1980). Fitzgerald *et al.* (1988), however, observed in AlGaAs/InGaAs/GaAs heterostructures that edge dislocations were stronger nonradiative recombination sites than 60°-type dislocations at the AlGaAs/InGaAs and InGaAs/GaAs interfaces.

Recombination processes and minority carrier lifetimes at dislocations have been investigated in GaAs (Balk *et al.*, 1976; Chu *et al.*, 1981) and GaP (Darby and Booker, 1977; Davidson and Rasul, 1977; Rasul and Davidson, 1977a,b; Titchmarsh *et al.*, 1977; Dimitriadis *et al.*, 1978). Titchmarsh *et al.* (1977) investigated the origin of dark spots in CL micrographs of GaP epitaxial layers and suggested that the core structures of screw, edge, and mixed dislocations are responsible for nonradiative recombination in this material. Dimitriadis *et al.* (1978), on the other hand, concluded that the primary effect is due to a Cottrell atmosphere of impurities and/or point defects. It appears likely that both dislocation core effects and Cottrell atmospheres of impurities and/or native point defects around dislocations have to be invoked to explain the myriad possible cases of recombination processes at dislocations. Booker *et al.* (1979) concluded that in GaP the recombination is mainly dependent on the diffusion of carriers to the dislocations (in contrast to the case of Si, where recombination is controlled mainly by the mechanism occurring at the dislocation). Dimitriadis (1984) reported the determination of the minority carrier lifetime at single dislocations in *n* -type GaP using measurements of the CL decay time of the band-edge green emission. From the temperature dependence of the lifetime at dislocations, it was concluded that at dislocations in GaP the dominant recombination center with an activation energy of 0.15 eV is associated with S-donor/Cu complexes (it is inconclusive whether this level lies in the upper or lower half of the gap).

The most direct evidence on dislocation recombination mechanisms, however, is provided by spectroscopic CL studies in CL-STEM systems as exemplified in Figures 6.18 and 6.19. The general conclusion of a review of many such studies was that the observed effects are the result of impurity segregation to the dislocations (Steeds, 1989).

Chu *et al.* (1981) reported CL studies of the effect of Te and Se doping levels in GaAs on the precipitation of dopants at and away from dislocations. Cathodoluminescence dark dot and dot-and-halo contrast (explained in Figures 6.2 and 6.3) were observed in samples with Te doping concentrations from about 1×10^{17} to 5×10^{18} cm^{-3}. These results were explained in terms of nonradiative recombination at dislocations, at dislocations with precipitation loops, and at precipitation loops only. Darby *et al.* (1980) showed that Zn-precipitation-induced defects may lead to a significant decrease in the luminescence efficiency of Si-doped GaAs.

The minority carrier lifetime at single dislocations can be determined by using CL decay measurements, which can also be used for carrier lifetime mapping around dislocations (see Section 6.2).

As mentioned earlier (Section 6.1), the effect of keV-electron–beam irradiation on the mobility of dislocations in GaAs was reported and explained in terms of the recombination-enhanced glide of dislocations (Maeda *et al.*, 1983). The influence of plastic deformation on tne CL properties of GaAs and GaP crystals was described by Esquivel *et al.* (1973, 1976) and Davidson *et al.* (1975). The local reductions in the CL in these deformed materials were attributed to dislocations and slip bands.

7.2.3. Cathodoluminescence Assessment of Devices

Cathodoluminescence assessment of devices demonstrated that dislocations are undesirable in optoelectronic materials (1) for the enhanced recombination that they may produce themselves, and (2) for causing impurity segregation into Cottrell atmospheres and precipitates.

The value of CL in the assessment of GaAs LED materials was demonstrated by Trigg and Richards (1982). They showed that the dark lines found in their LEDs were present in the starting material and did not arise in the device processing. Frank and Gösele (1983) proposed a unified model that explains the degradation of these devices on the basis of the changes of the concentration of vacancies and/or antisite defects in the vicinity of dislocations.

Cathodoluminescence measurements on green-emitting GaP:N LEDs were reported by Haefner *et al.* (1981), Oelgart *et al.* (1982), and Löhnert and Kubalek (1983). The *p-n* junctions, in general, are fabricated by Zn diffusion or implantation (with subsequent annealing) into vapor phase epitaxial (VPE) GaP:N. Haefner *et al.* (1981) recorded CL line scans under forward bias to evaluate the internal luminescence efficiency of the bulk material near the *p-n* junction. Oelgart *et al.* (1982) studied the degradation of GaP:N LEDs and observed the formation of a deep nonradiative center in the *n*-region near the *p-n* junction; they proposed the formation of nonradiative centers enhanced by nonradiative recombination. Löhnert and Kubalek (1983), on the other hand, concluded from their EBIC and CL studies of green-emitting GaP diodes that (1) dislocations were not responsible for the degradation, (2) the luminescence efficiency on the *n*-side of the degraded devices was decreased, but the *p*-side was not affected significantly, and (3) the luminescence spectrum of degraded devices contained, in addition to the green luminescence at 560 nm, a weak red emission near 680 nm. The luminescence at 680 nm is due to Zn-O centers that are formed by zinc doping and unintentional oxygen. In the CL line scans recorded at 680 nm (i.e., with Zn-O luminescence), Löhnert and Kubalek (1983) observed a broadened profile toward the *n*-side of the junction in degraded diodes (Figure 7.12), indicating diffusion across the junction of zinc, some of which together with contaminant oxygen forms Zn-O centers. Thus, the degradation of green-emitting GaP diodes was ascribed to the formation on the *n*-side of the junction of nonradiative centers related to the diffused zinc (Löhnert and Kubalek, 1983).

Several other reports also indicated that the diffusion of various species may explain the degradation of light-emitting devices. Skeats *et al.* (1983) found in GaAlAs/GaAs stripe geometry, double-heterostructure lasers that the dark spot

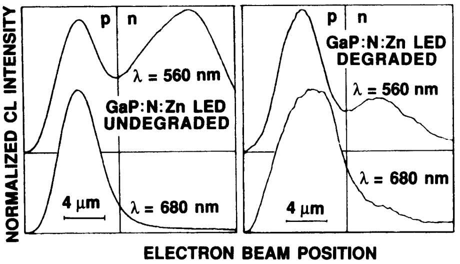

Figure 7.12. Monochromatic CL line scans across *p-n* junction of undegraded and degraded green-emitting GaP LED. (After Löhnert and Kubalek, 1983.)

arrays observed in the CL images of the active layers are due to copper diffusion into the device from the copper heat sinks. Due to the localized nature of the copper penetration, it was assumed that flaws, such as pinholes, in the *p*-side metalization are responsible for the copper diffusion, and it was emphasized that care should be exercized during device processing (Skeats *et al.*, 1983). Mahajan *et al.* (1984) attributed the formation of dark spot defects in InP/InGaAsP-aged LEDs to the migration of gold from the *p*-contact. As a result of the migration, Au-In intermetallics within the quaternary contact layer and inclusions associated with dislocations and multiple faults within the *p*-InP confining layer are formed, producing dark spot contrast in luminescence images (Mahajan *et al.*, 1984).

Transmission infrared CL was used to evaluate the defects and degradation in GaAlAs double-heterostructure LEDs by Chin *et al.* (1980), who concluded that devices undergo rapid degradation by the development of dark line defects (DLDs) that originate at dislocations and propagate due to minority carrier injection. Both transmission and emission CL were used by Cocito *et al.* (1983) to evaluate the defects in InGaAsP/InP heterostructures.

Liquid helium CL measurements on GaAlAs/GaAs double-heterostructure stripe lasers revealed changes in the CL spectra due to operation-induced, strain-enhanced defect migration (Wakefield, 1983). These studies revealed changes in the CL spectra obtained from the active layer under the stripe in a device that was operated for several thousand hours at 70°C. Cathodoluminescence spectral analysis indicated that the removal of the defect center (corresponding to a CL peak at about 815 nm) was by nonradiative recombination-enhanced migration of defects in the strain field within the device.

Low-temperature (10 K) CL observations of the channels of Schottky-gated GaAs FETs were described by Warwick *et al.* (1987), who found a correlation between the full width at half-maximum of the main edge luminescence band (~1.51-eV peak) and the threshold voltage of the transistor. It was also found that the band gap of GaAs shifts to smaller energies than in unprocessed GaAs. This was explained as being due to stress from the ohmic contacts (Warwick *et al.*, 1987). The presence of metalization-induced tensile strains up to 0.05% results in the reduction of the band gap by about 5 meV and the broadening of the luminescence band. In the channel, the stress also induces piezoelectric polarization, which causes changes in the mean threshold voltage by about 100 mV and, because of contact nonuniformities, results in undesirable variations of the threshold voltage of the transistors (Warwick *et al.*, 1987).

7.2.4. Depth-Resolved and Interface Studies

Depth-resolved CL studies in GaAs (Norris *et al.*, 1973; Woodcock *et al.*, 1975; Norris and Barnes, 1980; Norris and Peercy, 1981; Cone and Hengehold, 1983) showed that CL can be effectively used in studying shallow distributions of recombination centers due to ion implantation. An example was provided by Norris *et al.* (1973), who studied Cu^+-implanted GaAs. The GaAs sample was implanted at room temperature with a dose of 10^{15} Cu^+/cm^2 at 100 keV at an angle of 6–7° off axis to minimize channeling. For all the electron beam energies used, between 5 and 20 keV, the intensity of the observed luminescence bands in implanted samples was significantly quenched in comparison to the unimplanted case. The predicted range of 100-keV Cu^+ ions is 450 Å, which should be compared with the electron range of 1400 Å for 5-keV electrons and 1.6 μm for 20-keV electrons. Thus, the luminescence quenching of the CL at these electron energies indicated that the Cu and/or the implantation-induced damage had migrated far beyond the expected Cu-ion range (Norris *et al.*, 1973). Norris and Barnes (1980) also reported significant postrange damage effects due to shallow Ne^+ and Zn^+ ion implantation in Sn-doped GaAs. In this case, implantations were carried out using 100-keV Ne^+ (the projected ion range is about 1220 Å) or 200-keV Zn^+ (the projected ion range is about 780 Å) ions at substrate temperatures between 80 and 300 K. For the heavily Sn-doped GaAs, Norris and Barnes (1980) observed a substantial decrease in postrange defect introduction for samples implanted at 300 K, as compared with 80 K implants, which were subsequently annealed at 300 K. This effect, however, was not as pronounced in the lightly Sn-doped GaAs (Norris and Barnes, 1980). Norris and Peercy (1981) observed recovery of the luminescence in GaAs which was implanted with 200-keV Cd^+ ions and subsequently annealed with a pulsed laser. As a result of the annealing, the luminescence of the implanted sample increased by two to three orders of magnitude. The enhanced emission was within an order of magnitude of that in unimplanted, unannealed GaAs samples (Norris and Peercy, 1981). Woodcock *et al.* (1975) studied melt-grown and epitaxial GaAs doped by the implantation of silicon, sulfur, selenium, and tin with energies between 150 and 400 keV and doses from 10^{12} to 2×10^{15} ions/cm^2. Substrate temperatures during implantation were varied between 300 K (for lighter ions) and 600 K (for heavier ions). Annealing at 700°C produced *n*-type material in all cases. Cathodoluminescence spectroscopy of the implanted samples revealed a dominant broad band at low energies due to defects. It was proposed that a Ga vacancy complex with the implanted donor was responsible for one of the most intense

CL bands (Woodcock *et al.*, 1975). These studies indicated that under certain conditions of implantation dose and temperature some species diffuse in the material deeper than expected from the theory. (It was not clear, however, whether this occurred during the implantation or afterward during the annealing.) Defect migration during implantation was found to cause degradation of the substrate luminescence below layers implanted in p-type GaAs but not in epitaxial n-type material (Woodcock *et al.*, 1975).

As described in Section 6.3, the formation and evolution of interface states (with metal overlayer thickness) for various metals deposited on InP and GaAs were investigated by Viturro *et al.* (1986, 1987a,b) using low-energy CL spectroscopy, which revealed the energy levels that are localized at the interface. The energy distributions of the interface states were found to depend on the particular metal, the semiconductor, and its surface morphology (Figure 6.32). Viturro *et al.* (1986) explained the metal-deposition-induced emission peaks as being due to metal indiffusion and semiconductor outdiffusion that result in the formation of defect complexes responsible for the interface states. These results were found to be consistent with the Schottky-barrier heights of different metals on these semiconductors (Viturro *et al.*, 1986). An example of the application of low-energy CL spectroscopy to the analysis of surface-related states is presented in Figure 7.13 (Viturro *et al.*, 1986). This figure demonstrates the effect of submonolayer metal coverage on the ultrahigh-vacuum-cleaved InP (110) surface. Before the deposition of any metals, the clean ultrahigh-vacuum-cleaved InP surface exhibits only a near-band-edge emission centered at 1.35 eV. The deposition

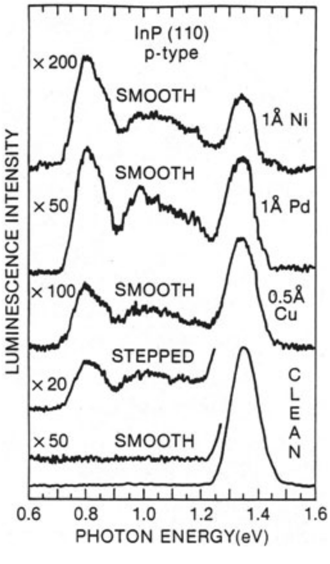

Figure 7.13. CL spectra of clean, mirrorlike p-InP (110) before and after submonolayer deposition of Ni, Pd, or Cu. The CL spectrum of the clean step-cleaved surface is shown for comparison. The electron beam energy is 1.5 keV. (After Viturro *et al.*, 1986.)

of about half a monolayer of these metals leads to the formation of a broad emission band at lower energies than the near-band-edge emission (Viturro *et al.*, 1986). Due to an increase in band bending, which reduces radiative recombination, the intensity of the near-band-edge emission decreases, as shown in Figure 7.13. This figure also reveals similar features at low energies in the CL spectra of a stepped portion of the ultrahigh-vacuum-cleaved surface. Since a high density of broken bonds is associated with the stepped surface, the similarities between the CL spectra shown in Figure 7.13 indicate that the initial deposition of various metals also produces broken bonds. The change in the CL spectrum as a function of the thickness of Au deposited on mirrorlike GaAs is shown in Figure 7.14 (Viturro *et al.*, 1986). The spectrum of a mirrorlike cleaved surface consists of a near-band-edge emission at 1.42 eV and a lower-energy broad emission structure. With the deposition of Au on mirrorlike *n*-type GaAs (110), the 0.8-eV emission is shifted slightly to lower energies for metal thicknesses of 0.5 and 5 Å, and, subsequently, with increasing metal thickness, a new band centered at 0.75 eV appears, dominating the emission for metal thicknesses ≥15 Å (Viturro *et al.*, 1986). The evolution of a new feature in the luminescence spectra in this case differs from the results obtained in InP (Figure 6.32). Figure 7.14 shows that the low-energy CL spectroscopy can be effectively used to distinguish between interface states formed by metal deposition and those related to the bulk (Viturro *et al.*, 1986, 1987a).

Viturro *et al.* (1987b), by providing spatially resolved measurements of the CL intensity of Al/InP, also demonstrated the existence of interface states at

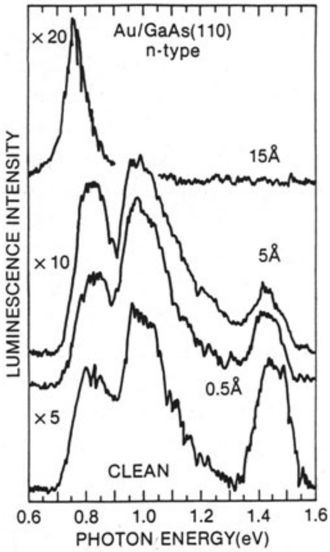

Figure 7.14. CL spectra of clean, mirrorlike *n*-GaAs (110) with increasing Au deposition. (After Viturro *et al.*, 1986.)

cleavage steps and the dependence of the CL emission on electron beam injection level. The density and spatial distribution of such states would imply different band bending and, therefore, different Schottky-barrier heights. Thus, low-energy CL spectroscopy reveals nonuniformities in charge transport and rectification at III-V metal-semiconductor interfaces (Viturro *et al.*, 1987b).

Using low-energy CL spectroscopy in conjunction with PL spectroscopy and soft x-ray photoemission, Viturro *et al.* (1988a,b) elucidated mechanisms of Schottky-barrier formation in III-V compound semiconductors. Their results, which revealed differences in interface properties between MBE-grown GaAs and melt-grown material, suggested a role for higher bulk defect densities in Schottky-barrier formation. Thus, it was concluded that both chemical interactions and the properties of bulk crystals can affect Schottky-barrier formation (Viturro *et al.*, 1988a). Viturro *et al.* (1988b) also provided experimental evidence for the origin of Fermi level "pinning" at metal–meltgrown–GaAs junctions. They showed that the presence of a high concentration of extrinsic defects (due, e.g., to native defect segregation from the bulk, interdiffusion, or chemical reaction) causes the pinning behavior. Thus, it was concluded that in melt-grown GaAs, it is atomic relaxation, rather than electronic, at metal-semiconductor interfaces that leads to the Schottky-barrier height insensitivity to metal work function (Viturro *et al.*, 1988b).

Interface properties of semiconductor heterostructures can be investigated by combining STEM with CL-STEM analysis. For example, Petroff and Logan (1980) investigated structural and compositional properties of interfaces between $Ga_{1-x}Al_xAs$ and GaAs layers grown by liquid phase epitaxy (LPE). These studies confirmed compositional variations at the interface. The Al concentration was found to vary on a scale of 10–50 μm in the plane of the interface. These variations, which were attributed to fast Al redistribution during the substrate dissolution period that initiates the growth of the LPE layer, will modify the conduction-band barrier height (Petroff and Logan, 1980). In addition, Petroff and Logan (1980) observed deep levels associated with Ge-doped $Ga_{1-x}Al_xAs$ layers and also features corresponding to variations in the Al concentration and impurity segregation producing recombination centers. The presence of these interfacial features are important for devices that require good carrier confinement and uniform injection (Petroff and Logan, 1980). Using low-temperature luminescence and transmission electron microscopy, Petroff *et al.* (1984) found that in GaAs quantum well (QW) superlatticies grown by molecular beam epitaxy on (100) GaAs, a getter smoothing effect of QW structures leads to impurity trapping and improved GaAs quantum wells with smooth interfaces.

Magnea *et al.* (1985) demonstrated an additional capability of CL spectroscopy in characterizing III-V compound heterostructure interfaces by applying a reverse-bias voltage and observing selective CL quenching at each layer. The latter is due to the fact that, with the application of a reverse-bias voltage, the edge of the depletion layer can reach each of the interfaces successively, resulting in selective CL quenching due to the electric field–induced separation of electron-hole pairs and the loss of minority carriers that diffuse to the depleted zone prior to recombination (Magnea *et al.*, 1985). They applied this method to InP/InGaAs and AlInAs/InGaAs interfaces. The CL spectrum (recorded at 17 K and zero bias) of an InP/$Ga_{0.47}In_{0.53}As$ avalanche photodiode with quaternary layers is shown in Figure 7.15. In this spectrum, the recombination bands associated with each layer are indicated in the figure. Each ternary (T) and quaternary (Q) layer exhibits two components separated by 20 meV. The relatively more intense CL bands from the ternary and quaternary layers were attributed to an exciton-ionized-donor complex, and the smaller peaks were attributed to donor-acceptor pair recombination. The effect of the reverse-bias voltage on the CL emission is shown in Figure 7.16, which reveals CL quenching at 17 K in the Q layers and at 17 and 300 K in the T layers, and which also presents the variations in the EBIC signal of the p^+-n junction. The punch-through voltages, derived from C-V measurements, of the InP/Q_1 and Q_1/Q_2 interfaces are indicated by double arrows. The behavior of the Q_1^1 emission was attributed by Magnea *et al.* (1985) to the progressive removal of holes generated in the InP. These holes diffuse and subsequently recombine in the Q_1 layer of the device. Increasing the reverse-bias voltage beyond the punch-through voltage leads the CL intensity to drop to zero due to the reduction in minority carrier density because of drift through the depletion zone. This is accompanied by an increase of the EBIC signal.

The behavior of the Q_1^2 emission is different. It increases at the punch-through voltage and then sharply drops to zero when the electric field reaches the

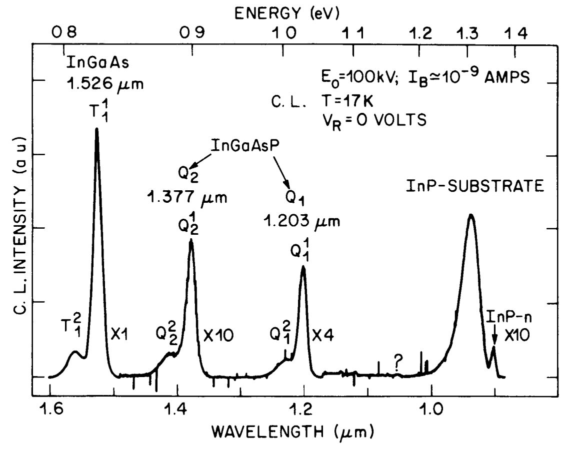

Figure 7.15. Low-temperature CL spectrum of an InP/$Ga_{0.47}In_{0.53}As$ avalanche photodiode with quaternary layer at zero bias voltage. (After Magnea *et al.*, 1985.)

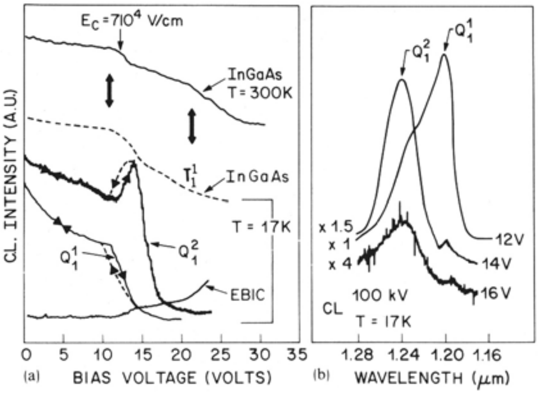

Figure 7.16. (a) Curves of CL quenching as a function of reverse bias voltage for an InP/$Ga_{0.47}In_{0.53}As$ avalanche photodiode. The punch-through voltages (deduced from C-V measurements) of the InP/Q_1 and Q_1/Q_2 interfaces are indicated by the double arrows. (b) CL spectra of the Q_1 layers recorded at different values of reverse bias voltage. (After Magnea *et al.*, 1985.)

critical field for total hole extraction. Magnea *et al.* (1985) attributed this effect, which is observed for the CL spectra in Figure 7.16b recorded for different values of the reverse-bias voltage around the punch-through value, to the competition between Q_1^1 and Q_1^2 transitions in the presence of an electric field. The presence of a hysteresis in the CL quenching curve was proposed to be due to a modification of the occupancy of interfacial deep centers with the electric field (Magnea *et al.*, 1985). This technique provides depth-resolved information on radiative and nonradiative processes at the heterostructure interfaces, and it may also be used to obtain spatially resolved monochromatic images of radiative centers and deep traps at the interface (Magnea *et al.*, 1985; Petroff, 1985).

Cathodoluminescence studies of the effect of heat treatment on the interaction of AuGeNi contact components with *n*-type InP were reported by Graham *et al.* (1985), who observed a reduction in CL intensity at the contact interface. However, unlike the AuGeNi/GaAs case in which Ge indiffusion into GaAs during heat treatment results in n^+ doping of the layer, no evidence of n^+ doping of the InP was observed despite the presence of Ge several microns into the material (Graham *et al.*, 1985).

7.2.5. Quantum Wells

Cathodoluminescence microcharacterization can be effectively applied to artificial structures, such as quantum wells. By using modern growth techniques (such as MBE) for epitaxial layers, it recently became possible to construct artificial structures in which layers of different materials and/or thickness alternate.

The period of the layers may be as small as a few monolayers. Such structures have the properties of two-dimensional (2D) or one-dimensional (1D) systems.

Cathodoluminescence studies of structures with carrier confinement to one and zero degrees of freedom in GaAs/AlGaAs QW wires and boxes were described by Cibert *et al.* (1986a) and Petroff (1987). In these structures, the carriers are confined by surrounding a semiconductor layer with wider band-gap layers. For layer thicknesses <500 Å, such structures exhibit quantum properties. If the in-plane width of the smaller band-gap layer is sufficiently fine to form a wire (<1000 Å), carrier confinement with one degree of freedom for motion along the wire will produce a QW wire. Confinement of carrier motion to zero degrees of freedom will be obtained for the smaller band-gap layer region in the form of a box. Such increasing carrier confinement will greatly affect the electrical properties of the layer, and, in fact, increased carrier mobilities and new device properties are expected for the quantum wires (Sakaki, 1980). The carrier confinement will also influence the optical properties of the layer as the result of changes in the spectra of carrier energies and in the relaxation of excited carriers and interactions between them.

Low-dimensional structures can be produced by using local interdiffusion between the narrow and wider band-gap material (Petroff, 1987). Such a localized change in the band gap can be realized in GaAs/AlGaAs quantum wells by interdiffusing selectively the Ga and Al across the interface (Cibert *et al.*, 1986a,b; Petroff, 1987). Such QW structures were produced by Ga ion implantation and rapid thermal annealing, using implantation-enhanced interdiffusion of Ga and Al across the GaAs/AlGaAs interfaces (Cibert *et al.*, 1986b). The enhancement of the interdiffusion is related to the presence of implantation-induced defects. GaAs single quantum wells with a typical thickness of 50 Å, surrounded by 500 Å $Al_{0.35}Ga_{0.65}As$ barriers, were grown by MBE with a 5000 Å GaAs buffer layer on (100) GaAs (Cr-doped) substrates. For use as ion-implantation masks, arrays of metal pads (100 × 100 μm) and thin lines and dots (with sizes $500\ \text{Å} \leq w \leq 1\ \mu\text{m}$) were deposited on the sample surface by electron beam lithography. Following Ga^+ ion implantation at room temperature and the removal of the metal masks by etching, rapid thermal anneal of the ion-damaged structures was performed at 900°C. Low-temperature (≤15 K) CL microscopy and spectroscopy (using STEM) were used for microcharacterization of the QW structures (Cibert *et al.*, 1986a).

Cathodoluminescence spectra for a series of quantum well wires of differing mask widths are presented in Figure 7.17. For mask sizes smaller than 3000 Å, on the high-energy side, a new series of luminescence lines develop, which are attributed to transitions between excited and ground levels of electrons within the quantum well (Cibert *et al.*, 1986a). The measured energy of the CL lines as a function of the metal mask width is presented in Figure 7.18, which also shows scatter (within a 2–3 meV range) in energy values for the same line measured on different QW wires with the same nominal mask size. The monochromatic CL

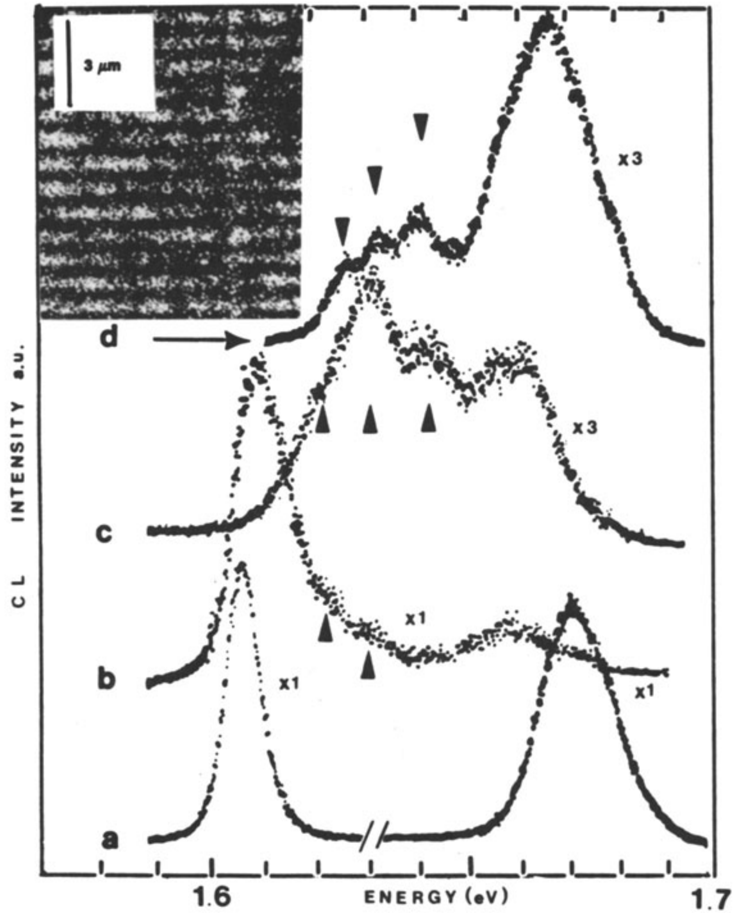

Figure 7.17. Low-temperature (≤15 K) CL spectra of (a, left) wide masked areas, (a, right) wide interdiffused areas, and of a series of quantum well wires with mask widths of (b) 4500 Å, (c) 1700 Å, (d) 1400 Å. The insert is a monochromatic CL micrograph (recorded at 1.647 eV) of the quantum well wires, which appear as bright areas. (After Petroff 1987.)

images (see the insert in Figure 7.17), recorded at energies corresponding to the new luminescence lines, show nonuniformities of the CL along the QW wire axis. The apparent width of the quantum well wires in the CL monochromatic image is defined by the carrier diffusion length (which is about 1 μm). The nonuniformities in the monochromatic CL images were found to be related to the fact that the energies of the new luminescence lines are shifted by about 2–3 meV from point to point along the wire (Cibert *et al.*, 1986a). This was attributed to

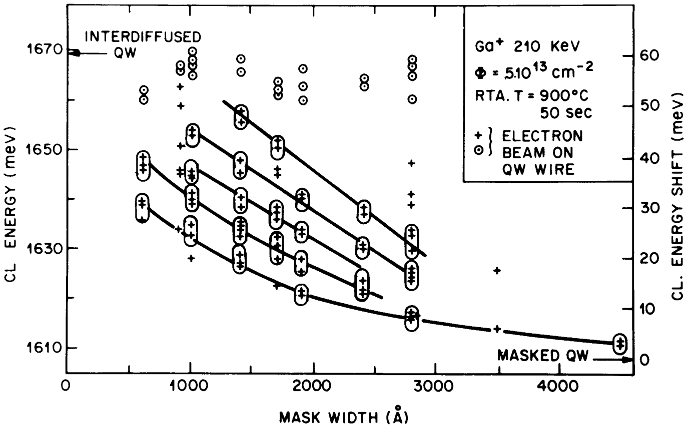

Figure 7.18. Low-temperature CL line energy as a function of mask width for quantum well wires. The arrows correspond to large masked or implanted areas. A cluster of points around the same energy indicates measurements on several quantum well wires with the same nominal mask size. (After Cibert *et al.*, 1986a.)

changes in the local width of the QW wires due to the presence of defects in the implanted interdiffused areas affecting the lateral interdiffusion (Petroff, 1987). Qualitatively similar results were reported for quantum well boxes, shown in Figure 7.19, formed with an array of metal dots 2800 Å in size (Cibert *et al.*, 1986a). The monochromatic CL image shows nonuniformities in the luminescence intensity from one box to another (Figure 7.19), since not all the QW boxes are identical in the array (Cibert *et al.*, 1986a; Petroff, 1987). In fact, monochromatic CL images recorded at photon energies differing by a few meV from that used in Figure 7.19 were reported to reveal boxes that are missing in that micrograph (Cibert *et al.*, 1986a; Petroff, 1987).

Petroff *et al.* (1987) demonstrated the application of low-temperature CL-STEM in the analysis of the abrupt interface produced by growth interruption during MBE growth of GaAs/AlGaAs single quantum wells and also of the interdiffused interface produced by Ga^+ ion implantation and annealing. Cathodoluminescence spectroscopy and microscopy revealed that growth interruption produces islands (i.e., atomically flat areas in an interface with monolayer thickness fluctuations) with sizes between about 0.6 μm and 1.5 μm. Similar results were reported by Bimberg *et al.* (1987), who quantified the reduction of the roughness of the QW interfaces with increasing growth interruption time by correlating the interface roughness with luminescence line shapes. As pointed out by Petroff *et al.* (1987), the estimation of island size should include several effects: (1) minority carrier diffusion; (2) capture by the quantum well (a thinner quantum well may have a lower cross section); (3) parallel transport of the carrier and

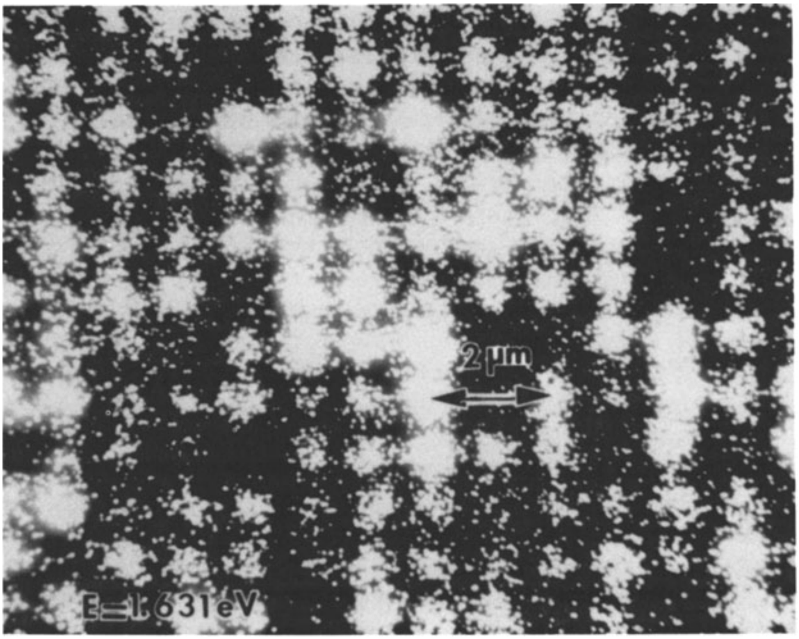

Figure 7.19. Monochromatic CL micrograph (recorded at 1.631 eV) of quantum well boxes, which appear as bright spots. (After Cibert *et al.*, 1986a.)

transfer of the exciton within the quantum well (in this case, thermal-effect-induced drift toward the thicker region of the quantum well may lead to carrier or exciton confinement due to the lower confinement energy); (4) tailing of the carrier wave function from one region of the quantum well into another that is less thick (this can lead to carrier excitation in a region near to that excited by the electron beam); and (5) efficient confinement of the electron beam–generated carrier or exciton to the thickest regions of the quantum well. The implantation-enhanced interdiffusion process was demonstrated to produce high-quality interfaces and fabricate QW structures (Cibert *et al.*, 1986b; Petroff *et al.*, 1987). The CL analysis of the QW wires and QW boxes indicated that the relative quantum efficiency of the QW box is several times that of the QW wire with the same mask size. The efficiency of the QW wire was found to be about twice that of a quantum well with the same thickness (Petroff *et al.*, 1987).

Bimberg *et al.* (1985b, 1986) applied time-resolved CL to undoped and Be-doped GaAs multiple quantum wells (MQW) of various thicknesses. Their results demonstrated that excitonic decay dominates carrier recombination in a quantum well for excess carrier densities less than 10^{17} cm^{-3}, and that structural

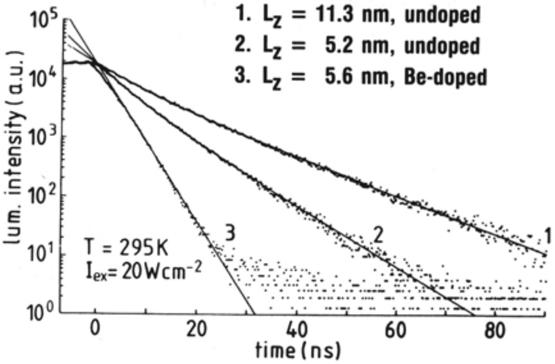

Figure 7.20. Room temperature CL decay (after long pulse excitation) of quantum wells with different widths L_z. (After Bimberg *et al.*, 1985b.)

localization induces an increase of intrinsic excitonic recombination probabilities as compared with carrier capture by impurities or traps, which are increasingly bypassed with decreasing QW width. This effect is illustrated in Figure 7.20, which shows the CL decay of quantum wells taken at room temperature for samples with different width and acceptor concentration. The radiative recombination probability increases with decreasing L_z, which is manifested by the decrease of lifetime (in agreement with theoretical predictions). Doping leads to the decrease of luminescence lifetime due to the participation of the additional excitonic radiative recombination channels. In contrast, recombination in bulk epitaxial GaAs occurs stepwise via impurities (Bimberg *et al.*, 1985b).

7.2.6. Microcharacterization of Stresses in Epitaxial Layers

7.2.6.1. Mismatched Heterostructures

III-V compounds grown on silicon and other lattice mismatched substrates are attractive systems for a variety of device applications (Milnes, 1986). These heterostructures would make it possible to integrate optical devices in the III-V compounds with, for example, silicon circuitry on a monolithic chip. III-V compounds offer a wide range of applications in optoelectronic devices; Si, on the other hand, offers both a convenient electronic device technology and a large area substrate that is mechanically stronger than GaAs and also has a larger thermal conductivity. Heterostructures based on III-V compounds, such as GaAs, AlAs, InAs, InP, and GaP, and their ternary and quaternary combinations, for example, are also of considerable interest in various device applications.

The major issues of concern in epitaxial heterostructures, such as GaAs layers grown on Si substrates (GaAs/Si) are (1) the presence of high dislocation densities (10^7–10^8 cm^{-2}) due to the lattice constant mismatch between GaAs and Si, (2) stresses in the GaAs/Si epitaxial layers due to the difference in thermal expansion coefficients of these materials (the stress is thought to arise during cooldown from a stress-relaxed condition at the growth temperature), and (3) the presence of antiphase domains. In such heterostructures, the defect densities are significantly reduced in regions away from the heterojunction interface (Sheldon *et al.*, 1985b). However, although the properties of the epitaxial layers are expected to improve as the layer thickness increases, for thicknesses greater than about 5 μm the layers often contain microcracks. Other dislocation-blocking techniques, such as growth interrupts, thermal cycling, and the incorporation of strained-layer superlattices can be successfully used (Sheldon *et al.*, 1988; Yamaguchi *et al.*, 1988). The presence of stress in the epitaxial layers grown on mismatched substrates is troublesome in device applications, since it leads to the modification of the band structure of the epitaxial layer and thus affects its optical and electrical properties. In addition, there is evidence that stress-induced migration of dislocations is most likely responsible for the degradation of optoelectronic devices based on GaAs grown on mismatched substrates (Yao *et al.*, 1987). CL analysis can reveal the presence of various defects, including microcracks, as well as nonuniformities in the optical properties of the epitaxial layers. In addition, the CL technique, in conjunction with the well-characterized behavior of light hole (LH) and heavy hole (HH) luminescence transitions in GaAs under stress (Zemon *et al.*, 1986), is a powerful tool for analyzing the spatial uniformity of stress in these epitaxial layers. Such CL studies can reveal, for example, variations in stress associated (1) with the presence of microcracks in GaAs layers grown on Si substrates (Yacobi *et al.*, 1987) and (2) with the patterning of GaAs layers grown on both InP and Si substrates (Yacobi *et al.*, 1988a, 1989).

A typical example of the effect of microcracks on the optical properties of 10-μm-thick GaAs/Si (grown by MOVPE) layers is illustrated in Figure 7.21 (Yacobi *et al.*, 1987). In Figure 7.21a, the solid lines represent microcracks. Monochromatic images, shown for wavelengths of 819 nm and 829 nm in Figures 7.21b,c, respectively, illustrate the variation in luminescence contrast between regions near the microcracks and in the interior of the cells (defined as the areas enclosed by microcracks). It is evident from these micrographs that the dominant CL emission at $\lambda = 819$ nm is from the region of the microcracks, whereas the most intense CL emission at $\lambda = 829$ nm is from the interior of the cell. Variations of the CL intensity are also observable in the center of the cell, as well as at the intersections of the microcracks (Figure 7.21). Such variations are attributed to both nonradiative recombination at defects, such as dislocations, and to the surface roughness present in this particular GaAs layer. In general, surface roughness leads to nonuniform excitation, which may result in CL inten-

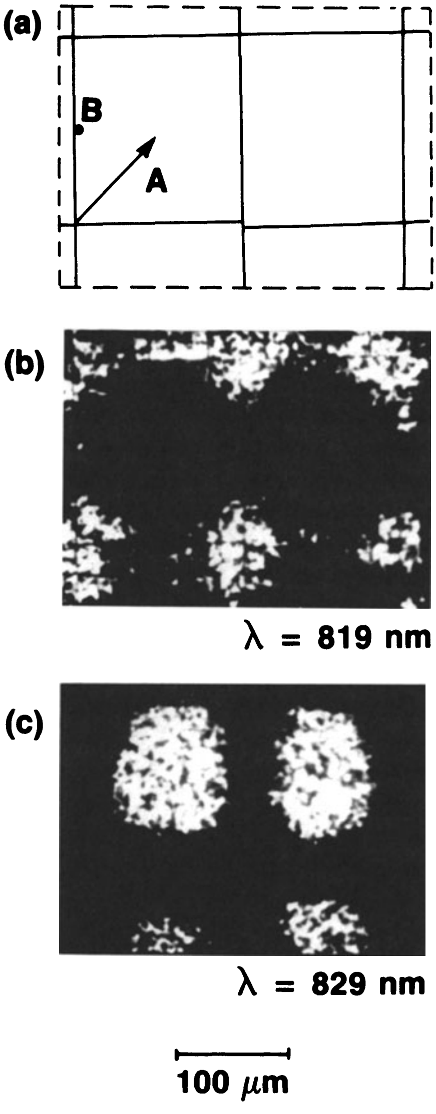

Figure 7.21. (a) Schematic diagram of a region of an MOVPE GaAs/Si sample containing microcracks indicated by the solid lines. Line *A* and point *B* indicate the positions where CL spectra were taken. (b) A monochromatic CL image recorded at 819 nm. (c) A monochromatic CL image recorded at 829 nm. The sample temperature is about 15 K. (After Yacobi *et al.*, 1987.)

sity variations. However, although another GaAs/Si sample (with a 5.7-μm GaAs layer grown by MBE) studied had a very smooth surface, it also exhibited similar CL contrast (Figure 7.22). Thus, at least in the latter case, this CL contrast can be identified with high defect densities. (Typical dislocation densities in these samples are between 10^7 and 10^8 cm^{-2}). However, although in these cases the CL contrast is most probably due to dislocations, derivations of their exact

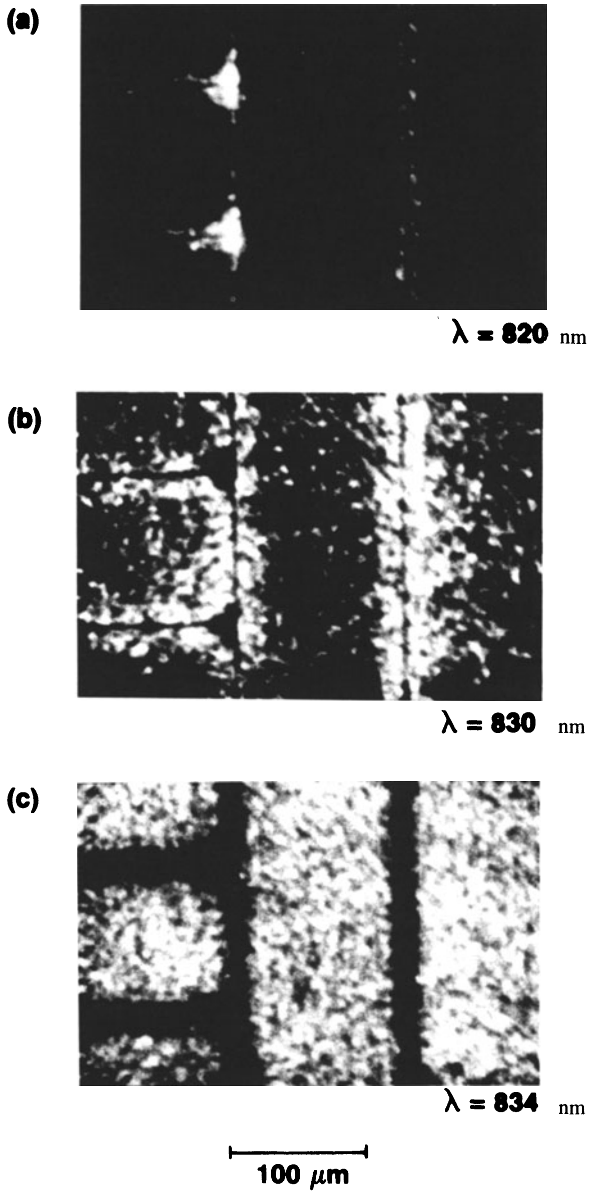

Figure 7.22. Monochromatic CL images of an MBE GaAs/Si sample containing microcracks indicated by the solid lines: (a) a monochromatic CL image recorded at 820 nm; (b) a monochromatic CL image recorded at 830 nm; (c) a monochromatic CL image recorded at 834 nm. The sample temperature is about 15 K. (After Yacobi and Sheldon, unpublished.)

concentration at this level would be unreliable (Section 6.1). (Transmission electron microscopy observations would be a reliable means for the determination of such high dislocation densities.)

Figure 7.23 presents CL spectra (recorded at about 15 K) as a function of position across the cell. For simplicity, only a few spectra are shown. These are the spectra from the intersection of two microcracks (spectrum a), 30 μm away from the intersection (spectrum b) along line A in Figure 7.21(a), and 70 μm away from the intersection (spectrum c) along line A. The luminescence peak taken at the intersection of two microcracks (spectrum a) is at 818.6 nm, while away from that intersection (spectra b and c), the peak shifts to longer wavelengths. In addition, in both spectra b and c, a shoulder is observed representing a second peak at shorter wavelengths. The peak wavelength of 818.6 nm at the intersection of two microcracks is similar to that of unstressed GaAs. The CL peaks obtained in the center of the cell occur at 828.7 and 823 nm. The dominant long-wavelength CL peak was identified as a HH exciton transition ($E_{1/2}$) and the shorter wavelength peak observed in spectra b and c was related to a LH exciton transition ($E_{3/2}$), as indicated in Figure 7.23 (Zemon *et al.*, 1986, 1987). The shift of $E_{1/2}$ to longer wavelengths accompanied by the increasing splitting between $E_{1/2}$ and $E_{3/2}$ (shown in spectra a, b, and c) is indicative of a monotonic increase in stress with distance from the intersection of two microcracks.

Figure 7.24 presents a detailed plot of the CL peak energies as a function of distance from the intersection of two microcracks (along line A in Figure 7.21a). For a distance greater than 20 μm, the data are consistent with a uniform biaxial tensile stress increasing from about 1 to 1.8 kbar (Zemon *et al.*, 1986, 1987). The latter is lower than the 2.5 kbar observed at liquid He temperatures in samples with no microcracks (Zemon *et al.*, 1987). It, therefore, would appear that, at least for the cell dimensions studied, microcracks reduce the overall stress in

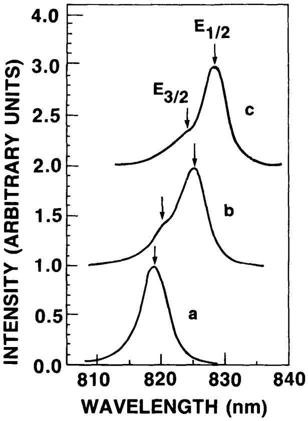

Figure 7.23. 15 K CL spectra of an MOVPE GaAs/Si specimen taken at different points along line *A* of Figure 7.21a: spectrum (a) is taken at the intersection of two microcracks, spectrum (b) at 30 μm from the intersection, and spectrum (c) at 70 μm from the intersection. Arrows indicate light ($E_{3/2}$) and heavy ($E_{1/2}$) hole exciton peaks. (After Yacobi *et al.*, 1987.)

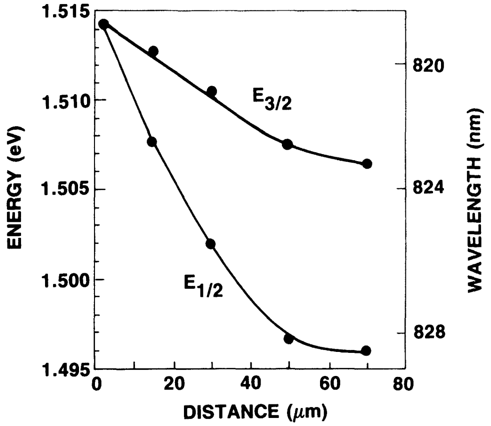

Figure 7.24. 15 K CL energy peaks as a function of distance from the intersection of the microcracks along line *A* in Figure 7.21a. $E_{3/2}$ and $E_{1/2}$ denote light and heavy exciton transitions, respectively. (After Yacobi *et al.*, 1987.)

these epitaxial layers. Moreover, the stress is lowest (i.e., close to zero) and the total luminescence intensity is highest at the intersection of the microcracks. Since the oscillator strengths of $E_{3/2}$ and $E_{1/2}$ are in the ratio of 3 : 1 (Pollak and Cardona, 1968), at zero stress where the $E_{3/2}$ and $E_{1/2}$ transitions are degenerate, a higher luminescence intensity is expected. This may explain in part the higher luminescence intensity at the intersections of the microcracks. Also note that in contrast to the stress relief at the intersections of the microcracks, along a microcrack (away from the intersection, for example, at point B in Figure 7.21a), the CL spectrum consisted of a dominant peak at 824.5 nm and a shoulder at 820 nm. At the edge of the microcrack, however, the two components of biaxial tension may not be equal, as will be discussed later for patterned layers.

In general, the CL results for the MBE GaAs/Si sample (5.9-μm GaAs layer) were similar to those described for the MOVPE sample. A monochromatic CL image at 820 nm (see Figure 7.25) indicates that the CL intensity between the microcracks separated by about 20 μm is nearly uniform, which suggests uniform stress. This was confirmed by analyzing the CL spectra between the microcracks.

Spectral analysis in all the samples studied indicated that the stress at the intersection of two microcracks is relieved. Since the microcracks are essentially naturally formed boundaries, these observations suggest studies of patterned epitaxial layers. In such epilayers, stress reduction can be achieved in a controlled manner, i.e., by patterning or selected-area epitaxy (Sheldon *et al.*, 1985a; Matyi *et al.*, 1987), and this would have important implications for device applications of heteroepitaxial structures.

A CL analysis of patterned GaAs was presented by Yacobi *et al.* (1988a, 1989). For the study of the stress variations in patterned heteroepitaxial layers, GaAs was grown using MBE on both InP and Si substrates. The thicknesses of

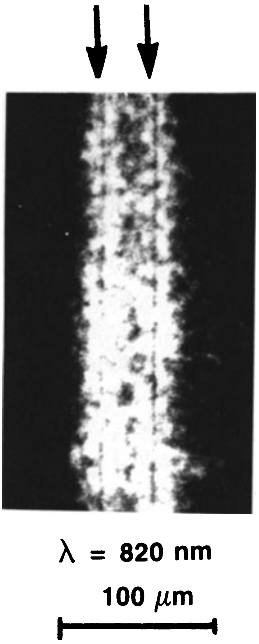

Figure 7.25. Monochromatic CL image recorded at 820 nm of an MBE GaAs/Ge/Si sample. Microcracks are indicated by arrows. The temperature was about 15 K. (After Yacobi *et al.*, 1987.)

the epitaxial layers were 4.25 μm for GaAs/InP and 2.7 and 5.9 μm for GaAs/Si, respectively. (For the latter system, a thin Ge buffer layer was grown prior to the GaAs deposition.) Epitaxial layers were patterned using standard photolithography techniques followed by etching (Yacobi *et al.*, 1988a).

As in the previous case of the microcracks, the energy positions of the LH and HH transitions and the separations between them were used for the quantitative analysis of the spatial variations of stress across etched patterns in GaAs. Cathodoluminescence observations indicated that the stress was predominantly uniaxial near the edge and changed to biaxial away from the edge of patterned regions. More importantly, it was found that, analogously to the case of the intersection of the microcracks, the stress is close to zero at convex corners and in small rectangular regions of the order of 10 μm. At concave corners, however, the stress is biaxial.

The epilayers were patterned to contain "frames" and "islands." The width of a frame was defined as the separation s between the adjacent outer and inner boundaries of a side, and the size of an island was defined as d. Various values of s and d between 10 and 200 μm for frames and 10 and 60 μm for islands were used. A 10-μm frame surrounding a 10-μm island is shown in Figure 7.26. Figure 7.27 shows monochromatic CL images of a GaAs/Si sample (the GaAs layer thickness was 5.9 μm) at 818, 824, and 832 nm. Note that in this figure, the lines (denoted by arrows) running across the patterned regions correspond to microcracks, which were accentuated by the etching. This figure clearly demonstrates that the convex corners and the edges in the patterned regions emit at shorter wavelengths than do the interiors of these regions. Variations of CL intensity in the interior of the patterned regions, which are clearly visible in Figures 7.27b,c, are due to the defects, such as dislocations and stacking faults.

Similar results were observed in the case of the GaAs/InP sample, shown in Figure 7.28. Figure 7.28a is a secondary electron image of the GaAs/InP sample containing patterned regions of different sizes. Frames examined are denoted as F1, F2, and F3 (partially visible) with frame widths of about 10, 80, and 200 μm, respectively. These frames surround rectangular patterned regions of different sizes, i.e., $d \sim 10$ μm in frame F1 and ~60 μm in frame F2. Figures 7.28b,c, which are monochromatic CL images at 818 and 824 nm, respectively, again exhibit CL variations, similar to the previous case of the GaAs/Si sample. In the case of GaAs/Si the magnitude of the stress is larger (~2.5 times at 4.2 K) than that observed in the GaAs/InP system because of the larger difference in the thermal expansion coefficients between the epilayer and the substrate for the former case. This is consistent with the lower magnitude of stress observed in the GaAs/InP system (~1 kbar at 4.2 K).

Examples of CL spectra recorded near the patterned edges and convex corners of the 80-μm frame (F3 of Figure 7.28a) are shown in Figure 7.29. Spectrum A was obtained from a region located approximately in the middle of frame F3 (denoted by M in Figure 7.28a). Two peaks, a dominant one at 823.8 nm (1.505 eV) and a subsidiary one at 820.4 nm (1.511 eV) are observed. These

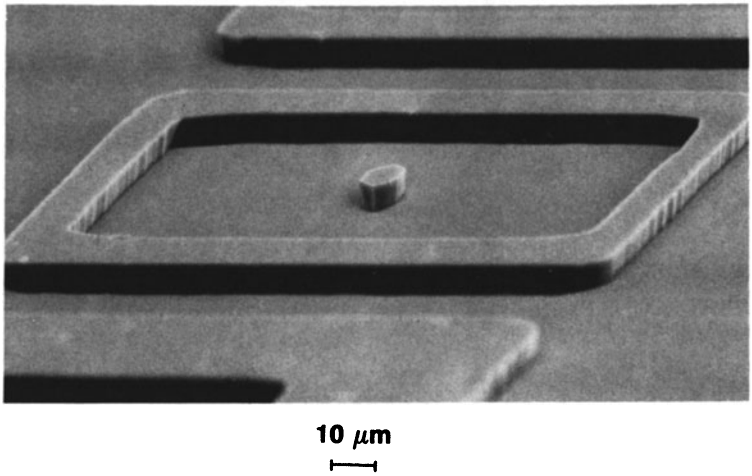

Figure 7.26. Example of a patterned GaAs/InP heterostructure. (After Yacobi *et al.*, 1989.)

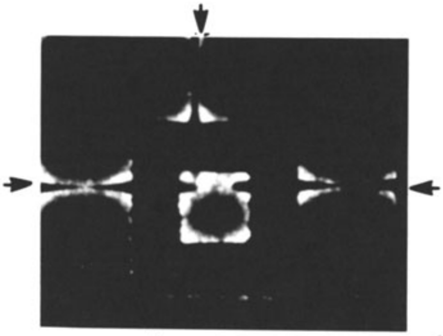

(a) λ = 818 nm

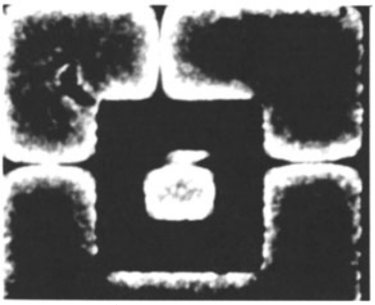

(b) λ = 824 nm

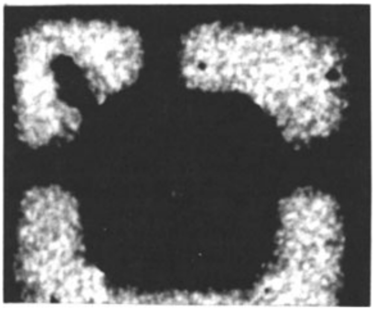

(c) λ = 832 nm

Figure 7.27. Monochromatic CL images of the GaAs/Si sample recorded at (a) 818 nm; (b) 824 nm; and (c) 832 nm. Microcracks are indicated by arrows in (a). The sample temperature is about 20 K. (After Yacobi *et al.*, 1989.)

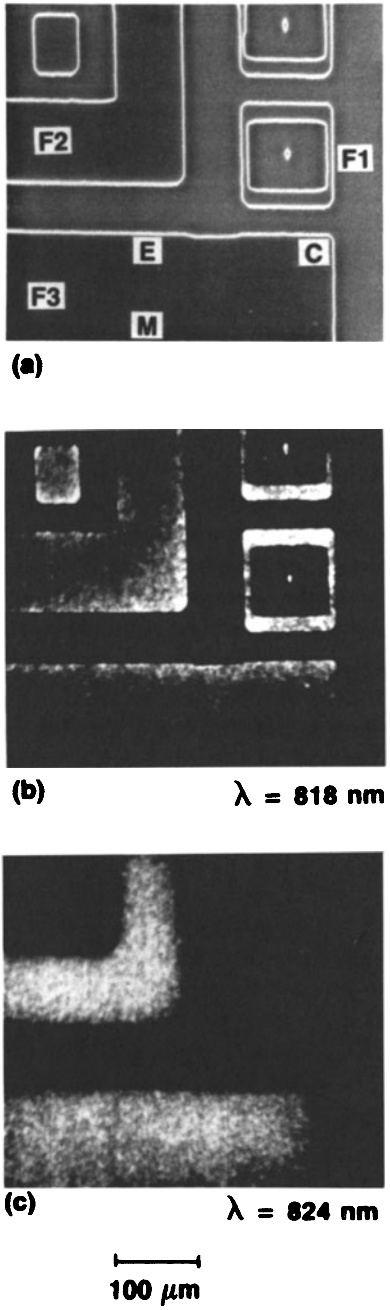

Figure 7.28. (a) A secondary electron image of a patterned region of the GaAs/InP sample; F1, F2 and F3 denote frames, and C (corner), E (edge), and M (middle) indicate the positions where CL spectra were taken (as shown in Figure 7.29). (b) A monochromatic CL image recorded at 818 nm. (c) A monochromatic CL image recorded at 824 nm. The sample temperature is about 20 K. (After Yacobi *et al.*, 1989.)

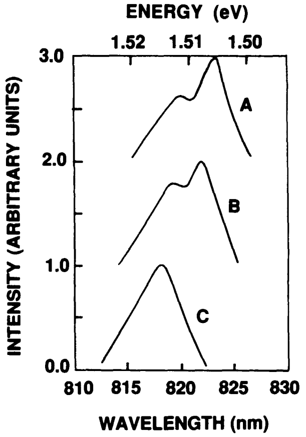

Figure 7.29. CL spectra of the GaAs/InP sample taken at different positions on frame F3 (see Figure 7.28a): spectrum A was taken in the middle (M) of the frame, spectrum B at the edge (E), and spectrum C at the corner (C). The temperature was about 20 K. (After Yacobi *et al.*, 1988a.)

peaks are associated with HH and LH transitions observed in the low-temperature luminescence as a result of the in-plane stress in the heteroepitaxial GaAs (Zemon *et al.*, 1986, 1987). At the edges of the patterned regions (denoted by *E* in Figure 7.28a), away from the corners, the CL spectrum (see spectrum *B* in Figure 7.29) is shifted to shorter wavelengths, with the splitting between the two peaks remaining the same (within experimental error). Spectrum *C* in Figure 7.29 was taken at a convex corner denoted by *C* in Figure 7.28a. Identical spectra were obtained at all the convex corners examined as well as in rectangular regions with dimensions ≤10 μm. In this spectrum we observe only one peak at about 818 nm (~1.515 eV) which is close to the value expected for unstressed GaAs.

The results of analyses of these observations in the GaAs/InP sample are summarized in Figures 7.30 and 7.31. Figure 7.30 shows the peak energies

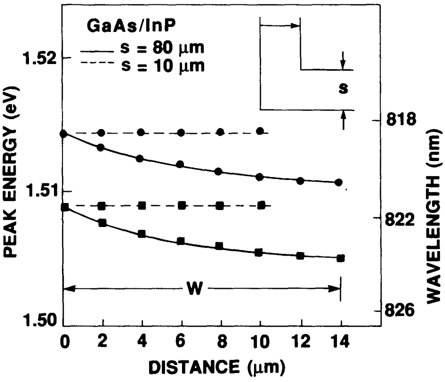

Figure 7.30. The CL peak energy for GaAs/InP as a function of distance *x* along the width of frame F2 (the horizontal arrow in the inset indicates schematically the line along which distance was measured). (After Yacobi *et al.*, 1989.)

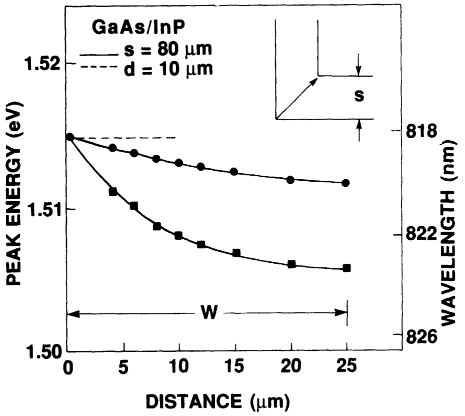

Figure 7.31. The CL peak energy for GaAs/InP as a function of distance x along the line from the convex corner to the concave corner of a frame (see inset). The dashed line represents the data for an island with dimensions ~ 10 × 10 μm^2. (After Yacobi *et al.*, 1989.)

measured at different points along the width of frame F2. The horizontal arrow in the inset of Figure 7.30 indicates schematically the line along which the distance was measured. A gradual shift of the two peaks to lower energies is observed in the first 10 μm from the edge (the transition region is denoted W), after which the peak energies remain constant. It is important that for a frame with $s \approx 10$ μm, no measurable change in peak energies as a function of distance was observed. Results obtained for the spectra taken along the line from the convex corner to the concave corner are shown in Figure 7.31. Only one peak at 1.515 eV (818.0 nm) is observed at the convex corner. With increasing distance x the spectrum splits into two components that shift to lower energies. For $x > 30$ μm the two peaks are at about 1.511 eV (820.4 nm) and 1.505 eV (823.8 nm), respectively. These observations can be explained by the following considerations. When the GaAs epilayer is under uniform biaxial tensile stress, the strain components parallel and perpendicular to the edge, $\epsilon_{\parallel}$ and $\epsilon_{\perp}$, respectively, are equal in magnitude. At the edge, $\epsilon_{\perp}$ is expected to be zero, since the lattice is free to relax perpendicular to the edge. Thus, at $x \approx 0$, we can assume $\epsilon_{\perp} \approx 0$ resulting in a uniaxial tensile stress parallel to the edge of the pattern. The gradual change in the CL peaks is due to the gradual increase of the biaxial component of the stress for increasing x.

It is known that the rates of decrease in the energies of the LH and HH transitions from their unstressed values are 4.85 meV/kbar and 10.23 meV/kbar, respectively, for in-plane biaxial tensile stress (Pollak and Cardona, 1968; Chandrasekhar and Pollak, 1977). For uniaxial tension parallel to $\langle 110 \rangle$, the LH and HH transitions decrease in energy from their unstressed values at a rate of ~6.1 meV/kbar and ~1.4 meV/kbar, respectively (Pollak and Cardona, 1968; Chandrasekhar and Pollak, 1977). Data for a distance greater than ~10 μm away from the edge (Figure 7.30) and for $x > 30$ μm from the convex corner (Figure 7.31) can be fitted to uniform biaxial tensile stress of about 1 kbar. Data recorded at the edges of patterned regions, however, are best fitted by assuming a uniaxial tensile stress of the same magnitude directed along the edge. With increasing distance from the edge, we assume that $\epsilon_{\perp}$ increases from 0 at $x = 0$ to its maximum value $\epsilon = \epsilon_{\perp} = \epsilon_{\|}$ at $x \geq 10$ μm.

At the intersection of two edges at a convex corner, stress is relieved since the strain components perpendicular to *both* edges are expected to be zero. This is consistent with our experimental observation of a single CL peak at about 1.515 eV (818.0 nm) in the convex corner. For rectangular islands with $d \leq 10$ μm, the stress is uniformly relieved (see the dashed line in Figure 7.31).

To examine the effect of epilayer thickness on the transition width *W*, a comparison was made of the CL measurements on two GaAs/Si samples with epilayer thicknesses of 2.7 and 5.9 μm. The transition width *W* for the 5.9-μm case is ~1.5 times larger than the value for the 2.7-μm sample. This clearly indicates that *W* scales with epilayer thickness as expected.

In summary, the stress in patterned GaAs grown on mismatched substrates gradually changes from uniaxial at the edge to biaxial away from the edge (within ~10 μm). For patterned islands with dimensions ~10 × 10 μm^2, the stress is relieved, leading to possibilities for improved heteroepitaxial device performance. In larger patterned regions, the stress-induced changes in the optical properties have important implications for the design of optoelectronic devices based on GaAs heteroepitaxy.

7.2.6.2. Quantum Wells

Cathodoluminescence microscopy and spectroscopy can also be applied to the analysis of metallization-induced stress variations in MQW structures. These structures are especially attractive for optoelectronic device applications because of the presence of excitons at room temperature. To produce device configurations, these structures always require some processing, such as metallization. This is used in MQW structures for the application of electric fields in order to modulate the optical properties of the layers, and to form metal strip-loaded optical waveguides (Hunsperger, 1982) and waveguides associated with the strain-induced variation in the refractive index produced underneath the edge of the metal stripes (Li Kam Wa *et al.*, 1985). Yacobi *et al.* (1988b) presented an experimental observation of the stress variations in GaAs/AlGaAs MQWs underneath the gold metal edges. From the shift of the luminescence peaks, they estimated the stress at these edges and the resulting change in the refractive index.

Figure 7.32 presents a schematic diagram of one of the structures studied by Yacobi *et al.* (1988b). Openings D1 and D2 of 50 and 150 μm in diameter, respectively, were chemically etched. The total thickness of the sample in the etched area was about 2 μm. The thickness of the top gold layer was 0.4 μm. Both room-temperature and low-temperature CL from the etched 150 μm open-

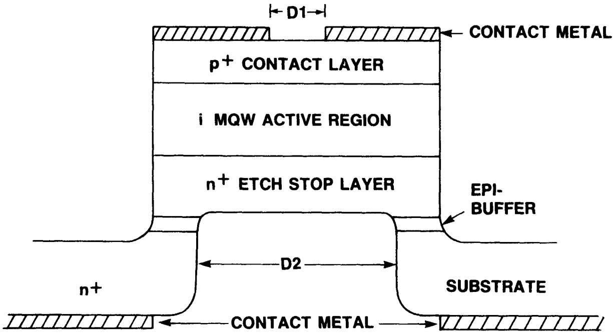

Figure 7.32. Schematic diagram of the sample used in CL measurements. The MQW active region contains 25 periods of 70-Å GaAs quantum wells separated by 80-Å $Al_xGa_{1-x}As$ barriers ($x \sim 0.2$). Openings D1 and D2 are 50 μm and 150 μm across, respectively, and the thickness of the contact metal is 0.4 μm. (After Yacobi *et al.*, 1988b.)

ing of the device were monitored in order to study the region underneath the top gold contact. Figure 7.33 presents the CL monochromatic image (recorded at 780 nm at ~20 K) of the MQW region. The dark ring in this micrograph corresponds to the region underneath the edge of the metal ring. Normalized luminescence spectra recorded at ~20 K from the dark ring (curve *B*) in Figure 7.33 and regions either side of the ring (curve *A*) are presented in Figure 7.34. The peak intensities of spectra *A* and *B* were similar within a factor of 2. The luminescence emission from the dark ring in Figure 7.33 is shifted by about 2 nm to longer wavelength with respect to the luminescence from the region away from the ring, indicating the presence of tensile stress of the order of 1 kbar in the region of the dark ring (Jagannath *et al.*, 1986). This observation is in qualitative agreement with the calculations of Kirkby *et al.* (1979) who predicted stress variations in the vicinity of the metalization edge. They showed that the stress is largest (by more than factor of 2) ~1 μm below the metal-semiconductor interface. This is consistent with the presence of a dark ring in Figure 7.33. Some small variations in the emission peak wavelength were also observed in regions away from the dark ring. These variations were found to be associated mainly with imperfect processing of these structures. Room-temperature CL measurements were also performed. The shift in the CL peak (~2 nm) was similar to the low-temperature result.

In another case, gold stripes, 100 μm wide and 0.4 μm thick separated by 8-μm openings, were deposited on the surface of the epitaxial layer. In this case, CL measurements were performed by using the edge-on configuration. These results are shown in Figure 7.35. Figure 7.35a is a backscattered electron image (BEI), which distinctively highlights a gold contact from the MQW structure. Also visible is an interface between the GaAs substrate and the MBE-grown

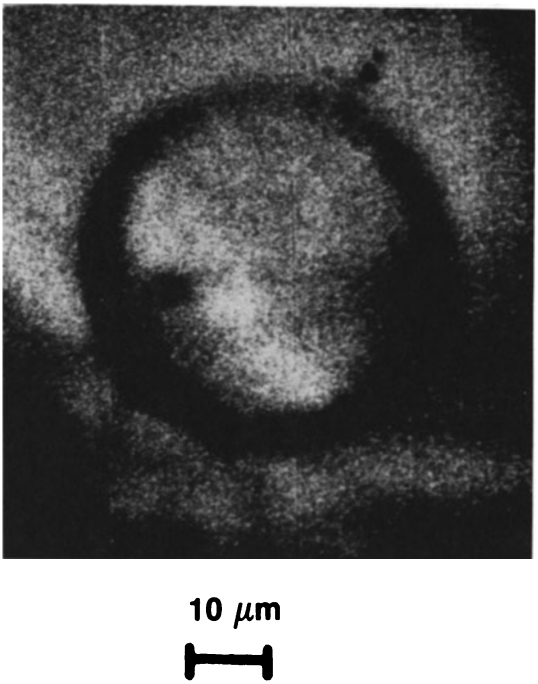

Figure 7.33. Monochromatic CL image of the sample, shown in Figure 7.32, recorded at 780 nm. The sample temperature was about 20 K. (After Yacobi *et al.*, 1988b.)

epitaxial layers. Figure 7.35b shows a low-temperature monochromatic CL image recorded at 790 nm, which is the peak of the emission spectrum from the quantum wells underneath the gold contact edges. Spectra recorded from the region between the bright regions (Figure 7.35b) indicate ~1.5-nm shift to shorter wavelength. This shift corresponds to the presence of a tensile stress of

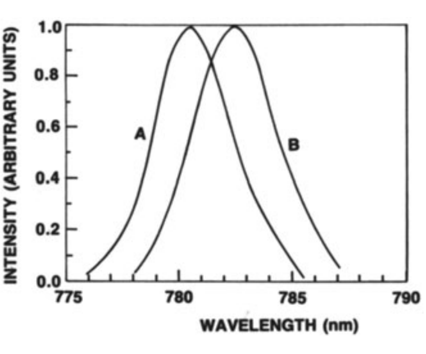

Figure 7.34. Normalized CL spectra (recorded at about 20 K) from the dark ring (see Figure 7.33), marked B, and a region away from the ring, marked A. The spectrum corresponding to the dark ring is shifted to longer wavelengths. (After Yacobi *et al.*, 1988b.)

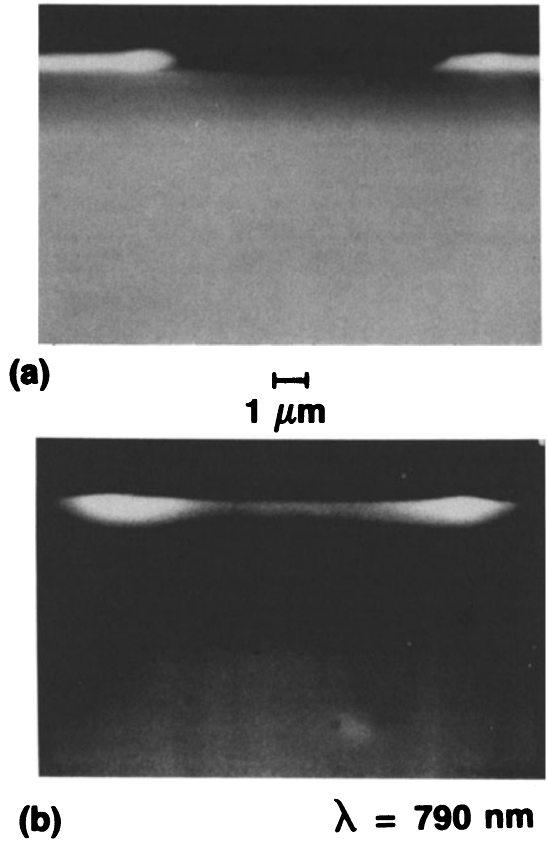

Figure 7.35. SEM micrographs of the waveguide structure: (a) backscattered electron image (BEI); (b) monochromatic CL image recorded at 790 nm. The thickness of the metal layer is about 0.4 μm. (After Yacobi *et al.*, 1988b.)

the order of 1 kbar in the QW region underneath the gold stripe edges. It is well known that the presence of stress in GaAs results in a change in the refractive index through the photoelastic effect (Kirkby *et al.*, 1979). A stress of ~1 kbar results in a change in the refractive index (Kirkby *et al.*, 1979) $\Delta n \approx 0.01$. This value of Δn is sufficient to support a single mode (at $\lambda \sim 1$ μm) in a ~1-μm-thick waveguide (Hunsperger, 1982). This result is consistent with the experimental observation of waveguiding in a similar geometry (Li Kam Wa *et al.*, 1985). The estimated change in the refractive index due to the stress-induced shift in the band gap (Pankove, 1971) is $\sim 10^{-3}$. Thus, it was concluded that the change in the refractive index is mainly due to the photoelastic effect.

In summary, CL microscopy and spectroscopy, in conjunction with the known behavior of the optical transitions in the presence of stress, can be effectively used for the quantitative analysis of spatial variations of stress in epitaxial layers.

7.3. II-VI Compounds

The Zn and Cd chalcogenides (compounds with O, S, Se, and Te) are all *n*-type as grown, except ZnTe, which is *p*-type. Only in CdTe can the conductivity type be changed by doping, and CdS and ZnSe can be doped to produce a small majority of holes, i.e., π-conductivity. [For general background on these materials see Aven and Prener, 1967, Ray, 1969, and the proceedings of the II-VI conferences: *J. Crystal Growth* **59** (1982), **72** (1985), and **86** (1987).] For device applications, it is possible to form heterojunctions in which the *n*- and *p*-sides of the junction are of different II-VI compound materials. It is also possible to use metal-semiconductor and metal-insulator-semiconductor contacts for carrier-injection device applications. All the II-VI compounds have direct band gaps (see Table 3.1), so efficient luminescence can be expected in these materials.

As mentioned in Section 3.1, in the phosphor field, a luminescence terminology is used which differs from that for semiconductors. The luminescence behavior of II-VI compounds, as that of other materials, is modified by the incorporation in the material of activators (luminescence center impurities) and coactivators (which increase the solubility of the activators). In II-VI compounds, activators (e.g., Cu, Ag, Mn) occupy group II cation lattice sites and act as deep acceptor levels, and some coactivators (e.g., Cl, Br, I) occupy anion sites and others (e.g., Al, Ga, In) occupy cation sites forming deep donor levels (see Table 7.1). Native defects, such as Zn and S vacancies, can provide self-

Table 7.1. Ionization Energies (in eV) of Donors and Acceptors in Some II-VI Compounds*

	CdS	CdTe	ZnS	ZnSe
Donors[a]				
Al, Ga, In, Cl, Br, I, F or native	0.024–0.032	0.011–0.022	>0.014 0.2–0.3[b]	0.021–0.023 0.19–0.21[b]
Acceptors				
Native-impurity complex	(E_G–0.09)	(E_G–0.056)		(E_G–0.16)
V_{Zn}^{-} or V_{Cd}^{-}		0.05		
V_{Zn}^{2-} or V_{Cd}^{2-}		E_G–0.6		
Cu		0.33–0.35	1.2	0.75
Ag		0.3–0.33		
Au		0.33–0.4		

[a] Not intentionally doped material but containing one or more of the indicated donor impurities.

[b] Levels observed in halogen-doped ZnS and ZnSe, but not necessarily identified as isolated donors.

*After Devlin, 1967.

activation and coactivation for the luminescence in these materials. As will be discussed in the following section, an important problem in device applications of the II-VI compounds is apparent "self-compensation" in these materials. This hypothetical phenomenon of the generation of native point defects of a type that compensate dopant atoms and prevent the formation of *p-n* junctions in these wide-band-gap semiconductors may be responsible for the absence of optoelectronic device applications.

Three types of "extrinsic" luminescence mechanism (see Section 3.2 and Figure 3.2) are important for the luminescence analysis of II-VI compounds. These are known in the phosphor field as the Lambe-Klick model (donor-to-free-hole transition, D^0h), the Schön-Klasens model (free-electron-to-acceptor transition, eA^0), and the Prener-Williams model (donor-acceptor pair recombination).

Luminescence centers and mechanisms of luminescence emission in II-VI compounds were described by Curie (1963), Shionoya (1966), and Ray (1969). Although some cases were described on the basis of a single mechanism, many details of II-VI luminescence are uncertain. Some important emission bands in these materials are, for example, self-activated and those involving impurities such as Cu, Ag, and Mn. The luminescence emission often detected in nominally undoped ZnS crystals is a broad band (with a maximum at about 2.6 eV) called *self-activated emission,* and it is essentially observed as a result of heat treatment of the material with a halogen such as Cl. Although various models for the self-activated emission were proposed, it appears that the luminescence center is a pair consisting of a zinc vacancy and a substitutional Cl impurity on an adjacent sulfur site, i.e. (V_{Zn}-Cl_S). The self-activated emission is thus a DAP recombination radiation with the transition occurring from the donor state of an isolated Cl ion (or other coactivators such as Al or Ga) to the (V_{Zn}-Cl_S) acceptor center. Several models were proposed for Cu center luminescence, which is strongly affected by the type and concentration of coactivators present in the material (Curie, 1963; Shionoya, 1966; Ray, 1969). Van Gool (1961) and Shionoya (1966) provided a diagram of the relation between the type (i.e., the color) of the luminescence and the concentrations of both the activators (Cu, Ag, Au) and coactivators (Al, Ga, In) in ZnS. The luminescence in ZnS associated with a transition metal such as Mn, which has an incomplete *d* electron shell, is due to the recombination via the inner atomic levels of the Mn^+ ion, i.e., due to transitions between energy levels corresponding to the excited states and the ground state of the Mn^+ ion.

In II-VI compounds, several broad luminescence bands are produced by the incorporation of various activators and coactivators in different amounts. The results of the dependence of luminescence properties on the concentration of activators and coactivators in ZnS were summarized by Shionoya (1966). Some of the luminescence data for ZnS are presented in Table 7.2, which lists the nearly Gaussian luminescence band-shape parameters, the peak energy and half-width.

Table 7.2. Luminescence Data (at 4 K) for ZnS Containing Different Activators and Coactivators*

Luminescence	Activator	Coactivator	Peak energy (eV)	Half-width (eV)
G-Cu (green-Cu)	Cu	Al	2.41	0.30
B-Cu (blue-Cu)	Cu	I	2.85	0.24
SA (self-activated)	—	Cl	2.59	0.29
R-Cu (red-Cu)	Cu	—	1.77	0.48
R-Cu, In (red-Cu, In)	Cu	In	1.82	0.47

*After Shionoya, 1966.

7.3.1. Self-Compensation in II-VI Compounds

Cathodoluminescence scanning electron microscopy studies contributed substantially to the recent elucidation of the mechanisms underlying the phenomenon of apparent self-compensation in the II-VI compounds. They are not used in single-crystal form in optoelectronic devices essentially because, except in the case of CdTe, *p-n* junctions cannot be made (Aven and Devine, 1973; Park and Shin, 1977).

Self-compensation is the formation of native point defects of a type that compensates dopant atoms added to change the conductivity type. This idea is plausible, since these compounds are partially ionic, so, for example, anion and cation vacancies can act as acceptors and donors, respectively. Thus, S vacancies in ZnS are classical *F*-centers (Schneider and Rauber, 1967; Pecheur *et al.*, 1977); i.e., these anion vacancies act as acceptors. In wider-band-gap compounds, when carrier-charge-sign-changing dopants are added, the energy gained on dropping an electron from the one energy level to the other, in compensation, can exceed the formation energy of the native defect. There will then be a thermodynamic driving force for self-compensation (Mandel, 1964; Mandel *et al.*, 1964; Title *et al.*, 1964; Morehead and Mandel, 1965; Chern *et al.*, 1975). The concentrations of native point defects can also be altered by growth, diffusion, or annealing under various pressures of one of the constituent elements of the compound, i.e., by controlling the deviations from exact stoichiometry. Self-compensation does not explain the observed "natural" conductivity signs. These charge carrier signs and their resistance to change have recently been shown to be due to a complex interplay of residual impurities, which are dominant, and nonstoichiometric effects (Pfister, 1980; Bhargava, 1982; Pautrat *et al.*, 1982). The effects produced are similar to those predicted by the earlier, simple self-compensation theories.

The *p*-type conductivity in the purest ZnTe crystals is due to Cu_{Zn} and Li_{Zn} acceptors (residual Cu and Li impurities on Zn sites) plus some Ag. This was established partly by PL studies. The radiative efficiency of Cu centers is low, but that of Li_{Zn} is high, so the spatial and spectral resolution of the SEM enables the effects of annealing under various pressures of Te to be studied (Bensahel and Dupuy, 1979a,b). It was found that during growth from the Te solvent, drops of Te, enriched with Zn and impurities, can be trapped either as isolated inclusions or decorating grain or subgrain boundaries. The as-grown and slowly cooled crystals contain 10^{14} Li_{Zn}/cm^3 or less. During annealing, the inclusions release their impurities, first the Cu and then the Li. The transition zones around the inclusions, where the higher Li_{Zn} concentrations occur, appear bright as can be seen on CL micrographs (Figure 7.36). It was concluded from these studies that the contrast in the micrographs in general was due not only to the dislocations and grain boundaries themselves but also due to the segregation of clusters (below the TEM resolution limit) involving Li (Bensahel and Dupuy, 1979a,b; Bensahel *et al.*, 1979a,b).

For CdTe, specimen temperatures <15 K were used to obtain adequate spectral resolution and intensity to study the behavior of Cu (Chamonal *et al.*, 1983). The general conclusions were similar to those for ZnTe. Specimens, into which Cu and In were diffused, were studied after various heat treatments. The acceptor Cu was found, for example, only in the bright areas in Figure 7.37, surrounding the black blobs in which the Cu was supersaturated and complex centers occurred. It was concluded that the Cu was probably diffusing rapidly along defects. At low temperatures, the Cu diffusion produced numerous black dots suggesting that, although it readily enters the crystal, it is concentrated around defects or in inactive or weakly active complex centers. This helps to explain the inconclusive results of previous studies of the electrical activity of Cu_{Cd} in CdTe. The dramatic enhancement of contrast even in room-temperature CL-SEM micrographs produced by the diffusion of Li into a crystal is illustrated

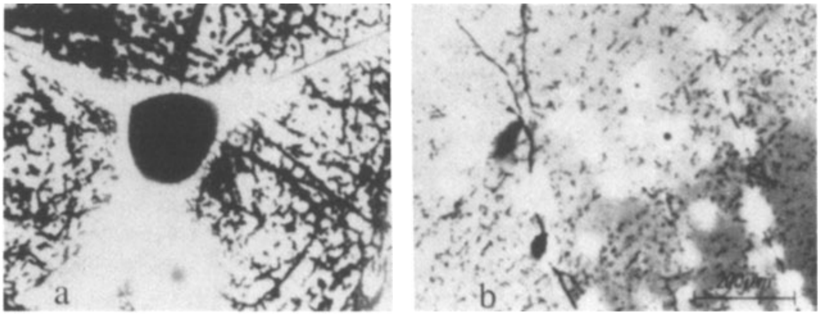

Figure 7.36. SEM CL micrograph of ZnTe, annealed for 15 min at 635°C, showing bright Li-enriched zones around (a) grain boundaries and an inclusion trapped at their intersection and (b) inclusions in the bulk of the crystal. (After Bensahel and Dupuy, 1979a.)

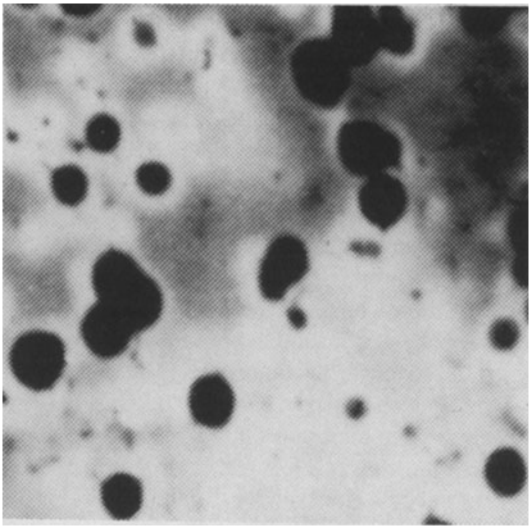

Figure 7.37. SEM CL micrograph of Cu-diffused CdTe at 10 K. The Cu is electrically active only in the bright regions surrounding the Cu-saturated black blobs. (After Chamonal *et al.*, 1983.)

in Figure 7.38. In a study of Cu diffusion into CdTe, however, James *et al.* (1986) observed a uniform CL with no detectable precipitates in their samples. They concluded that Cu did not segregate at dislocations and suggested that the CL quenching may be caused by the formation of a Cu-doping-related deep level. It would thus appear that these effects may also be sample-dependent.

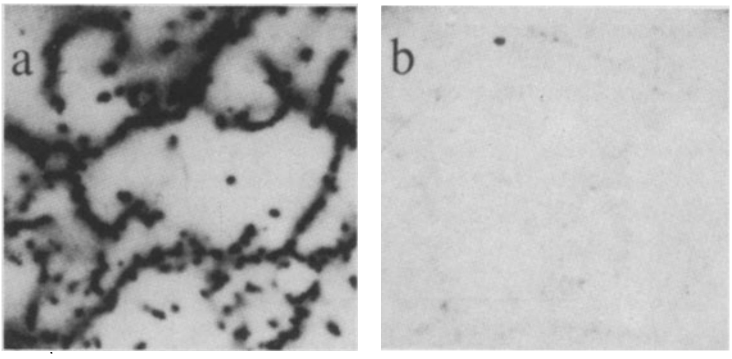

Figure 7.38. SEM CL micrographs of CdTe recorded at 300 K (a) after diffusing Li at 500°C for 1 h and (b) as grown and annealed similarly but without Li. The Li enhances both the radiative efficiency and the contrast. (After Chamonal *et al.*, 1983.)

7.3.2. Segregation and Defect Studies

Cathodoluminescence scanning electron microscopy studies of defects in II-VI compounds were first reported by Williams and Yoffe (1968, 1969, 1971). The local CL variations observed in striated ZnSe and ZnS in those studies were attributed to the crystal defect structure as deduced from TEM. These striated platelets are structurally nonuniform, consisting of parallel strips of different birefringence, all perpendicular to the common *c* axis. The various strips may have either the cubic structure (sphalerite), the hexagonal structure (wurtzite), or one of the many polytypic forms. Spectroscopic CL analysis at low temperatures revealed that the edge emission band contained characteristic bound exciton lines, which were ascribed to cubic and to hexagonal phase material. Yoffe *et al.* (1973) also obtained CL monochromatic images of these striated crystals. These studies together with later results by Holt and Culpan (1970) and Datta *et al.* (1977) showed that local variations in CL emission from faulted (structurally complex) ZnS crystals are due to changes in structure, impurity segregation, and/or internal electric fields. Structurally different areas in these faulted ZnS platelets can be identified from birefringence measurements (Brafman and Steinberger, 1966; Alexander *et al.*, 1970). Room-temperature values for the peak, E_p, of the CL edge emission band from the selected ZnS structures are given in Table 7.3. The regions in such ZnS platelets differ from each other in the stacking sequence of the basal planes. These structures can be characterized by a parameter β (Brafman and Steinberger, 1966), which represents the percentage of close-packed planes that are in a hexagonal nearest-neighbor environment. That is, these structures can be classified by a percentage of hexagonality β, which is 100% for hexagonal wurtzite (2H), 50% for polytype 4H, and 0% for cubic sphalerite (3C). The higher-order polytypes have values of β between those for the cubic and the 4H polytype structures. The band-gap shifts in wavelength linearly with β (Brafman and Steinberger, 1966), and thus it is to be expected that the CL edge emission peak of the 4H polytype will fall between those of the 3C and 2H structures in Table 7.3.

In these ZnS platelets, the existence of macroscopic internal electric fields

Table 7.3. Cathodoluminescence Edge Emission Peak Energies for Various ZnS Structures at Room Temperature*

Crystal structure	E_p (eV)
Hexagonal (wurtzite)	3.740 (331 nm)
4H polytype	3.706 (335 nm)
Cubic (sphalerite)	3.657 (339 nm)

*After Datta *et al.*, 1977.

(of up to 10^5 V cm^{-1}) has been established (Shachar *et al.*, 1970). These electric fields occur due to charged sheets of dislocations (Mardix and Steinberger, 1970), which result whenever there is a lattice-constant misfit between adjacent crystal structures.

Cathodoluminescence observations in these striated ZnS crystals provide evidence of the relative importance of the factors that contribute to local luminescence variations (see Datta *et al.*, 1977). As mentioned earlier, these are (1) structural changes, (2) impurity segregation, and (3) internal electric field effects. Figure 7.39 summarizes these observations. Figure 7.39a is a micrograph

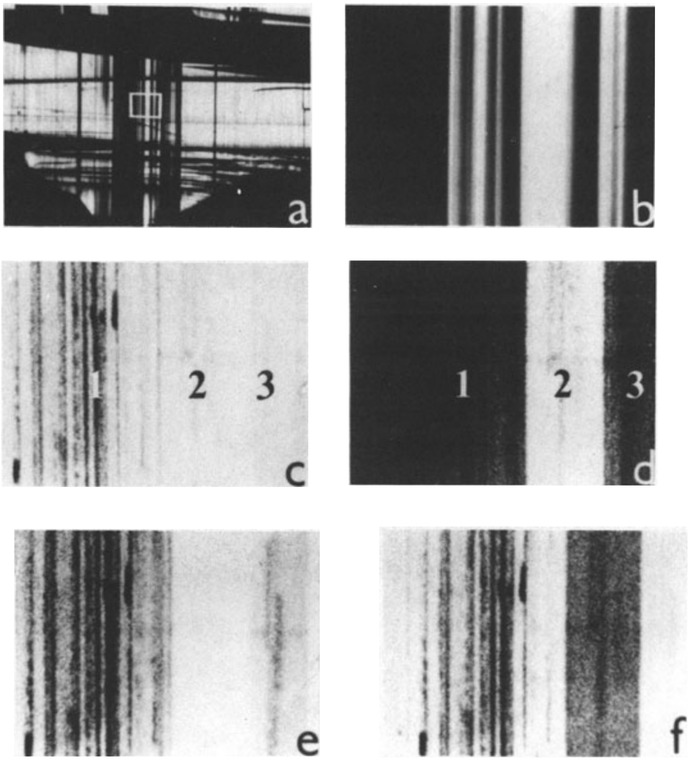

Figure 7.39. Micrographs of a striated ZnS platelet with the common *c* axis running horizontally: (a) a low-magnification polarized light micrograph of the whole platelet, showing the polytypic bands running vertically; the remaining micrographs are all of the area in the rectangle outlined in the center of the platelet; (b) an enlargement of the area outlined in (a); (c) a panchromatic CL SEM micrograph. The remaining pictures are monochromatic CL SEM micrographs recorded at the following emission wavelengths: (d) 328 nm (3.78 eV); (e) 334 nm (3.71 eV); (f) 344 nm (3.60 eV). The width of the area represented by the CL micrographs (c), (d), (e), and (f) is 308 μm. (After Datta *et al.*, 1977.)

of a faulted ZnS platelet under crossed polarizers in an optical microscope. As mentioned earlier, such ZnS platelets consist of numerous structurally different areas, which can be identified from birefringence measurements (Alexander *et al.*, 1970). Thus, the polytypic bands, which appear with different colors under crossed polarizers in an optical microscope, run perpendicularly to the polar *c* axis of the crystal. The other lines, running parallel to the *c* axis, are growth steps. Figure 7.39b is an enlargement of the area (containing various polytypes), where CL measurements were performed. Figure 7.39c is a panchromatic (all wavelengths) CL micrograph, and the remainder (figures d, e, and f) are monochromatic (one-wavelength) CL micrographs.

Region 1 in these micrographs was a heavily faulted cubic area, region 2 a 4H polytype, and region 3 a broad unfaulted cubic band. CL variations between the micrographs (which were recorded using different wavelengths) are due to the fact that each ZnS structure has an unique edge emission peak wavelength (see Table 7.3). Thus, depending on the wavelength used as signal for the micrograph, different regions appear light or dark. Equal volumes of each of these regions were examined under identical SEM conditions. Although regions 1 and 3 both have 3C structures, spectral analysis (see Figure 7.40) showed considerable reduction of the CL emission in region 1 as compared with region 3. This may be attributed to internal electric field quenching. The spatial resolution of the spectroscopic CL-SEM analysis was necessary for these observations.

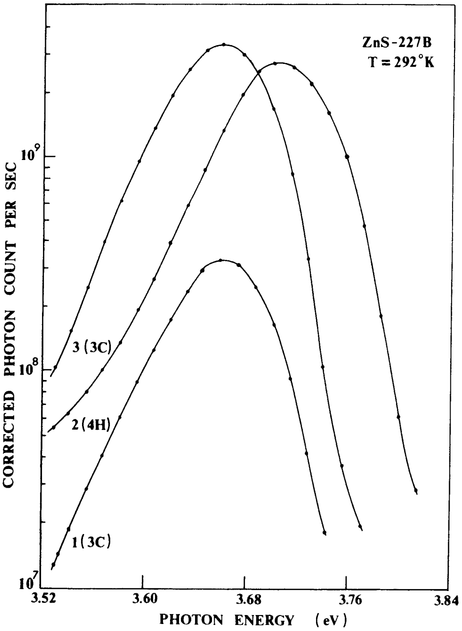

Figure 7.40. The CL edge emission bands obtained from the three numbered regions of Figure 7.39d. 3C denotes the cubic sphalerite structure, and 4H denotes a ZnS polytype. (After Datta *et al.*, 1977.)

Another important conclusion from these studies was that preferential impurity segregation occurred in these samples perpendicular to the *c* axis. Evidence of this is presented in the monochromatic CL micrographs and CL spectra of another ZnS sample in Figures 7.41 and 7.42. Using the data of edge emission peak energies for ZnS structures (see Table 7.3), structurally homogeneous regions were selected (see Figure 7.41). Thus it was established, and subsequently verified by birefringence measurements, that regions 1 and 2 were 3C and 4H polytypic structures, respectively. Figure 7.41 presents the panchromatic (Figure 7.41a) and monochromatic (Figure 7.41b, recorded at 523 nm) CL micrographs for this sample. Selected area spectra from the two structures are presented in Figure 7.42. Both the uncorrected (Figure 7.42a,c) and corrected (Figure 7.42b,d) spectra in this case clearly show that the impurity emission characteristics of the two adjacent areas are significantly different. From these spectra it is evident that the intense panchromatic luminescence in region 1 (cubic) is due to the broad impurity band peaking at 523 nm in the uncorrected case (Figures

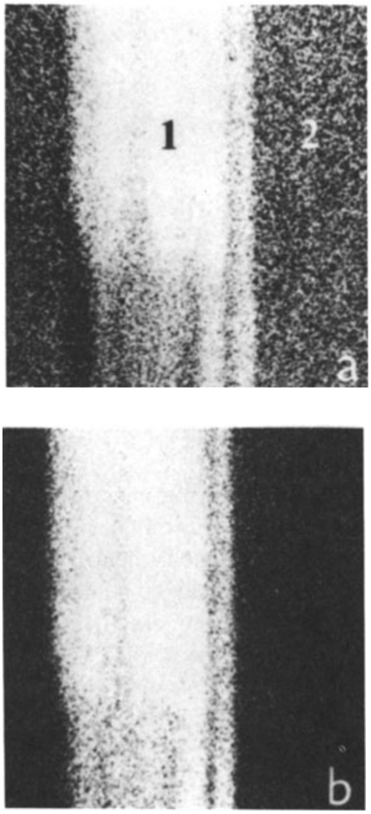

Figure 7.41. CL SEM micrographs of a ZnS platelet: (a) panchromatic and (b) monochromatic, recorded at 523 nm (2.37 eV). The region represented is 178 μm wide. (After Datta *et al.*, 1977.)

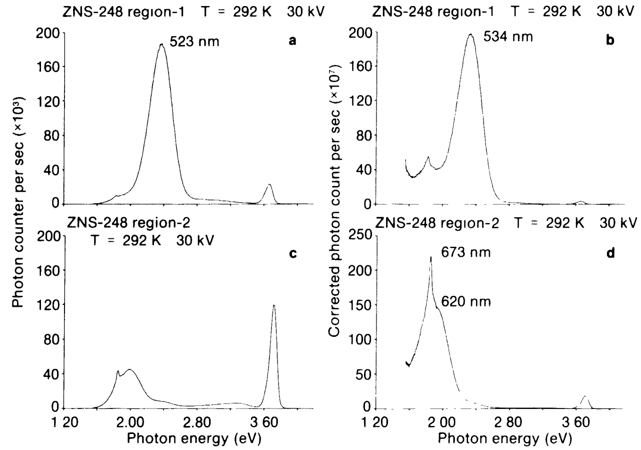

Figure 7.42. Uncorrected and corrected CL spectra of ZnS obtained from the two regions shown in Figure 7.41: (a) uncorrected spectrum from cubic region 1 and (b) the corrected spectrum; (c) uncorrected spectrum from 4H polytype region 2, and (d) the corrected spectrum for that region. The correction for the spectral response of the detector system affects both the positions and the intensities of the peaks. (After Datta *et al.*, 1977.)

7.41b and 7.42a), which is missing in the adjacent 4H polytype. Thus, Figure 7.41b demonstrates that in this ZnS sample, an impurity segregated to a region of the crystal of one structure in preference to the other. Note that the monochromatic micrograph in Figure 7.41b was recorded by using the uncorrected peak wavelength. In the corrected spectra, however, the different impurities present in the two adjacent areas are found to be of equal emission strengths. Thus, in principle, both regions in the panchromatic micrograph should appear as bright bands emitting at different wavelengths (provided corrected values of peak wavelengths were used for the video display, or a flat-band response detector was used).

Hence, using uncorrected data makes panchromatic CL images generally unreliable as proof of segregation. A selected area spectral analysis is necessary for less ambiguous identification of impurity segregation. Even monochromatic micrographs may be somewhat misleading. For example, the uncorrected peak energy of 523 nm used in Figure 7.41b in fact shifts substantially (to 534 nm) on correction. In principle, with further computerization of CL analysis, it would be feasible to use on-line computer-corrected spectral data in order to obtain corrected monochromatic images. If no such capability is available, one can still get more reliable segregation images by using flat-band response photomultipliers, such as the GaAs photocathode type.

CL-STEM and CL-TEM investigations of ZnS were reported by Pennycook and Howie (1980) and Roberts and Steeds (1982), respectively. The former investigated the effect of energy transfer from inner core electrons to valence excitations. Roberts and Steeds (1982) correlated the CL edge emission with structural disorder in CVD deposited polycrystalline ZnS.

In situ stress induced motion of dislocations in CdS and CdTe was investigated by Maeda *et al.* (1981) (see Section 6.1 and Figure 6.24).

Several reports described CL uniformity characterization of II-VI compounds. Cathodoluminescence studies of polycrystalline ZnSe showed the luminescence (both edge emission at 465 nm and the copper-red band at 630 nm) to be quenched at grain boundaries (Russell *et al.*, 1981). This was attributed to a possible segregation of impurities to the grain boundaries. A combination of CL and PL was used to detect Li segregation in certain regions of ZnTe crystals (Magnea *et al.*, 1979). Roberts *et al.* (1983), using 35 K CL data, identified and imaged inhomogeneous Cl donor concentrations in ZnSe.

Panchromatic CL microscopy was used by Bubulac *et al.* (1985) to investigate defects, such as dislocations, precipitates, and subgrain structure in CdTe substrate material and in $Hg_{1-x}Cd_xTe$ ($x \cong 0.93$) and CdTe epitaxial layers. High defect densities forming the boundaries of cells (subgrains) with dimensions between 140 and 300 μm were revealed in Bridgman-grown CdTe substrates (Bubulac *et al.*, 1985). In some samples, nonuniformities in the CL due to varying concentrations of background impurities were observed. Cadmium annealing followed by chemical etching, however, led to uniform CL efficiency as a result of impurity redistribution. It was also found that epitaxial CdTe tends to reproduce the subgrain structure of the CdTe substrate, whereas $Hg_{1-x}Cd_xTe$ ($x \cong 0.93$) epilayers contained no subgrains and reduced defect densities. It was suggested that the lower defect densities in this HgCdTe grown on CdTe could be due to slight lattice mismatch and/or the presence of Hg (Bubulac *et al.*, 1985).

7.3.3. Effects of Correction on Luminescence Spectra

Significant changes in the CL intensity, the shape of the luminescence band and the value of the peak photon energy are observed on the correction of luminescence spectra for the detector system response characteristics (Steyn *et al.*, 1976; Datta *et al.*, 1977, 1979a). These effects are much greater for some types of photomultipliers (S20 response) than for others (S1 response, for example). It was also found that broad emission bands undergo larger correction effects than do narrower bands. This can lead, for example, in the case of the self-activated (SA) luminescence in ZnS:Cl, to a sign reversal of the temperature coefficient of the SA peak (Datta *et al.*, 1979a). In other words, the peak of the uncorrected SA luminescence band shifted toward higher energies with increase in temperature, but after correction it shifted in the opposite direction (similar to the shift of the fundamental edge) in the samples studied by Datta *et al.* (1979a). Thus, the frequently reported temperature shift anomaly, which was thought to be characteristic of the SA emission peak in ZnS:Cl, was found to be an artifact of uncorrected spectra in this particular material. This effect can be demonstrated for the SA emission peak of ZnS:Cl measured between 78 and 292 K. The data in Table 7.4 clearly demonstrate the effect of correction for the photomultiplier response (*QEF*) on the peak wavelength E_i. With correction, the peak wavelength at room temperature, for example, is shifted to longer wavelengths by 25 nm for the cubic structure and 20 nm for hexagonal structure. The peak position in this material has been found to vary between 450 and 470 nm at room temperature as a function of the type of activator and its concentration (Curie and Prener, 1967), and some inconsistency in the peak position of the SA luminescence may also be due to variations in the excitation energy used in PL measurements (Grasser *et al.*, 1971).

The effect of correction for the detector system response characteristics can be deduced from the CL detector response curve (Datta *et al.*, 1979a) shown in Figure 5.15. The fall of the curve with increasing wavelength has a larger effect on the broad bands obtained at 292 K than on the narrow bands obtained at 78 K (see Table 7.4). Although the shift due to correction is unidirectional at all temperatures, it causes the broad band to move further than the narrow band (see Figure 7.43). Thus, the peak energy shift with temperature changes direction. Also of importance is the fact that the correction (for this particular CL detector system) is such that the peak rate of photon emission of the SA luminescence band is really about 5×10^3 greater than that in the uncorrected spectrum. These changes in magnitude and shape are so significant that, in any quantitative CL analysis, correction for the detector system response characteristics is essential.

Impurity emission bands in ZnS have been grouped together according to the direction of peak energy shift and the change in half-width with respect to temperature (Shionoya *et al.*, 1964). In one group, including the blue-copper (B-Cu) and the green-copper (G-Cu) bands, the emission peaks move toward lower energies with increasing temperature, but the half-widths change little, remaining in the range from 0.2 to 0.3 eV. In the other group, the emission peaks of the

Table 7.4. Cathodoluminescence ZnS:Cl (SA) Band-Shape Parameters*

Structure	Temperature (K)	E_t (eV) Uncorrected	E_t (eV) Corrected	ΔE_t (eV)
Cubic	292	2.678 (463 nm)	2.539 (488 nm)	0.139
	200	2.670 (464 nm)	2.563 (484 nm)	0.107
	120	2.662 (466 nm)	2.580 (481 nm)	0.082
	78	2.654 (467 nm)	2.586 (479 nm)	0.068
Hexagonal	292	2.749 (451 nm)	2.634 (471 nm)	0.115
	78	2.728 (454 nm)	2.664 (465 nm)	0.064

*Peak position $E_t = E_0$ in eV both uncorrected and corrected; ΔE_t the difference in peak values. (After Datta *et al.*, 1979a).

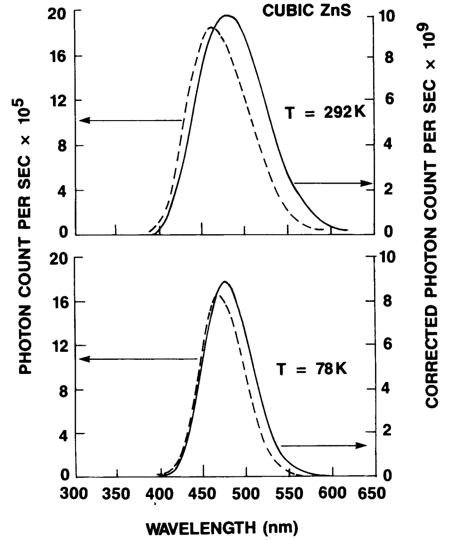

Figure 7.43. Corrected (solid) and uncorrected (dashed) self-activated CL bands of cubic ZnS:Cl at room and liquid nitrogen temperatures. (After Datta *et al.*, 1979a.)

SA, the R-Cu, and the R-Cu with In coactivator bands shift toward higher energies with increasing temperature, that is, in the direction opposite to that of the fundamental edge emission band in ZnS. The half-widths of bands in this group are from 0.3 to 0.5 eV at low temperatures and increase substantially at higher temperatures. To examine the effect of correction of luminescence spectra for detector response characteristics on such a grouping of impurity emission bands (Shionoya *et al.*, 1964), Datta *et al.* (1979a) investigated a number of impurity bands in ZnS. An example of correction of the blue emission band due to Ag activation of ZnS (B-Ag_I) with coactivation from group III or VII elements (Van Gool, 1961; Era *et al.*, 1968) is presented in Table 7.5. It is interesting to com-

Table 7.5. Cathodoluminescence Peak Energy as a Function of Temperature for the Edge (E_g) and the Uncorrected and Corrected B-Ag_I (E_j) Bands in Cubic ZnS*

T (K)	E_g (eV)	E_j (eV) Uncorrected	E_j (eV) Corrected	ΔE_j (eV)
292	3.658 (339 nm)	2.872 (432 nm)	2.806 (442 nm)	0.066
250	3.678 (337 nm)	2.830 (438 nm)	2.772 (447 nm)	0.058
200	3.704 (335 nm)	2.788 (445 nm)	2.734 (453 nm)	0.054
150	3.732 (332 nm)	2.734 (453 nm)	2.689 (461 nm)	0.045
100	3.760 (330 nm)	2.700 (459 nm)	2.671 (464 nm)	0.029
78	3.774 (328 nm)	2.688 (461 nm)	2.664 (465 nm)	0.024

*ΔE_j is the difference in peak value between the uncorrected and corrected bands of B-Ag_I. (After Datta *et al.*, 1979a).

pare the effect of correction on the emission data in Tables 7.4 and 7.5 for the SA and B-Ag_I bands. After correction for spectral response, the emission peak shift with temperature changes direction for the SA band but not for the B-Ag_I band. This occurs due to the fact that, although both these impurity bands in ZnS fall in approximately the same wavelength range, for the B-Ag_I band there is a relatively large difference of 29 nm between the uncorrected emission peaks at room and liquid nitrogen temperature, whereas in the same temperature range the uncorrected SA band shifts by only 4 nm (see Tables 7.4 and 7.5). The overall effect of correcting for the spectral response of the CL system used is always to increase the wavelength value. However, although the correction makes the SA bands pass through each other, resulting in a reversal of direction of the temperature shift, in the case of the B-Ag_I emission band, the large separation in wavelength (i.e., 29 nm) prevents such a reversal of direction.

Figure 7.44 presents the temperature dependence of the peak energies of the edge emission, the SA and the B-Ag_I emission bands in cubic ZnS. The corrected SA luminescence band shifts with cooling toward higher energies like the edge emission, which is in contrast with the B-Ag_I band. The occurrence of two straight line segments in the latter case is probably due to the influence of the second Ag band (UV-Ag_{II}) which appears for temperatures below 150 K (Datta *et al.*, 1979a). The major conclusion is that these observations are inconsistent with the suggestion that impurity bands in ZnS can be divided into two groups,

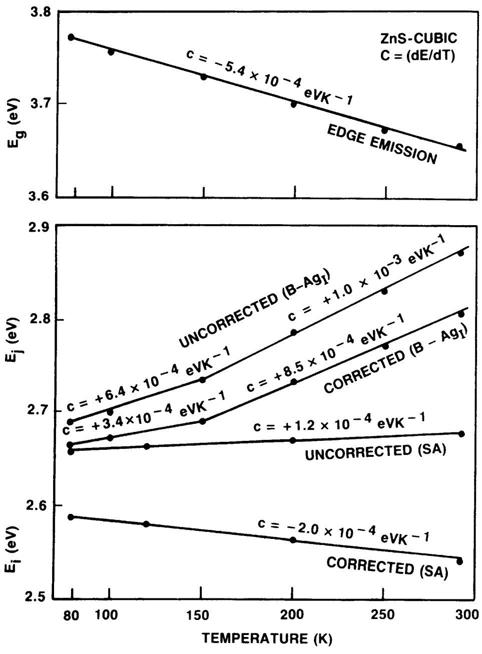

Figure 7.44. Plots of the peak photon energies (E_g, E_i, and E_j in eV) as functions of temperature for the edge, the self-activated, and the blue-silver emission bands, respectively, in cubic ZnS crystals. (After Datta *et al.*, 1979a.)

depending on the direction of the peak shift with temperature and their half-width values. Although such a classification is consistent for the SA and B-Ag_I uncorrected bands, it is not consistent with the corrected spectra of these extrinsic impurity bands, which have similar half-width values but different signs of the temperature coefficient *c*. Thus, it appears that the apparent temperature shift anomaly of the SA emission peak in some ZnS crystals is an artifact of uncorrected spectra. This emphasizes the importance of correction of luminescence spectra for the detector system response characteristics. It is possible that most of the irreproducibility and the anomalies in the literature may be accounted for by correcting luminescence spectra.

Thomas *et al.* (1984) found that the sign of the temperature shift of the peak of the self-activated luminescence depends also on the concentration of Cu in the material. At low Cu concentrations the peak shifts to higher energies with decreasing temperature. For Cu concentrations greater than about 3×10^{16} atoms cm^{-3}, however, the peak shifts to lower energies on cooling. In order to explain these observations, Thomas *et al.* (1984) proposed a model for ZnS:Ga,Al involving recombination between distant donors and complex centers consisting of the (Ga_{Zn}^{+}-Al_{Zn}^{3+}) A-center coupled with the copper green Cu_{Zn}^{+} acceptor at low Cu concentrations and with the copper blue (Cu_{Zn}^{+}-Cu_I^{+}) isoelectronic hole trap at higher Cu concentrations.

Thus, it appears that both the correction of luminescence spectra for the detector system response characteristics and the presence of impurities may lead to changes in the temperature behavior of the luminescence spectra in these materials. Before any universal correlations are attempted, it is essential to account for these factors.

7.3.4. Depth-Resolved and Interface Studies

Depth-resolved CL investigations of ZnS and CdS (Norris *et al.*, 1973), CdTe (Norris *et al.*, 1977), ZnTe (Norris, 1980, 1982a), and CdSe (Norris, 1982b) have demonstrated the great advantage of CL in studying ion-implantation-induced postrange defect introduction in these materials.

The effect of the electron beam injection level on the CL spectra of a nominally undamaged ZnS using an electron excitation energy of 8 keV is shown in Figure 7.45 (Norris *et al.*, 1973). It is significant that, although the position and shape of the blue band are injection-level-dependent, the relative CL intensities of the red and blue bands are not strongly affected by the injection level. This relative injection-level independence of the spectrum of ZnS is in contrast with the significant effect of injection level on the CL spectral shape in GaAs (see Section 6.3). Thus, in ZnS, any significant modifications of the CL spectrum as a function of excitation depth are expected to be a result of depth variations of luminescence center concentrations. Moreover, both the CL intensity and shape dependencies on the excitation energy should be considered. Figure 7.46 shows depth-resolved CL spectra excited with beam penetration depths between 76 Å

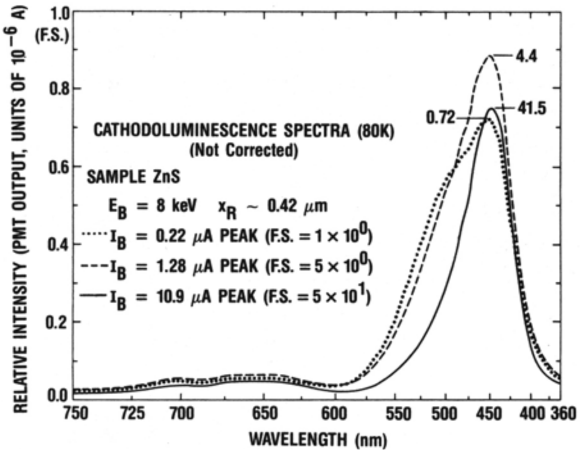

Figure 7.45. CL spectra from a ZnS sample at 80 K using 8-keV electron beam excitation. Although the location and shape of the blue band depends on the injection level, the relative intensities of the red and blue bands are nearly independent of injection level. This electron beam injection level independence of the relative CL intensities of the red and blue bands is observed for excitation energies from 1 to 20 keV at 80 and 300 K. (After Norris *et al.*, 1973.)

and 1.44 μm in unimplanted CdTe (Norris *et al.*, 1977). Despite the fact that a constant total injection level was used, significant CL intensity variations occur as a result of competition between surface and bulk recombination processes.

The CL spectra of nominally undamaged ZnS crystals reveal that the ratio of red-to-blue emission decreases significantly as a function of the excitation energy (beam voltage) (see Figure 7.47; Norris *et al.*, 1973). The presence of the red CL band in this sample was attributed to depth-resolved disorder, nonstoichiometry, or surface contamination (Norris *et al.*, 1973). An additional broad emission between 600 and 750 nm, which appears only at 1 keV, indicates that surface effects or damage near the surface of the crystal may be responsible for this feature.

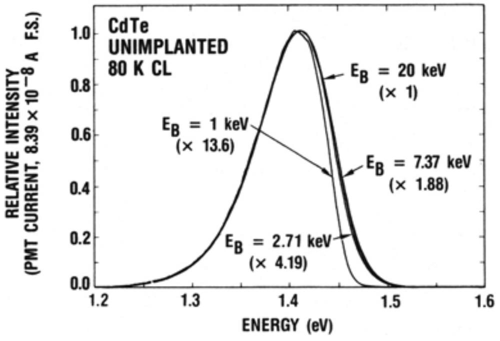

Figure 7.46. Normalized CL spectra as a function of excitation depth in an unimplanted CdTe sample at 80 K. The shape differences between the spectra are due to injection level effects in this heavily doped material rather than to depth effects. (After Norris *et al.*, 1977.)

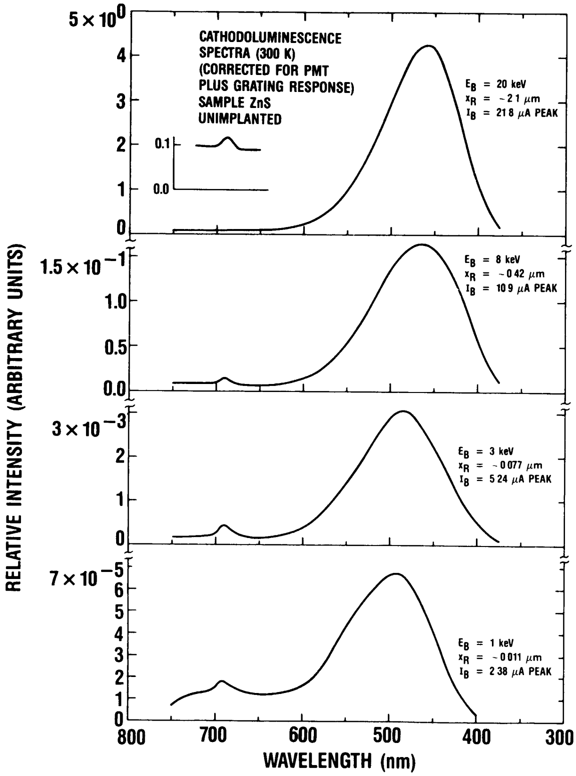

Figure 7.47. Depth-resolved CL spectra from a nominally undamaged ZnS sample at 300 K. The inherent near-surface red band in this case indicates that luminescence profiling by layer removal methods may sometimes lead to incorrect results. (After Norris *et al.*, 1973.)

The surprisingly high depth resolution (the nominal range for 1-keV excitation, for example, is 110 Å) in this material with a much higher carrier diffusion length was attributed to the enhanced surface recombination and/or the disorder-induced reduction of the carrier diffusion length near the surface (Norris *et al.*, 1973). The CL spectra of an Ar^+-implanted (and unannealed) ZnS sample are presented in Figure 7.48, which shows (compared to Figure 7.47) the implantation-induced modification of the shapes and intensities of the CL spectra at low energies. Similar results were obtained from Cu^+-implanted ZnS samples. Thus, the featureless spectra obtained from shallow depths in Figure 7.48 are due to ion-implantation damage rather than doping effects of the implanted ion species (Norris *et al.*, 1973). Similar effects of ion-implantation-induced lattice damage were observed in CdS crystals (Norris *et al.*, 1973).

As mentioned in Section 6.3, CL studies in CdTe demonstrated that implantation-induced damage in the material may occur beyond the projected ion range

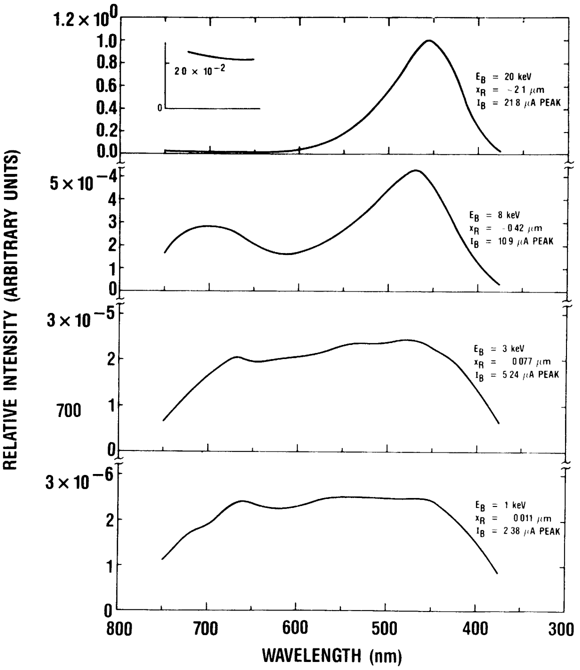

Figure 7.48. Depth-resolved CL spectra from a ZnS sample at 300 K (corrected for PMT plus grating response) following a shallow Ar^+ implant (240 keV, $5.5 \times 10^{14}/cm^2$, 300 K). Note the significant quenching of the luminescence at low excitation energies in comparison with Figure 7.47. (After Norris *et al.*, 1973.)

of implants (Figure 6.30). Such a case was revealed, for example, in the depth-resolved CL spectra of a 100-keV Xe^+-implanted In-doped CdTe sample which was etched to a depth of about 1400 Å. The presence of the implantation-induced 1.2-eV band in that case suggested that the defects associated with that band are present at depths several thousand angstroms beyond the projected ion range (Norris *et al.*, 1977). Similar anomalous (postrange) implantation-induced introductions of defects were also observed in other II-VI compound semiconductors. It was suggested that this process may be due to the interaction of ionization with dynamic stress or phonon flux effects during ion implantation (Norris *et al.*, 1977; Norris and Barnes, 1980). Postrange implantation-induced defect introduction was studied in ZnTe by Norris (1980, 1982a), who concluded that to minimize the postrange damage it is favorable to use higher substrate temperatures (e.g., 300 K as compared with 80 K) during ion implantation. The CL studies also indicated that V_{Zn}- and/or V_{Te}-related centers are formed in the postrange region in ZnTe (Norris, 1982a). In CdSe crystals, postrange radiative effects were associated with V_{Cd} formation (Norris, 1982b). Norris and Peercy (1983) also reported that defect reactions can occur during ion implantation and pulsed laser annealing in CdTe. Their results indicated that, in some cases, prior Cd-vapor heat treatment can affect the defect reactions during laser annealing and substantially improve the postrange luminescence recovery (Norris and Peercy, 1983).

As outlined in Section 6.3, Brillson *et al.* (1985) and Viturro *et al.* (1986) demonstrated the power of depth-resolved CL analysis in characterizing subsurface metal-semiconductor interfaces. An example of the CL analysis of UHV-cleaved CdS before and after 50 Å Cu deposition and pulsed laser annealing is illustrated in Figure 6.31. It was revealed that the luminescence intensity of the Cu-deposition-induced weak peak at about 1.28 eV is significantly enhanced, suggesting the formation of the compound Cu_2S (Brillson *et al.*, 1985). In contrast to the Cu-case, similar experiments on laser annealing (at 0.1 J/cm^2) of Al layers produced two emission lines at 1.3 and 1.65 eV (Figure 7.49). The relative reduction of the CL intensities of these peaks by a subsequent laser anneal of 0.2 J/cm^2 (Figure 7.49) suggests that they are associated with the formation of lattice defects (Brillson *et al.*, 1985). Additional information about these defect-related peaks can be obtained from the electron beam energy dependence of the CL spectra (Figure 7.50). The relative enhancement of the 1.3-eV peak at a lower excita-

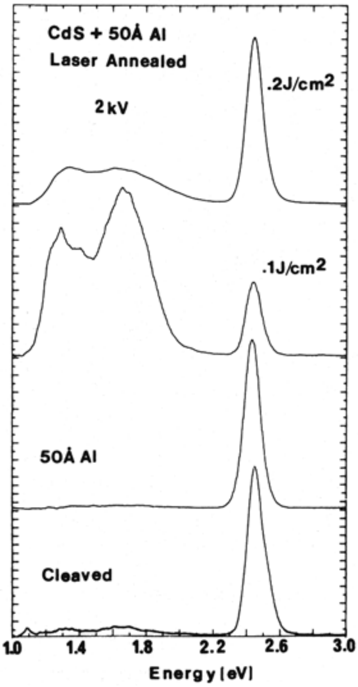

Figure 7.49. CL spectra obtained with 2-keV-electron-beam irradiation of ultrahigh-vacuum-cleaved CdS after *in situ* deposition of 50 Å Al, and after *in situ* laser annealing with increasing energy density. (After Brillson *et al.*, 1985.)

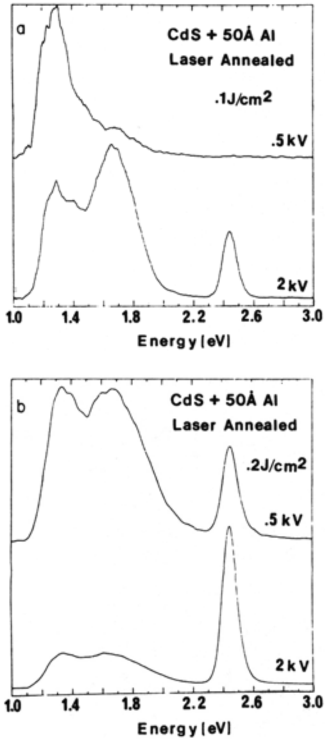

Figure 7.50. CL spectra as a function of electron beam energy for ultrahigh-vacuum-cleaved CdS with a 50-Å Al overlayer, laser annealed with energy density (a) 0.1 J/cm^2 and (b) 0.2 J/cm^2. (After Brillson *et al.*, 1985.)

tion energy (i.e., at 0.5 kV) suggests that the 1.3-eV-related transitions occur closer to the surface than those associated with the 1.65-eV emission state (Figure 7.50a). Additional laser annealing results in a decrease of both defect-related features relative to the near-band-edge emission (Figure 7.50b). Furthermore, no relative increase of the 1.3-eV band (which is shifted to 1.35 eV) is observed at lower excitation energies. These observations are consistent with a reduction in the defect density near the surface at higher annealing power levels, and they also indicate that the defect density associated with the 1.35-eV luminescence is reduced (relative to the 1.65-eV emission) with additional annealing (Brillson *et al.*, 1985). These results show that this CL technique can be effectively used in (1) analyzing the chemical interactions at metal-semiconductor interfaces that produce new interfacial phases, and (2) monitoring the effects of thermal processing (Brillson *et al.*, 1985).

7.3.5. Cathodoluminescent Laser Action

As mentioned earlier in this chapter, apparently because of the self-compensation mechanism occurring in most II-VI compounds, *p-n* junctions in these materials cannot be formed. Thus, since II-VI injection lasers cannot be made, CL laser emission in these materials is of considerable interest. (In III-V compounds, laser action can be produced by injection at *p-n* junctions, which is of greater practical value, so CL laser emission is of little interest.) In principle, different electron beam–pumped II-VI compounds can offer media for lasing at specified wavelengths in the visible and UV.

Although there were numerous reports of laser action induced by electron bombardment of both platelet crystals and films of II-VI compounds, none of them involved studies in the SEM (for a review, see Holt, 1974). Attempts by Williams and Yoffe (1969) to observe laser action in II-VI compounds in the SEM were unsuccessful, since an electron beam energy of 30 keV (and a 500-Å-diameter electron probe and current densities of up to 100 A cm^{-2}) was lower than the beam voltages used in most cases of CL laser action (Holt, 1974). The threshold values of the electron beam current and voltage were also found to depend strongly on the surface coating, and the threshold beam current for given conditions was also found to vary widely from one specimen to another and from one part of a particular crystal to another. Thus, careful selection of material and surface processing are required. The availability of higher-brightness electron guns in the SEMs may also help in achieving laser action in the CL mode of the SEM.

8

Phosphors

8.1. Introduction

Phosphors by definition are materials that emit photons with a high efficiency and are of practical interest precisely for their luminescence, including cathodoluminescence. The unusual properties of these materials were discovered long before the development of such devices as cathode-ray-tube (CRT)-based instruments, in which phosphors found one of their most important applications. Currently phosphors are also used in fluorescent lamps, electroluminescent flat-panel displays, x-ray screens, scintillators, infrared-to-visible converters, electron microscope fluorescent screens, and color television screens (for a review, see Pappalardo, 1987). In the latter application, for example, ZnS:Ag is used for the blue component, ZnS:Cu,Al for the green component, and Y_2O_3:Eu^{3+} or Y_2O_2S:Eu^{3+} for the red component. In ZnS phosphors, with high CL efficiency, the mechanism of emission is that of donor-acceptor pairs. The emission peak wavelength (i.e., the color) of light produced by a particular phosphor depends on the impurities present in the material. Table 8.1 lists some of the phosphors used in cathode-ray tubes.

The main obstacle to the development of new phosphors is that, despite the advances in solid-state physics, there is little known about the materials science of these substances, so phosphor research is of a more empirical nature. Cathodoluminescence processes in this class of materials were reviewed by Garlick (1950, 1966), Curie (1963), Ouweltjes (1965), and Kazan (1985). Phosphors are polycrystalline powders or films with typical grain size from less than a micron to several microns and larger. Their band gap is usually larger than 3 eV, so they are transparent to visible light. The particular color of light emitted by a phosphor depends on the activators (and coactivators) present in materials such as ZnS, or (for a given activator) on the composition of a phosphor such as ZnCdS, in which the color varies with changing Cd content (see Table 8.1). Phosphor powders are usually produced by firing the constituent elements of the material,

Table 8.1. Cathode-Ray Phosphors

Material	Activator	Color of luminescence	Applications
ZnS	Ag	Blue	TV
ZnS	Cu	Green	Oscilloscope
ZnCdS	Ag	Blue, green, yellow to red with increasing Cd content	TV, data display
ZnCdS	Cu	Green, yellow to orange-red with increasing Cd content	TV, data display
ZnO	Zn	Blue-green	Low-voltage applications
Zn_2SiO_4	Mn	Green	Data display, projection TV
Y_2O_2S	Eu	Red	Color TV
Y_2O_3	Eu	Red	Color TV, projection TV
YVO_4	Eu	Red	Color TV
Y_2O_2S	Tb	Green	Color TV, projection TV
Gd_2O_2S	Tb	Green	Color TV, data display
$Y_3Al_5O_{12}$	Tb	Yellow-green	High-luminosity display, special CRTs
$Y_3Al_5O_{12}$	Ce	Yellow-green	Flying-spot scanner
Y_2SiO_5	Ce	Blue	Flying-spot scanner

the activator, and a flux (which promotes crystallization) at high temperatures. Phosphor screens are coated by spraying, pouring, or settling, for example.

Traditionally, phosphors are used in the form of powders. For improved resolution and better thermal contact, phosphors can be deposited as thin films. Such films are also used in EL flat-panel displays. A major concern is the much reduced light output normal to the film plane as compared with powder phosphors. A large fraction of the light from phosphors in thin films is trapped and "piped" along the plane to the edge of the structure. This reduces the CL efficiency of thin-film layers as compared with powder phosphors. It is, however, possible to minimize this waveguiding effect by roughening the surface and/or incorporating antireflection coatings (Theis and Wengert, 1985).

Despite the diminishing efforts in phosphor research, there were some areas of renewed interest. One was due to the demand for CRT phosphors for information display applications. These require higher resolution, more emphasis on contrast (rather than brightness), a longer operating life, high electron beam current operation, and minimized screen flicker. One of the materials that attracted renewed interest in this context is Mn-doped zinc silicate (Zn_2SiO_4:Mn), otherwise known by its mineral name willemite. One of the main difficulties in obtaining a better material for these applications is the requirement to improve both the luminous efficiency and the persistence of the phosphor, since this would require a trade-off (Brownlow and Chang, 1983).

The fact that the electron penetration depth depends on the accelerating voltage of the incident electrons makes it possible to obtain variations in color in the so-called penetration phosphors. Such voltage-sensitive phosphors can be obtained by depositing successive phosphor layers or by using a blend of two phosphors, providing different colors and different brightness-voltage characteristics (Lehmann, 1981; Okamoto *et al.*, 1982). In the latter case, one phosphor is uncoated material with a linear voltage dependence of the CL intensity, and the other phosphor is coated with a nonluminescent surface layer that has to be penetrated by electrons in order to reach the luminescent core. Thus, while the emission color of the uncoated phosphor is obtained at low voltages, the mixed emission color of the two phosphors is obtained at high voltages. The main disadvantage of such a system is the difficulty in obtaining high color resolution. This is difficult because the luminescence from the uncoated phosphor increases continuously with electron beam voltage, so above some dead voltage (related to the coated phosphor) the emission colors of the phosphors will be mixed. A possible solution to this problem was suggested by Okamoto *et al.* (1982), who replaced the uncoated phosphor component of the mixture with a layered phosphor deposited on nonluminescent core particles. Thus, in the latter case, the CL intensity decreases as electrons penetrate through the phosphor layer at higher accelerating voltages. Okamoto *et al.* (1982) demonstrated that greater flexibility in obtaining different colors as a function of electron beam voltage can be realized by mixing, for example, red-emitting (Zn,Cd)S:Ag layers deposited on SiO_2 particles with green-emitting Zn_2SiO_4:Mn particles coated with undoped ZnS or (Zn,Cd)S layers.

Low-voltage (of the order of 50 V) CL phosphors have also attracted substantial interest (Akagi *et al.*, 1978; Oda *et al.*, 1978; Kukimoto *et al.*, 1979). Such materials would allow significant reduction of accelerating voltages in cathode-ray tubes, and they may also find applications in flat-panel color displays. In these applications, the phosphor should have a sufficiently low resistivity to prevent charging, and it should contain an appropriate luminescence center. Using the Zn extraction treatment of the material, Akagi *et al.* (1978), Oda *et al.* (1978), and Kukimoto *et al.* (1979) prepared low-resistivity crystals and powder phosphors of ZnS and ZnSe containing Ag or Cu activators with an Al coactivator that exhibited blue, green, and red low-voltage cathodoluminescence (Figures 8.1, 8.2).

Another typical application of phosphors is in the fluorescent lamp, a glass vessel coated with phosphor powder on the inside and filled with a mixture of one or more noble gases (such as neon, argon, and krypton) and a small amount of mercury vapor. The atoms of the gas emit photons during an electric discharge between electrodes at the ends of the tube. The ultraviolet photons produced due to the excitation of mercury atoms are absorbed in the phosphor coating, which reemits photons at longer wavelengths in the visible. (For more details on fluorescent lamps, see Jack and Vrehen, 1986). This is an example of a large Stokes shift. The wavelength mixture of the emitted light can be selected by using an appropriate phosphor coating.

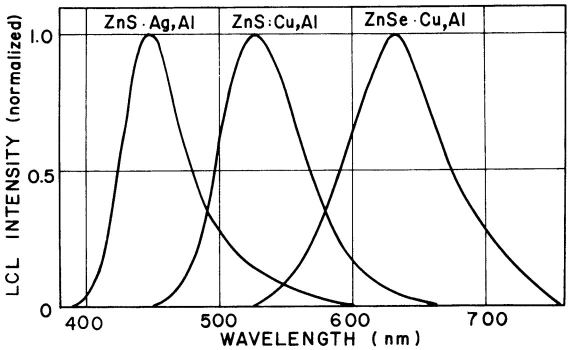

Figure 8.1. Low-voltage (~ 50 V) CL spectra for low-resistivity crystals of ZnS:Ag,Al, ZnS:Cu,Al and ZnSe:Cu,Al. (After Kukimoto *et al.*, 1979.)

Numerous reports have appeared on the dependence of the CL intensity on the excitation conditions. This is an important property of phosphors, since it relates the brightness to the electron beam current. Typically, the light intensity increases linearly with increasing electron beam current density. At the levels of electron beam current density that are characteristic of a particular material, this dependence exhibits saturation (i.e., it falls below linear dependence). Several recent reports indicate that the saturation behavior in various phosphors may be related to activator ground-state depletion and Auger-type relaxation (Imanaga *et al.*, 1980; Kuboniwa *et al.*, 1980; McColl, 1982; De Leeuw and Hooft, 1983).

Linearity of luminescence intensity under high electron beam currents is an important feature of advanced screens. Unfortunately, ZnS materials, which have the highest maximum CL efficiency, exhibit saturation under high electron beam

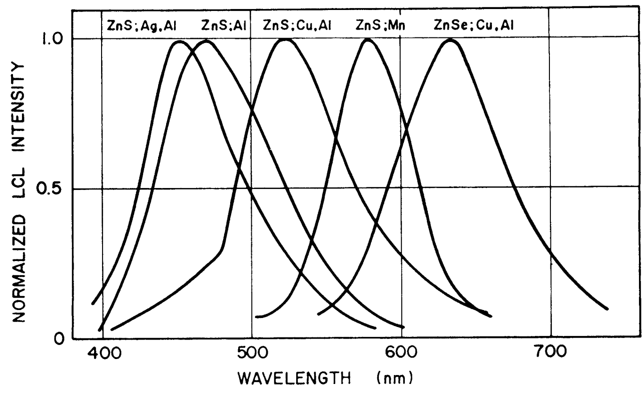

Figure 8.2. Low-voltage (~ 50 V) CL spectra for low-resistivity powder phosphors. (After Kukimoto *et al.*, 1979.)

densities. Other phosphors with high linearity characteristics are thus of great importance. Rare earths have become attractive alternatives for phosphor screens (Maestro, 1985; Pappalardo, 1987). The internal 4*f* shell in rare earths is shielded by the outer 5*s* and 5*d* shells, so the optical absorption and emission spectra that are due to transitions between discrete energy levels of the ion are quite insensitive to external perturbations. An important application of rare earths is in color television. The Eu^{3+}-activated compounds $Y_2O_3{:}Eu^{3+}$ and $Y_2O_2S{:}Eu^{3+}$ provide a superior alternative to (Zn,Cd)S:Ag as the red component in color cathode-ray tubes. The main advantage of these rare-earth phosphors, compared with the less expensive II-VI compound phosphors, is the high brightness in the red and the high color saturation. An additional advantage of materials such as $Y_2O_3{:}Eu$ is that their efficiency is not affected significantly by higher operating temperatures of up to about 400°C. In comparison, operating-temperature-induced reductions of efficiency occur at much lower temperatures (below 100°C) in ZnS:Ag, for example (Kazan, 1985).

The luminescence properties of phosphors under electron beam excitation are usually analyzed by using a relatively simple system containing an electron gun, a photomultiplier, an oscilloscope (for time-resolved brightness measurements), and an optical microscope (for brightness measurements of small regions, i.e., the spot brightness). Three modes of excitation can be used: continuous, pulsed, and raster. Problems associated with some of the measurements using such a system were outlined by Stevens (1978). These problems are related mainly to multiexcitation effects in the raster method. It was concluded that the most adequate method for the characterization of phosphors is a spot brightness measurement with a single line-scan raster or with a stationary pulsed beam (Stevens, 1978).

8.2. Cathodoluminescence Efficiency of Phosphors

In the development of phosphors, it is important to relate their maximum efficiency to materials properties. This helps in developing models for phosphor systems that go beyond empirical treatments, and it may help in predicting materials with high CL efficiency. Semiempirical treatments of the CL power conversion efficiency were presented by Garlick (1950, 1966), Bril and Klasens (1952), Ludwig and Kingsley (1970), Lehmann (1971), Alig and Bloom (1977), Alig *et al.* (1980, 1981), Robbins (1980), and Alig (1983).

Cathodoluminescence efficiency is basically determined by the efficiency of generating electron-hole pairs. Primary electrons can lose their energy by generating optical phonons or by ionization scattering, leading to the formation of electron-hole pairs. Thus, the average energy required to generate an electron-hole pair includes phonon losses. The quantum yield of electron-hole pairs is largely determined by the loss parameter, i.e., by the ratio of the energy lost in the generation of phonons to that in ionization scattering. Unlike the semiempirical treatments of the loss parameter in earlier work, Inoue (1984) presented a model that relates the loss parameter to materials constants. For a linear dependence of the luminescence intensity on the electron beam current density and the accelerating voltage, CL efficiency can be expressed as (Inoue, 1984)

$$\eta_p = (1-\gamma)h\nu Y\eta \qquad (8.1)$$

where γ is the backscattered coefficient, $h\nu$ is the energy of the emitted photon, Y is the limiting quantum yield of electron-hole pairs, which is basically the inverse of the average energy required for the formation of an electron-hole pair, and η is the radiative recombination efficiency. If γ does not vary significantly for various materials, then in an ideal situation ($\eta \approx 1$) the maximum CL efficiency for a given host-activator system $\eta_p \propto Y$. Inoue (1984) evaluated explicitly the quantum yield of electron-hole pairs in terms of the band-gap energy E_g and phonon loss parameters S_d and S_p related to the optical phonon deformation potential and the polar-mode electrostatic interactions, respectively. Inoue showed that these phonon loss parameters are in turn determined by materials parameters, such as E_g, the lattice constant, the mass density, the covalency, the optical phonon energy, and the effective dielectric constant.

Examples of the CL efficiency of some CRT phosphors are listed in Table 8.2. An important point concerning the accuracy of the measurement of the CL efficiency of phosphors should be made here. Kano and Uchida (1983) investigated the effect of the phosphor screen packing density on the CL intensity. Contrary to the expectation that the increase in the packing density would be beneficial, a 6% enhancement of the CL was observed in phosphors with reduced packing densities. This was explained by a model assuming the capture of backscattered electrons in rougher screen surfaces.

The external luminescence efficiency of phosphors deteriorates under prolonged electron beam excitation. Such phosphor degradation, which increases with the excitation density, limits the lifetime of cathode-ray displays. Thus, this

Table 8.2. Maximum Power Efficiency of Some CRT Phosphors*

Phosphor	Efficiency (%)
ZnS:Ag,Cl (blue TV)	25
(Zn,Cd)S:Cu,Al (green TV)	18
Y_2O_2S:Eu (red TV)	11
Y_2O_2S:Tb	18
Zn_2SiO_4:Mn	8
ZnS:Mn	5

*After Kazan, 1985.

effect is of major importance in selecting phosphors for applications such as information displays, which demand long operating lives and high beam current operation. A systematic analysis of phosphor degradation was provided by Klaassen *et al.* (1987), who expressed the external luminescence efficiency at low excitation density (i.e., such that saturation effects are not important) as

$$\eta_{\text{ext}} = h\nu Y \eta_t \eta f_{\text{ext}} \tag{8.2}$$

where η_t, the transfer efficiency, is the quantum efficiency for the transfer of the energy of electron-hole pairs to activator ions, η is the radiative recombination efficiency of the activator ions, and f_{ext} is a factor that accounts for the fact that not all photons generated in the phosphor are able to leave through its surface due to optical absorption and reflection losses. Note that changes in the backscattered electron correction in this case are disregarded. In terms of the parameters in equation (8.2), degradation effects were considered by Klaassen *et al.* (1987) to be due to changes in η_t, η, and f_{ext}. A decrease of η_t can be due to a decrease in the energy flow to the activator, or to an increase of energy losses in the host lattice. The former cause will be reflected in saturation behavior that starts at lower excitation densities than in unexposed phosphor. A decrease in η_t in this case is due to a substantial reduction of the effective luminescent centers. An increase of energy losses in the host lattice is due to enhanced surface losses and an increase of bulk "killers" (Klaassen *et al.*, 1987). A reduction of τ_{nr} of the activator ions in the excited state may lead to a reduction of η [see equation (3.26)]. And finally, f_{ext} may be affected by changes in such optical properties of the material as the refractive index and/or absorption coefficient. Such changes may occur due to the production of color centers, for example, and/or to the deposition on the phosphor particles of a polymerlike absorbing layer caused by the presence of residual gases in the vacuum chamber. All these degradation mechanisms and experiments designed to separate their effects were analyzed by Klaassen *et al.* (1987) in several phosphors.

8.3. Cathodoluminescence Characterization of Phosphors

There have been numerous reports on CL emission characteristics, efficiency, linearity characteristics, and degradation phenomena of phosphors. However, although phosphors are ideal materials for CL studies, few articles reported the CL microcharacterization of phosphors using electron microscopy techniques. One possible reason for this failure to apply CL-SEM to phosphors is that, although CL microscopy techniques were advancing, the industrial research effort on phosphors was subsiding.

A recent demonstration of the power of CL-SEM, augmented by energy-dispersive x-ray spectroscopy (EDS), in analyzing phosphors was presented by Richards *et al.* (1984), who investigated fluorescent lighting phosphors. Such studies, combining CL microscopy and spectroscopy with compositional information from the individual powder particles, are especially helpful in identifying inferior materials that contain, for example, "rogue particles" or components with a low efficiency. These studies are also useful in optimizing parameters such as packing density, coating thickness, and particle size distribution of phosphors.

Earlier fluorescent lighting phosphors were complex halophosphates emitting a broad white spectral band. More recent phosphors are mixtures of narrower-band emitters: for example, $(Ba,Mg_2)Al_{16}O_{27}:Eu^{2+}$ (BAM), (Ce,Tb)-$MgAl_{11}O_{19}$ (CAT), and $Y_2O_3:Eu^{3+}$ (YOE). They emit in the blue, green, and red, respectively. The CL and PL (UV excitation) spectra of these phosphors are similar, so they can usefully be compared.

An example of the power of CL (in conjunction with EDS) in the identification of rogue particles and the cause of non-uniformity is that of CAT phosphor characterization (Richards *et al.*, 1984). An acceptable CAT particle should give three room temperature emission bands at 490, 550, and 590 nm. Poor CAT materials give broadened spectra, as shown in Figure 8.3, including emission with a shorter decay time at 520 nm. A monochromatic CL image recorded at 520 nm can thus be used to locate the rogue particles, and, subsequently, EDS analysis can provide compositional information. An analysis of such rogue particles revealed a Ce : Tb ratio of 1 : 3 instead of the expected ratio of 2 : 1 in the normal CAT material. In the secondary electron, CL, and x-ray SEM micrographs in Figure 8.4, the nonuniformity in CL properties corresponds to the variation in the distribution of Al and Tb. The processing step that caused the anomalous emission was identified as being the formulation or, more likely, the blending of the powder.

In some applications, a mixture of phosphors emitting primary colors (i.e., narrow-band spectra) is used to give a white light with a preferential tone by

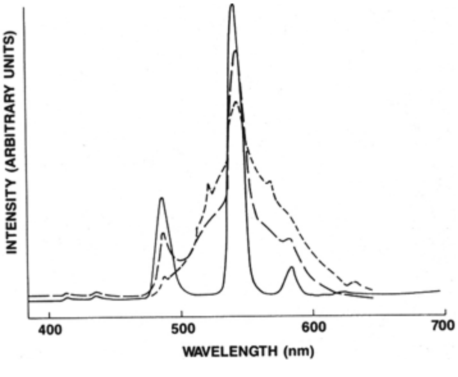

Figure 8.3. CL spectra (continuous curve) from normal (white) and (dashed curves) anomalous (yellow) CAT phosphor particles. (After Richards *et al.*, 1984.)

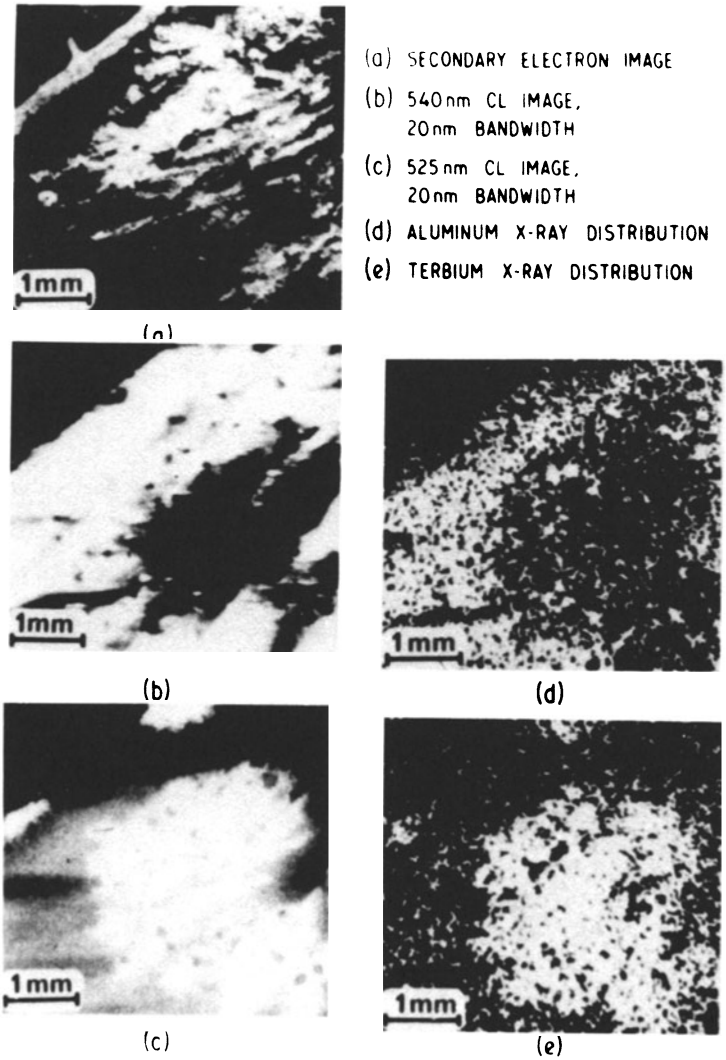

Figure 8.4. (a) Secondary electron, (b) and (c) CL, and (d) and (e) x-ray SEM micrographs of a region of a yellow and white CAT phosphor showing the surface topography, the nonuniform CL emission at 540 and 525 nm, and the distribution of Al and Tb in the material. (After Richards *et al.*, 1984.)

varying the proportions of phosphors in the blend. One such blend contains BAM (blue emitter), CAT (green emitter), and YOE (red emitter), which results in the series of band emissions shown in Figure 8.5. In this case, because individual phosphor particles produce well-separated narrow-band emission spectra, the blend components can be easily identified from CL measurements (Figure 8.6).

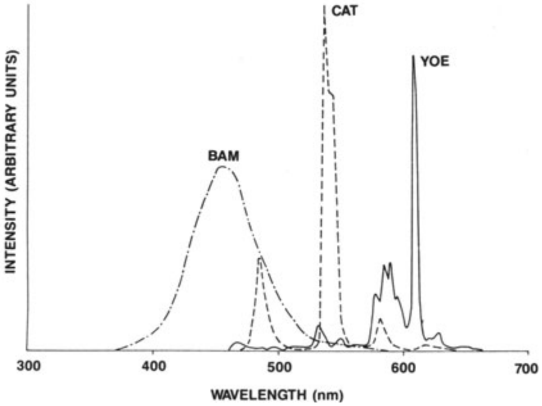

Figure 8.5. CL spectra of a blend of BAM, CAT, and YOE phosphors. (After Richards *et al.*, 1984.)

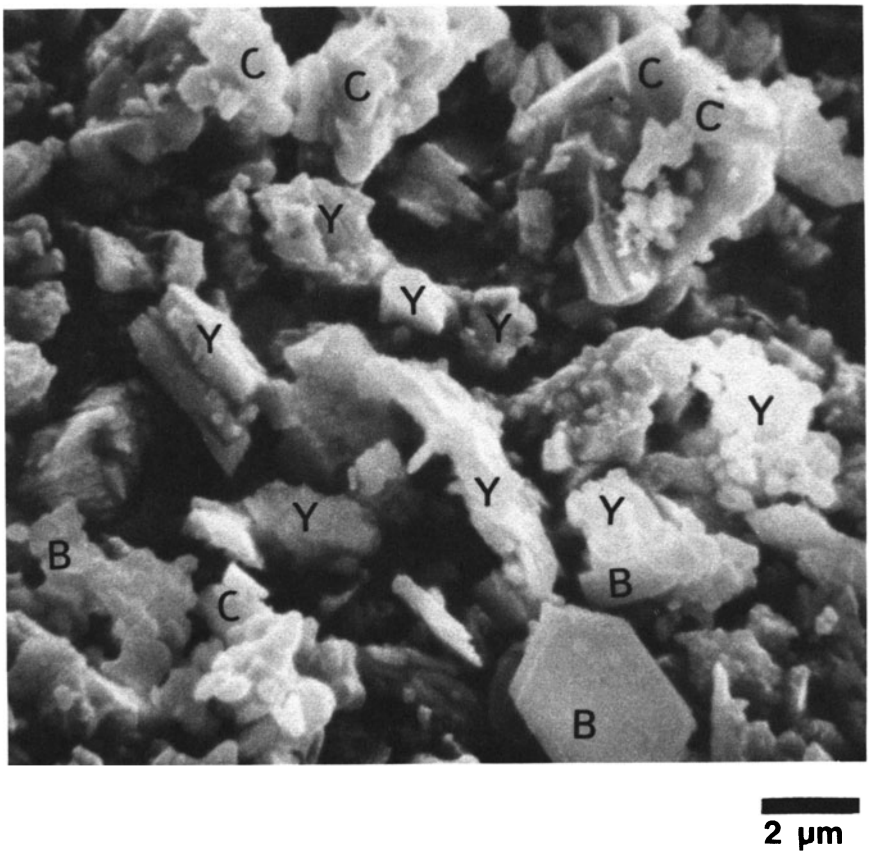

Figure 8.6. Secondary electron image of a blend of BAM (B), CAT (C), and YOE (Y) phosphor particles. The individual phosphors were identified from CL measurements. (After Richards *et al.*, 1984.)

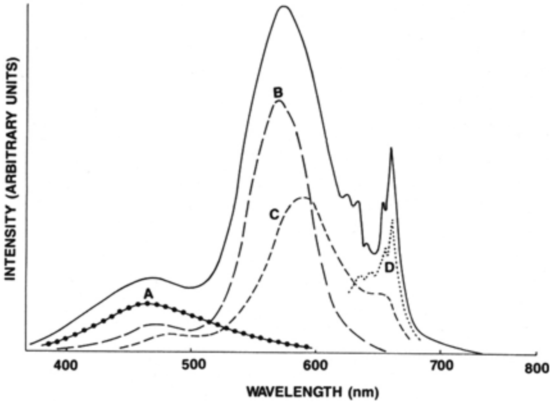

Figure 8.7. The CL spectrum of a blend Neoline soft phosphor (solid line) and the CL spectra of its four components: strontium phosphate (A), calcium halophosphate (B), strontium orthophosphate (C), and magnesium fluorogermanate (D). (After Richards *et al.*, 1984.)

In some cases, such as BAM and CAT phosphors, CL spectra provide a more reliable means of identification than does x-ray analysis.

Although more difficult, such an analysis of phosphor blends may also be performed in the case of overlapping broadband emission spectra. This occurs, for example, with "Neoline soft," which appears to be a promising material for new deluxe lamps. The CL spectrum of the blend is shown in Figure 8.7 as a solid line. Using CL monochromatic imaging recorded at 450, 570, 575, and 654 nm, Richards *et al.* (1984) determined the location and composition of particles corresponding to the four components in the blend. The CL spectra of these components are shown in Figure 8.7 with their probable identification. These are strontium phosphate emitting at ~450 nm, calcium halophosphate emitting at ~570 nm, strontium orthophosphate emitting at ~575 nm, and magnesium fluorogermanate emitting at ~654 nm.

Richards *et al.* (1984) also demonstrated the usefulness of CL-SEM analysis for *in situ* studies of phosphor lamp coatings by examining tube sections with various viewing angles.

Preliminary results indicated that the incorporation of a hot SEM stage for temperature stability studies and accelerated life testing to identify degradation mechanisms will also be of great benefit for phosphor applications.

9

Ceramics

9.1. Introduction

Ceramics comprise a wide range of materials, which have found a great variety of applications due, for example, to their hardness and refractory properties (i.e., resistance to heat and corrosion). Ceramics, from the materials science point of view, include all nonmetallic inorganic solids that may contain as constituents both metallic and nonmetallic elements held together by mixed ionic and covalent bonding. With this definition, even semiconductors, phosphors, and minerals would be considered as ceramic materials, so some materials that are often considered as ceramics are treated in other chapters.

In a comprehensive introduction to the field of ceramics, Kingery *et al.* (1976) distinguished between two major groups of ceramic materials: traditional ceramics and new ceramics. The former are defined as materials that are used in the silicate industries (clay products, cement, silicate glasses). New ceramics include, for example, *ferroelectric ceramics* (e.g., $BaTiO_3$), *electrooptic ceramics* (e.g., $LiNbO_3$), *pure oxide ceramics* (e.g., Al_2O_3, MgO), *nuclear fuels* (e.g., UO_2), *magnetic ceramics, ceramic nitrides, ceramic carbides, ceramic borides,* and *glass ceramics.* Some current areas of application of advanced ceramics are the electrical industry (insulators), reactors (nuclear fuels), rocketry and aviation (critical temperature-resistant parts), machining (cutting tools), efficient engines, and the electronics industry (both as components and actual devices). The applications of CL analysis to ceramics are not as widespread as this grouping of ceramics. However, CL studies of certain ceramics have attracted considerable interest, and these will be described in this chapter. The materials studied are *electronic ceramics* (for example, ferroelectrics, electrooptic ceramics, ZnO), *pure oxides,* and *glasses.* (Values of the band gaps of some ceramics are listed in Table 9.1.)

Commonly, the electronic ceramics are polycrystalline and polyphase mate-

Table 9.1. Values of the Band Gaps of Some Ceramics*

Material	Band gap E_g (eV)
SiO_2	8
MgO	8
CaO	9
Al_2O_3	7.4
UO_2	5.2
TiO_2	5
NiO	4.2
$LiNbO_3$	4
$SrTiO_3$	3.3
$BaTiO_3$	3

*After Kingery *et al.*, 1976.

rials with grain sizes between about 1 and 10 μm. The properties and the microstructure of the grains and grain boundaries have a major influence on these materials, and the control of the composition and microstructure of the grains and grain boundaries are crucial in developing and utilizing electronic ceramics. Thus, it is essential to explore these materials with microcharacterization techniques that allow the determination of microstructure and provide information on the electrical, elemental, and chemical properties of the grains and grain boundaries. In this context, CL microscopy and spectroscopy can provide important information on, for example, the composition and uniformity of luminescent ceramic materials. Especially important issues in electronic ceramics are those related to the grain boundaries. It has been established, for example, that (1) the grain boundaries are paths for the rapid diffusion for various impurities, (2) the grain boundaries generally have an associated space-charge layer controlled by the defect structure of the material, and (3) grain boundary segregation, precipitation, and oxidation typically affect a wide variety of properties of electronic ceramics (Kingery, 1981).

Typical examples of the effect of the microstructure and composition of grains and grain boundaries on the operation of devices based on ceramic materials occur in barium titanate ($BaTiO_3$) positive-temperature-coefficient (PTC) resistors, and ZnO varistors.

The use of ceramic materials, such as $BaTiO_3$, in PTC resistors is based on the behavior of the grain boundary layer of ferroelectric semiconductors in a small temperature range around the Curie temperature; above this temperature, the electrical resistance of *n*-doped polycrystalline $BaTiO_3$ material increases several orders of magnitude. This behavior arises from potential barriers at the grain boundaries. The formation of potential barriers at the grain boundaries is thought to be due to acceptor states that compensate the conduction electrons in the grain boundary region. The height of the potential barriers is temperature-dependent, and it increases at the Curie temperature, leading to an increase in the electrical resistance. As will be outlined in the following section, the CL technique can elucidate some features of grain boundaries in this material.

Grain boundaries are also important in the operation of ZnO varistors (i.e., variable resistors) that are used as solid-state switches. In this application, the polycrystalline ZnO consists of semiconducting ZnO grains and a matrix of insulating grain boundary material. The electrical properties of such a material can be highly nonlinear. At low voltages, because of the insulating grain boundary barriers, the electrical conductance is low. At higher voltages, conduction occurs across the insulating grain boundaries through the ZnO grains. Strongly nonlinear current-voltage characteristics in this material are similar to those of two back-to-back diodes, which in this case are formed as a result of the presence of negative charge at the grain boundary surrounded by positively charged donor states in the double depletion zones in the adjacent ZnO grains. The current-voltage relation (i.e., the voltage that corresponds to the switching to the highly conducting state) can be adjusted by doping of the ZnO grains, by controlling the composition of the grain boundary phase and by varying the microstructure (i.e., the size of the ZnO grains and the width of the insulating layers between the grains). Cathodoluminescence analysis can be used to investigate the microstructure and the grain boundaries in this material.

Among electronic ceramics, electrooptic ceramics (such as lithium niobate, $LiNbO_3$) have attracted increasing interest in optical communication and optical computing applications. The basis of such applications is the electrooptic effect, i.e., the change in refractive index of a material with electric field. In addition to the currently used monocrystalline $LiNbO_3$, possibilities of using ferroelectric electrooptic ceramic materials, such as $BaTiO_3$ and $KNbO_3$, are of considerable interest.

Among advanced ceramics, the so-called glass ceramics have also attracted increasing interest. During the preparation of these materials, nucleation species promote the formation of fine crystalline grains, resulting in greater strength and temperature resistance than in noncrystalline glasses.

The following sections will outline applications of CL microscopy and spectroscopy to some of these ceramic materials. The power of the CL technique, especially in characterizing grain boundaries of electronic ceramic materials, will be demonstrated.

9.2. Electronic Ceramics

An early application of CL microscopy to the visualization of the grain boundary potential barriers in PTC-type $BaTiO_3$ ceramics was reported by Ihrig and Klerk (1979), who were the first to provide CL images of this material. They

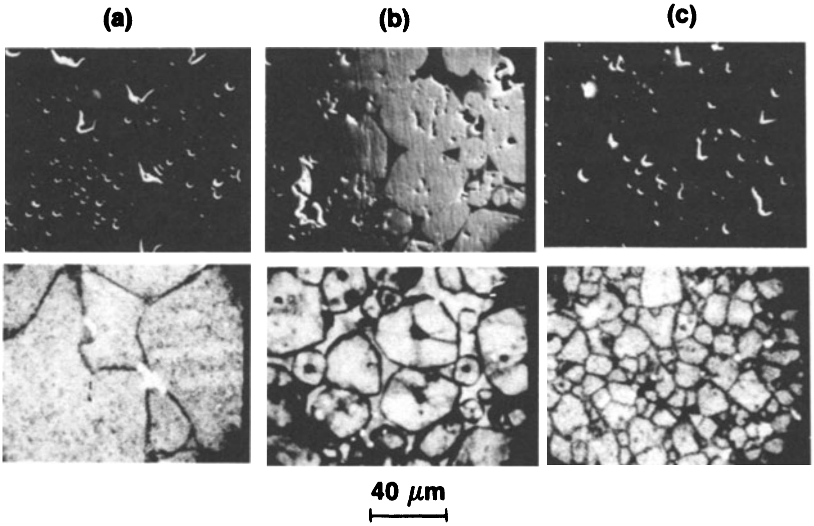

Figure 9.1. Secondary electron images (top row) and CL images (bottom row) of PTC-type $BaTiO_3$ ceramics. The color of the $BaTiO_3$ grains is greenish and of the second phase reddish for materials with (a) Sb-doping and 3 mol% TiO_2 excess, (b) Sb-doping and 20 mol% TiO_2 excess, and (c) Y-doping and 3 mol% TiO_2 excess. (After Ihrig and Klerk, 1979.)

reported that the $BaTiO_3$ grains appeared green, as did undoped Y-, La-, and Sb-doped materials prepared and treated in oxidizing or reducing atmospheres. Thus, it was concluded that the luminescence was not caused by doping or defects such as anion or cation vacancies, but was due to the fundamental emission in the material (i.e., the recombination of electrons in the conduction band with holes in the valence band) (Ihrig and Klerk, 1979). Figure 9.1 summarizes these observations. The secondary and CL images of Sb-doped and Y-doped materials were recorded at room temperature about 100° below the Curie point. In the CL images, the grain boundaries appear darker than the grains (see Figure 9.1). In these samples, in addition to the green $BaTiO_3$ grains surrounded by the dark boundaries, a reddish second phase was also observed (Ihrig and Klerk, 1979). Dark grain boundaries were reported in the CL images of PTC-type materials only; they were absent in undoped materials and in PTC materials that had been reduced and had lost their PTC behavior (Figure 9.2). In addition, dark grain boundaries, absent in La-doped $BaTiO_3$, appeared after the samples were oxidized at temperatures above 1250°C, which also resulted in PTC behavior as determined from the resistivity curves (Ihrig and Klerk, 1979). Thus, the existence of the grain boundary potential barriers below the Curie temperature was directly demonstrated. It was concluded that the presence of the depletion layers at the grain boundaries results in the CL quenching in the grain boundary regions

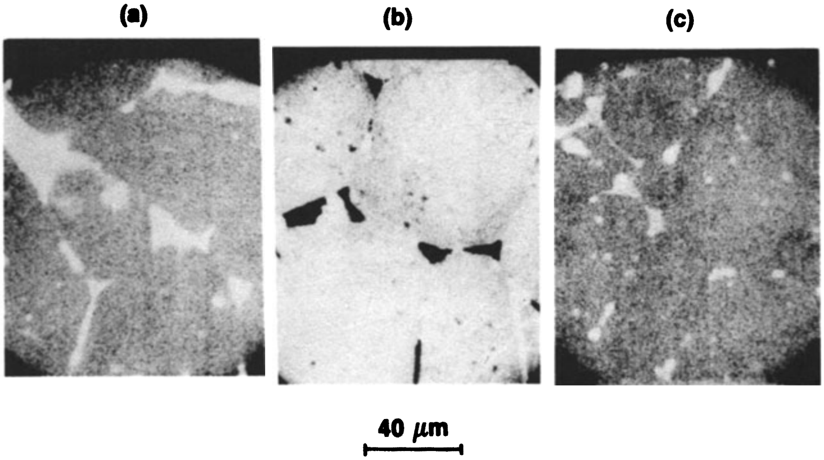

Figure 9.2. Cathodoluminescence images of the $BaTiO_3$ ceramic with 3 mol% TiO_2 excess: (a) undoped, nonconducting $BaTiO_3$ sintered in air; (b) material as in (a) but additionally reduced at 1200°C for ½ h to obtain good electrical conductivity; (c) Sb-doped, formerly PTC-type $BaTiO_3$ ceramic reduced at 800°C for ½ h; the PTC effect has vanished due to the reduction treatment. (After Ihrig and Klerk, 1979.)

(Ihrig and Klerk, 1979). Panchromatic CL imaging, however, was not sufficient to explain details of the CL mechanisms. Ihrig *et al.* (1981) also determined that the CL spectra of $BaTiO_3$, $SrTiO_3$, and TiO_2 were similar (Figure 9.3), and the location and shape of the luminescence did not depend on doping and heat treatments in reducing atmospheres. The luminescence was interpreted as a fundamental transition of local character in the TiO_6 octahedron.

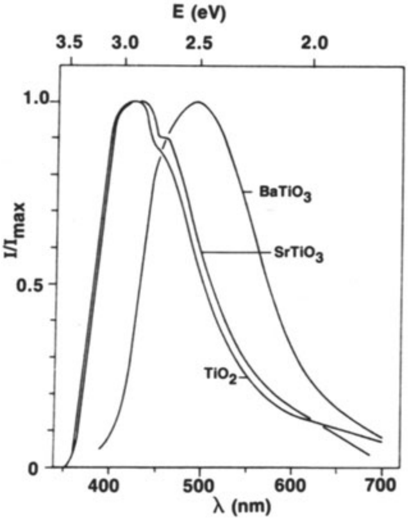

Figure 9.3. Cathodoluminescence spectra of typical $BaTiO_3$, $SrTiO_3$, and TiO_2 ceramics, which were reduced at 1200°C for ½ h. (After Ihrig *et al.*, 1981.)

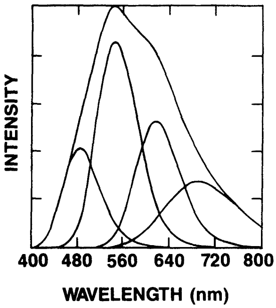

Figure 9.4. $BaTiO_3$ ceramic. The fitted curve of the measured CL spectrum (recorded at 77 K) with its four Gaussian components. (After Koschek and Kubalek, 1983.)

As mentioned in Section 9.1, the PTC effect was related to acceptor states at the boundaries of the $BaTiO_3$ grains. Cathodoluminescence observations by Koschek and Kubalek (1983, 1985a) demonstrated the existence of high-Ba-vacancy concentrations in the grain boundary zone. The CL properties of the $BaTiO_3$ grains were studied by Koschek and Kubalek (1983), who found that the CL spectra were composed of several Gaussian bands (see Figure 9.4). The luminescence intensities of the bands were found to depend strongly on the specimen temperature and on the oxygen partial pressure during the sintering process. The deconvoluted CL bands (Figure 9.4) were associated with transitions involving Ba vacancies (see Figure 9.5) (Koschek and Kubalek, 1983). The results were in agreement with the prediction that a higher Ba vacancy concentration is expected for a higher value of the oxygen partial pressure. The assumption that the grain boundary depletion zones are caused by Ba vacancies acting as acceptors was supported by further studies using CL microscopy and spectroscopy (Koschek and Kubalek, 1985a).

For CL panchromatic imaging, two types of detectors were used: a photomultiplier (with spectral range of 300 to 850 nm) and a Ge detector (with spectral range of 800 to 1800 nm). In the $BaTiO_3$ CL contrast inversion was observed. With the photomultiplier, the grains appeared bright, and the grain boundaries were dark. With the Ge detector, panchromatic CL images revealed

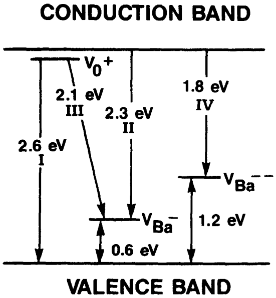

Figure 9.5. Recombination processes in the $BaTiO_3$ grains. The observed transitions are marked I to IV. (After Koschek and Kubalek, 1983.)

the opposite: the grains appeared dark, and the grain boundary zones were bright. The second phase in the material also appeared bright. In order to explain their observations, Koschek and Kubalek (1985a) proposed that, assuming equal recombination rates in the grain and in the grain boundary region, the recombination in the visible range would be quenched, provided an additional level corresponding to an infrared transition is present in the band gap of the $BaTiO_3$. The theoretical calculations of the band scheme for $BaTiO_3$ provided by Daniels and Hardtl (1976) showed that such an infrared recombination can be related to the doubly ionized Ba vacancies. (Note that there is a discrepancy between the level of the doubly ionized Ba vacancy shown in Figure 9.5 and the theory, which predicts a level 1.6 eV above the valence band.) Since the presence of Ba vacancies could result in CL quenching in the visible range, the observed dark boundaries were taken to indicate a high Ba vacancy concentration in the grain boundary regions (Koschek and Kubalek, 1985a).

Llopis *et al.* (1984) reported CL microscopy and spectroscopy studies of $LiNbO_3$. They observed three emission bands, at 410, 525, and 580 nm, which were strongly affected by the deformation of the surface region. The luminescence band at 410 nm was attributed to the normal niobate groups, and the bands at 525 and 580 nm were attributed to disturbed niobate groups (i.e., groups with the Nb ions occupying Li sites). In addition, it was concluded that the band at 580 nm was related to the electron beam excitation of the sample. It was observed that irradiation with high electron beam currents resulted in substantial damage and quenching of the CL signal. Deformation of the surface region (i.e., mechanical indentation) was found to cause CL intensity enhancement in the cracked areas (Llopis *et al.*, 1984).

Cathodoluminescence analyses of grain boundary phenomena in ZnO varistor ceramics were reported by Löhnert and Kubalek (1983). As mentioned in the introduction, the nonlinear électrical characteristics of this material are related to the grain boundaries. In their studies, Löhnert and Kubalek (1983) attempted to confirm the idea that oxygen is responsible for the properties of the grain boundaries (Einzinger, 1978). Oxygen is thought to be incorporated at the grain boundaries where material, which is typically *n*-type, becomes intrinsic. This results in the formation of a *n-i-n* structure between adjacent grains with the potential barrier causing nonlinear electrical properties. Löhnert and Kubalek (1983) investigated pure air-sintered ZnO ceramics and found that the oxygen content near the grain boundaries was significantly enhanced. These observations are summarized in Figure 9.6, which presents a panchromatic CL image of pure ZnO ceramic (Figure 9.6a) and the normalized CL spectra recorded in the interior of the grain (denoted *G*) and in the bright grain boundary region (denoted *B*) (see Figure 9.6b). Spectrum *B* is usually observable in material sintered in pure oxygen, and spectrum *G* is typically observed in material sintered in pure nitrogen, which appears to support the proposal of the effect of oxygen at the grain boundaries (Löhnert and Kubalek, 1973). Unfortunately, these CL observations were in-

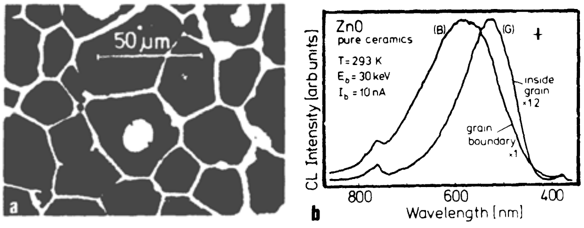

Figure 9.6. (a) Panchromatic CL image of pure ZnO ceramic, and (b) the normalized CL spectra measured inside the grain (G) and in the grain boundary region (B). (After Löhnert and Kubalek, 1983.)

conclusive, since no substantial nonlinearity in the electrical properties was detected in these samples. Löhnert and Kubalek (1983) concluded that if oxygen does indeed play a crucial role in the nonlinear behavior of varistors, its influence must be substantially stronger than in the pure material. It was also pointed out that the foregoing CL analysis could not be applied to varistor ceramics where the luminescence is dominated by centers associated with metal-oxide additives (Löhnert and Kubalek, 1983). Additional complications (or ambiguities) in interpreting the results were caused by the fact that, as the CL images of varistor devices indicated, the concentration of these centers also increased at the grain boundary regions (Löhnert and Kubalek, 1983).

A CL analysis of ZnO ceramics was reported by Piqueras and Kubalek (1985a), who observed CL quenching in the visible range and a shift of the emission band to longer wavelengths with deformation (see Figure 9.7). The CL quenching was attributed to dislocation-related nonradiative recombination centers produced by mechanical damage. To relate the presence of vacancies to luminescence effects, Piqueras and Kubalek (1985b) performed studies of CL quenching produced by irradiation with 2.6-MeV electrons. Their analysis indicated that defects in the zinc sublattice (possibly vacancies acting as electron traps) caused CL quenching.

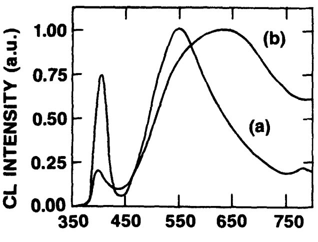

Figure 9.7. Cathodoluminescence spectra of ZnO ceramic: (a) undamaged area and (b) damaged area. (After Piqueras and Kubalek, 1985a.)

9.3. Pure Oxides

The application of CL analysis to alkaline-earth oxides has elucidated issues related to deformation-induced defects in these materials. Several reports revealed that plastic deformation causes a significant enhancement of the luminescence from the deformed regions in, for example, MgO (Llopis *et al.*, 1978; Datta *et al.*, 1979b, 1980b), CaO (Llopis and Piqueras, 1983), and SrO (Llopis *et al.*, 1985). The CL emission was found to depend on the type of deformation (i.e., compression or indentation). These observations were generally attributed to point defects or dislocations produced on the slip bands during deformation. Specifically, Llopis *et al.* (1978) observed in their panchromatic CL images of plastically deformed MgO that slip bands emitted a blue luminescence, which was ascribed to recombination at vacancies generated by slip. In contrast, the blue CL in indented MgO was attributed to the formation of interstitials (Veled-nitskaya *et al.*, 1975), and Pennycook and Brown (1979) proposed that the dilatation-induced reduction of the band gap around a dislocation results in visible luminescence.

Chaudhri *et al.* (1980) observed in the CL micrographs of indented MgO that the luminescence intensity from screw dislocations was substantially higher than that from the edge dislocations. They also commented that since the screw dislocations generate steps on the surface, the steps might have reflected light more efficiently. Chaudhri *et al.* (1980) also remarked that their results contradicted the model of the effect of dilatation-induced gap reduction at dislocations, since the dilatation around a screw dislocation is zero.

Datta *et al.* (1979b) used monochromatic CL microscopy as well as CL spectroscopy to analyze MgO crystals. In undeformed MgO, they obtained a CL spectrum containing two overlapping blue bands with peaks at 425 nm and 488 nm; in addition, a broad red band with a number of unresolved peaks (the strongest at about 770 nm) was also present. (The red band was attributed to iron impurities.) After plastic deformation, the red band was unaffected, but in the blue region one broad band (with enhanced intensity) at 466 nm was observed (Datta *et al.*, 1979b). Monochromatic CL micrographs (recorded at 466 nm) showed that the enhanced emission originated from the slipped planes of the crystal. The CL observations on MgO crystals containing a higher concentration of iron (and apparently already deformed) revealed additional features in the red band (Figure 9.8a) (Datta *et al.*, 1980b). The presence of several bands with peaks at about 688, 706, 723, and 747 nm, which are clearly observable in Figure 9.8a, provided stronger support for ascribing these bands to iron doping, since they were more intense and better defined. In addition, although these bands are unaffected by deformation, annealing in reducing atmospheres, which is known to alter the valence state of iron ions, significantly modifies the form of the bands (Datta *et al.*, 1980b).

The CL spectrum from single slip lines of the deformed sample is a broad

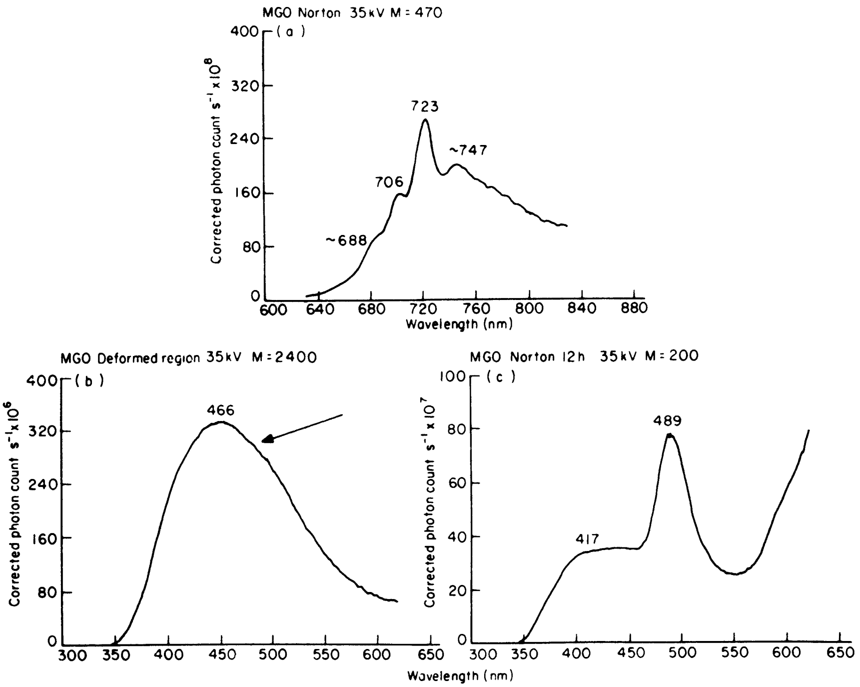

Figure 9.8. Corrected CL emission bands from deformed MgO crystals containing 200–250 ppm of iron: (a) CL spectrum in the red region; (b) CL spectrum in the blue region obtained from a slip line after deformation; (c) CL spectrum in the blue region after annealing for 12 h at 1530 K in an oxidizing atmosphere (air). (After Datta *et al.*, 1980b).

intense band with the peak at 466 nm (Figure 9.8b). The band with the peak at 488 nm in undeformed samples appears as a feature in the curve indicated by the arrow. It was also found that, although the intense blue band was not affected by annealing in reducing atmospheres, annealing in air at 1530 K for 12 h changes the band to the form shown in Figure 9.8c. This figure reveals several luminescence features indicating the presence of different bands caused by several defect configurations, which could explain the variations in peak values reported in the literature. Figure 9.9 presents the monochromatic CL image (recorded at 420 nm) of a deformed MgO specimen. Llopis *et al.* (1982) investigated the CL from dislocations in undeformed MgO crystals of different purities and doped with iron. They observed that, although dislocations in slip bands in deformed crystals exhibited enhanced emission, dislocations in undeformed crystals showed lower CL emission. This was attributed to decoration of dislocations (in undeformed crystals) by impurities and/or point defects (Llopis *et al.*, 1982). These observations also appeared to show that iron quenches the CL from defects. Thus, it

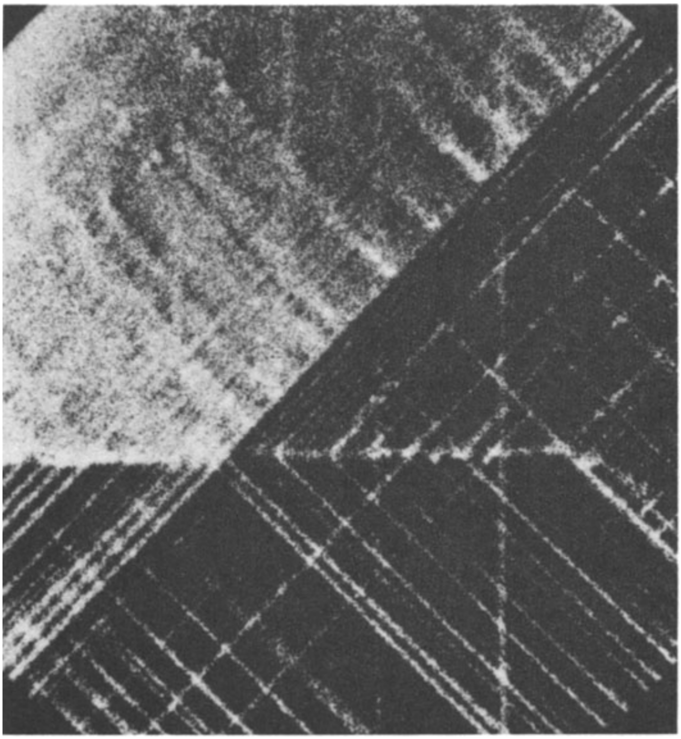

Figure 9.9. Monochromatic (420 nm) CL micrograph of an MgO specimen compressed 1.27%. The width of the area represented is approximately 900 μm. (After Datta *et al.*, 1980b.)

appears that the effects of impurities and point defects have to be considered in order to explain luminescence from defects in MgO.

Czernuszka and Page (1985) and Rincon *et al.* (1987) demonstrated the power of CL in analyzing phase distributions in ZrO_2-based ceramics, which are attractive materials because of their toughening properties. The improved toughness in these materials is related to the tetragonal-to-monoclinic phase transformation in phase mixtures and composites. Czernuszka and Page (1985) observed (1) enhanced luminescence associated with the monoclinic phase occurring on grain boundaries or produced by deformation and (2) luminescence quenching in cubic-plus-tetragonal material grain boundaries and in the deformed regions associated with hardness indentations and wear tracks. Rincon *et al.* (1987) obtained CL spectra with broad and sharp bands that were related to the different phases of mullite-ZrO_2. Enhancement of the 500-nm luminescence band was correlated with the increased concentration of the monoclinic ZrO_2 phase (Rincon *et al.*, 1987). As remarked by Czernuszka and Page (1985), the ability to obtain information on the spatial distribution of monoclinic material makes CL a powerful microcharacterization tool for the analysis of these ceramics.

The advantages of the CL-SEM mode in the analysis of the wear of ceramics and ceramic cutting tools were demonstrated by Enomoto *et al.* (1986 and references therein) and Brandt and Mikus (1987 and references therein), respectively. The former analyzed the wear damage (due to sliding contact) of magnesia, alumina, and diamond in terms of the presence of various types of defects. Brandt and Mikus used the CL mode in conjunction with x-ray microanalysis to investigate the changes in alumina-based ceramic cutting tools during machining steel. The major conclusion of the study was that chemical reactions with oxidized workpiece material and nonmetallic inclusions result in the formation of iron and magnesium aluminates, which have higher yield strengths, leading to reduced wear rates (Brandt and Mikus, 1987).

9.4. Glasses

Several luminescence studies, including CL, of defects in SiO_2 have been reported; however, no unambiguous correlations of luminescence bands with specific defects have been established yet. Jones and Embree (1976) observed a CL band at 4.77 eV (260 nm) in crystalline and at 4.28 eV (290 nm) in amorphous SiO_2 and correlated it with oxygen vacancies. The bulk samples were irradiated with high-energy neutrons and/or γ-rays in order to generate oxygen vacancies; and in thin-film material, oxygen vacancies were produced by heating the sample in a flowing CO/CO_2 atmosphere at 900°C for several hours. Optical absorption and spin resonance measurements were used to derive the oxygen vacancy concentrations. Figures 9.10 and 9.11 present luminescence spectra for crystalline and amorphous samples. In each spectrum, several bands are observed; and the individual spectra correspond to samples that were irradiated with different doses of neutrons (Jones and Embree, 1976). The luminescence band at 4.77 eV (260 nm) in the crystalline samples and at 4.28 eV (290 nm) in the amorphous samples was the only one proportional to the oxygen vacancy concentrations. In thin-film SiO_2, the band at 4.28 eV also appeared to correlate with the trapped positive charge in the layer. Hence, Jones and Embree (1976) concluded that the luminescence bands at 4.77 eV in crystalline and 4.28 eV in amorphous SiO_2 were related to the oxygen vacancy.

The properties of SiO_2 films are important in devices, and several CL studies, with the objective of analyzing defects in SiO_2 layers, have been reported (Koyama, 1980a; McKnight and Palik, 1980; Skuja and Entzian, 1986). No consistent correlations between the CL bands and specific defects, however, have been found. Koyama (1980a) observed the following CL bands in SiO_2 thin films: *A* at 290 nm (4.27 eV), *B* at 415 nm (2.99 eV), *C* at 560 nm (2.21 eV), and *D* at 650 nm (1.91 eV) (Figure 9.12). As can be seen in Figure 9.12, in some

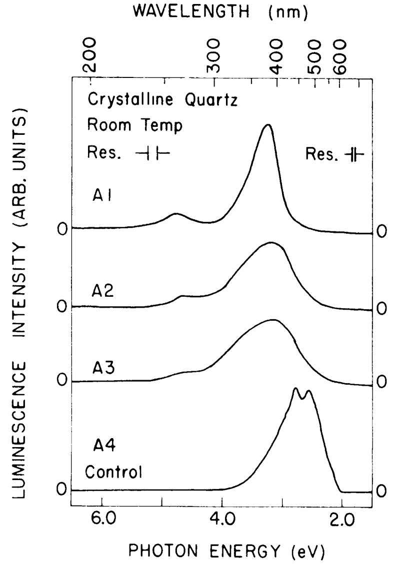

Figure 9.10. Cathodoluminescence from bulk crystalline SiO_2 samples excited by a 10-keV electron beam at 4.5×10^{-5} A/cm^2. Labels A1 through A3 indicate samples irradiated with various doses of fast neutrons. (After Jones and Embree, 1976.)

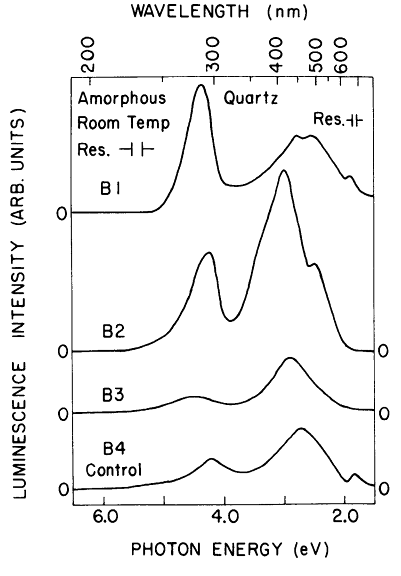

Figure 9.11. Cathodoluminescence from bulk amorphous SiO_2 samples excited by a 10-keV electron beam at 4.5×10^{-5} A/cm^2. Labels B1 through B3 indicate samples irradiated with fast neutrons or γ-rays and MeV electrons. (After Jones and Embree, 1976.)

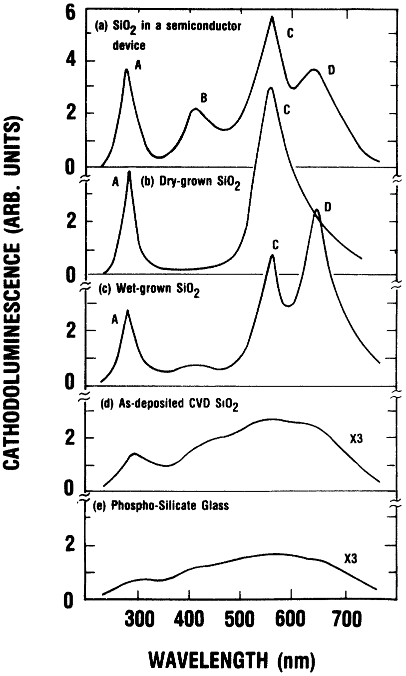

Figure 9.12. Cathodoluminescence spectra from (a) SiO_2 layers in a semiconductor device, (b) dry-grown SiO_2, (c) wet-grown SiO_2, (d) as-deposited CVD SiO_2, and (e) phosphosilicate glass. The electron energy was 20 keV and the electron beam current density was 1.5×10^{-5} A/cm^2. (After Koyama, 1980a.)

types of film certain bands were absent. To elucidate the impurities incorporated in the films (from, say, diffusion of intentional dopants in devices and metal contacts) and the adsorption of carbon and water onto the surface of the film, they introduced As, P, Al, C, and H into the films by ion implantation. Figure 9.13 presents the CL spectra of the ion-implanted films (Koyama, 1980a). Comparison of Figures 9.12 and 9.13 revealed changes in the CL spectra. The most apparent change occurred in the spectrum of dry-grown SiO_2 (compare Figures 9.12b and 9.13d), in which band *B* appeared due to carbon implantation. Koyama (1980a) argued that the appearance of this peak was related to the implanted impurities rather than to implantation-induced contamination or damage. Depth-resolved CL studies confirmed that the luminescence center associated with band *B* was related to the presence of carbon in the film. From the analysis of the CL results, Koyama (1980a) also concluded that bands *A* and *C* were due to electron beam–induced defects, and that band *D* might have originated from residual OH and/or adsorbed H_2O. Koyama (1980b) also demonstrated the power of monochromatic CL imaging for microcharacterization of irradiation-induced damage and processing-induced contamination in SiO_2 layers on a conventional large-scale integrated device.

McKnight and Palik (1980) studied CL intensities from SiO_2 films on silicon as a function of time, temperature, and electron beam current. They reported

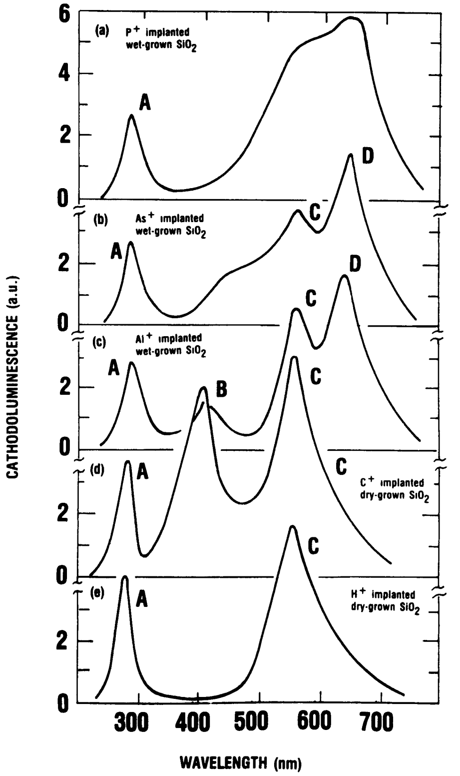

Figure 9.13. Cathodoluminescence spectra of SiO_2 ion-implanted with (a) phosphorus, 140 keV, 4 × $10^{15}/cm^2$, (b) arsenic, 140 keV, 4 × $10^{15}/cm^2$, (c) aluminum, 100 keV, 1 × $10^{15}/cm^2$, (d) carbon, 100 keV, 1 × $10^{16}/cm^2$, and (e) hydrogen, 30 keV, 4.5 × $10^{15}/cm^2$. The electron energy was 20 keV and the electron beam current density was 1.5 × 10^{-5} A/cm^2. (After Koyama, 1980a.)

CL bands at 1.9, 2.7, and 4.3 eV. The CL intensities were found to vary (for constant electron beam current) over a few minutes. The low-temperature and time-dependent luminescence results indicated a close relation between the luminescence centers associated with the 2.7-eV (blue) and 4.3-eV (UV) bands. The time-dependent luminescence results obtained as a function of temperature are shown in Figure 9.14. The decay curves of the UV and blue lines at low temperature, shown in Figures 9.14c,d are similar, suggesting a close relationship between the centers responsible for the two lines (McKnight and Palik, 1980). This conclusion, however, was contradicted by the current saturation behavior of these two lines, thus preventing any consistent conclusions. It was also found that the 1.9-eV (red) line showed no connection to the blue and the UV lines. McKnight and Palik (1980) attributed the low-temperature CL time decays to the long-term capture of, for example, the electron. The time-dependent increase of the intensity observed in some cases (Figure 9.14b) was ascribed to electron beam damage (Mitchell and Denure, 1973).

Skuja and Entzian (1986) compared their CL measurements on amorphous SiO_2 (which showed bands at 1.9, 2.7, and 4.3 eV) to PL spectra of irradiated or

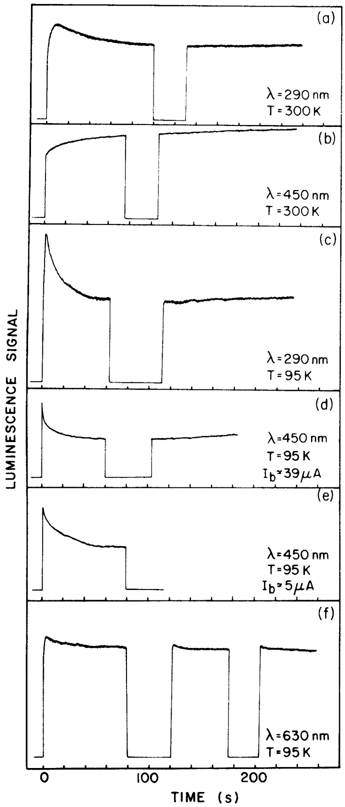

Figure 9.14. Time-dependent CL signals for a 825-Å dry-oxide film showing fatiguing and damage effects. All the data were taken with beam voltage $V_b = 800$ V. The steps in the curves represent drops of the signal to zero occurring when the beam was deflected from the sample: (a) $\lambda = 290$ nm, $T = 300$ K, $I_b = 40$ μA; (b) $\lambda = 450$ nm, $T = 300$ K, $I_b = 40$ μA; (c) $\lambda = 290$ nm, $T = 95$ K, $I_b = 38$ μA; (d) $\lambda = 450$ nm, $T = 95$ K, $I_b = 39$ μA; (e) $\lambda = 450$ nm, $T = 95$ K, $I_b = 5$ μA; (f) $\lambda = 630$ nm, $T = 95$ K, $I_b = 46$ μA. (After McKnight and Palik, 1980.)

oxygen-deficient amorphous SiO_2. They questioned the correlation between the 4.3-eV CL band and the oxygen vacancy by Jones and Embree (1976), and suggested different assignments for the observed CL bands. Thus, the CL band at 1.9 eV was attributed to a nonbridging oxygen center, and the CL bands at 2.7 and 4.3 eV were assigned to the triplet and singlet luminescence of a twofold coordinated silicon center. This assignment of the bands at 2.7 and 4.3 eV to transitions from excited states of the same defect is consistent with the observation (McKnight and Palik, 1980) of a close relationship between the centers that are responsible for the two bands.

Atkinson and McMillan (1974) demonstrated the value of the CL-SEM mode for the analysis of the microstructure of glass ceramics. They observed CL contrast, which could distinguish the lithium disilicate crystalline phase from the glassy matrix.

Several examples of the application of CL microscopy and spectroscopy to ceramic materials, including optical fibers, were described by Trigg (1985). To obtain low-loss fibers with a high refractive index core surrounded by a lower refractive index cladding layer, one deposits successive layers of silica inside a silica glass tube by chemical vapor deposition. The innermost layers are doped with Ge to increase the refractive index near the center. Fibers (with diameters about 100 μm) are drawn from a preform (with a typical diameter of 1 cm) obtained from the glass tube. Trigg (1985) demonstrated that CL can be effectively used for the analysis of the Ge distribution in the preform and in the fiber. A broad CL band with the peak at 400 nm was obtained from the Ge-doped core, and a broad CL band with the peak at 460 nm was obtained from the envelope of the preform. CL line scans were used for a semiquantitative analysis of the Ge distribution across the central region of the optical fiber preform. Assymetry of the distribution profile, which was related to poor control of the deposition conditions, was obtained, indicating possible substantial optical loss in the final fiber.

10

Minerals

10.1. Introduction

Most cathodoluminescence analyses of minerals are performed in relatively simple, but valuable (despite their limited spatial resolution), optical CL microscopes described in Section 5.4 (Hagni, 1987). An x-ray detector attachment developed by Marshall *et al.* (1987) for the Luminoscope (Nuclide), in addition to the CL capability, provides a powerful characterization technique for studies of minerals. The symposium "Cathodoluminescence Microscopy Applications in Process Mineralogy" (Hagni, 1987), including a bibliography by Barker (1987) with several hundred references, and earlier reviews of the CL of minerals (Remond, 1977; Nickel, 1978; Hagni, 1985) and a book by Marshall (1988) indicate that optical CL microscopy of minerals has become a significant field.

For some minerals, such as diamonds, CL-SEM and CL-STEM are used, as will be described in the following section. CL-SEM microcharacterization is demonstrated in Figure 10.1, which presents a secondary electron image (Figure 10.1a) and monochromatic CL images (Figures 10.1c,d) of a natural diamond. The monochromatic CL micrographs were recorded by using wavelengths corresponding to the peaks of the emission spectrum of the diamond shown in Figure 10.1b. There is little correlation between the CL images and the secondary electron image. Each wavelength used for this imaging can in principle be associated with particular luminescence centers (i.e., impurities or other point defects), so the monochromatic CL images resolve their distributions.

Minerals are often extremely complex and variable. Difficulties with CL observations on minerals (and phosphors as well) may arise due to long decay time luminescence in panchromatic images. This produces smearing of the image (see Figure 10.2); i.e., long streaks appear in the scan direction. One solution to this problem, in addition to avoiding such areas, is to obtain monochromatic micrographs recorded at wavelengths well away from the long-decay luminescence band.

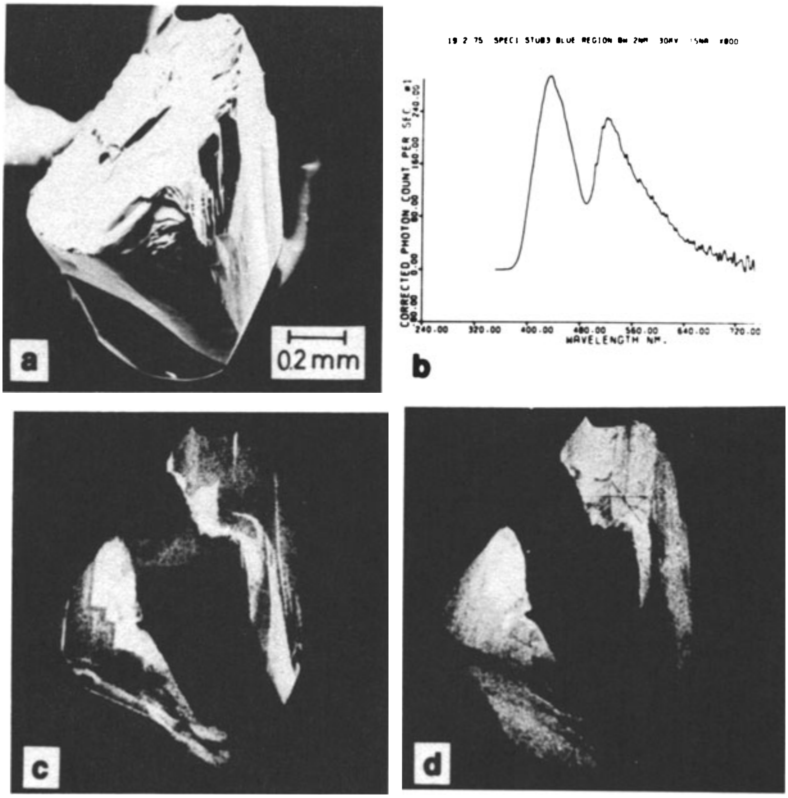

Figure 10.1. A natural diamond: (a) secondary electron image; (b) CL emission spectrum; (c) monochromatic (516 nm) CL image; (d) monochromatic (444 nm) CL image. The bandwidth was 2 nm, the electron beam voltage 30 kV, the electron beam current 15 nA, and the magnification × 800. (After Steyn *et al.*, 1976.)

10.2. Cathodoluminescence Studies of Diamond

Cathodoluminescence in diamond was first observed more than a century ago (Crookes, 1879). More recent studies include, for example, the work of Kiflawi and Lang (1976), Hanley *et al.* (1977, and references therein), Lang (1977, 1980), Pennycook *et al.* (1980), and Yamamoto *et al.* (1984).

A recent review by Walker (1979) outlines the optical properties and a qualitative classification system (and its inconsistencies) for diamonds. Many optical emission features in type Ia diamonds are related to the presence of nitrogen, and type IIb diamond, containing boron, is a *p*-type semiconductor. The common CL band in all types of diamond, both natural and high-pressure synthesized material, is the "band A" luminescence, which is attributed to donor-ac-

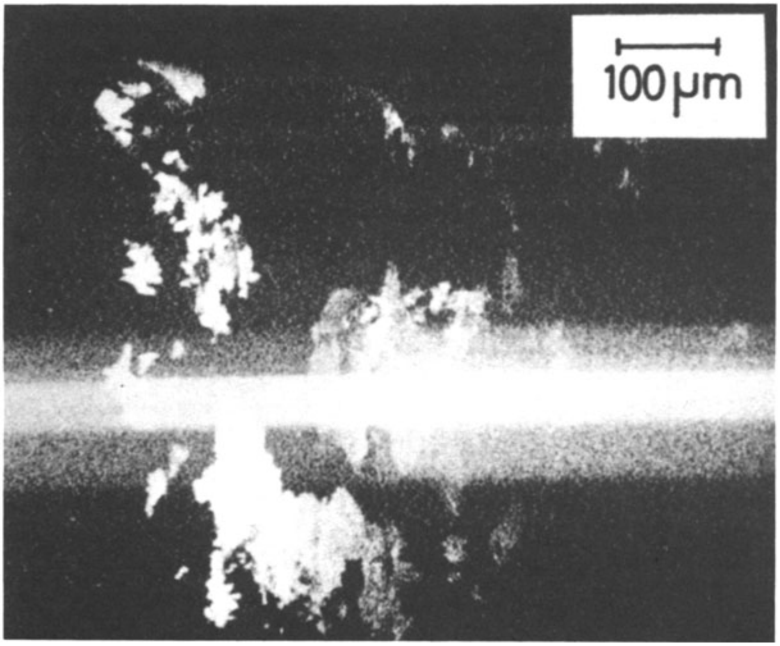

Figure 10.2. Smearing due to the emission of long-persistence CL by a particle of mineralogical ZnS in an ore sample. The scan direction was from left to right. This panchromatic CL image was taken at × 140. (After Steyn *et al.*, 1976.)

ceptor pair recombination (Dean, 1965). The peak of this broadband luminescence occurs between 2.2 and 3.1 eV, depending on the type of diamond (Walker, 1979). The variation in the energy position of this luminescence band was explained as being due to the differences in separation between donors and acceptors in natural diamond (where close pairs predominate) and synthetic diamond (where the separation is larger).

Lang (1980) studied synthetic diamonds and observed a strong emission in the near-infrared in CL topographs. The emission was attributed to the vibronic system with a strong zero-phonon line at 1.40 eV. The emission was confined to {111} growth sectors and was partially localized. Lang concluded that a defect more complex than a single substitutional nitrogen was responsible.

Comparisons of CL and STEM images of natural type IIb diamond revealed luminescence at energies less than the band gap at individual dislocations (Pennycook *et al.*, 1980). No correlation of the CL with dislocation type was found. Both screw dislocations and 60° dislocations appeared equally luminescent, and both types were also observed to be nonluminescent. The emission from dislocations was attributed to the local reduction of the band gap due to the dislocation strain field (Pennycook *et al.*, 1980). CL variations observed along dislocations

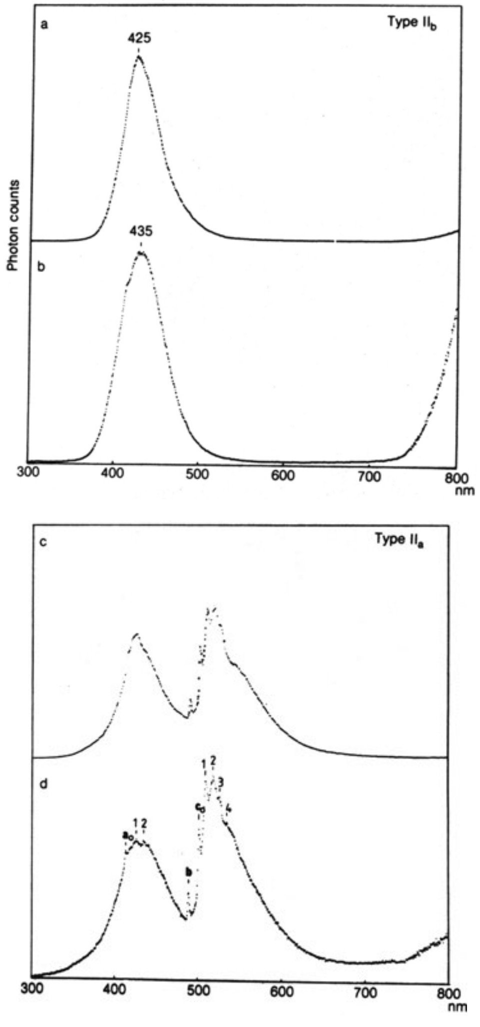

Figure 10.3. CL spectra from type IIb and IIa diamonds taken over large specimen areas using 100 kV electrons at 89 K: (a) raw data from type IIb; (b) spectrum from type IIb corrected for instrument response; (c) raw data from type IIa; (d) corrected spectrum from type IIa. The instrument resolution is 1 nm. (After Yamamoto *et al.*, 1984.)

suggested local dissociation into partial dislocations or varying impurity segregation at the dislocation core (Pennycook *et al.*, 1980).

Yamamoto *et al.* (1984) used CL microscopy and spectroscopy in conjunction with transmission electron microscopy for the analysis of individual dislocations in type IIb diamond. CL spectra were obtained from individual dislocations of types determined from the transmission electron microscope observations. A broad (0.416-eV FWHM) emission at 435 nm was found to be polarized along the dislocation line. Some of their observations are presented in Figures 10.3, 10.4, and 10.5.

The CL spectra, both raw and corrected, for two samples are presented in Figure 10.3. Spectra a and c present the raw data, and b and d are the spectra corrected for the instrumental response (Yamamoto *et al.*, 1984). A broad band

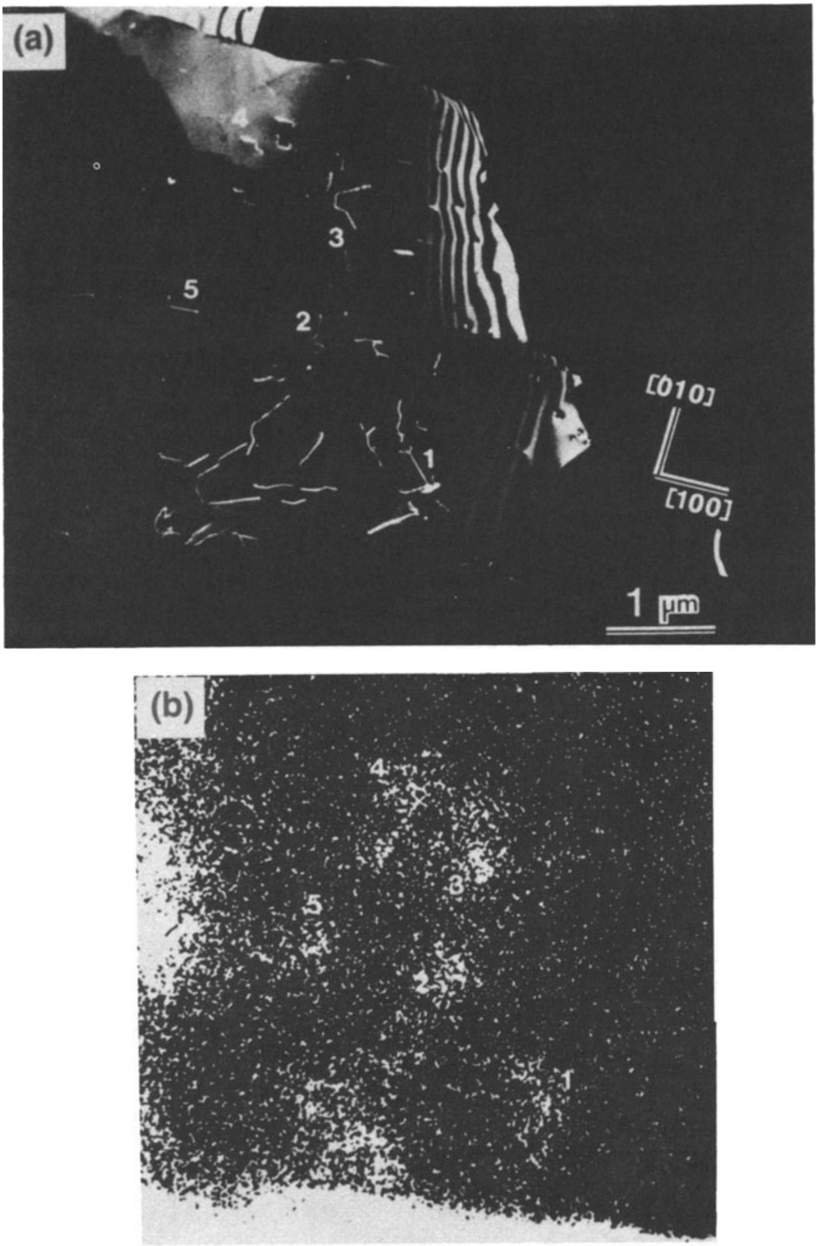

Figure 10.4. (a) Dark-field transmission electron microscope image of type IIb diamond taken at 100 kV using the $(\bar{2}20)$ reflection. (b) CL image of the same area recorded using the 425-nm emission at 89 K. Dislocations 1–5 are luminescent. (After Yamamoto *et al.*, 1984.)

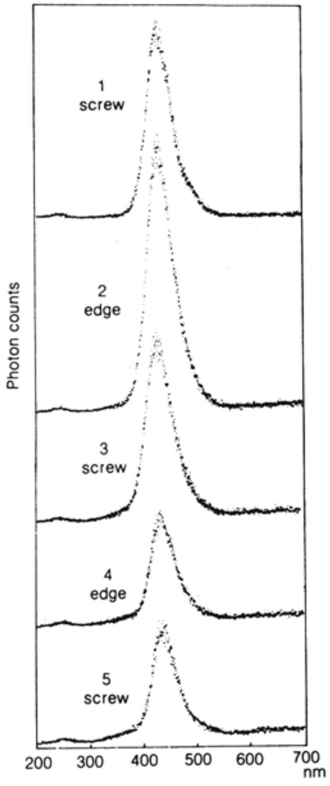

Figure 10.5. CL spectra from individual dislocations, 1–5, excited by 100-kV electrons at 89 K, recorded using 24-nm bandpass slits. (After Yamamoto *et al.*, 1984.)

with peak at 425 nm occurred in the raw spectrum of Figure 10.3a. The peak shifted to 435 nm on correction. Another sample (Figure 10.3c,d), which was irradiated by a 1-MeV electron beam before the experiment, showed fine peaks in the spectrum. The emission peak a_0 and the following peaks on that emission band were identical to the N3 emission system, which is related to nitrogen in type Ia diamonds; and the peak c_0 and the following peaks were related to the H3 emission system, which is mainly produced in type Ia diamond by radiation damage and subsequent annealing and which has also been reported in type IIa diamond (Sumida and Lang, 1981).

Transmission electron microscope and monochromatic CL observations are summarized in Figure 10.4, which reveals luminescent spots in the CL image that correspond to dislocations identified in the transmission electron microscope dark-field image. In agreement with other studies (Kiflawi and Lang, 1976; Hanley *et al.*, 1977; Lang, 1977; Pennycook *et al.*, 1980), the 425-nm band emission was observed to be localized at certain dislocations in the type IIb sample but not in type IIa. Also in agreement with other reports, Yamamoto *et al.* (1984) observed that, although the 425-nm emission was due to dislocations, not all dislocations were luminescent. The dislocations were identified from transmission electron microscope studies, but no correlation between the luminescence and the type of dislocation was found. It was also concluded that the large size of the bright spots due to dislocations in the CL image was a result of the poor CL resolution caused by the minority carrier diffusion. CL spectra obtained from individual dislocations of different types are shown in Figure 10.5. The similarity of the CL emission bands from several types of dislocation indicated that the luminescence was not related to the type of dislocation. These and observations on the polarization of the emitted light and measurements as a function of temperature allowed Yamamoto *et al.* (1984) to eliminate several possible mechanisms for the dislocation emission. They concluded that the model of dislocation-strain-field-induced local reduction of the band gap (Pennycook *et al.*, 1980) was inconsistent with their observations, as were models of emission due to impurities decorating the dislocation lines and of transitions between localized deep-level dislocation states. Thus, the dislocation emission was attributed to donor-acceptor pairs arranged along the dislocation core. The impurities were considered to be N, which provides a deep donor state and B, which forms a shallow acceptor level. The proposed luminescence mechanism supported the earlier proposal of Hanley *et al.* (1977).

It has been demonstrated that diamond films can be prepared using chemical vapor deposition (CVD) methods, in which the reaction gas is a hydrocarbon (such as methane, CH_4) mixed with hydrogen (for a review, see Angus and Hayman, 1988). Applications of thin-film diamond may include both passive and active semiconductor device components such as heat sinks and high-temperature devices, as well as coatings and optical components.

Cathodoluminescence spectra (recorded at 80 K) of epitaxial diamond films grown on {100} and {111} faces of natural diamond crystals and of polycrystalline films grown on substrates such as silicon, copper, and tungsten were reported by Vavilov *et al.* (1980). Variations in these CL spectra were attributed to differences in the defect structures formed during growth on these different faces. The effects of nitrogen or boron doping on CL spectra were also examined (Vavilov *et al.*, 1980).

Cathodoluminescence scanning electron microscopy and spectroscopy of diamond films grown on silicon substrates by microwave and magnetomicrowave plasma CVD were reported by Kawarada *et al.* (1988). They observed broadband visible luminescence, attributed to band A emission, with the peak between 2.4 and 2.8 eV, depending on the deposition conditions. Visible CL images revealed that, in the samples with the luminescence peak at 2.45 eV, the {100} faces of diamond particles were bright and the {111} faces were dark. These results are similar to those obtained from high-pressure synthesized diamond (Woods and Lang, 1975). In some samples, the CL peak was shifted to higher energy (2.8 eV). This was attributed to the lower nitrogen content in these films (Kawarada *et al.*, 1988).

Robins *et al.* (1989) reported CL microscopy and spectroscopy studies of diamond films and particles grown by the hot-filament CVD method. By comparing their results with those available in the literature on natural and synthetic diamond, the CL emission bands at 2.156 and 2.326 eV were attributed to a nitrogen-vacancy complex, the 2.82-eV band was associated with dislocations, the 3.188-eV band was associated with the interstitial nitrogen or a nitrogen-carbon-interstitial complex, and the 1.675-eV feature was attributed to a neutral vacancy. Cathodoluminescence microscopy of diamond particles, grown under similar conditions to the films, also indicated (in agreement with the previous study by Kawarada *et al.*, 1988) that luminescence features are associated primarily with {100} faces (Robins *et al.*, 1989).

10.3. Characterization of Ore Minerals

As mentioned in the introduction, CL studies of ore minerals using an optical CL microscope can be considered as a specialized research field. Detailed descriptions of the many mineralogical materials are beyond the scope of this book. Reviews of the subject by Remond (1977), Nickel (1978), and Hagni (1985, 1987) provide information such as the luminescence color and probable activators for a wide variety of minerals.

Cathodoluminescence microscopy can be effectively used to determine the location and distribution of impurities in minerals, to observe textures that cannot be recognized with an optical microscope, and to detect and identify minerals, their phases, and the distribution of the phases present. For detailed discussions, see Hagni (1985, 1987), Barker and Wood (1987), and Marshall (1988).

Cathodoluminescence microscopy and spectroscopy have been also demonstrated to be effective tools in the analysis of meteorites (Steele, 1986).

11

Future Developments

11.1. Quantitation of Cathodoluminescence Analysis

Problems in the quantitation of CL analysis were outlined in preceding chapters. The development of quantitative CL analysis is one of the greatest challenges in this field. The development of sensitive and calibrated detection systems and of interpretive theory and semiempirical intensity- and band-shape-parameter-concentration relations are required. Because (1) CL can provide nondestructive microcharacterization of optical and electronic properties of solids, (2) CL detection limits can be much lower than those attainable by the x-ray mode, and (3) there is a general trend toward the computerization of electron microscopy the development of quantitative CL is so desirable as to be almost inevitable. Initial steps toward quantitation have been taken. The work of Warwick (1987) is encouraging, and MARS-correction (*m*ixed injection level, *a*bsorption, total internal *r*eflection, and *s*urface recombination) should be developed. Further developments of quantitative CL should also involve Monte Carlo calculations of the generation of excess carriers.

An additional problem arises in the CL analysis of samples with internal electric fields associated with depletion zones or with doping inhomogeneities. In such cases, the analysis also involves the drift (charge collection, i.e., separation) of the excess carriers in these regions.

The trend toward computerization of electron microscopy and its modes will continue, and with parallel developments of the CL and SDLTS modes, quantitative CL analysis will become more feasible.

11.2 Extensions in Wavelength

Ultraviolet CL can be detected by using appropriate photomultipliers. Thus, wider-band-gap materials can be studied.

Extensions into the infrared began with the appearance of the first CL detection systems operating in the near-infrared region (Cumberbatch *et al.*, 1981; Myhajlenko *et al.*, 1983a,b). These systems use solid-state detectors and can employ Fourier transform spectrometers. The extension of the technique further into the infrared is motivated by increasing interest in the application of the CL mode to, for example infrared detector arrays as well as to polymers and biological studies. This could also lead to the creation of a "thermal" mode, overlapping with the recent development of a "thermal wave" or electroacoustic mode of the SEM (Balk and Kultscher, 1983; Holt, 1985 and references therein).

11.3. Instrumental Developments and Additional Materials

Analyses of electron beam–sensitive materials in the CL mode could be improved by using low-voltage SEM (LVSEM). Efficient use of the SEM at voltages around 1 kV became possible with the achievement of high spatial resolution and source brightness at low energies in a modern generation of instruments (for a brief review, see Pawley, 1984). Since the secondary electron yield is close to unity at these low voltages, charging effects are minimized, and high-resolution images of such nonconducting (uncoated) materials as ceramics and biological specimens can be obtained with little or no damage. Low-energy CL spectroscopy in a relatively simple vacuum system was demonstrated by Brillson *et al.* (1985), Brillson and Viturro, (1988) and Viturro *et al.* (1986, 1987a,b, 1988a,b) in studies of metal-semiconductor interfaces (see Chapters 5 and 6). They also demonstrated that low-energy CL spectroscopy can be used to obtain information on nonuniformities in charge transport and rectification at metal-semiconductor junctions. Further improvements of this powerful tool for the analysis of interfacial states would include (1) the use of cryogenic temperatures to obtain sharp and enhanced CL emission for the identification of deep levels, (2) obtaining time-resolved CL to derive recombination times, and the densities and capture cross sections of these levels, and (3) obtaining "maps" of electronic properties of interest (Brillson and Viturro, 1988).

Low-voltage CL microscopy and spectroscopy may also become useful in studies of metals. Cathodoluminescence from metals may be expected as a result of transition radiation and/or bremsstrahlung, and luminescence can be produced by surface-roughness-coupled radiation from surface plasmons (Artamonov and Samarin, 1979; Chung *et al.*, 1980; Kretschmann *et al.*, 1980). With electron beam energies of 1 keV or less, the CL spectrum of silver films was shown to contain a peak at 3.73 eV (the volume plasmon energy) attributed to transition radiation and/or bremsstrahlung, and a peak at about 3.6 eV associated with roughness-coupled radiation from surface plasmons (Chung *et al.*, 1980). The position and the intensity of the latter peak were found to depend strongly on surface roughness, and in fact, for rough films, that peak dominated the luminescence (Chung *et al.*, 1980). Thus CL spectroscopy can be used to characterize the roughness of metal surfaces. Since low-voltage CL is generated primarily near the surface, it is also expected to be greatly affected by adsorbed species, which therefore can be evaluated using low-voltage CL analysis (Artamonov and Samarin, 1979).

Recently, there have been increasing applications of CL analysis techniques to organic materials. Polymers and biological-medical specimens yield low intensities of emission and are sensitive to beam damage. Both problems are eased by the use of low-temperature stages (Hörl and Roschger, 1980). The importance of such specimens has resulted in a considerable volume of work reviewed by De Mets (1974), Bröcker and Pfefferkorn (1979), Pfefferkorn *et al.* (1980), and Holt (1984). The CL mode has many advantages that will undoubtedly be exploited with further developments of CL techniques, low-temperature stages, and signal processing and image analysis. The simultaneous availability of secondary electron imaging and the x-ray mode provides a powerful means for the analysis of biological specimens.

Bibliography

Books on Solid State Physics

Ashcroft, N. W., and Mermin, N. D., *Solid State Physics* (Saunders, Philadelphia, 1976). An advanced text.

Blakemore, J. S., *Solid State Physics* (Cambridge University Press, Cambridge, 1985). An introduction to solid-state physics; deals more thoroughly with semiconductors and excess carrier phenomena.

Bube, R. H. *Electronic Properties of Crystalline Solids* (Academic Press, New York, 1974). An advanced text with more thorough treatment of optical properties and recombination processes.

Burns, G. *Solid State Physics* (Academic Press, Orlando, 1985). An introduction to basic concepts of solid-state physics; also deals with such topics in solid-state physics as surface science and artificial structures.

Kittel, C. *Introduction to Solid State Physics* (Wiley, New York, 1986). An advanced text useful for reference.

Smith, R. A. *Semiconductors* (Cambridge University Press, Cambridge, 1978). A thorough account of the basic theory of semiconductors.

Wert, C. A., and Thomson, R. M. *Physics of Solids* (McGraw-Hill, New York, 1970). An introductory text.

For additional references on various topics in solid state physics, see texts by Blakemore (1985) and Burns (1985).

Books on Optical Properties of Inorganic Solids

Abeles, F. (Editor). *Optical Properties of Solids* (North-Holland, Amsterdam, 1972).

Balkanski, M. (Editor). *Handbook on Semiconductors. Vol. 2. Optical Properties of Solids.* (North-Holland, Amsterdam, 1980).

Bergh, A. A., and Dean, P. J. *Light-Emitting Diodes* (Clarendon Press, Oxford, 1976).

Blakemore, J. S. *Semiconductor Statistics* (Pergamon, New York, 1962).

Bube, R. H. *Photoconductivity of Solids* (Wiley, New York, 1960).

Curie, D. *Luminescence in Crystals* (Methuen, London, 1963).

Di Bartolo, B. (Editor). *Luminescence of Inorganic Solids* (Plenum, New York, 1978).

Goldberg, P. (Editor). *Luminescence of Inorganic Solids* (Academic Press, New York, 1966).

Greenaway, D. L., and Harbeke, G. *Optical Properties and Band Structure of Semiconductors* (Pergamon, Oxford, 1968).

Leverenz, H. W. *An Introduction to Luminescence of Solids* (Dover, New York, 1968).

Lumb, M. D. (Editor). *Luminescence Spectroscopy* (Academic Press, New York, 1978).

Moss, T. *Optical Properties of Semiconductors* (Butterworths, London, 1959).

Moss, T. S., Burrell, G. J., and Ellis, B. *Semiconductor Opto-Electronics* (Wiley, New York, 1973).

Pankove, J. I. *Optical Processes in Semiconductors* (Dover, New York, 1971). A valuable source with much technical information on optical properties and processes in semiconductors.

Rose, A. *Concepts in Photoconductivity and Allied Problems* (Wiley, New York, 1963).

Seraphin, B. O. (Editor). *Optical Properties of Solids—New Developments* (North-Holland, Amsterdam, 1976).

Townsend, P. D., and Kelly, J. C. *Colour Centres and Imperfections in Insulators and Semiconductors* (Chatto and Windus, Sussex University, 1973).

Willardson, R. K., and Beer, A. C. (Editors), *Semiconductors and Semimetals. Vol. 3. Optical Properties of III-V Compounds.* (Academic Press, New York, 1967).

Williams, E. W., and Hall, R. *Luminescence and the Light Emitting Diode* (Pergamon, Oxford, 1978).

Books Devoted to Scanning Electron Microscopy

Ehrenberg, W., and Gibbons, D. J. *Electron Bombardment Induced Conductivity* (Academic Press, London, 1981).

Goldstein, J. I., Newbury, D. E., Echlin, P., Joy, D. C., Fiori, C., and Lifshin, E. (Editors). *Scanning Electron Microscopy and X-ray Microanalysis* (Plenum, New York, 1981).

Goldstein, J. I., and Yakowitz, H. (Editors). *Practical Scanning Electron Microscopy* (Plenum, New York, 1975).

Heinrich, K. F. J. *Electron Beam X-ray Microanalysis* (Van Nostrand, New York, 1981).

Holt, D. B., and Joy, D. C. (Editors). *SEM Microcharacterization of Semiconductors* (Academic Press, London, 1989).

Holt, D. B., Muir, M. D., Grant, P. R., and Boswarva, I. M. (Editors). *Quantitative Scanning Electron Microscopy* (Academic Press, London, 1974).

Joy, D. C., Romig, Jr., A. D., and Goldstein, J. I. (Editors). *Principles of Analytical Electron Microscopy* (Plenum, New York, 1986).

Newbury, D. E., Joy, D. C., Echlin, P., Fiori, C. E., and Goldstein, J. I. *Advanced Scanning Electron Microscopy and X-ray Microanalysis* (Plenum, New York, 1986).

Oatley, C. W. *Scanning Electron Microscopy. I. The Instrument* (Cambridge University Press, Cambridge, 1972).

Reimer, L., *Scanning Electron Microscopy* (Springer-Verlag, New York, 1985).

Thornton, P. R. *Scanning Electron Microscopy—Application to Materials and Device Science* (Chapman and Hall, London, 1972).

Wells, O. C. *Scanning Electron Microscopy* (McGraw-Hill, New York, 1974).

References

Akagi, K., Kukimoto, H., and Nakayama, T. (1978). *J. Luminescence* **17,** 237.

Alexander, E., Kalman, Z. H., Mardix, S., and Steinberger, I. T. (1970). *Philos. Mag.* **21,** 1237.

Alig, R. C. (1983). *Phys. Rev.* **B27,** 968.

Alig, R. C., and Bloom, S. (1977). *J. Electrochem. Soc.* **124,** 1136.

Alig, R. C., Bloom, S., and Inoue, M. (1981). *J. Phys. (Paris)* **42,** C6-484.

Alig, R. C., Bloom, S., and Struck, C. (1980). *Phys. Rev.* **B22,** 5565.

Angus, J. C., and Hayman, C. C. (1988). *Science* **241,** 913.

Artamonov, O. M., and Samarin, S. N. (1979). *Radiation Effects* **40,** 201.

Ashen, D. J., Dean, P. J., Hurle, D. T. J., Mullin, J. B., and White, A. M. (1975). *J. Phys. Chem. Solids* **36,** 1041.

Atkinson, D. I. H., and McMillan, P. W. (1974). *J. Mater. Sci. Lett.* **9,** 692.

Aven, M., and Devine, J. Z. (1973). *J. Luminescence* **7,** 195.

Aven, M., and Prener, J. S. (Editors) (1967). *Physics and Chemistry of II-VI Compounds,* North-Holland, Amsterdam.

Bakker, J., de Poorter, J., Bartels, W. J., V. Dongen, T., Nijman, W., and Stady, W. T. (1980). *J. Electron. Mater.* **9,** 311.

Balk, L. J. (1988). *Advances in Electronics and Electron Physics* **71,** 1.

Balk, L. J., and Kubalek, E. (1973). *Beitr. Electronenmikroskop. Direktabb. Oberfl.* **6,** 551.

Balk, L. J., and Kubalek, E. (1977). In *Scanning Electron Microscopy 1977*/I, ed. O. Johari, SEM Inc., Chicago, p. 739.

Balk, L. J., Kubalek, E., and Menzel, E. (1976). In *Scanning Electron Microscopy 1976,* ed. O. Johari, SEM Inc., Chicago, p. 257.

Balk, L. J., and Kultscher, N. (1983). In *Microscopy of Semiconducting Materials,* Oxford, IOP Conf. Ser. No. 67 (IOP, Bristol), p. 387.

Barker, C. E. (1987). In *Process Mineralogy VI,* ed. R. D. Hagni, The Metallurgical Society of AIME, p. 159.

Barker, C. E., and Wood, T. (1987). In *Process Mineralogy VI,* ed. R. D. Hagni, The Metallurgical Society of AIME, p. 137.

Barrett, D. L., McGuigan, S., Hobgood, H. M., Eldridge, G. W., and Thomas, R. N. (1984). *J. Crystal Growth* **70,** 179.

Batstone, J. L., and Steeds, J. W. (1985). In *Microscopy of Semiconducting Materials* (IOP, Bristol), p. 383.

Bebb, H. B., and Williams, E. W. (1972). In *Semiconductors and Semimetals,* Vol. 8, eds. R. K. Willardson and A. C. Beer, Academic Press, New York, p. 181.

Bensahel, D. and Dupuy, M. (1979a). *Phys. Stat. Sol.* **a55,** 203.

Bensahel, D. and Dupuy, M. (1979b). *Phys. Stat. Sol.* **a56,** 99.

Bensahel, D., Dupuy, M., and Pfister, J. C. (1979a). *Phys. Stat. Sol.* **A55,** 211.

Bensahel, D., Magnea, N., and Dupuy, M. (1979b). *Solid State Commun.* **30,** 467.

Bergh, A. A., and Dean, P. J. (1976). *Light Emitting Diodes,* Clarendon Press, Oxford.

Bhargava, R. N. (1982). *J. Cryst. Growth* **59,** 15.

Bimberg, D., Christen, J., Fukunaga, T., Nakashima, H., Mars, D. E., and Miller, J. N. (1987). *J. Vac. Sci. Technol.* **B5,** 1191.

Bimberg, D., Christen, J., Fukunaga, T., Nakashima, H., Mars, D. E., and Miller, J. N. (1988). *Superlattices and Microstructures* **4,** 257.

Bimberg, D., Christen, J., Steckenborn, A., Weimann, G., and Schlapp, W. (1985b). *J. Luminescence* **30,** 562.

Bimberg, D., Christen, J., Werner, A., Kunst, M., Weimann, G., and Schlapp, W. (1986). *Appl. Phys. Lett.* **49,** 76.

Bimberg, D., Münzel, H., Steckenborn, A., and Christen, J. (1985a). *Phys. Rev. B* **31,** 7788.

Bishop, H. E. (1974). In *Quantitative Scanning Electron Microscopy,* eds. D. B. Holt, M. D. Muir, P. R. Grant, and I. M. Boswarva, Academic Press, New York, p. 41.

Blakemore, J. S., and Rahimi, S. (1984). In *Semiconductors and Semimetals,* Vol. 20, eds. R. K. Willardson and A. C. Beer, Academic Press, New York, 1984, p. 233.

Bode, M., Jakubowicz, A., and Habermeier, H. U. (1987). In *Proceedings of the Second International Symp. on Defect Recognition and Image Processing in III-V Compounds (DRIP II),* Elsevier, New York, p. 155.

Bond, E. F., Haggis, G. H., and Beresford, D. (1974). *J. Microscopy* **100,** 271.

Booker, G. R. (1981). In *Microscopy of Semiconducting Materials* (IOP, Bristol), p. 203.

Booker, G. R., Ourmazd, A., and Darby, D. B. (1979). *J. Phys.* **40,** Suppl. 6, p. C6–19.

Boulou, M., and Bois, D. (1977). *J. Appl. Phys.* **48,** 4713.

Brafman, O., and Steinberger, I. T. (1966). *Phys. Rev.* **143,** 501.

Brandt, G., and Mikus, M. (1987). *Wear* **115,** 243.

Breitenstein, O. (1982). *Phys. Stat. Sol.* **a71,** 159.

Breitenstein, O. (1987). In *Microscopy of Semiconducting Materials* (IOP, Bristol), p. 787.

Breitenstein, O., and Heydenreich, J. (1983). *J. Phys. Colloq.* **44,** C4, 207.

Breitenstein, O., and Heydenreich, J. (1985). *Scanning* **7,** 273.

Breitenstein, O., and Heydenreich, J. (1989). In *SEM Microcharacterization of Semiconductors,* eds. D. B. Holt and D. C. Joy, Academic Press, London, 1989.

Breitenstein, O., and Wosinski, T. (1983). *Phys. Stat. Sol.* **a77,** K107.

Bresse, J. F., and Papadopoulo, A. C. (1987). *Appl. Phys. Lett.* **51,** 183.

Bresse, J. F., and Papadopoulo, A. C. (1988). *J. Appl. Phys.* **64,** 98.

Bril, A., and Klasens, H. A. (1952). *Philips Res. Repts.* **7,** 401.

Brillson, L. J. (1985). *Appl. Surf. Sci.* **22/23,** 948.

Brillson, L. J., Richter, H. W., Slade, M. L., Weinstein, B. A., and Shapira, Y. (1985). *J. Vac. Sci. Technol.* **A3,** 1011.

Brillson, L. J., and Viturro, R. E. (1988). *Scanning Microscopy* **2,** 789.

Bröcker, W., and Pfefferkorn, G. (1978). In *Scanning Electron Microscopy 1978*/I, ed. O. Johari, SEM Inc., Chicago, p. 333.

Bröcker, W., and Pfefferkorn, G. (1979). In *Scanning Electron Microscopy 1979*/II, ed. O. Johari, SEM Inc., Chicago, p. 125.

Bröcker, W., and Pfefferkorn, G. (1980). In *Scanning Electron Microscopy 1980*/II, ed. O. Johari, SEM Inc., Chicago, p. 298.

Brownlow, J. M., and Chang, I. F. (1983). *IEEE Trans. Electr. Dev.* **ED-30,** 479.

Bubulac, L. O., Tennant, W. E., Edwall, D. D., Gertner, E. R., and Robinson, J. C. (1985). *J. Vac. Sci. Technol.* **A3,** 163.

Calverley, A., and Wight, D. R. (1970). *Solid State Electronics* **13,** 382.

Cargill, G. S. (1980). *Nature* **286,** 691.

Carlsson, L., and van Essen, C. G. (1974). *J. Phys. E* **7,** 98.

Casey, H. C. (1967). *J. Electrochem. Soc.* **114,** 153.

Casey, H. C., and Jayson, J. S. (1971). *J. Appl. Phys.* **42,** 2774.

Casey, H. C., and Kaiser, R. H. (1967). *J. Electrochem. Soc.* **114,** 149.

Casey, H. C., and Stern, F. (1976). *J. Appl. Phys.* **47,** 631.

Casey, H. C., and Trumbore, F. A. (1970). *Mater. Sci. Eng.* **6,** 69.

Chamonal, J. P., Molva, E., Dupuy, M., Accomo, R., and Pautrat, J. L. (1983). *Physica* **116B**, 519.

Chandrasekhar, M., and Pollak, F. H. (1977). *Phys. Rev.* **B15,** 2127.

Chase, B. D., and Holt, D. B. (1973). *Phys. Stat. Sol.* **a19,** 467.

Chaudhri, M. M., Hagan, J. T., and Wells, J. K. (1980). *J. Mater. Sci.* **15,** 1189.

Chen, R. T., Holmes, D. E., and Asbeck, P. M. (1984). *Appl. Phys. Lett.* **45,** 459.

Chern, S. S., Vydynath, H. R., and Kroger, F. A. (1975). *J. Solid State Chem.* **14,** 33.

Chew, H. G., Cullis, A. G., Warwick, C. A., Robbins, D. J., Hardeman, R. W., and Gasson, D. B. (1985). In *Microscopy of Semiconducting Materials* (IOP, Bristol), p. 129.

Chin, A. K., Camlibel, I., Caruso, R., Young, M. S. S., and Von Neida, A. R. (1985). *J. Appl. Phys.* **57,** 2203.

Chin, A. K., Caruso, R., Young, M. S. S., and Von Neida, A. R. (1984). *Appl. Phys. Lett.* **45,** 552.

Chin, A. K., Keramidas, V. G., Johnston, W. D., Mahajan, S., and Roccasecca, D. D. (1980). *J. Appl. Phys.* **51,** 978.

Chin, A. K., Mahajan, S., and Ballman, A. A. (1979c). *Appl. Phys. Lett.* **35,** 784.

Chin, A. K., Temkin, H., Mahajan, S., Bonner, W. A., Ballman, A. A., and Dentai, A. G. (1979b). *J. Appl. Phys.* **50,** 5707.

Chin, A. K., Temkin, H., and Roedel, R. J. (1979a). *Appl. Phys. Lett.* **34,** 476.

Chu, Y. M., Darby, D. B., and Booker, G. R. (1981). In *Microscopy of Semiconducting Materials* (IOP, Bristol), p. 331.

Chung, M. S., Callcott, T. A., Kretschmann, E., and Arakawa, E. T. (1980). *Surf. Sci.* **91,** 245.

Cibert, J., Petroff, P. M., Dolan, G. J., Pearton, S. J., Gossard, A. C., and English, J. H. (1986a). *Appl. Phys. Lett.* **49,** 1275.

Cibert, J., Petroff, P. M., Werder, D. J., Pearton, S. J., Gossard, A. C., and English, J. H. (1986b). *Appl. Phys. Lett.* **49,** 223.

Clark, S., and Stirland, D. J. (1981). In *Microscopy of Semiconducting Materials* (IOP, Bristol), p. 339.

Cocito, M., Papuzza, C., and Taiariol, F. (1983). In *Microscopy of Semiconducting Materials* (IOP, Bristol), p. 273.

Cohen, M. L., and Chadi, D. J. (1980). In *Optical Properties of Solids,* edited by M. Balkanski, Vol. 2 of *Handbook of Semiconductors,* edited by T. S. Moss, North-Holland, Amsterdam, p. 155.

Cohn, A., and Caledonia, G. (1970). *J. Appl. Phys.* **41,** 3767.

Cone, M. L., and Hengehold, R. L. (1983). *J. Appl. Phys.* **54,** 6346.

Cottrell, A. H. (1964). *The Mechanical Properties of Matter,* Wiley, New York.

Crookes, W. (1879). *Phil. Trans. Roy. Soc. London, Part I,* p. 135.

Cumberbatch, J. J., Davidson, S. M., and Myhajlenko, S. (1981). In *Microscopy of Semiconducting Materials* (IOP, Bristol), p. 197.

Curie, D. (1963). *Luminescence in Crystals,* Methuen, London, 1963.

Curie, D., and Prener, J. S. (1967). In *Physics and Chemistry of II-VI Compounds,* eds. M. Aven and J. S. Prener, North-Holland, Amsterdam, p. 433.

Cusano, D. A. (1964). *Solid State Commun.* **2**, 353.

Czernuszka, J. T., and Page, T. F. (1985). *J. Am. Ceram. Soc.* **68,** C-196.

Daniels, J., and Hardtl, K. H. (1976). *Philips Res. Repts.* **31,** 489.

Darby, D. B., Augustus, P. D., Booker, G. R., and Stirland, D. J. (1980). *J. Microscopy* **118,** 343.

Darby, D. B., and Booker, G. R. (1977). *J. Mater. Sci.* **12,** 1827.

Datta, S., Aeberli, K. E., Boswarva, I. M., and Holt, D. B. (1980b). *J. Microscopy* **118,** 367.

Datta, S., Boswarva, I. M., and Holt, D. B. (1979b). *J. Phys. Chem. Solids* **40,** 567.

Datta, S., Dhillon, P. S., Holt, D. B., and Juhasz, C. (1980a). In *Scanning Electron Microscopy 1980/*I, ed. O. Johari, SEM Inc., Chicago, p. 279.

Datta, S., Yacobi, B. G., and Holt, D. B. (1977). *J. Mater. Sci.* **12,** 2411.

Datta, S., Yacobi, B. G., and Holt, D. B. (1979a). *J. Luminescence* **21,** 53.

Davidson, S. M. (1977). *J. Microscopy* **110,** 177.

Davidson, S. M., Cumberbatch, T. J., Huang, E., and Myhajlenko, S. (1981). In *Microscopy of Semiconducting Materials* (IOP, Bristol), p. 191.

Davidson, S. M., and Dimitriadis, C. A. (1980). *J. Microscopy* **118,** 275.

Davidson, S. M., Iqbal, M. Z., and Northrop, D. C. (1975). *Phys. Stat. Sol.* **a29,** 571.

Davidson, S. M., and Rasul, A. (1976). *J. Phys. E: Sci. Instrum.* **9,** 1.

Davidson, S. M., and Rasul, A. (1977). In *Scanning Electron Microscopy 1977,* ed. O. Johari, SEM Inc., Chicago, p. 225.

Davidson, S. M., and Vaidya, A. W. (1977). In *Proc. Internat. Symp. on GaAs and Related Compounds,* ed. C. Hilsum, Institute of Physics, Bristol, p. 287.

Davies, G. (1979). In *The Properties of Diamond,* ed. J. E. Field, Academic Press, London, p. 165.

Dean, P. J. (1965). *Phys. Rev. A* **139,** 588.

Dean, P. J. (1966). In *Luminescence of Inorganic Solids,* ed. P. Goldberg, Academic Press, New York, p. 119.

Dean, P. J. (1982). *Cryst. Growth Characterization* **5,** 89.

Dean, P. J. (1983). In *Collective Excitations in Solids,* ed. B. Di Bartolo, Plenum, New York, p. 247.

De Leeuw, D. M., and Hooft, G. W. (1983). *J. Luminescence* **28,** 275.

De Mets, M. (1974). In *Principles and Techniques of Scanning Electron Microscopy,* Vol. 2, ed. M. A. Hayat, Van Nostrand Reinhold, New York.

De Mets, M., Howlett, K. J., and Yoffe, A. D. (1974). *J. Microscopy* **102,** 125.

Devlin, S. S. (1967). In *Physics and Chemistry of II-VI Compounds,* eds. M. Aven and J. S. Prener, North-Holland, Amsterdam, p. 551.

Di Bartolo, B., ed. (1978). *Luminescence of Inorganic Solids,* Plenum, New York.

Dimitriadis, C. A. (1984). *Solid State Commun.* **52,** 279.

Dimitriadis, C. A., Huang, E., and Davidson, S. M. (1978). *Solid State Electronics* **21,** 1419.

Ding, J., Chang, J. S. C., and Bujatti, M. (1987). *Appl. Phys. Lett.* **50,** 1089.

Dixon, J. R., and Ellis, J. M. (1961). *Phys. Rev.* **123,** 1560.

Dobrilla, P., Blakemore, J. S., McCamant, A. J., Gleason, K. R., and Koyama, R. Y. (1985). *Appl. Phys. Lett.* **47,** 602.

Donolato, C. (1978). *Optik* **52,** 19.

Donolato, C. (1983). *Appl. Phys. Lett.* **43,** 120.

Donolato, C., and Venturi, P. (1982). *Phys. Stat. Sol.* **a73,** 377.

Dow, J. D., and Redfield, D. (1972). *Phys. Rev.* **B5,** 594.

Dow, D., Smith, D. L., and Lederman, F. L. (1973). *Phys Rev.* **B8,** 4612.

Drozdov, N. A., Patrin, A. A., and Tkachev, V. D. (1976). *Sov. Phys. JETP Lett.* **23,** 597.

Duncan, K. R., Eaves, L., Randane, A., Roys, W. B., Skolnick, M. S., and Dean, P. J. (1984). *J. Phys. C: Solid State Phys.* **17,** 1233.

Dupuy, M. (1983). *J. Phys. (Paris)* **44,** Suppl. 9, C4–277.

Ehrenberg, W., and Gibbons, D. J. (1981). *Electron Bombardment Induced Conductivity and Its Applications,* Academic Press, London, p. 66.

Einzinger, R. (1978). *Appl. Surf. Sci.* **1,** 329.

Enomoto, Y., Yamanaka, K., and Saito, K. (1986). *Wear* **110,** 239.

Era, K., Shionoya, S., and Washizawa, Y. (1968). *J. Phys. Chem. Solids* **29,** 1827.

Esquivel, A. L., Lin, W. N., and Wittry, D. B. (1973). *Appl. Phys. Lett.* **22,** 414.

Esquivel, A. L., Sen, S., and Lin, W. N. (1976). *J. Appl. Phys.* **47,** 2588.

Everhart, T. E., Herzog, R. F., Chang, M. S., and DeVore, W. J. (1972). In *Proc. 6th Internat. Conf.*

on X-ray Optics and Microanalysis, eds. G. Shinoda, K. Kohra, and T. Ichinokawa, Univ. of Tokyo Press, Tokyo, p. 81.

Everhart, T. E., and Hoff, P. H (1971). *J. Appl. Phys.* **42,** 5837.

Farvacque, J. L., Ferre, D., and Vignaud, D. (1983). *J. de Physique* **44,** Suppl. 9, p. C4–115.

Fitzgerald, E. A., Ashizawa, Y., Eastman, L. F., and Ast, D. G. (1988). *J. Appl. Phys.* **63,** 4925.

Fornari, R., Franzosi, P., Salviati, G., Ferrari, C., and Ghezzi, C. (1985). *J. Crystal Growth* **72,** 717.

Frank, W., and Gösele, U. (1983). *Physica* **116B,** 420.

Franzosi, P., Salviati, G., Genova, F., Stano, A., and Taiariol, F. (1986). *J. Crystal Growth* **75,** 521.

Garlick, G. F. J. (1950). *Advan. Electron.* **2,** 151.

Garlick, G. F. J. (1966). In *Luminescence of Inorganic Solids,* ed. P. Goldberg, Academic Press, New York, 1966.

Gatos, C. H., Vaughan, J. J., Lagowski, J., and Gatos, H. C. (1981). *J. Appl. Phys.* **52,** 1464.

Gaw, C. A., and Reynolds, C. L. (1981). *Electronics Lett.* **17,** 285.

Gibson, J. M., Tung, R. T., Pimentel, C. A., and Joy, D. C. (1985). In *Microscopy of Semiconducting Materials* (IOP, Bristol), p. 173.

Giles, P. L. (1975). *J. de Microscopie* **22,** 357.

Goldstein, J. I., Newbury, D. E., Echlin, P., Joy, D. C., Fiori, C., and Lifshin, E. (1981). In *Scanning Electron Microscopy and X-ray Microanalysis,* Plenum Press, New York.

Graham, R. J., Myhajlenko, S., and Steeds, J. W. (1985). *J. Appl. Phys.* **57,** 1311.

Graham, R. J., Spence, J. C. H., and Alexander, H. (1987). In *Characterization of Defects in Materials,* eds. R. W. Siegel, J. R. Weertman, and R. Sinclair, Materials Research Society, Pittsburgh, PA, p. 235.

Grasser, R., Roth, G., and Scharmann, A. (1971). *Z. Phys.* **249,** 91.

Hackett, W. H., Saul, R. H., Dixon, R. W., and Kammlott, G. W. (1972). *J. Appl. Phys.* **43,** 2857.

Haefner, H., Morawetz, H., and Oelgart, G. (1981). *Phys. Stat. Sol.* **a63,** 495.

Hagni, R. D. (1985). In *Applied Mineralogy,* eds. W. C. Park, D. M. Hausen, and R. D. Hagni, AIME, New York, p. 41.

Hagni, R. D. (1987). In *Process Mineralogy VI,* ed. R. D. Hagni, The Metallurgical Society of AIME, p. 37.

Hall, R. N. (1952). *Phys. Rev.* **87,** 387.

Hanley, P. L., Kiflawi, I., and Lang, A. R. (1977). *Philos. Trans. Roy. Soc.* **A284,** 329.

Hastenrath, M., Balk, L. J., Löhnert, K., and Kubalek, E. (1980). *J. Microscopy* **118,** 303.

Hastenrath, M., and Kubalek, E. (1982). In *Scanning Electron Microscopy 1982/*I, ed. O. Johari, SEM Inc., Chicago, p. 157.

Hastenrath, M., Löhnert, K., and Kubalek, E. (1981). In Inst. Phys. Conf. Ser. No. 61, p. 47.

Haynes, J. R. (1955). *Phys. Rev.* **98,** 1866.

Henderson, B. (1972). *Defects in Crystalline Solids,* Arnold, London.

Henderson, B. (1978). *Contemp. Phys.* **19,** 225.

Henderson, B., and Wertz, J. E. (1968). *Advances in Physics* **17,** 749.

Heydenreich, J., and Breitenstein, O. (1985). In *Microscopy of Semiconducting Materials* (IOP, Bristol), p. 319.

Heydenreich, J., and Breitenstein, O. (1986). *J. Microscopy* **141,** 129.

Hirth, J. P., and Lothe, J. (1968). *Theory of Dislocations,* McGraw-Hill, New York.

Holt, D. B. (1962). *J. Phys. Chem. Solids.* **23,** 1353.

Holt, D. B. (1974). In *Quantitative Scanning Electron Microscopy,* eds. D. B. Holt, M. D. Muir, P. R. Grant, and I. M. Boswarva, Academic Press, London.

Holt, D. B. (1974). In *Quantitative Scanning Electron Microscopy,* eds. D. B. Holt, M. D. Muir, P. R. Grant, and I. M. Boswarva, Academic Press, London.

Holt, D. B. (1981). In *Microscopy of Semiconducting Materials* (IOP, Bristol), p. 165.

Holt, D. B. (1985). In *Crystal Growth of Electronic Materials,* ed. E. Kaldis, Elsevier Science, New York, p. 343.

Holt, D. B. (1989). In *SEM Microcharacterization of Semiconductors,* eds. D. B. Holt and D. C. Joy, Academic Press, London, chap. 6.

Holt, D. B., and Chase, B. D. (1968). *J. Mater. Sci.* **3,** 178.

Holt, D. B., and Chase, B. D. (1973). *Phys. Stat. Sol.* **a20,** 135.

Holt, D. B., Chase, B. D., and Censlive, M. (1973). *Phys. Stat. Sol.* **a20,** 459.

Holt, D. B., and Culpan, M. (1970). *J. Mater. Sci.* **5,** 546.

Holt, D. B., and Datta, S. (1980). In *Scanning Electron Microscopy 1980*/I, ed. O. Johari, SEM Inc., Chicago, p. 259.

Holt, D. B., and Lesniak, M. (1985). In *Scanning Electron Microscopy 1985*/I, ed. O. Johari, SEM Inc., Chicago, p. 67.

Holt, D. B., and Saba, F. M. (1985). In *Scanning Electron Microscopy 1985*/III, ed. O. Johari, SEM Inc., Chicago, p. 1023.

Honda, T., Ishii, Y., Miyazawa, S., Yamazaki, H., and Nanishi, Y. (1983). *Jpn. J. Appl. Phys.* **22,** L270.

Hopfield, J. J. (1959). *J. Phys. Chem. Solids* **10,** 110.

Hörl, E. M., and Mügschl, E. (1972). In *Proc. 5th Eur. Congr. Elect. Microsc. (EMCON 72),* Institute of Physics, London, p. 502.

Hörl, E. M., and Roschger, P. (1980). In *Scanning Electron Microscopy 1980*/I, ed. O. Johari, SEM Inc., Chicago, p. 285.

Huang, H. C. W., Aliotta, C. F., and Ho, P. S. (1982). *Appl. Phys. Lett.* **41,** 54.

Hull, D., and Bacon, D. J. (1984). *Introduction to Dislocations,* Pergamon, Oxford.

Hunsperger, R. G. (1982). *Integrated Optics: Theory and Technology,* Springer-Verlag, New York.

Hutchinson, H. J., and Myhajlenko, S. (1984). *Philos. Mag.* **B50,** L49.

Hutson, A. R. (1984). In *Proceedings of the Thirteenth International Conference on Defects in Semiconductors,* eds. L. C. Kimerling and J. M. Parsey, Jr., The Metallurgical Society of AIME, New York, p. 367.

Ihrig, H., Hengst, J. H. T., and Klerk, M. (1981). *Z. Physik B-Condensed Matter* **40,** 301.

Ihrig, H., and Klerk, M. (1979). *Appl. Phys. Lett.* **35,** 307.

Imanaga, S., Yokono, S., and Hoshina, T. (1980). *Japan. J. Appl. Phys.* **19,** 41.

Inoue, M. (1984). *J. Appl. Phys.* **55,** 1558.

Jack, A. G., and Vrehen, Q. H. F. (1986). *Philips Tech. Rev.* **42,** 342.

Jagannath, C., Koteles, E. S., Lee, J., Chen, Y. J., Elman, B. S., and Chi, J. Y. (1986). *Phys. Rev.* **B34,** 7027.

Jakubowicz, A. (1985a). *J. Appl. Phys.* **57,** 1194.

Jakubowicz, A. (1985b). *J. Appl. Phys.* **58,** 4354.

Jakubowicz, A. (1986). *J. Appl. Phys.* **59,** 2205.

Jakubowicz, A. (1987). In *Scanning Microscopy,* Vol. 1, Scanning Microscopy International, Chicago, p. 515.

Jakubowicz, A., Bode, M., and Habermeier, H. U. (1987). In *Microscopy of Semiconducting Materials* (IOP, Bristol), p. 763.

James, K. M., Flood, J. D., Merz, J. L., and Jones, C. E. (1986). *J. Appl. Phys.* **59,** 3596.

Jaros, M. (1982). *Deep Levels in Semiconductors,* Adam Hilger, Bristol.

Jones, C. E., and Embree, D. (1976). *J. Appl. Phys.* **47,** 5365.

Jones, G. A. C., Nag, B. R., and Gopinath, A. (1973). In *Scanning Electron Microscopy 1973*/II, ed. O. Johari, SEM Inc., Chicago, p. 309.

Joy, D. C. (1986). *J. Microscopy* **143,** 233.

Joy, D. C., Newbury, D. E., and Davidson, D. L. (1982). *J. Appl. Phys.* **53,** R81.

Kamejima, T., Shimura, F., Matsumoto, Y., Watanabe, H., and Matsui, J. (1982). *Japan. J. Appl. Phys.* **21,** L721.

Kanaya, K., and Okayama, S. (1972). *J. Phys. D: Appl. Phys.* **5,** 43.

Kaniewski, J., Warminski, T., Bugajski, M., and Mroziewicz, B. (1981). *J. Phys. D: Appl. Phys.* **14,** 127.

Kano, T., and Uchida, Y. (1983). *Japan. J. Appl. Phys.* **22,** 1842.

Kasahara, J., Arai, M., and Watanabe, N. (1986). *Japan. J. Appl. Phys.* **25,** L85.

Kawarada, H., Nishimura, K., Ito, T., Suzuki, J., Mar, K. S., Yokota, Y., Hiraki, A. (1988). *Japan. J. Appl. Phys.* **27,** L683.

Kazan, B. (1985). *Displays* **6,** 85.

Keil, T. H. (1966). *Phys. Rev.* **144,** 582.

Kiflawi, I., and Lang, A. R. (1976). *Philos. Mag.* **33,** 697.

Kingery, W. D. (1981). In *Advances in Ceramics,* Vol. 1, eds. L. M. Levinson and D. C. Hill, The American Ceramic Society, Columbus, OH, p. 1.

Kingery, W. D., Bowen, H. K., and Uhlmann, D. R. (1976). *Introduction to Ceramics,* Wiley, New York.

Kirkby, P. A., Selway, P. R., and Westbrook, L. D. (1979). *J. Appl. Phys.* **50,** 4567.

Klaassen, D. B. M., and de Leeuw, D. M. (1984). *J. Luminescence* **31/32,** 687.

Klaassen, D. B. M., de Leeuw, D. M., and Welker, T. (1987). *J. Luminescence* **37,** 21.

Klein, C. A. (1968). *J. Appl. Phys.* **39,** 2029.

Klick, C. C., and Schulman, J. H. (1957). In *Solid State Physics,* Vol. 5, eds. F. Seitz and D. Turnbull, Academic Press, New York, p. 97.

Knox, R. S. (1963). *Theory of Excitons,* Academic Press, New York.

Knox, R. S. (1983). In *Collective Excitations in Solids,* ed. B. Di Bartolo, Plenum, New York, p. 183.

Koschek, G., and Kubalek, E. (1983). *Phys. Stat. Sol.* **a79,** 131.

Koschek, G., and Kubalek, E. (1985a). *J. Am. Ceram. Soc.* **68,** 582.

Koschek, G., and Kubalek, E. (1985b). *Scanning* **7,** 199.

Kotera, M., Murata, K., and Nagami, K. (1981). *J. Appl. Phys.* **52,** 997.

Koyama, H. (1980a). *J. Appl. Phys.* **51,** 2228.

Koyama, H. (1980b). *J. Appl. Phys.* **51,** 2304.

Kretschmann, E., Callcott, T. A., and Arakawa, E. T. (1980). *Surf. Sci.* **91,** 237.

Kuboniwa, S., Kawai, H., and Hoshina, T. (1980). *Japan. J. Appl. Phys.* **19,** 1647.

Kukimoto, H., Oda, S., and Nakayama, T. (1979). *J. Luminescence* **18/19,** 365.

Kyser, D. F., and Wittry, D. B. (1964). In *The Electron Microprobe,* eds. T. D. McKinley, K. F. J. Heinrich, and D. B. Wittry, Wiley, New York, p. 691.

Labusch, R., and Schröter, W. (1980). In *Dislocations in Solids,* Vol. 5, ed. F. R. N. Nabarro, North-Holland, Amsterdam, p. 127.

Lang, A. R. (1977). *J. Crystal. Growth* **42,** 625.

Lang, A. R. (1980). *Philos. Mag.* **B41,** 689.

Lang, D. V. (1974). *J. Appl. Phys.* **45,** 3023.

Lannoo, M., and Bourgoin, J. (1981). *Point Defects in Semiconductors I. Theoretical Aspects,* Springer-Verlag, Berlin.

Lax, M. (1978). *J. Appl. Phys.* **49,** 2796.

Leamy, H. J. (1982). *J. Appl. Phys.* **53,** R51.

Lehmann, W. (1971). *J. Electrochem. Soc.* **118,** 1164.

Lehmann, W. (1981). *J. Electrochem. Soc.* **128,** 1787.

Levin, E. R., and Ladany, I. (1978). *J. Appl. Phys.* **49,** 3025.

Lesniak, M., Unvala, B. A., and Holt, D. B. (1984). *J. Microscopy* **135,** 255.

Li Kam Wa, P., Sitch, J. E., Mason, N. J., Roberts, J. S., Robson, P. N. (1985). *Electron. Lett.* **21,** 26.

Lin, W. N., and Wittry, D. B. (1976). *J. Appl. Phys.* **47,** 4129.

Liu, S. S., Cass, T. R., and Stevenson, D. A. (1977). *J. Electron. Mater.* **6,** 237.

Llopis, J., Ballesteros, C., Gonzalez, R., and Chen, Y. (1984). *J. Appl. Phys.* **56,** 460.

Llopis, J., Ballesteros, C., and Piqueras, J. (1985). *Phys. Stat. Sol.* **a90,** 359.

Llopis, J., and Piqueras, J. (1983). *J. Appl. Phys.* **54,** 4570.

Llopis, J., Piqueras, J., and Ballesteros, C. (1982). *Phys. Stat. Sol.* **a70,** 739.

Llopis, J., Piqueras, J., and Bru, L. (1978). *J. Mater. Sci.* **13,** 1361.

Löhnert, K., Hastenrath, M., Balk, L. J., and Kubalek, E. (1981). In *Microscopy of Semiconducting Materials* (IOP, Bristol), p. 179.

Löhnert, K., Hastenrath, M., and Kubalek, E. (1979). In *Scanning Electron Microscopy 1979/I*, ed. O. Johari, SEM Inc., Chicago, p. 229.

Löhnert, K., and Kubalek, E. (1983). In *Microscopy of Semiconducting Materials* (IOP, Bristol), p. 303.

Löhnert, K., and Kubalek, E. (1984). *Phys. Stat. Sol.* **a83,** 307.

Ludwig, G. W., and Kingsley, J. D. (1970). *J. Electrochem. Soc.* **117,** 348.

MacDonald, N. N., and Everhart, T. E. (1965). *Appl. Phys. Lett.* **7,** 267.

Maeda, K., Nakagawa, K., Takeuchi, S., and Sakamoto, K. (1981). *J. Mater. Sci.* **16,** 927.

Maeda, K., Sato, M., Kubo, A., and Takeuchi, S. (1983). *J. Appl. Phys.* **54,** 161.

Maeda, K., and Takeuchi, S. (1981). *Japan. J. Appl. Phys.* **20,** L165.

Maeda, K., and Takeuchi, S. (1983). *J. de Physique* **44,** C4-375.

Maestro, P. (1985). *J. Less-Common Metals* **111,** 43.

Magnea, N., Bensahel, D., and Pfister, J. C. (1979). *Solid State Commun.* **29,** 35.

Magnea, N., Petroff, P. M., Capasso, F., Logan, R. A., Alavi, K., and Cho, A. Y. (1985). *Appl. Phys. Lett.* **46,** 1074.

Mahajan, S., Chin, A. K., Zipfel, C. L., Brasen, D., Chin, B. H., Tung, R. T., and Nakahara, S. (1984). *Mater. Lett.* **2,** 184.

Mahr, H. (1962). *Phys. Rev.* **125,** 1510.

Mahr, H. (1963). *Phys. Rev.* **132,** 1880.

Mandel, G. (1964). *Phys. Rev.* **134,** A1073.

Mandel, G., Morehead, F., and Wagner, P. R. (1964). *Phys. Rev.* **136,** A826.

Marciniak, H. C., and Wittry, D. B. (1975). *J. Appl. Phys.* **46,** 4823.

Mardix, S., and Steinberger, I. T. (1970). *J. Appl. Phys.* **41,** 5339.

Marek, J., Geiss, R., Glassman, L. M., and Scott, M. P. (1985). *J. Electrochem. Soc.* **132,** 1502.

Markham, J. J. (1959). *Rev. Mod. Phys.* **31,** 956.

Marklund, S. (1983). *J. de Physique* **44,** Suppl. 9, p. C4–25.

Marshall, D. J. (1988). *Cathodoluminescence of Geological Materials,* Unwin Hyman, Winchester, Mass., 1988.

Marshall, D. J., Giles, J. H., and Mariano, A. (1987). In *Process Mineralogy VI,* ed. R. D. Hagni, Metallurgical Society of AIME, p. 117.

Matyi, R. G., Shichijo, H., Moore, T. M., and Tsai, H-L. (1987). *Appl. Phys. Lett.* **51,** 18.

McColl, J. R. (1982). *J. Electrochem. Soc.* **129,** 1546.

McKnight, S. W., and Palik, E. D. (1980). *J. Non-Cryst. Solids* **40,** 595.

Menniger, H., Voigt, G., Raidt, H., Fabig, H., and Maege, J. (1978). *Phys. Stat. Sol.* **a48,** 407.

Menzel, E., and Kubalek, E. (1979). In *Scanning Electron Microscopy 1979/I*, ed. O. Johari, SEM Inc., Chicago, p. 305.

Milnes, A. G. (1973). *Deep Impurities in Semiconductors,* Wiley, New York.

Milnes, A. G. (1983). In *Advances in Electronics and Electron Physics,* Vol. 61, Academic Press, New York.

Milnes, A. G. (1986). *Solid State Commun.* **29,** 99.

Mitchell, J. P., and Denure, D. G. (1973). *Solid-State Electron.* **16,** 825.

Miyazawa, S., Honda, T., Ishii, Y., and Ishida, S. (1984). *Appl. Phys. Lett.* **44,** 410.

Miyazawa, S., and Hyuga, F. (1986). *IEEE Trans. Electron Devices* **ED-33,** 227.

Miyazawa, S., and Ishii, Y. (1984). *IEEE Trans. Electron Devices* **ED-31,** 1057.

Miyazawa, S., Ishii, Y., Ishida, S., and Nanishi, Y. (1983). *Appl. Phys. Lett.* **43,** 853.

Miyazawa, S., and Wada, K. (1986). *Appl. Phys. Lett.* **48,** 905.

Monemar, B., and Lagerstedt, O. (1979). *J. Appl. Phys.* **50,** 6480.

Morehead, F. F., and Mandel, G. (1965). *Phys. Rev.* **137,** A924.

Muir, M. D., Grant, P. R., Hubbard, G., and Mundell, J. (1971). In *Proc. 4th Annual SEM Symp. (IITRI, Chicago),* p. 401.

Myhajlenko, S. (1984). In *Electron Microscopy and Analysis,* Inst. Phys. Conf. Ser. No. 68, p. 111.

Myhajlenko, S., Batstone, J. L., Hutchinson, H. J., and Steeds, J. W. (1984). *J. Phys. C: Solid State Phys.* **17,** 6477.

Myhajlenko, S., Davidson, S. M., and Hamilton, B. (1983b). In *Microscopy of Semiconducting Materials,* Oxford, p. 327.

Myhajlenko, S., and Ke, W. K. (1984). *J. Phys. E.: Sci. Instrum.,* **17,** 200.

Myhajlenko, S., Ke, W., and Hamilton, B. (1983a). *J. Appl. Phys.* **54,** 862.

Nabarro, F. R. N., ed. (1979–1983). *Dislocations in Solids,* Vols. I–VI, North-Holland, Amsterdam.

Nanishi, Y., Ishida, S., Honda, T., Yamazaki, H., and Miyazawa, S. (1982). *Jpn. J. Appl. Phys.* **21,** L335.

Neumark, G. F., and Kosai, K. (1983). In *Semiconductors and Semimetals,* Vol. 19, eds. R. K. Willardson and A. C. Beer, Academic Press, New York, p. 1.

Newbury, D. E., Joy, D. C., Echlin, P., Fiori, C. E., and Goldstein, J. I. (1986). *Advanced Scanning Electron Microscopy and X-ray Microanalysis,* Plenum, New York.

Nickel, E. (1978). *Minerals Sci. Engng.* **10,** 73.

Niedrig, H. (1982). *J. Appl. Phys.* **53,** R15.

Norris, C. B. (1980). *J. Appl. Phys.* **51,** 1998.

Norris, C. B. (1982a). *J. Appl. Phys.* **53,** 5172.

Norris, C. B. (1982b). *J. Appl. Phys.* **53,** 5177.

Norris, C. B., and Barnes, C. E. (1980). *J. Appl. Phys.* **51,** 5764.

Norris, C. B., Barnes, C. E., and Beezhold, W. (1973). *J. Appl. Phys.* **44,** 3209.

Norris, C. B., Barnes, C. E., and Zanio, K. R. (1977). *J. Appl. Phys.* **48,** 1659.

Norris, C. B., and Peercy, P. S. (1981). *Appl. Phys. Lett.* **39,** 351.

Norris, C. B., and Peercy, P. S. (1983). *Radiation Effects* **69,** 267.

Oda, S., Akagi, K., Kukimoto, H., and Nakayama, T. (1978). *J. Luminescence* **16,** 323.

Oelgart, G., Haefner, H., Reulke, R., and Joachim, F. (1982). *Phys. Stat. Sol.* **a71,** 89.

Okamoto, F., Oka, T., and Kato, K. (1982). *Japan. J. Appl. Phys.* **21,** 1135.

Ouweltjes, J. L. (1965). In *Modern Materials,* Vol. 5, ed. B. W. Gonser, Academic Press, New York.

Pankove, J. I. (1966). *J. Phys. Soc. (Jpn.)* **21,** 298.

Pankove, J. I. (1971). *Optical Processes in Semiconductors,* Dover, New York.

Pankove, J. I., ed. (1984). In *Semiconductors and Semimetals,* Vol. 21, eds. R. K. Willardson and A. C. Beer, Academic Press, New York.

Pappalardo, R. G. (1987). In *Spectroscopy of Solid-State Laser-Type Materials,* ed. B. Di Bartolo, Plenum, New York.

Park, Y. S., and Shin, B. K. (1977). In Topics in Applied Physics, Vol. 17, ed. J. I. Pankove, Springer, Berlin, p. 133.

Pasemann, L., and Hergert, W. (1986). *Ultramicroscopy* **19,** 15.

Pautrat, J. L., Magnea, N., and Faurie, J. P. (1982). *J. Appl. Phys.* **53,** 8668.

Pawley, J. (1984). In *Proc. 42nd Ann. Meet. Electron Microscopy Society of America,* p. 440.

Pecheur, P., Kauffer, E., and Gerl, M. (1977). In *Radiation Effects in Semiconductors 1976,* Conf. Series No. 31, Inst. Phys. Bristol and London, p. 458.

Pennycook, S. J., and Brown, L. M. (1979). *J. Luminescence* **18/19,** 905.

Pennycook, S. J., Brown, L. M., and Craven, A. J. (1980). *Philos. Mag.* **A41,** 589.

Pennycook, S. J., Craven, A. J., and Brown, L. M. (1977). In *Developments in Electron Microscopy and Analysis,* Inst. Phys. Conf. Ser. No. 36, London, p. 69.

Pennycook, S. J., and Howie, A. (1980). *Philos. Mag.* **41,** 809.

Petroff, P. M. (1981). In *Defects in Semiconductors,* eds. J. Narayan and T. Y. Tan, North-Holland, Amsterdam, p. 457.

Petroff, P. M. (1985). In *Microscopic Identification of Electronic Defects in Semiconductors,* Vol. 46, eds. N. M. Johnson, S. G. Bishop, and G. D. Watkins, Materials Research Society, Pittsburgh, PA, p. 433.

Petroff, P. M. (1987). In *Microscopy of Semiconducting Materials* (IOP, Bristol), p. 187.

Petroff, P. M., Cibert, J., Gossard, A. C., Dolan, G. J., and Tu, C. W. (1987). *J. Vac. Sci. Technol.* **B5,** 1204.

Petroff, P. M., and Lang, D. V. (1977). *Appl. Phys. Lett.* **31,** 60.

Petroff, P. M., Lang, D. V., Strudel, J. L., and Logan, R. A. (1978). In *Scanning Electron Microscopy 1978*/I, ed. O. Johari, SEM Inc., Chicago, p. 325.

Petroff, P. M., and Logan, R. A. (1980). *J. Vac. Sci. Technol.* **17,** 1113.

Petroff, P. M., Logan, R. A., and Savage, A. (1980a). *J. Microscopy* **118,** 255.

Petroff, P. M., Logan, R. A., and Savage, A. (1980b). *Phys. Rev. Lett.* **44,** 287.

Petroff, P. M., Miller, R. C., Gossard, A. C., and Wiegmann, W. (1984). *Appl. Phys. Lett.* **44,** 217.

Petroff, P. M., Weisbuch, C., Dingle, R., Gossard, A. C., and Wiegmann, W. (1981). *Appl. Phys. Lett.* **38,** 965.

Pfefferkorn, G., Bröcker, W., and Hastenrath, M. (1980). In *Scanning Electron Microscopy 1980*/I, ed. O. Johari (IOP, Bristol), p. 251.

Pfister, J. C. (1980). *Rev. Phys. Appl.* **15,** 707.

Pierce, B. J., and Hengehold, R. L. (1976). *J. Appl. Phys.* **47,** 644.

Piqueras, J., and Kubalek, E. (1985a). *Solid State Commun.* **54,** 745.

Piqueras, J., and Kubalek, E. (1985b). *Phys. Stat. Sol.* **a91,** 569.

Pollak, F. H., and Cardona, M. (1968). *Phys. Rev.* **172,** 816.

Prener, J. S., and Williams, F. E. (1956). *J. Chem. Phys.* **25,** 361.

Rao-Sahib, T. S., and Wittry, D. B. (1969). *J. Appl. Phys.* **40,** 3745.

Rao-Sahib, T. S., and Wittry, D. B. (1974). *J. Appl. Phys.* **45,** 5060.

Rasul, A., and Davidson, S. M. (1977a). In *Gallium Arsenide and Related Compounds* (IOP, Bristol), p. 306.

Rasul, A., and Davidson, S. M. (1977b). In *Scanning Electron Microscopy 1977*/I, ed. O. Johari, SEM Inc., Chicago, p. 233.

Ray, B. (1969). *II-VI Compounds,* Pergamon, Oxford.

Reimer, L. (1985). *Scanning Electron Microscopy,* Springer-Verlag, New York.

Remond, G. (1977). *J. Luminescence* **15,** 121.

Reynolds, D. C., and Collins, T. C. (1981). *Excitons, Their Properties and Uses,* Academic, New York.

Richards, B. P., Trigg, A. D., and King, W. G. (1984). *Scanning* **6,** 8.

Rincon, J. M., Fernandez, P., and Llopis, J. (1987). *Appl. Phys.* **A44,** 299.

Robbins, D. J. (1980). *J. Electrochem. Soc.* **127,** 2694.

Robbins, D. J., and Dean, P. J. (1978). *Advances in Phys.* **27,** 499.

Roberts, S. H., Grande, M., and Dean, P. J. (1983). In *Microscopy of Semiconducting Materials* (IOP, Bristol), p. 337.

Roberts, S. H., and Steeds, J. W. (1982). *J. Crystal Growth* **59,** 312.

Robins, L. H., Cook, L. P., Farabaugh, E. N., and Feldman, A. (1989). *Phys. Rev.* B **39,** 13367.

Roedel, R. J., Von Neida, A. R., Caruso, R., and Dawson, L. R. (1977). *Extended Abstracts,* Vol. 77-2, Electrochemical Society, Princeton, N.J., p. 857.

Rose, A. (1963). *Concepts in Photoconductivity and Allied Problems,* Wiley, New York.

Rosencwaig, A. (1982). *Science* **218,** 223.

Rosencwaig, A., and White, R. M. (1981). *Appl. Phys. Lett.* **38,** 165.

Russell, G. J., Waite, P., and Woods, J. (1981). In *Microscopy of Semiconducting Materials* (IOP, Bristol), p. 371.

Saba, F. M., and Holt, D. B. (1985). In *Microscopy of Semiconducting Materials* (IOP, Bristol), p. 389.

Sakaki, H. (1980). *Japan. J. Appl. Phys.* **19,** L735.

Samuel, L., Brada, Y., Burger, A., and Roth, M. (1987). *Phys. Rev.* B **36,** 1174.

Sauer, R., Weber, J., Stolz, J., Weber, E. R., Kusters, K. H., and Alexander, H. (1985). *Appl. Phys.* **A36,** 1.

Schick, J. D. (1981). In *Scanning Electron Microscopy 1981*/I, ed. O. Johari, SEM Inc., Chicago, p. 295.

Schick, J. D. (1985). In *Scanning Electron Microscopy 1985*/I, ed. O. Johari, SEM Inc., Chicago, p. 55.

Schiller, C., and Boulou, M. (1975). *Philips Tech. Rev.* **35,** 239.

Schneider, J., Holton, W. C., Estle, T. L., and Rauber, A. (1963). *Phys. Lett.* **5,** 312.

Schneider, J., Rauber, A., Dischler, B., Estle, T. L., Holton, W. C. (1965). *J. Chem. Phys.* **42,** 1839.

Schneider, J., and Rauber, A. (1967). *Solid State Commun.* **5,** 779.

Seiler, H. (1983). *J. Appl. Phys.* **54,** R1.

Shachar, G., Brada, Y., Alexander, E., and Yacoby, Y. (1970). *J. Appl. Phys.* **41,** 723.

Shaw, D. A., and Thornton, P. R. (1968). *J. Mater. Sci.* **3,** 507.

Sheldon, P., Dick, J. R., and Hayes, R. E. (1985a). *J. Vac. Sci. Technol.* **A3,** 883.

Sheldon, P., Jones, K. M., Al-Jassim, M. M., and Yacobi, B. G. (1988). *J. Appl. Phys.* **63,** 5609.

Sheldon, P., Yacobi, B. G., Jones, K. M., and Dunlavy, D. J. (1985b). *J. Appl. Phys.* **58,** 4186.

Shimizu, R., Ikuta, T., Everhart, T. E., and DeVore, W. J. (1975). *J. Appl. Phys.* **46,** 1581.

Shionoya, S. (1966). In *Luminescence of Inorganic Solids,* ed. P. Goldberg, Academic Press, New York, p. 205.

Shionoya, S., Koda, T., Era, K., and Fujiwara, H. (1964). *J. Phys. Soc. Japan* **19,** 1157.

Shockley, W. (1950). *Electrons and Holes in Semiconductors,* Van Nostrand, Princeton.

Shockley, W., and Read, W. T. (1952). *Phys. Rev.* **87,** 835.

Simmons, J. G., and Taylor, G. W. (1971). *Phys. Rev.* **B4,** 502.

Sippel, R. F. (1968). In *Proc. Internat. Conf. Luminescence, 1966,* Vol. 2, p. 2079.

Skeats, A. P., Wakefield, B., and Robertson, M. J. (1983). *J. Appl. Phys.* **54,** 1232.

Skettrup, T. (1978). *Phys. Rev.* **B18,** 2622.

Skuja, L. N., and Entzian, W. (1986). *Phys. Stat. Sol.* **a96,** 191.

Spitzer, W. G. (1967). In *Semiconductors and Semimetals,* Vol. 3, eds. R. K. Willardson and A. C. Beer, Academic Press, New York, p. 17.

Steckenborn, A. (1980). *J. Microscopy* **118,** 297.

Steckenborn, A., Munzel, H., and Bimberg, D. (1981a). In *Microscopy of Semiconducting Materials* (IOP, Bristol), p. 185.

Steckĕnborn, A., Munzel, H., and Bimberg, D. (1981b). *J. Luminescence* **24/25,** 351.

Steeds, J. W. (1989). *Rev. Phys. Appl.* **24,** C6–65.

Steele, I. M. (1986). *American Mineralogist* **71,** 966.

Stevens, M. T. (1978). *J. Electrochem. Soc.* **125,** 288.

Steyn, J. B., Giles, P., and Holt, D. B. (1976). *J. Microscopy* **107,** 107.

Stierwalt, D. L., and Potter, R. F. (1967). In *Semiconductors and Semimetals,* Vol. 3, eds. R. K. Willardson and A. C. Beer, Academic Press, New York, p. 71.

Stirland, D. J., Grant, I., Brozel, M. R., and Ware, R. M. (1983). In *Microscopy of Semiconducting Materials* (IOP, Bristol), p. 285.

Stoneham, A. M. (1975). *Theory of Defects in Solids,* Oxford University, Oxford.

Street, R. A. (1976). *Advances in Physics* **25,** 397.

Street, R. A., Searle, T. M., and Austin, I. G. (1975). *Philos. Mag.* **32,** 431.

Swaminathan, V., Anthony, P. J., Pawlik, J. R., and Tsang, W. T. (1983). *J. Appl. Phys.* **54,** 2623.

Suezawa, M., Sasaki, Y., and Sumino, K. (1983). *Phys. Stat. Sol.* **a79,** 173.

Sumi, H., and Toyozawa, Y. (1971). *J. Phys. Soc. Jpn.* **31,** 342.

Sumida, N., and Lang, A. R. (1981). *Philos. Mag.* **43,** 1277.

Sze, S. M. (1981). *Physics of Semiconductor Devices,* Wiley, New York.

Theis, D. (1977). *J. Phys. Chem. Solids* **38,** 1125.

Theis, D., and Wengert, R. (1985). *J. Electrochem. Soc.* **132,** 2507.

Thomas, A. E., Russell, G. J., and Woods, J. (1984). *J. Phys. C: Solid State Phys.* **17,** 6219.

Thomson, J. J. (1897). *Philos. Mag.* **44,** 293.

Thurmond, C. D. (1975). *J. Electrochem. Soc.* **122,** 1133.

Titchmarsh, J. M., Booker, G. R., Harding, W., and Wight, D. R. (1977). *J. Mater. Sci.* **12,** 341.

Title, R. S., Morehead, F., and Mandel, G. (1964). *Phys. Rev.* **136,** A300.

Toyozawa, Y. (1959). *Progress Theoret. Phys. (Kyoto)* **22,** 455; Suppl. 12, 111.

Toyozawa, Y. (1964). Institute for Solid State Physics, Tokyo Technical Report A119 (unpublished).

Trigg, A. D. (1985). In *Scanning Electron Microscopy 1985*/III, ed. O. Johari, SEM Inc., Chicago, p. 1011.

Trigg, A. D., and Richards, B. P. (1982). *IEE Proc.* **129,** 33.

Urbach, F. (1953). *Phys. Rev.* **92,** 1324.

Vale, B. H., and Greer, R. T. (1977). In *Scanning Electron Microscopy 1977*/I, ed. O. Johari, SEM Inc., Chicago, p. 241.

Van Bueren, H. G. (1960). *Imperfections in Crystals,* North-Holland, Amsterdam.

Van Gool, W. (1961). *Philips Res. Repts. Suppl.* **3,** 1.

Van Opdorp, C. (1977). *Phillips Res. Repts.* **32,** 192.

Van Roosbroeck, W. (1955). *J. Appl. Phys.* **26,** 380.

Van Roosbroeck, W., and Shockley, W. (1954). *Phys. Rev.* **94,** 1558.

Varshni, Y. P. (1967). *Physica* **34,** 149.

Vavilov, V. S., Gippius, A. A., Zaitsev, A. M., Deryagin, B. V., Spitsyn, B. V., and Aleksenko, A. E. (1980). *Sov. Phys. Semicond.* **14,** 1078.

Velednitskaya, M. A., Rozhanskii, V. N., Comolova, L. F., Saparin, G. V., Schreiber, J., and Brummer, O. (1975). *Phys. Stat. Sol.* **a32,** 123.

Veth, H., and Teichler, H. (1984). *Philos. Mag.* **B49,** 371.

Vine, J., and Einstein, P. A. (1964). *Proc. IEE* **111,** 921.

Viturro, R. E., Shaw, J. L., and Brillson, L. J. (1987b). *J. Vac. Sci. Technol.* **B5,** 1125.

Viturro, R. E., Shaw, J. L., Brillson, L. J., Woodall, J. M., Kirchner, P. D., Pettit, G. D., and Wright, S. L. (1988b). *J. Vac. Sci. Technol.* **B6,** 1397.

Viturro, R. E., Shaw, J. L., Mailhiot, C., Brillson, L. J., Tache, N., McKinley, J., Margaritondo, G., Woodall, J. M., Kirchner, P. D., Pettit, G. D., and Wright, S. L. (1988a). *Appl. Phys. Lett.* **52,** 2052.

Viturro, R. E., Slade, M. L., and Brillson, L. J. (1986). *Phys. Rev. Lett.* **57,** 487.

Viturro, R. E., Slade, M. L., and Brillson, L. J. (1987a). *J. Vac. Sci. Technol.* **A5,** 1516.

Von Roos, O. (1983). *J. Appl. Phys.* **54,** 1390.

Wada, K., Kozen, A., Fushimi, H., and Inoue, N. (1988). *Japan. J. Appl. Phys.* **27,** L1952.

Wakefield, B. (1983). In *Microscopy of Semiconducting Materials* (IOP, Bristol), p. 315.

Wakefield, B., and Davey, S. T. (1985). In *Microscopy of Semiconducting Materials* (IOP, Bristol), p. 373.

Wakefield, B., Eaves, L., Prior, K. A., Nelson, A. W., and Davies, G. J. (1984b). *J. Phys. D: Appl. Phys.* **17,** L133.

Wakefield, B., Leigh, P. A., Lyons, M. H., and Elliot, C. R. (1984a). *Appl. Phys. Lett.* **45,** 66.

Walker, J. (1979). *Rep. Prog. Phys.* **42,** 1606.

Wang, F. C., and Bujatti, M. (1984). *IEEE Electron. Device Lett.* **EDL-5,** 188.

Warwick, C. A. (1986). *J. Appl. Phys.* **59,** 4182.

Warwick, C. A. (1987). Scanning Microscopy, Vol. 1, Scanning Microscopy International, Chicago, p. 51.

Warwick, C. A., and Booker, G. R. (1983). In *Microscopy of Semiconducting Materials* (IOP, Bristol), p. 321.

Warwick, C. A., and Brown, G. T. (1985). *Appl. Phys. Lett.* **46,** 574.

Warwick, C. A., Gill, S. S., Wright, P. J., and Cullis, A. J. (1985). In *Microscopy of Semiconducting Materials* (IOP, Bristol), p. 365.

Warwick, C. A., Kitching, S. A., Allenson, M., Gill, S. S., and Woodward, J. (1987). In *Microscopy of Semiconducting Materials* (IOP, Bristol), p. 757.

Werkhoven, C., Van Opdorp, C., and Vink, A. T. (1978/79). *Philips Technical Review* **38,** 41.

Williams, E. W., and Bebb, H. B. (1972). In *Semiconductors and Semimetals,* Vol. 8, R. K. Willardson and A. C. Beer, Editors, Academic Press, New York, p. 321.

Williams, P. M., and Yoffe, A. D. (1968). *Philos. Mag.* **18,** 555.

Williams, P. M., and Yoffe, A. D. (1969a). *Nature* **221,** 952.

Williams, P. M., and Yoffe, A. D. (1969b). *Radiation Effects* **1,** 61.

Williams, P. M., and Yoffe, A. D. (1971). *Radiation Effects* **9,** 139.

Winston, H. V., Hunter, A. T., Olsen, H. M., Bryan, R. P., and Lee, R. E. (1984). *Appl. Phys. Lett.* **45,** 447.

Wittry, D. B. (1958). *J. Appl. Phys.* **29,** 1543.

Wittry, D. B. (1966). *Appl. Phys. Lett.* **8,** 142.

Wittry, D. B. (1982). In *Electron Beam Interactions with Solids for Microscopy, Microanalysis and Microlithography,* eds. D. F. Kyser, H. Niedrig, D. E. Newbury, and R. Shimizu, SEM, Inc., Chicago, p. 99.

Wittry, D. B. (1984). *J. Phys. (Paris)* **45,** Suppl. 2, C2–855.

Wittry, D. B., and Kyser, D. F. (1964). *J. Appl. Phys.* **35,** 2439.

Wittry, D. B., and Kyser, D. F. (1965). *J. Appl. Phys.* **36,** 1387.

Wittry, D. B., and Kyser, D. F. (1966). *J. Phys. Soc. Japan* **21,** Suppl. p. 312.

Wittry, D. B., and Kyser, D. F. (1967). *J. Appl. Phys.* **38,** 375.

Woodcock, J. M., Shannon, J. M., and Clark, D. J. (1975). *Solid State Electronics* **18,** 267.

Woodham, R. G., and Booker, G. R. (1987). In *Microscopy of Semiconducting Materials,* Oxford, p. 781.

Woods, G. S., and Lang, A. R. (1975). *J. Crystal Growth.* **28,** 215.

Wu, C. J., and Wittry, D. B. (1978). *J. Appl. Phys.* **49,** 2827.

Yacobi, B. G. (1980). *Phys. Rev. B* **22,** 1007.

Yacobi, B. G. (1980). *Phys. Rev. B* **22,** 1007.

Yacobi, B. G. (1985). In *Microscopy of Semiconducting Materials* (IOP, Bristol), p. 349.

Yacobi, B. G., Datta, S., and Holt, D. B. (1977). *Philos. Mag.* **35,** 145.

Yacobi, B. G., Elman, B., Jagannath, C., Masum Choudhury, A. N. M., and Urban, M. (1988b). *Appl. Phys. Lett.* **52,** 1806.

Yacobi, B. G., and Herrington, C. R. (1985). *J. Electron Microscopy Techn.* **2,** 509.

Yacobi, B. G., and Herrington, C. R. (1986). *J. Electron Microscopy Techn.* **3,** 343.

Yacobi, B. G., and Holt, D. B. (1986). *J. Appl. Phys.* **59,** R1.

Yacobi, B. G., Jagannath, C., Zemon, S., and Sheldon, P. (1988a). *Appl. Phys. Lett.* **52,** 555.

Yacobi, B. G., Zemon, S., Jagannath, C., and Sheldon, P. (1989). *J. Crystal Growth* **95,** 240.

Yacobi, B. G., Zemon, S., Norris, P., Jagannath, C., and Sheldon, P. (1987). *Appl. Phys. Lett.* **51,** 2236.

Yamaguchi, M., Yamamoto, A., and Itoh, Y. (1986). *J. Appl. Phys.* **59,** 1751.

Yamaguchi, M., Yamamoto, A., Tachikawa, M., Itoh, Y., and Sugo, M. (1988). *Appl. Phys. Lett.* **53,** 2293.

Yamamoto, N., Spence, J. C. H., and Fathy, D. (1984). *Philos. Mag.* **B49,** 609.

Yao, T., Okada, Y., Kawanami, H., Matsui, S., Imagawa, A., and Ishida, K. (1987). In *Heteroepitaxy on Silicon II,* eds. F. C. C. Fan, J. M. Phillips, and B-Y. Tsaur, Materials Research Society, Pittsburgh, PA, p. 63.

Yin, S. Y., and Wittry, D. B. (1983). *J. Appl. Phys.* **54,** 360.

Yoffe, A. D., Howlett, K. J., and Williams, P. M. (1973). In *Proc. VIth Ann. SEM Symp.,* IITRI, Chicago, p. 301.

Yoshida, S., Sakuma, E., Misawa, S., and Gonda, S. (1984). *J. Appl. Phys.* **55,** 169.

Zemon, S., Jagannath, C., Koteles, E. S., Shastry, S. K., Norris, P., Lambert, G., Choudhury, A. N. M., and Armiento, C. A. (1987). In *Gallium Arsenide and Related Compounds, 1986,* ed. W. T. Lindley (IOP, Bristol), p. 141.

Zemon, S., Shastry, S. K., Norris, P., Jagannath, C., and Lambert, G. (1986). *Solid State Commun.* **58,** 457.

Index